Aerodynamic loads on slender wings in unsteady motion measured by a new technique.

Cadwallader, R.

Award date:
1975

Awarding institution:
University of Bath

AERODYNAMIC LOADS ON SLENDER WINGS IN UNSTEADY MOTION MEASURED BY A NEW TECHNIQUE

submitted by R. CADWALLADER B.Sc.

for the degree of Doctor of Philosopy

of the University of Bath

1 9 7 5

R. Cadwallader

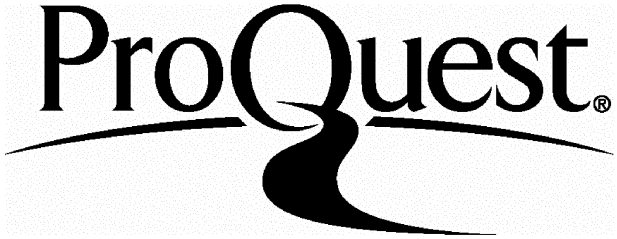

SUMMARY

An experiment has been performed to demonstrate the use of a new technique for measuring the unsteady longitudinal derivatives of slender wings at low speeds. The technique used a stationary fluid medium, water, and a model wing was towed through the water with its flight path constrained to follow a fixed cam rail. The normal force and pitching moment on the wing were measured by strain gauges fixed to its sting support.

The new technique had the following advantages over traditional oscillatory methods:

(i) The ratio of aerodynamic forces to inertia forces was high because water was used as the fluid.

(ii) It was able to discriminate the $\dot{w}$, q and $\dot{\theta}$ derivatives.

(iii) Any non-linearity in the derivatives could be studied without interference of transient effects.

The longitudinal derivatives $z_{\dot{w}}$, z_q, $z_{\dot{\theta}}$, $m_{\dot{w}}$, m_q, $m_{\dot{\theta}}$, for the AGARD model G planform were measured but there was a good deal of experimental scatter, particularly in the z derivatives. The m derivatives compared well with results from oscillatory tests but the z derivatives did not compare so well. A correlation was obtained between the theoretical virtual mass and the transient behaviour of the normal force at the start of the plunging and constant q manoeuvres. The derivatives which cannot normally be measured independently, z_q and m_q, were measured to a better degree of accuracy than the other derivatives.

Photographs of the paths of the vortex cores were obtained using the hydrogen bubble technique. The photographs were not of sufficient accuracy to enable a correlation to be made with the strain gauge measurements but a difference in the position of the vortices for positive and negative pitching rates was observed.

It was concluded that the new technique could be successfully applied to the measurement of the derivatives for a slender wing but that modifications would be necessary to improve the precision of the measurements.

CONTENTS

APPENDICES

LIST OF TABLES

LIST OF FIGURES

LIST OF SYMBOLS

		Units
A	Aspect ratio $= b^2/S$	-
b	Wing span $= 2s$	in, cm
C_N	Normal force coefficient	-
$C_{M.733c_o}$	Pitching moment coefficient measured about $0.733c_o = \frac{M_{.733c_o}}{\frac{1}{2}\rho V^2 S c_o}$	-
$C_{M.795c_o}$	Pitching moment coefficient measured about $0.795c_o = \frac{M_{.795c_o}}{\frac{1}{2}\rho V^2 S c_o}$	-
c_o	Centre line chord length	in, cm
c	mean chord length	in, cm
D	D-operator for differential equations	-
E	Young's Modulus	$lbf/in^2, N/m^2$
I	Second moment of area	in^4, cm^4
l	Length of horizontal linkage arm	in, cm
M	Pitching moment	lbfin, Nm
m	Virtual mass	slugs, Kg
$m_{\dot{w}}$	Pitching moment derivative $= \frac{\Delta C_M}{\dot{w}c_o/V^2}$	-
m_q	Pitching moment derivative $= \frac{\Delta C_M}{qc_o/V}$	-
$m_{\dot{\theta}}$	Pitching moment derivative $= \frac{\Delta C_M}{\dot{\theta}c_o/V}$	-
N	Normal force	lbf, N
q	Pitching rate at constant incidence (i.e. $q = \dot{\gamma}$ WHEN $\dot{\alpha} = 0$)	deg/sec or rad/sec
S	Wing area	in^2, cm^2
s	Wing semi-span	in, cm
t	Time	sec
V	Free stream speed	ft/sec, m/sec
u	Horizontal speed of trolley	ft/sec, m/sec

W	Weight	lbf,N
w	Vertical speed	ft/sec,m/sec
$\dot{w}$	Vertical acceleration	ft/sec,m/sec
x	Horizontal distance	in,cm
Z	Force in direction of Z axis	lbf,N
z	Vertical distance	in,cm
$z_{\dot{w}}$	Normal force derivative $= \frac{\Delta C_N \cos\alpha_o}{\dot{\omega} c_o / V^2}$	-
z_q	Normal force derivative $= \frac{\Delta C_N \cos\alpha_o}{q c_o / V}$	-
$z_{\dot{\theta}}$	Normal force derivative $= \frac{\Delta C_N \cos\alpha_o}{\dot{\theta} c_o / V}$	-
α	Wing incidence	deg,rad
γ	Flight path angle	deg,rad
θ	Attitude	deg,rad
ν	Kinematic viscosity	$ft^2/sec, m^2/sec$
ρ	Density	$slug/ft^3, Kg/m^3$

1. INTRODUCTION

The behaviour of aircraft in response to atmospheric turbulence and to the controls is an important ingredient in their safe and efficient operation. At the design stage it is necessary to solve the aerodynamic equations of motion which describe the response, and in order to do this, estimates of the aerodynamic derivatives must be available. The complete stability matrix covers both lateral and longitudinal derivatives but here the longitudinal derivatives due to $\dot{w}$, q, $\dot{\theta}$ only have been considered.

In the past, the longitudinal derivatives of aircraft with high aspect ratio wings and conventional tailplanes were relatively easy to predict because most of the pitching derivative came from the tailplane and the wing contribution was usually less than 10% (ref. 1). The $\dot{w}$ derivative was small and linear lifting surface theory was adequate for its estimation. There was also a great deal of flight test data of similar planforms which could be used.

As speeds grew higher and wing sweep angles became larger the contribution of the wing increased. For tailless aircraft, such as Concorde, the wing contribution to the derivatives became all-important. This type of aircraft is characterised by poor damping in pitch, leading to a poorly damped short period oscillation (ref. 2). Two slender wing

research aircraft, the BAC221 and HP115, have contributed greatly to knowledge of this type of aircraft and the imminent introduction of Concorde and Tu144 into airline service will further this knowledge. Owing to the comparatively small number of slender wing designs so far flown however, there is a lack of flight test data to carry over to new designs. Methods of prediction are mostly based on linear theories ranging from the simple slender wing theory of Jones (ref. 3), through the lifting surface theory of Garner (ref.4), to the indicial aerodynamic theories of Watkins (ref. 5), Tobak (ref. 6) and others. Many of these are only applicable to a particular range of frequencies. More recently Garner and Lehrian (ref.7) have produced a theory which is valid for any frequency. Randall (ref. 8) has developed a non-linear theory based on the separated flow model of Brown and Michael (ref. 9). Whilst this evolution has led to improved accuracy, model tests are still necessary to provide definitive results, particularly where the effects of nacelles, forebodies etc. are present.

Accepting the need for model tests, there have traditionally been two methods:

(i) Free flight. This has been used by Turner, Ross and Edwards (ref. 10) for the AGARD model G planform at transonic speeds. This method has the advantages that there are no wall effects, particularly important at

transonic speeds, and that it is possible to obtain the complete aircraft response. The tests have to be carried out on an opportunity basis, however, and the yield of data in a reasonable timescale is poor. In addition, the test conditions cannot be controlled to the same extent as in a wind tunnel.

(ii) Sinusoidal oscillation in a wind tunnel. This can be done by a free vibration technique whereby the damping derivatives are found by measuring the rate of decay of oscillations, though it is more usual nowadays to use a forced vibration method. The resultant force and its phase angle are measured, the quadrature component giving the damping derivative and the in-phase component giving the sum of the mechanical stiffness and normal acœleration derivatives. A summary of the experimental techniques has been given by Bratt (ref. 11). The forced vibration method has been applied to slender wings by Wright (ref. 12) and Thompson and Fail (ref. 13). This technique, although the most commonly used, has the following drawbacks:

(a) To obtain measurable aerodynamic loads in a wind tunnel, high pitching and heaving rates must be used which, in turn, give large model inertia effects. The model inertias are usually eliminated by measuring the derivatives wind-off.

This still involves the acceleration of a mass of air, the so called 'virtual mass', the theory of which is itself not firmly established.

(b) $\dot{\theta}$ and $\dot{w}$ are changing continually during the cycle so that any derivatives which are time dependent will also be frequency dependent. This effect is usually investigated by testing at different frequencies. For some of the derivatives the frequency effect is not significant, while for others, such as the $\dot{w}$ derivatives, there is a marked frequency effect (ref. 14). For wings with non-linear lift characteristics such as those considered here, the derivatives also vary with the amplitude, so that further tests have to be made using different amplitudes. Since rigid body frequencies for real aircraft tend to be rather lower than the frequencies desirable for wind-tunnel work, there is a problem of extrapolating data which includes transient effects. In addition, the assumption that the derivative is independent of rate is usually made to facilitate the analysis of the results, so that any non-linearity is obscured.

(c) Using a stationary model it is difficult to measure all the derivatives required. In particular, for longitudinal motion, it is not normally possible to separate the $\dot{w}$

derivative and the q derivative. Usually, a heaving or pitching oscillation is performed and it is assumed that the pure pitching derivative (changing attitude without changing incidence) is the difference between the $\dot{w}$ and $\dot{\theta}$ derivatives. As there are large model inertia effects in the $\dot{w}$ derivatives it is difficult to measure these accurately. At Cornell Aeronautical Laboratory, Statler, Tufts and Hirtreiter (ref. 15) developed a facility which was able to simulate pure pitching motion by using a sting driven by two eccentrics. It was able to simulate any combination of heaving and pitching in sinusoidal oscillation and therefore measure the derivatives separately. The results were inconclusive, however, the $\dot{w}$ derivatives in particular being very inaccurate.

The programme of this present research began when in 1970 Wingham (ref. 16) proposed a new technique for measuring the longitudinal derivatives of slender wings. The aim was to over come the major drawbacks of existing methods using simple and inexpensive apparatus and instrumentation. He proposed using a stationary fluid medium, water, and a moving model. Because of the low Reynolds number at practicable speeds, this method is only applicable to slender sharp-edged wings whose flow pattern is not sensitive to changes in Reynolds number.

Furthermore, the flow is incompressible so that the region of most current practical interest, the transonic regime, cannot be studied. Despite these drawbacks, this technique has several major advantages over the oscillatory technique:

(i) Water provides large aerodynamic forces at low speeds so that the aerodynamic forces are much bigger than the model inertia forces.

(ii) Any flight path encountered in real flight, including horizontal acceleration, can be simulated under controlled test conditions enabling easy separation of the effects of fundamental unsteady motions.

(iii) No oscillation is involved so that non-linear aerodynamic derivatives and transient effects can be studied.

The basic principles of this technique are shown diagrammatically in Fig. 2.01. The model was sting mounted, the sting being carried on a parallel linkage. The flight path and attitude of the model were controlled by a cam rail acting through the parallel linkage. The forces on the model were measured by strain gauges attached to the sting.

The emphasis of this research was on development and proving of the new technique by measuring the longitudinal aerodynamic derivatives of a slender sharp-edged wing having an AGARD Model G planform. Measurements from oscillatory tests were to be used as a comparison for the derivatives. Since very few

results were available for the $\dot{w}$ derivatives and none at all for the q derivatives, theoretical values were to be used for comparison. The tank readily lent itself to the application of flow visualisation techniques and it was hoped to obtain a correlation between the measured forces and moments and the positions of the leading edge vortex cores.

The research was sponsored by MOD(PE) and the author received a SRC studentship.

2. DESCRIPTION OF THE SYSTEM

2.1 General layout

The basic principles of the apparatus are shown schematically in Fig. 2.01. The model was carried through the water on a strain gauged sting which measured the normal force and pitching moment exerted on the model by the water. The sting was connected via a parallel linkage to a cam rail which controlled the flight path and incidence of the model. The linkage was free to slide vertically on a trolley travelling along horizontal rails. A drawing of the complete system is shown in Fig. 2.02 and photographs of the system in Figs. 2.03, 2.04, 2.05. The system can be divided into five main elements

(i) the tank

(ii) the trolley and parallel linkage

(iii) the cam rail

(iv) the winching system

(v) instrumentation

The facility was designed to allow flow visualisation techniques to be used. This is described more fully in Chapter 5.

2.2. Specification of unsteady motions

Before embarking on the design it was necessary to determine the range of parameters which would approximate to real flight conditions. A model with a root chord of 6in(15.2cm) travelling at

5ft/sec (1.52m/sec) was originally selected to give adequate forces with a reasonable size of facility. This speed was later found to be too high and a speed of 2.8ft/sec (0.85m/sec) was used. This gave a Reynolds number, based on root chord c_o, of 1.138×10^5. As explained in the introduction, this was very low but was adequate to give separated flow on a sharp edged model.

To provide a basis for determining the range of movement of the model, the take-off manoeuvre was selected as a typical example of unsteady motion: a study of ref. 17 showed that, during this manoeuvre, incidence and attitude may change by about $\frac{1}{2}$ deg. per chord length travelled. Also, forward speed and vertical speed may change by about 1% per chord length travelled. It was originally intended to test at up to four times these rates, ie. 2 deg. per chord length travelled, but it was found to be difficult to set the rail sufficiently accurately to measure any derivatives much below this rate. In the end the highest rate used was 4 deg. per chord length travelled. It was also intended to have a test run of 10 chord lengths but this proved impossible at the higher rates of change because of restricted vertical travel. In these cases the test run was reduced in length.

To separate the effects of different parameters it was decided to concentrate on the following

four types of motion:

(i) Forward acceleration at constant incidence and attitude

(ii) Normal acceleration at constant attitude and constant forward speed (plunging)

(iii) Rotation at constant incidence at constant forward speed (constant q)

(iv) Attitude and incidence increasing together at constant forward speed (pitching)

Case (i) could not be investigated in the timescale but the other cases were chosen to provide the $z_{\dot{w}}$, z_q, $z_{\dot{\theta}}$, $m_{\dot{w}}$, m_q, $m_{\dot{\theta}}$ derivatives. These motions are shown in Fig. 2.06b and the methods of achieving them in Fig. 2.07. These, then, were the basic requirements of the system. Specifications of the individual parts of the facility follow in their own sections.

2.3 Mechanical details

2.3.1 The tank

2.3.1.1 Specification

(i) The cross-section of the tank must be such that the model does not experience significant wall effects.

(ii) It must be long enough to accommodate acceleration and braking distances and a test section 5ft (1.5m) long.

(iii) It must be covered over most of its surface to suppress surface waves

(iv) It must permit flow visualisation.

2.3.1.2 Dimensions

The main considerations in deciding on the tank dimensions were the necessity of providing enough room to allow the range of movement required and to minimise the effect of wall constraint on the flow over the wing.

A test length of 5ft (1.5m) (equivalent to 10 wing chords) and a depth of 9in (23cm) were necessary to accommodate the maximum vertical translation. A tank length of 3 times the test length, ie. 15ft (4.62m) was considered adequate to include the acceleration and braking distances.

The wall effect was present in both steady and unsteady results. For this reason only the change in wall effect was considered important, particularly as the theory of wall constraint for slender wings was not very precise anyway. The calculation of the wall effect may be found in section 3.11. This showed that for a tank section 2ft 6 in (77cm) deep and 1ft (30cm) wide the correction for change in wall constraint would be small.

A tank 2ft 6in (77cm) deep and 1ft(30cm) wide provided an adequate track width for the trolley and was also convenient from a structural point of view. It was thought that the structural and operating penalties of a

larger tank would not be justified in view of the small gains from reduction of wall constraint.

2.3.1.3 Construction

To permit flow visualisation the tank had to be glass walled with a minimum of framing obstructing the view. Perspex walls were considered but rejected due to their poor quality for photographic work. The tank is shown in Figs. 2.02 and 2.03.

The tank floor was a single length of 1ft (30cm) x 4in (10cm) channel section carried on eight legs which extended above the tank floor to form the frame for the glass. Between the legs the side panels were glass, as also were the ends. The glass was rubber mounted to prevent local stress concentrations. Turnbuckles at the bottom of the legs were used to brace them and provide the correct spacing at the top.

As originally designed, the middle legs proved too flexible, causing a side panel to crack along the diagonal from the top of a middle leg to the bottom of an end leg. These were stiffened so that when the tank was filled with water the deflection at the top of the leg was less than 0.025in(0.63mm).

The maximum stress in the glass side panels

is given by the formula (ref. 18)

$$s = \frac{k_1 w L^2}{t^2}$$

where L = depth of tank
t = thickness of glass
w = pressure at bottom of tank
k_1 = constant depending on length of side panel and edge conditions

It was assumed that the frame did not deflect and the edge condition was simply supported. This overestimated the stress as the rubber mounting gave a condition somewhere between simply supported and built in. For ordinary plate glass, $\frac{3}{8}$in(9.5mm) thick, this gave a stress of 3200lbf/in^2 (22×10^6 N/m^2) which was well within the working stress for glass of 10000lbf/in^2 (69×10^6 N/m^2).

The mounting of the glass and sealing caused several problems aggravated by the design of the tank. As shown in Fig. 2.08, the glass panel was mounted on the outer faces of the floor section and top rail and on the inner faces of the legs, causing stress concentrations in the corners. Clamping plates were used to secure the glass on the outer face. This left a channel 1in(2.54cm) deep by $\frac{1}{2}$in(1.27cm) wide for the glass to sit in with a rubber mounting. Initially, flat rubber strip $\frac{3}{32}$in(2.5mm) thick was used on each face to provide the rubber mounting. Due to irregularities in the frame this set up stresses in the glass which caused

it to crack. This problem was overcome by replacing the rubber strip with soft rubber tubing 0.12in (3mm) bore and 0.02in ($\frac{1}{2}$mm) wall thickness. This problem would not have arisen if the glass had been mounted on the inside face of all the main structure with the clamping plates on the inside face of the glass.

Sealing, around the edges of the glass and over clamping bolts, was provided by Prestik 5925, a type of waterproof putty in ribbon form made by Bostik Ltd. The design of the tank again caused problems here because the putty had to be applied after the glass had been mounted. Several attempts were made to cure leaks by using motor car underseal and weatherproofing tape but none were completely satisfactory. It was found, however, that leaks occurred most often when the tank was emptied and refilled, especially if allowed to dry out in between. A week after filling most of the leaks had disappeared.

The tank was painted with a zinc chromate primer and a top coat of Epidura, a two component paint made by Atlas.

The tank structure was also used to carry the main trolley rails along its top members. These rails were small gauge flat bottom pattern made from aluminium alloy. They were mounted on spacers and levelled with shims to an

accuracy of ± 0.005in (0.125mm). The last 2ft (61cm) were bent up to provide emergency braking should the trolley fail to stop at the end of its run. When it reached this part of the rail the trolley automatically disengaged from the towing rope.

The perspex roof of the tank is shown in Fig. 2.09. It was made up of six quickly detachable sections which could be removed to enable the model to be lifted out. There was a 1in (2.54cm) gap down the centre to allow passage of the parallel linkage.

The main structure of the tank was also used to carry the pulleys for the winching system and the cam rail supporting structure.

2.3.2 The trolley and parallel linkage

2.3.2.1 Specification

(i) The model had to be controlled in pitch and vertical displacement by the cam rail.

(ii) Bearings and pivots had to be free of play so that the model would follow the cam rail exactly.

(iii) Provision had to made for counter-balancing the linkage.

(iv) The trolley had to carry the model and also a television or cine camera.

2.3.2.2 The parallel linkage

The parallel linkage is shown in Fig. 2.10 with its dimensions. The sting was 11.5in(29.2cm)

long from the centre of rotation of the model to the forward vertical arm. This governed the length of the rearward arms whose centre of rotation was directly above that of the model. The rearward arms had ball race pivots at the vertical slide block and at the vertical arms. The bearings in the top of the vertical arms were carried in machined aluminium blocks. These were connected to a fork at the bottom by cadmium plated streamlined section tubing, the pivots at the lower end being carried on sealed single row ball races in the lower sting mounting arm. The sting itself was detachable from the lower arm.

The complete linkage was pivoted on a vertical slide block which ran on two linear bearings on a silver steel pillar. The linkage was originally prevented from rotating in a horizontal plane about this pillar by a horizontal restraining arm which ran on bearings on a vertical member of the trolley frame. It was found that this allowed the linkage to twist about an axis through the centre of the four upper rearward arms. To prevent this, the restraining arm was removed and the existing arms stiffened and extended behind the vertical arms by the addition of aluminium channel sections. The extensions carried surface ball bearings which were free to run over a

vertical guide plate attached to a trolley member, thereby reducing twist and preventing rotation about a horizontal axis. This guide plate is shown in Fig. 2.11. The rearward arms were also extended in front of the vertical slide to carry counterbalancing weights, if these had proved necessary. The rearward arms were free to pivot through approximately 30° and could be clamped at any angle within this range. It was also possible to clamp the vertical slide in a fixed position relative to the pillar.

2.3.2.3 The sting

The sting is shown in Figs. 2.12, 2.13, 2.14. It was machined from HE30 aluminium alloy to dimensions chosen to provide a measurable strain gauge output without a large end deflection. The dimensions of the sting along with the strain at the measuring stations and end deflection are given in Appendix 1. One end of the sting was bolted to the lower sting mounting arm and a stud was located in the other end to carry the model wing. A streamlined fairing (sting shield) enclosed the sting and was attached to the lower sting mounting arm.(Fig.2.13). This reduced the aerodynamic loads experienced by the sting itself.

2.3.2.4 The model wing

The wing was made from 16 gauge aluminium

alloy with an AGARD model G planform. The edges had a 0.25in(0.66cm) chamfer on both sides to give a sharp edge. The wing is shown in Fig. 2.15.

2.3.2.5 The trolley

The pillar was carried in a frame made from square section aluminium tubing which formed the trolley shown in Figs. 2.16, 2.17, 2.18. On the original trolley an additional arm extended over the side of the tank to carry a television or cine camera for use in flow visualisation studies. It was found that the cameras were too heavy, however, and this arm was not used.

The trolley ran on four 4in(10cm) diameter flanged cast iron wheels fitted with roller bearings and running on hardened steel spindles. The spindles were clamped to two side members of the trolley and their back-to-back distance could be adjusted using shims. The flanges were relieved 1^{o} to prevent binding on the rails.

Counterbalancing of the parallel linkage assembly was provided by Negator springs whose restoring force is independent of extension. These were fixed to the trolley frame and their free ends attached to the horizontal arms of the linkage. This enabled the springs to counterbalance both the vertical slide and the parallel linkage without increasing the weight

carried by the slide. The right amount of counterbalancing was achieved by trial and error.

2.3.2.6 The cam followers

The follower arrangement is shown in Fig. 2.19. One of the upper rearward arms had a smaller arm attached to it which carried two ball races equally spaced either side of the centre of rotation of the arms. By positioning the front follower under the rail and the rear follower above the rail the weight of the linkage kept them in contact with the rail. Too little counterbalancing distorted the rail and transmitted vibration to the sting due to dirt on the rail. Too much counterbalancing prevented the wheels following the rail profile due to the inertia of the linkage. The followers could be arranged to simulate four different motions as follows:

(i) With the linkage arms and vertical slide free and both followers in contact with the rail, the attitude could be increased while maintaining constant incidence.

(ii) With the linkage arms clamped and one follower in contact with the rail, it could undergo normal acceleration at constant attitude (plunging).

(iii) With the vertical slide clamped and one follower on an extended arm in contact with the rail, the incidence and attitude

could be changed at the same rate (pitching).

(iv) With both the vertical slide and linkage arms locked a run could be made at constant incidence and attitude.

A quadrant was fixed to the horizontal arm to allow the follower arm to be fixed in different positions relative to the model, allowing a range of initial incidences to be selected.

2.3.3 The cam rail

The first rail design was a flat strip of aluminium 0.2in (5mm) thick by 2in (5cm) wide, with slotted brackets every 1ft (30cm) of its length. These were bolted to the Dexion framework which provided vertical slots for the clamping bolts. This rail was then fully adjustable to any desired profile. It was found to be very difficult to obtain a smooth transition between the curved profile and the straight parts of the rail at the start and finish of the run. The thickness of the rail necessary to resist distortion under the weight of the followers made it difficult to set up an accurate profile with the number of supports provided. Moreover, there was no certainty that the profile would be exactly the same if it was set up for a repeat run.

Without machining the profile from a single

piece of metal, it was not possible to achieve instantaneous transition from the straight part of the run to the curved profile. Furthermore, instantaneous transition could only be achieved by the use of two rails when two followers were used as in the case of the constant q runs. In theory, when the leading follower was on the curved profile and the trailing follower was on the horizontal rail, the rate of rotation and normal acceleration were half the final value. This still left the problem of overcoming the inertia of the slide and arms. In view of this it was decided to accept a transition to the curved profile and concentrate attention on the curved profile itself. A better profile was obtained by screwing a thinner steel strip (0.1in ($2\frac{1}{2}$mm)) onto a profile machined from marine plywood which was then mounted onto the Dexion framework. This limited the experimental programme to a fixed range of flight profiles. An example of one of these profiles is shown in Fig. 2.20. The fixed profiles were more accurate than the previous rail and they eliminated any variability in setting up the profile for repeat runs. Four profiles were made which produced non dimensional rates of 0.0175, 0.035, 0.0525 and 0.07. Fig. 2.21 shows the type of cam rail used for the constant $\dot{\theta}$ runs. These runs required only a straight line profile as explained in 3.4.3.

2.3.4 The winching system

2.3.4.1 Specification

(i) It had to provide a speed range between 1ft/sec (30cm/sec) and 5ft/sec (1.30m/sec).

(ii) It had to provide constant speed during the run whilst undergoing changing load.

(iii) The trolley had to start smoothly so that vibrations induced at the start of the run did not interfere with measurements during the run.

(iv) The cable had to release the trolley at the end of the run.

(v) It had to be capable of producing a constant acceleration during the test.run.

2.3.4.2 Components

The winching system consisted of an endless towing cable which was guided round a series of pulleys and wound on a drum which was in turn driven by an electric motor through a reduction gearbox. The motor had an automatic brake which operated when the supply to the motor was switched off.

2.3.4.3 Towing wire and pulleys

An endless wire was used to give positive location of the trolley relative to the winching drum. The wire was wound four times round the winching drum and was guided by pulleys along the top of the tank, just beneath the trolley, and round the back of the tank. The

stranded steel wire was 0.125in (3mm) diameter with a maximum safe working load of 220lbf (980N). The ends of the wire were joined by a turnbuckle which was used to adjust the cable tension in conjunction with an adjustable pulley at one end of the tank. A ferrule on the return section of the cable (behind the tank) operated limit switches to stop the motor at the end of the run. Further limit switches operated on the trolley itself to prevent the trolley over-running.

The drive was taken from the turnbuckle onto a fork mounted on the trolley via the spring and damper shown in Fig. 2.22. The fork allowed the trolley to disengage from the cable when it rose up the braking slope. The best spring and damper rates were found using an analogue computer. A step input of velocity was considered since the acceleration time of the motor was extremely short. Taking the weight of the trolley as 60lbf (266N), a spring of stiffness 10lbf/in(175N/M) and damping of 20lbf/ft/sec (30N/M/sec) gave a trolley speed within 1% of cable speed within 0.62 secs of starting with a maximum acceleration of 1.7g as shown in Fig. 2.23. The damper was of the rotary vane type made by Kinetrol Ltd.

2.3.4.4 Selection of motor

Four different types of electric motor were considered. These were:

(i) A d.c. motor with a variable resistance in series with the field or armature winding, This would have provided an easily varied speed but would have been very sensitive to changes in load.

(ii) A synchronous a/c motor with external speed control by means of gearing. This would have given a precise output speed but was not readily obtainable in the size required.

(iii) An a.c. induction motor with external speed control by means of gearing. This would give a steady output speed especially if running much below full load. These motors were cheap and readily available.

(iv) A d.c. motor with thyristor control. This was the most sophisticated method and the only one that could be programmed to give a constant acceleration. It could give a speed range of 10:1.

It was decided to concentrate on the constant speed cases to begin with and for this reason an a.c. induction motor with gearing was selected ((iii) above). It was thought that this would reduce the delays associated with developing a control system for the d.c. motor. The d.c. motor was, in fact, never used as there was not sufficient time to do the constant acceleration runs.

2.3.4.5 Size of motor

There were three parts of the run to consider when determining the size of the motor required.

(i) the acceleration

(ii) the constant speed test run

(iii) the braking distance

Tests on a.c. motors showed that the acceleration distance was very short because the starting torque was very much higher than the full load torque. The load on the motor during the test run arose from two sources - the drag on the model and the reaction of the followers on the cam rail. These were subject to change during the run and the following changes represent the worst possible case: consider a model of 6in (15cm) chord and 3in (7.5cm) span travelling at 5ft/sec(1.30m/sec) and changing its incidence from 0° to 30° during the run.

Maximum change in $C_D = 0.7$

at 5ft/sec $\Delta D = 0.7 \times \frac{1}{2} \times 1.94 \times 25 \times {}^{9}/_{144}$

$= 1.05$lbf

$\therefore \Delta P = 5.25$ft lbf/sec (7watts)

Assuming no counterbalancing then

Reaction on rail = $W \tan \gamma$

and $W = 16$ lbf

$\gamma = 30^{\circ}$

$\Delta R = 16 \times 0.577$

$= 9.2$ lbf

$\Delta P = 46$ft lbf/sec (63 watts)

Therefore it was possible for the power requirement to change by up to 50ft lbf/sec (70 watts) during the run. For a ½HP(373 watt) motor this represented a change in load from 0 to 18% full load and approximately a 1% change in speed.

As previously mentioned the running speed was reduced to 2.8 ft/sec (0.71m/sec). In addition the maximum change of incidence during the run was 16° and the followers were counter-balanced. This reduced the change in load during the run to negligible proportions.

A 3 phase ½HP(373watts) motor made by Brook Motors Ltd. was selected. It was fitted with an automatic drum brake and a reduction gearbox to give an output speed of 200rpm.

2.3.4.6 Gearing

Five pairs of gears, of 12DP, were selected to give a range of speeds from 1ft/sec(30cm/sec) to 5ft/sec(130cm/sec) with a 5.30in (13.5cm) diameter winching drum at the gearbox output speed of 200rpm.

2.4 Quantities to be measured

(i) Normal force and pitching moment (N,M)

(ii) Distance travelled in relation to cam rail (x)

(iii) Attitude and incidence of model (θ, α)

(iv) Normal acceleration of model ($\dot{w}$)

(v) Forward speed (V)

2.5 Instrumentation

2.5.1 Normal force and pitching moment

Normal force and pitching moment were measured by strain gauges mounted on the sting shown in Fig. 2.14. The strain gauges used were made by Micromeasurements Ltd., and available from Welwyn Electric Ltd. They were foil gauges, type EA-13-125AD-120 with a grid 0.125in (3.2mm) square, a resistance of 120 ohms, gauge factor 2.05 and self-temperature compensated for aluminium.

The normal force was derived from the four gauge bridge circuit shown in Fig. 2.24 and the moment from the bridge circuit in Fig. 2.25. The normal force was obtained by measuring the difference in bending moment at two stations of the same section modulus. The moment was obtained by measuring the difference in bending moment at two stations of different section moduli. This is known as the focused modulus concept. The derivation of the normal force and pitching moment is given in Appendix 1.

The first sting was made from commercial grade aluminium but after some calibration problems were encountered it was thought that the sting might have a non-linear stress-strain curve. A high grade aluminium alloy, HE30, was used for the second sting which provided the results for the $\dot{w}$ and q derivatives. The first sting was used later for the $\dot{\theta}$ derivatives when

it was discovered that the calibration difficulties were due to ageing of the strain gauge cement. (See 2.5.1.1)

2.5.1.1 Cementing and waterproofing gauges

The cementing of the gauges was very important as this dictated how well the strain in the gauge reflected the strain in the sting. It was discovered during static calibrations of the first sting that the level of strain was dependent on the way in which the sting was loaded and that some apparent strain remained when the sting was unloaded. This was first attributed to the material used in making the sting, which was apparently confirmed when this 'hysteresis' effect did not occur with the new sting. When this new sting had been in use some time however, this effect reappeared. It was thought that this was probably due to ageing of the cement. New gauges were applied with another type of cement, the original type of cement having been discontinued by the manufacturers. The new cement was epoxycement AE10 made by Micromeasurements Ltd.

Of equal importance to the cement was the insulation of the gauges. Any leakage to earth would alter the resistance in the arms of the bridge circuit leading to spurious results. As the sting was operating under water it was

especially important to provide thorough insulation of the gauges and lead in wires. Fig.2.26 shows the application of the gauges and waterproofing. A primary coat of polyurethane varnish was applied to bare wires and the p.v.c. insulation on the lead-in wires was treated with a nitrile rubber compound, the p.v.c. insulation not being completely waterproof in itself. The whole installation was then covered with several coats of a polysulphide epoxy compound (M-coat G by Micromeasurements Ltd.).

2.5.1.2 Power supply

The strain gauge bridges were supplied by separate d.c. power supplies with 6 volts across two arms. This gave a power density of 5 watt/in^2 on each strain gauge which was within the recommended limits for these gauges. After an initial warming up period of about 20 minutes there was no discernible short term drift of the power supplies.

2.5.1.3 U/V recorder

A U/V recorder with a 6in (1.5cm) wide chart and 12 channels was used, employing 3 of the available channels. The normal force and pitching moment were recorded using C.40 galvanometers having a sensitivity of 0.067mV/cm, a resistance of 42 ohm and a natural frequency of 40Hz. The signal from the strain

gauge bridge had to be amplified before being put onto the U/V recorder.

2.5.1.4 Amplifiers

Differential amplifiers were used on each bridge giving a gain of 50. This gain was then reduced by resistances in series with the galvanometers. The pitching moment bridge used a higher gain than the lift bridge to give approximately the same trace amplitude on the U/V recorder using similar galvanometers.

For measuring the q derivatives a high gain amplifier was used incorporating a cut-off and zero-shift to enable only part of the signal to appear on the chart recorder. The effect of the high gain amplifier on the signal is shown in Fig. 2.27. The complete circuit with low gain amplifiers is shown in Fig. 2.28. The high gain amplifier circuit is shown in Fig. 2.29.

2.5.1.5 Filters

Excitation from various sources, though mainly from the trolley wheels, caused the sting to vibrate. The principal frequency was 17.5Hz, one of the natural frequencies of the sting. This produced considerable noise on the signals which was reduced by the use of a notch filter tuned to 17.5Hz. Higher frequency noise, from other sting vibrations and electrical interference was removed by a low-pass filter

with a break point at 14Hz. The circuit diagrams of the filters are shown in Fig.2.30. The calculation of the characteristics of these filters is given in Appendix 2. The use of filters introduced a phase lag into the signal which had to be allowed for when taking measurements from the U/V chart.

The effect of the filters cam be seen in Figs. 2.31, 2.32, 2.33. Fig. 2.31 shows the unfiltered signal which is very difficult to analyse accurately. The use of the notch filter (Fig. 2.32) removed the 17.5Hz noise, but left some high frequency noise, especially at the beginning and end of the manoeuvre. This noise was removed (as shown in Fig. 2.33) by the low-pass filter. All the strain gauge instrumentation is shown in Fig. 2.34.

2.5.2 Distance travelled

The position of the trolley was recorded by using a magnet on the trolley to operate the reed switches set in metre rules at 4in (10cm) intervals along the side of the track, as shown in Fig. 2.35. When the magnet closed a reed switch the circuit was completed and an impulse was recorded by a galvanometer in the U/V recorder. A $4\frac{1}{2}$v battery was used to supply the circuit and a galvanometer with a sensitivity of 25mv/cm and natural frequency of 1000 Hz was used.

The shape of the impulse on the U/V recorder chart demonstrates that the lag in the galvanometer was effectively zero.

2.5.3 Attitude and incidence of model

It was not considered necessary to provide continuous monitoring of the attitude of the model during a test run since the attitude was determined by the initial attitude and its position relative to the cam rail. The angle of the upper arms was measured using a clinometer with the trolley positioned at regular intervals along the track, the position of the trolley being measured relative to the reed switches.

It would not have been possible to provide an angular measurement during a test run to the accuracy of a clinometer.

The incidence of the model was determined by the attitude and the arrangement of the followers. To determine the relationship between the angle of the upper arms and the angle of the model, the normal force curve was plotted for positive and negative incidences to determine the zero-lift angle. This was taken as zero incidence since a symmetrical model was used.

2.5.4 Normal acceleration

This was determined by the shape of the cam rail. Using one follower and with the horizontal

arms clamped, the displacement of the vertical slide was measured using a pointer and a scale clamped to the trolley framework. This was done at regular intervals along the track.

2.5.5 Trolley speed

The trolley was driven by an induction motor which showed very little variation in speed because it ran well below full load. (See 2.3.4.4) The speed of the trolley was calibrated by comparing the spacing of the timing impulses of the reed switches with the U/V recorder timer marks using a high paper speed. This was also used as a convenient check on speed during the actual test runs. The test runs were carried out at a speed of 2.8 ft/sec (0.85m/sec).

2.6 Experimental procedure

The normal force and pitching moment signals were recorded on the U/V recorder at a chart speed of 4in/sec (10cm/sec) and a strain gauge bridge voltage of 6 volts. A period of about 20 minutes was allowed for the instruments to warm up after switching them on. Three runs were made at a speed of 2.8ft/sec (0.85m/sec) for each condition and average values taken. Any obviously spurious results were omitted. Between each run a period of 20 minutes was allowed for the water in the tank to settle.

For the unsteady runs, three rail profiles

were used giving positive and negative rates for $\frac{\dot{w}c_o}{V^2}$, $\frac{qc_o}{V}$ and $\frac{\dot{\theta}c_o}{V}$ of 0.07, 0.0525, 0.035. These rates corresponded to changes of 4°, 3°, and 2° per root chord length of forward travel. For the highest rate, 0.07, the attitude and/or incidence changed by 16° in each test run. For the other two rates, 0.0525 and 0.035, the change was 12°. A lower rate of 0.0175 was tried but it was found to be impossible to distinguish any measurements from the normal experimental scatter. In the cases of runs at constant q and constant $\dot{\theta}$, the pitching axis was at $0.667c_o$ from the wing apex.

As previously mentioned, (2.51) a different sting was used for the pitching manoeuvres. Because the two stings did not have the focus of the pitching moment bridge in the same place, the pitching moment was measured about a different wing datum, but keeping the pitching axis in the same place.

2.6.1 Steady runs at constant incidence

The trolley was set up with both the slide and the linkage arms clamped, so that the wing was positioned in the centre of the tank. The incidence could be altered by adjusting the position of the linkage arms. A long test run was possible as no cam rail was used. Runs were made at positive and negative incidence at

intervals of 2° to find the zero-lift angle and check the expected symmetry of the model.

2.6.2 Runs at constant $\dot{w}$ (plunging)

The trolley was set up as shown in Fig. 2.07(a) with the vertical slide free and the linkage arms clamped to the vertical slide. One follower was used, resting on the top of the rail. The initial incidence was set up using a clinometer. Runs were made at initial incidences of 24°, 20°, 16°, and 12° for negative $\dot{w}$ (decreasing incidence) and 0°, 4°, 8°, and 12° for positive $\dot{w}$ (increasing incidence). Positive and negative rates of $\dot{w}$ were made possible for one cam rail by inverting the model.

The second sting, made from HE30 aluminium alloy, was used which had its measuring axis at $0.733c_0$. The notch filter was used to filter the output signal from the sting.

2.6.3 Runs at constant q

The trolley was set up as shown in Fig.2.07(b) with the slide free and the linkage arm free to rotate. Two followers were used, the rear one resting on top of the rail and the front one on the underside of the rail. The incidence (which remained constant throughout the run) was set up at the beginning of the run by moving the follower arm relative to the linkage arms and

securing it to the quadrant. The quadrant had a fixed number of holes to give 9 incidences which were measured with a clinometer. The cam rail was the same as that used for the constant $\dot{w}$ runs (Fig. 2.20). The same sting was also used with the measuring axis at $0.733c_o$.

The output signals from the sting were amplified using the high gain amplifiers and filtered through the notch filter and low pass filter.

2.6.4 Runs at constant $\dot{\theta}$ (pitching)

The trolley was set up as shown in Fig.2.07(c) with the vertical slide damped to the trolley and the linkage arms free to rotate. One follower was used, fixed at the end of the linkage arm where it joined the vertical arm. The initial incidence was set by adjusting the height of the slide relative to the cam rail and then clamping it to the trolley. The first sting was used for these runs with its measuring axis at $0.795c_o$. This sting showed a slight asymmetry in the calibration for positive and negative incidence. For this reason the cam rail was altered to maintain a positive load for positive and negative rates of pitch.

The output signals were filtered through the notch filter and low-pass filter.

3. CALIBRATION AND CORRECTIONS

3.1 General

The establishment of calibration factors and corrections to be applied was essential to provide a basis on which the experimental measurements were to be made. Prior to taking experimental measurements the outputs of the strain gauge bridge circuits were calibrated and the accuracy of the position marking of the reed switches and the shape of the rail profiles were checked. After the experimental measurements were taken, corrections were applied to them to compensate for errors caused by the limitations of the system. These corrections were:

(i) Correction for error in normal force and pitching moment caused by change in weight component normal to the sting associated with change in attitude of the model.

(ii) Correction for error in normal force and pitching moment caused by inertia of the model.

(iii) Correction to measured incidence due to deflection of the sting under aerodynamic load.

(iv) Correction to dynamic pressure due to change in speed along the flight path for constant horizontal velocity.

(v) Correction to distance travelled due to lag caused by electrical filters and galvanometers.

(vi) Effect of wall constraint on the flow over the model.

Table 3.01 shows which of these corrections were applicable in each manoeuvre.

As explained in 2.5.1 it was necessary to use a different sting for the constant $\dot{\theta}$ manoeuvres (sting no. 1) because of problems experienced with the sting used in the constant $\dot{w}$ and constant q manoeuvres (sting no.2). Separate calibrations were therefore required for the two stings. In addition, different combinations of amplifiers and filters were used in the constant $\dot{w}$ and constant q manoeuvres, making it necessary to perform a total of 3 different sting calibrations.

3.2 Calibration of sting to measure output voltages for applied normal force and pitching moment

The circuit diagrams of the strain gauge bridges and amplifiers are shown in Figs. 2.28, 2.29, 2.30. The derivation of the theoretical strain gauge bridge output and the dimensions of the sting are given in Appendix 1 and Figs. 2.24,2.25.

3.2.1 Calibration technique

The sting was calibrated using the calibration bar shown in Fig, 3.01 which was screwed onto the sting in place of the wing, and loads applied by hanging weights from the bar at the 4 locating grooves. For each load the readings of normal force and pitching moment were taken from the U/V trace. The calibrations were performed for the complete

system including the appropriate amplifiers, filters, and U/V recorder. The signal lag introduced by these components is dealt with in 3.10.

Additional readings were taken using a digital voltmeter (DVM) to give a more accurate check on the linearity of the calibration. (The DVM could be read to 0.1mV in a maximum 25mV output for 0.6lbf (2.7N)) An example of one of these calibrations is shown in Fig. 3.02. The greater accuracy of the DVM was also used to find the correction for the influence of pitching moment in the normal force signal. In theory (see Appendix 1) the normal force calibration should have been independent of the point at which the load was applied. In practice, however, machining tolerances and waterproofing thickness modified the section moduli and made the normal force output dependent on the moment of the normal force. Fig. 3.02 shows the difference in the normal force calibration for loads applied 2.75in(7cm) apart to be 0.2mV/lbf/in. Since the position of the aerodynamic centre was known to within 0.1in (2.5mm) the calibration error was negligible.

By plotting the output of the pitching moment bridge circuit for loads applied at the 4 measuring stations, as in Fig. 3.04, and plotting the gradients of load against deflection

at these stations, as in Fig. 3.05, the focus of the bridge was given by the point where the gradient was zero. For the applied loads, the pitching moment was measured about the focus and the calibration plotted in Fig. 3.06. It was necessary to perform separate calibrations for the two stings because small differences in section thickness at the measuring stations could have a large effect on the position of the focus. For example, if the section thicknesses were 0.151in (3.82mm) and 0.266in (6.75mm) instead of 0.1524in (3.85mm) and 0.264in (6.70mm) respectively, the focus of the bridge would be 2.85in (7.0cm) from M_1 instead of 3in (7.61cm) from M_1. Variations in the thickness of the waterproofing would have a similar effect. Thus, two different stings would be unlikely to have exactly the same bridge focus within normal machining tolerances.

In all cases the pitching axis was kept fixed so that the two stings measured the pitching moment about a different wing datum.

To find the pitching axis and the measuring axis, the positions of the calibration bar and the trailing edge of the model were measured with a travelling microscope. These positions were related to a datum on the sting which was in turn at a known distance from the rear mounting face of the sting.

3.2.2 Calibration of sting no. 2 for steady runs at constant incidence and plunging manoeuvres

The calibration was performed with a supply voltage of 6v± 0.002V and the signal amplified with the low gain amplifier and filtered by the 17.5Hz notch filter. The normal force calibration is shown in Fig. 3.03 which gave a calibration factor0.4551bf/cm (2.02N/cm). The pitching moment calibration is shown in Figs. 3.04, 3.05, 3.06. The focus of the bridge was at $0.733c_o$. The original pitching moment calibration shown here (Fig. 3.06) was later altered by putting a resistor in series with the galvanometer to give a greater deflection on the U/V trace. The bridge was re-calibrated to give the calibration shown in Fig. 3.07 (0.05361bf ins/cm (0.00605Nm/cm))

3.2.3 Calibration of sting no. 2 with high gain amplifiers for constant q manoeuvres

This calibration was performed with a bridge voltage of 6.00± 0.002 volts and using both notch and low-pass filters with the high-gain amplifiers. As a check on the linearity over the range of loads likely to be encountered, two calibrations were performed, one starting with zero load and the other with 0.4lbf (1.78N) load. The initial steady load was backed-off using the high-gain amplifiers. The load was increased in steps of 0.01lbf (0.045N). Since the same sting was used for the plunging results, the focus of

the pitching moment bridge remained in the same place. This was checked but the calibration is not shown here. The normal force calibration is shown in Fig. 3.08 and the pitching moment calibration in Fig. 3.09. The normal force calibration factor was 0.0057 lbf/cm (0.0253N/cm) (a gain of 8.0) and the pitching moment calibration factor 0.00841bf in/cm (0.00095Nm/cm) (a gain of 6.4).

3.2.4 Calibration of sting no. 1 for pitching manoeuvres

The calibration was performed with a supply voltage of 6V ± 0.002V and the signal amplified with the low-gain amplifier and filtered by the 17.5Hz notch filter and the 14Hz low-pass filter. The normal force calibration is shown in Fig.3.10 and the pitching moment calibrations in Figs. 3.11, 3.12, 3.13. In this case, the pitching moment focus was at $0.795c_0$ to give the same pitching axis as for sting no. 2. The calibration factors were 0.0428 lbf/cm (0.19N/cm) for the normal force bridge and 0.0591 lbf in/cm (0.0067 Nm/cm) for the pitching moment bridge. As a further check on the suitability of sting no.1, some runs were performed at constant incidence to compare the measurements with the measurements using sting no. 2. The agreement between the two was very good.

3.3 Measurement of trolley position and speed by the use of reed switches

The point at which the switches operated, relative to the overhead position of the magnet, was measured using the graduations on the metre rule. All of the reed switches operated at a point between 0.15in(0.38cm) and 0.05in (0.13cm) before the magnet was directly overhead. The impulses on the U/V trace were used to measure the trolley speed by recording at a fast paper speed and measuring their separation in relation to the U/V timer marks.

3.4 Determination of errors in cam rail profiles

3.4.1 Profile used for plunging manoeuvre

The vertical displacement of the rails was measured by setting up the parallel linkage for a plunging manoeuvre and measuring the displacement of the vertical slide using a pointer on the vertical slide and a scale attached to the trolley. The scale could be read to an accuracy of $\pm$ 0.010in ($\pm$.25mm). The vertical displacement was related to the position of the reed switches so that no other indication of displacement was needed on the output traces. The variation of the vertical displacement of the rail with the distance along the track (as measured by the reed switches) is shown in Fig. 3.14 for $\frac{\dot{w}c_o}{V^2} \simeq 0.07$, 0.0525, 0.035. They show good agreement with the

desired profile except near the start and finish where difficulty was encountered in blending the curved profile into the horizontal part of the rail.

3.4.2 Profile used for constant q manoeuvre

This was the same rail as was used for the plunging manoeuvre. The angle of the rails was measured by setting up the parallel linkage for the constant q manoeuvre using both followers (Fig. 2.07). The angle of the linkage arms was measured at regular intervals along the rail using a clinometer and these measurements were related to the position of the reed switches. The clinometer could be read to an accuracy of 1 minute of arc. The variation of rail angle with distance along the track is shown in Fig. 3.15 for $\frac{qc_o}{V} = 0.07, 0.0525, 0.035$.

They show good agreement with the desired profile except for the first 6in (15cm) and the last 6in (15cm) of the rail. This is because the followers were spaced 6in (15cm) apart and consequently during the initial and final phases of the run, one of the followers was still on the straight part of the rail. During this period the rate of rotation and normal acceleration were half their final value. To overcome this, two rails would be necessary, one for each follower.

3.4.3 Profile used for pitching manoeuvre

The rail is shown in Fig. 2.21. The horizontal sections of the rail were set up to a mean displacement to give the best approximation to a sine curve over a range of incidences and the ramp adjusted to blend with them. The correction to pitching rate due to a straight ramp is shown in Fig. 3.16. The use of a straight ramp in place of a sine curve involved a maximum error of 2% in $\dot{\theta}$. This was small in relation to the other errors.

The choice of one fixed ramp for several ranges of incidence (from 24° to 12° and from 12° to 0°) introduced an error in the terminal incidence of the model. This was allowed for in the measurement of the trace. In addition to this error there was an error in the horizontal displacement proportional to the cosine of the angle of the linkage arms. This was also allowed for by measuring the starting point of each run relative to the reed switches and using Fig. 3.17 to correct the positions at which measurements were taken.

3.5 Correction for errors in normal force and pitching moment due to change in weight component normal to the sting associated with the change in attitude of the model

Because the attitude of the model changed during a manoeuvre, a correction had to be applied to

the results to allow for the change in the component of weight acting in the direction of the normal force and for the associated moment.

3.5.1 Theoretical correction due to attitude of model

To calculate this correction, the sting and wing were divided into discrete sections as shown in Fig. 3.18 and the total mass and c.g. calculated. This analysis gave the following results for the sting in air;

Weight of wing and sting = 0.0981bf (0.435N)

C.g. of wing+sting = 6.4in from M_1 (16.2cm)

Moment about pitching moment focus ($0.733c_0$) = -0.08431bf.in.(0.0095Nm)

When the sting was immersed in water it experienced a buoyancy force which reduced the corrections to:

Effective weight of wing+sting = 0.0611bf (0.271N)

Moment about pitching moment focus = -0.0525 lbf.in. (0.0059Nm)

Changes in attitude of the wing altered the component of the weight normal to the sting. The increments in normal force and pitching moment were given by:

$$\Delta N = 0.061(1-\cos\theta) \text{ lbf}$$

$$\Delta M = -0.0525(1-\cos\theta) \text{ lbf.in}$$

These corrections are shown in Fig. 3.19

3.6 Correction for error in normal force and pitching moment due to model and sting inertia

Although the model inertia effect was small compared with the aerodynamic forces, a correction for it

was obtained using the weight and c.g. calculated for the correction due to change in attitude. The corrections are shown in Fig. 3.20 for the normal accelerations used in the plunging and constant q manoeuvres.

3.7 Measurement of corrections due to change in attitude of model and model inertia

To verify the theoretical corrections experimentally, the model was rotated at constant incidence (constant q manoeuvre) in still air. To measure the small increments in normal force and pitching moment, high gain amplifiers were used. In this manoeuvre the model experienced the effect of acceleration and change of attitude. It was found to be difficult to obtain a static calibration of the effect of attitude, due to drift in the amplifiers over the relatively long time interval involved.

The results are shown in Figs. 3.21 to 3.26. The runs were at two angles of incidence, $11\frac{1}{2}^{o}$ and 17^{o}, and three normal accelerations $\frac{\dot{w}c_o}{V^2} = 0.07, 0.0525, 0.035$. The results show very good agreement with the calculated results, which are also shown in Figs. 3.21 to 3.26. In view of this Fig. 3.19 was used to correct the results for change in attitude of the sting and Fig. 3.20 to correct the results for normal acceleration.

3.8 Deflection of sting under aerodynamic load

The load on the wing created by its motion through the water, caused bending of the sting, resulting in a displacement of the wing and an increase in its incidence. The displacement of the wing did not affect the results but the increase in incidence had to be allowed for to find the true incidence of the wing.

The calculation of the deflection is shown in Appendix 2. Fig. A2.2 shows the deflection and slope diagrams for the application of a 0.6lbf(2.7N) load. The deflection is shown in Table 3.02 along with results measured using a telescope to measure the end slope of the sting under a range of applied loads.

3.9 Change in speed and dynamic pressure along the flight path

The system was designed to give the trolley a constant horizontal speed. In the case of the plunging manoeuvre (constant $\dot{w}$) and the rotation at constant incidence (constant q), the flight path changed its angle relative to the horizontal plane. The change in flight path angle caused a change in speed along the flight path (Fig. 3.27), the horizontal component of the speed remaining constant. The maximum change in flight path angle of 16° resulted in an increase in speed of about 4%. The change in speed was not significant in its effect

on the non-dimensional plunging and q rates but a 4% increase in speed meant an 8% increase in dynamic pressure which had to be allowed for when calculating the aerodynamic coefficients. The corrections for the change in speed and dynamic pressure are shown in Figs. 3.27, 3.28. Although the change in flight path angle also meant an acceleration along the flight path, it was very small and was considered to have a negligible effect on the results.

3.10 Correction to distance travelled due to lag caused by electrical filters and galvanometers

The galvanometers used in the U/V trace recorder were second-order mechanical system and therefore introduced a lag between the input of the signal and its record on the trace. The impulses from the reed switches which were used to determine the model position along the flight path, were recorded on a galvanometer with a natural frequency of 1000Hz and damping ratio of 0.64. The lag of this signal was about 1 microsecond, which was negligible compared to the lag of the low frequency galvanometer. The galvanometers used to record the output of the strain gauges had a natural frequency of 40Hz and a damping ratio of 0.64. The lag of these galvanometers was more significant. In addition, the use of filters to smooth the signal introduced further lags. The theoretical calculation of the

lag associated with each component is given in Appendix 3. The total lag of several of these components in series is given simply by addition.

3.10.1 Experimental measurement of lag

To check the theoretical values, two calibrations were carried out on the filters and galvanometers:

(i) A standard calibration of each filter to find its response to various imput frequencies. The frequency response showing gain and phase shift is shown for the notch filter in Fig. 3.29 and for the low-pass filter in Fig. 3.30.

(ii) Measurement of the lag of the whole circuit using an analogue computer programmed to simulate the output from the strain gauge bridges equivalent to a test run. The analogue signal was fed into the circuit in place of the strain gauge signal. As a comparison, the same signal was fed into an A1000 galvanometer similar to the one on which the reed switch impulses were recorded. The gain was adjusted to give the same output signal amplitude in each case and the time lag between the two signals was measured from the trace. An example of one of these traces is shown in Fig. 3.31.

3.10.2 Comparison of theoretical and measured lags

The theoretical lag from Appendix 3 (Figs.A.3.1, A.3.2, A.3.3) shows that the phase lags for the

notch filter, low-pass filter and galvanometer were nearly constant after $\frac{1}{2}$ chord length travel. The transient had nearly disappeared by this time and the small constant displacement was not significant. The frequency response of the notch filter (Fig. 3.29) shows the notch frequency at $17\frac{1}{2}$Hz and the low-pass filter had its break-point at 14Hz (Fig. 3.30). These results confirm the theoretical design values and give confidence in the values of lag calculated from them. The results of the calibration using an analogue signal (Figs. 3.32, 3.33) were disappointing in their poor accuracy. The mains ripple on the trace caused some difficulty in measuring the phase lag between the two traces, the maximum separation being only 0.055 secs. (see Fig. 3.31). In addition, any drift in one of the signals affected the measured lag. It was felt that the analogue calibration was more useful as an illustration of the frequency response and calculated results than as a means of actually measuring the lag.

It was therefore possible to apply a constant time lag to all the results during the steady part of the test run depending on which filters were used. This made the correction very simple to use in practice. The lag of each component is given below

Lag of notch filter	= 0.036 secs.
Lag of low-pass filter	= 0.011 secs.
Lag of galvanometer	= 0.005 secs.
Total lag (maximum)	= 0.052 secs.

3.11 Wall constraint

No correction due to tank wall constraint has been applied to the results because both steady and unsteady results were measured in the same tank under the same conditions. In view of the uncertainty in the accuracy of the theory for the effect of wall constraint on slender wings, it was felt that this approach was justified. The theory for slender wings (ref. 19) does, however, show that the correction(based on R.T.Jones slender wing theory which in itself is only exact at zero lift) is of the same order as classical lifting line theory.

Although there was no variation in the cross-section of the tank, the elevation of the model was changing during some of the manoeuvres. The variation was confined to the centre of the tank, $\pm 4\frac{1}{2}$in (11.4cm) from the centre line. To assess the effect of this variation in height of the model a simple model using the method of images was constructed. The wing was replaced by a horseshoe vortex in a closed rectangular box and the walls were replaced by a series of images. Part of the image system is shown in Fig. 3.34.

The use of lifting line theory was considered accurate enough if the effect was small, for the reasons mentioned above.

The images of the trailing vortices induce a downwash at the wing which results in an apparently higher incidence. The bound vortex gives an apparent curvature to the airflow which gives the wing a camber effect. A more detailed explanation may be found in ref. 20.

The net effect of trailing vortices is an apparent increase in the incidence of the wing of 0.622° when situated at the centre of the tank and 0.65° when situated $4\frac{1}{2}$in (11.4cm) above or below the centre of the tank. Although the corrections themselves may seem large, the difference, 0.028°, is very small and well within the scatter of results.

The bound vortex system induces an effective camber of the centre line chord of $4\frac{1}{2}$ minutes of arc which, again, is quite negligible.

Attempts to measure the change in wall effect resulted in measurements within the normal experimental scatter

3.12 Overall accuracy

After all the corrections due to the physical limitations had been applied, reading error and instrument errors remained. The most significant of these was reading error in the measurement of the U/V trace deflection. For the plunging and pitching manoeuvres, the trace could be read to an

accuracy of $\pm$ 0.5mm when account was taken of the mains ripple on the trace. This represented an error of $\pm$ 0.004 in C_N and $\pm$ 0.0013 in C_M.

The noise on the U/V traces for the constant q manoeuvres was much greater and therefore the reading accuracy was poorer. For these traces, it was possible to read to an accuracy of $\pm$ 2.0mm, an error of $\pm$ 0.002 in C_N and $\pm$ 0.0005 in C_M.

Although these errors were small in relation to the total C_N and C_M, the measurement of the derivatives involved taking the difference of two nearly equal values which made them significant.

The reading error quoted here is intended to take into account small disturbances causing vibration of the sting and small irregularities in the rails. The experimental scatter goes beyond the reading error in some cases because the effects of disturbances and rail irregularities are very difficult to quantify. A policy of finding a 'best fit' line for the results has been adopted in view of the uncertainty in quantifying the true error band.

4. RESULTS

The results fall into four sections according to the type of manoeuvre, all runs being performed at constant horizontal speed. These manoeuvres are as follows:

(i) Steady runs at constant incidence and constant attitude. These provided the steady normal force and pitching moment curves for comparison with the unsteady results.

(ii) Runs at constant attitude, the incidence varying with flight path angle. (Plunging)

(iii) Runs at constant incidence, the attitude varying at the same rate as the flight path angle. (q runs)

(iv) Runs along a horizontal flight path, the incidence and attitude varying together at the same rate. (pitching)

Fig. 2.06 shows the co-ordinate system used and the flight paths of the unsteady motions. The derivatives were referred to wind axes and have been corrected to convert the normal force to a force in the direction of the z axis. This did not affect the moment derivatives.

The flight paths are shown for positive rate of $\dot{w}$, q and $\dot{\theta}$. The relationship between the derivatives (assuming linearity) is given by:

$$\theta = \alpha + \gamma = \frac{\omega}{V} + \gamma$$

$$\dot{\theta} = \frac{\dot{\omega}}{V} + q$$

Hence $\underline{z_{\dot{\theta}} = z_{\dot{w}} + z_q}$

and $\underline{m_{\dot{\theta}} = m_{\dot{w}} + m_q}$

4.1 Steady runs at constant attitude and incidence

The U/V recorder trace, Fig. 4.01, shows a steady test run starting from rest. After the initial impulse was over and the speed became constant, the lift and pitching moment were constant to within ± 0.5mm of trace deflection. There was a steady 50Hz mains ripple on the traces.

The variation of C_N with α is shown in Fig. 4.02. The values of C_N for positive and negative values of α relative to the zero-lift angle show good agreement. This indicates there was no asymmetry in the model. It also confirms that the supporting structure did not have a significant effect on the flow pattern behind the wing (Fig. 4.03). The results show most scatter at the lower incidences, which may be due to the low Reynolds number. Because the aluminium alloy wing was subject to slight corrosion in the water, it was not possible to produce a razor sharp leading edge. The small leading edge radius may have affected the weak flow separation at low angles of incidence but had little effect on the well-established separation at high angles of incidence.

For comparison, other results shown are wind tunnel results from ref.21 and theoretical results calculated from ref. 22. The latter agree exactly with the experimental points from the tank. This is not as satisfactory as it first appears, however, because no correction for wall constraint has been applied to the experimental results. The accuracy

of the ref. 22 data is given as between $\pm$ 0.05rad^{-1} and $\pm$ 0.1rad^{-1} in normal force curve slope. This represents an incidence increment of $\pm$ 0.13deg to $\pm$ 0.26 deg at a C_N of about 1.0. The wall constraint calculated in 3.11 gives an effective incidence increase of about 0.63 deg which represents an error in C_N of 1½% to 2%. Different thickness distributions for the wings used in ref. 22 and the wing used here, or support interference, might account for the difference in normal force.

The results from ref. 21 give higher values of C_N although a zero-lift angle correction and wall constraint correction have not been applied to them. Using the same approach to find the wall effect as in 3.11, the increase in incidence is approximately 0.4 deg at a C_N of about 1.0 for the ref. 21 results. The zero-lift angle correction is approximately 0.7 deg. The wing used in ref. 21 had a very different thickness distribution and it is thought that this may account for some of the remaining difference.

The ref. 21 results were measured on a sting-supported wing which was mounted on a large A-frame downstream of the wing. The blockage of this A-frame in the lower half of the tunnel caused a curvature of the flow up over it. This curvature gave an effective increase in the incidence of the wing. As the steady results were not considered important by the RAE, this curvature in the flow was

not measured but it is thought to have given an effective increase in incidence of about 1 deg.

The variation of $C_{M.733c_0}$ with α shown in Fig. 4.04 exhibits the same characteristics as the variation of C_N with α (Fig. 4.02). Here, however, the pitching moment starts to fall below the theoretical curve (ref. 22) at high incidence. This is consistent with the effect of wall constraints. The RAE results have had no wall constraint corrections applied but the zero incidence pitching moment is zero.

The variation of $C_{M.733c_0}$ with C_N (Fig.4.05) shows there is some movement of the aerodynamic centre with incidence. It moves forward slightly as incidence increases but then tends to move back to its original position as the incidence increases still more. Ref. 22 follows the results up to high incidence until the pitching moment starts to fall off. The ref. 21 results match the tank results very closely with a slight shift due to a negative pitching moment at zero-lift. These comparisons gave confidence in the ability of the system to measure the forces on the wing with good repeatability. They also showed that the effects of wall constraint, support structure and Reynolds number were not likely to invalidate the results.

4.2 Unsteady motion

4.2.1 Presentation of unsteady results

4.2.1.1 Plunging and pitching manoeuvres

The variations of C_M and C_N for the plunging and pitching manoeuvres have been shown in simplified form in Fig. 4.06. (This figure exaggerates ΔC_N but it is only intended as an illustration.) The figure is essentially a copy of the U/V trace with the corrections applied. Positive and negative rates are shown on the same figure for variation over the same range of incidence and the quasi-steady variation of C_N with incidence is given for comparison. The increment in $C_N(\Delta C_N)$ between the unsteady manoeuvre and the quasi-steady value for $\frac{x}{c_o} > 1$ has been taken from Fig. 4.06a and plotted against incidence in Fig. 4.06b, ΔC_N being plotted in such a way that where $\dot{w}$ or $\dot{\theta}$ changes from positive to negative at $\alpha = 0^\circ$ the plot is continuous. ΔC_N from Fig. 4.06b has been divided by the non-dimensional rates $\frac{\dot{w}c_o}{V^2}$ or $\frac{\dot{\theta}c_o}{V}$ and plotted against incidence in Fig. 4.06c for all three rates. Fig. 4.06c was used to establish whether there was any significant effect of rate on the derivative. The best line through the points in Fig. 4.06c was transferred back to Fig.4.06b.

For the pitching moment measurements, C_M and ΔC_M have been plotted using their respective

measuring axes throughout to avoid compounding errors in converting individual measurements to the pitching axis. Fig. 4.06c is not a true derivative therefore. For later comparison of the three derivatives $m_{\dot{w}}$, m_q, $m_{\dot{\theta}}$ and for comparison with the results from other sources, the pitching moments have been converted to the pitching axis.

4.2.1.2 Constant q manoeuvre

These have been plotted in a different manner to the plunging and pitching results since there was no change in incidence during the manoeuvre and only ΔC_N and ΔC_M were measured (see Fig. 4.07). Corrections were applied to the trace measurements and the corrected results presented as shown in simplified form in Fig. 4.08. The 'steady' value of ΔC_N from the middle of the manoeuvre was plotted against rate for each incidence (Fig. 4.08b) to establish whether the derivative concept could be applied within the accuracy of the results. If this were the case, the derivative measured by the slope of Fig. 4.08b was plotted against incidence in Fig. 4.08c.

4.2.2 Plunging manoeuvre

A typical U/V recorder trace is shown in Fig. 4.09. The traces have a mains ripple evident and also a ripple at a higher frequency. There were no significant irregularities in the

rail to cause large fluctuations in the trace. At the end of the run, the transition from a curved profile to the straight rail section was not very good and this is reflected at the end of the trace. An example of the measurements from a plunging manoeuvre with corrections is shown in Table 4.01.

4.2.2.1 Variation of C_N with plunging rate and incidence

The variation of C_N with $\frac{x}{c_o}$ (Figs.4.10 to 4.13) show a marked transient behaviour at the beginning of the test runs, particularly with a positive $\dot{w}$ (increasing incidence). After the transient has finished, ΔC_N is negative for positive $\dot{w}$ at high incidences and positive for positive $\dot{w}$ at low incidences. This can be seen clearly in Fig. 4.14 which shows ΔC_N plotted against incidence, the transient results having been omitted.

To obtain ΔC_N from Figs. 4.10 to 4.13 involves differencing two large numbers and in consequence there is a lot of scatter. To fit a mean line through all the points, the values of ΔC_N were converted to $z_{\dot{w}}$ by dividing by $\frac{\dot{w}c_o}{V^2}$ as shown in Fig. 4.15. The best line through the points was transferred back to Fig. 4.14.

Although there is a lot of scatter in Fig. 4.15 it is considered that the drawn line gives an accurate reflection of the trend of the results. The scatter is much greater for

the results at lower values of $\frac{\dot{w}c_o}{V^2}$ because the measured ΔC_N was smaller for the same accuracy in the measurement of C_N. There is no apparent difference in the derivative due to different rates of $\frac{\dot{w}c_o}{V^2}$. A difference in the derivative for positive and negative values of $\frac{\dot{w}c_o}{V^2}$ is apparent, however, When the derivative is converted back to values of ΔC_N and re-plotted on Fig. 4.14, the scatter in ΔC_N is shown to be of the same order for the three rates.

An attempt is made to explain the variation of the $z_{\dot{w}}$ derivative, from negative at low incidence to positive at high incidence in the following section.

4.2.2.2 'Virtual mass and vortex lag' theory

The $z_{\dot{w}}$ derivative can be treated as a combination of two effects (see Fig. 4.16)

(i) The virtual mass of the flow field associated with the wing (see Appendix 3)

(ii) The lag in the establishment of the new flow field associated with the new incidence.

The result of these two effects is shown diagrammatically in Fig. 4.16. The virtual mass is given by ref. 23 as 0.015 slugs. Assuming a step change in acceleration during the plunging manoeuvre, which is very nearly true, this virtual mass will give an immediate

force on the wing which remains constant throughout the manoeuvre and is of opposite sign to the acceleration vector.

Superimposed on the virtual force (virtual mass x normal acceleration) is the effect of the lag in the adjustment of the flow field to the new conditions. This lag results in a component of the normal force in the same direction as the acceleration vector.

The two effects are mutually opposed, the virtual mass giving a negative $z_{\dot{w}}$ and the lag effect giving positive $z_{\dot{w}}$. As the lift curve is non-linear, it is to be expected that the lag effect would be greater at high incidence where the lift slope is greatest. This is consistent with the variation of $z_{\dot{w}}$ with α which is negative at low incidence and positive at high incidence.

A series of experiments performed at the N.P.L. (ref. 24), in which a wing in a water tunnel was given a step change in w (and hence in incidence α), showed that the leading edge vortices had reached the equilibrium position appropiate to its new incidence in the time taken for the wing to travel one chord length, when the initial incidence was zero. If the movement is considered as an exponential movement of the vortices with a time constant $\tau = 0.33c_0$ then the position of the vortex can

be written:

$$z = z_{final}(1 - e^{-x/0.33c_o})$$

Further, if we argue that z is directly proportional to incidence α, we get

$$\alpha_{eff} = \alpha(1 - e^{-x/0.33c_o})$$

for a step change in α.

Using this result and applying it to a constant $\dot{w}$ (a constant $\dot{\alpha}$) we obtain

$\dot{\alpha}_{eff} = \dot{\alpha}(1 - e^{-t/\tau})$ where $\tau = 0.33c_o/V$

$$\alpha(t) = \alpha_o + \int_o^t \dot{\alpha}(1 - e^{-t/\tau})\,dt$$

$$\alpha(t) = \alpha_o + \left[\dot{\alpha}t + \dot{\alpha}\tau e^{-t/\tau}\right]_o^t$$

$$= \underline{\dot{\alpha}t - \dot{\alpha}\tau(1 - e^{-t/\tau})} \quad \ldots\ldots\ldots (i)$$

Hence, the time lag is a constant, τ, for large values of t. Now as this result applies to the lag of the vortices, it is only the non-linear part of the normal force which is affected. In the case of the model G wing, the normal force can be expressed as:

$$C_N = a\alpha + b\alpha^2$$

Differentiating; $\frac{dC_N}{d\alpha} = a + 2b\alpha$

hence $\Delta C_N = (a + 2b\alpha)\Delta\alpha$

Ignoring the linear component, a, we obtain

$$\underline{\Delta C_N = 2b\alpha\Delta\alpha} \quad \ldots\ldots (ii)$$

Now from (i), $\Delta\alpha = -\dot{\alpha}\tau(1 - e^{-t/\tau})$

$$\therefore \quad \underline{\Delta C_N = -2b\alpha.\dot{\alpha}\tau(1 - e^{-t/\tau})}$$

For $t/\tau > 1$ this can be approximated to

$$\Delta C_N = -2b\alpha.\dot{\alpha}\tau$$

and $\underline{z_{\dot{w}} = 1.67\alpha}$ where $b = 5.04$

$\tau/c_o = 0.33$

and α is in rads.

According to slender wing theory (ref.3)

there is no lag in the establishment of the flow field and $z_{\dot{w}}$ is purely the virtual mass term.

Combining these two results gives the variation of $z_{\dot{w}}$ shown in Fig. 4.47. The difference between the zero incidence slender wing value and the virtual mass term is because the slender wing theory integrates spanwise strips as opposed to chordwise strips. The measured value of $z_{\dot{w}}$ is less negative at zero incidence than the result given by the above analysis and increases non-linearly with incidence. The analysis has several major deficiencies however:

(i) No allowance is made for lag in the bound vorticity. Indicial aerodynamic theory suggests there is a lag in the development of the bound vorticity and this would have the effect of increasing $z_{\dot{w}}$ in a positive sense. All practical considerations lead to the conclusion that there is a lag in the bound vorticity.

(ii) The effect of the build-up in the vorticity is much more complicated than has been suggested here. Ref. 24 shows that the movement of the vortex is different for increasing and decreasing incidence and is different again for movement between two incidences. Furthermore, it is not known

how the strength of the vortex is affected during the plunge.

In view of these reservations it is perhaps not surprising that the simple 'virtual mass + vortex lag' theory does not give a very accurate picture of the value of $z_{\dot{w}}$. It does, however, explain the general trend of $z_{\dot{w}}$ from a negative value at low incidence to a positive one at high incidence.

In an attempt to examine the transient behaviour of the normal force, Figs 4.17, 4.18 were plotted showing the results for time corresponding to $\frac{x}{c_o} < 1$. Given the uncertainty in the accuracy of the results during the transient part of the manoeuvre, the transient behaviour appears to confirm the simple theory outlined previously.

4.2.2.3 Variation of $C_{M.733c_o}$ with plunging rate and incidence

The variations of $C_{M.733c_o}$ with distance travelled (Figs 4.19 to 4.22) did not show the same marked transient behaviour as the C_N results but the results for $\frac{x}{c_o} < 1$ have been omitted when measuring ΔC_M for Fig. 4.23 because of the uncertainty about their accuracy. Figs. 4.23 and 4.24 show the same order of experimental scatter as the C_N results.

It is much more difficult to apply a simple theory to the $m_{\dot{w}}$ derivative than to the $z_{\dot{w}}$

derivative. This is because small differences in the point of action of the normal force can have a large effect on the pitching moment. The pitching moment was measured about a point close to the predicted centroid of the virtual mass. It would thus be reasonable to expect the pitching moment to exhibit the same sort of transient behaviour as the normal force, but this is not the case. It is not clear whether the observed transient is due to real effects or to the recording system.

By combining $\frac{\Delta C_{M.7.33c_o}}{\dot{w}c_o/V^2}$ and $z_{\dot{w}}$ it is possible to find the point of action of the two components of $z_{\dot{w}}$. As $\Delta C_{M.733c_o}$ is zero at zero incidence, the virtual mass component must act through this point, $0.733c_o$. This agrees with slender wing theory (Appendix 4). Taking an average of the values of $\Delta C_{M.733c_o}$ at higher incidences, it is found that the component of $z_{\dot{w}}$ due to the vortex lag acts at a point $0.61c_o$ for positive $\dot{w}$ and $0.58c_o$ for negative $\dot{w}$. This is very close to the aerodynamic centre of the steady normal force, $0.582c_o$.

4.2.3 Constant q manoeuvre

The pitching moment and normal force were recorded on separate U/V traces. Typical ones are shown in Figs. 4.25 and 4.26. The

amplification of the signal also amplified the noise, the high frequency noise being particularly noticeable on the pitching moment trace. During the 'steady' part of the trace, it was possible to draw a mean line through the trace which yielded consistent results.

An example of the measurements from a constant q manoeuvre with corrections is shown in Table 4.02 and Fig. 407. Fig. 4.07 demonstrates the transient behaviour at the beginning and end of the manoeuvre. The shaded centre section has been used to provide the results for the steady manoeuvre.

4.2.3.1 Variation of C_N with q and incidence

Fig. 4.27 shows C_N, obtained from figures similar to Fig. 4.07, plotted against $\frac{qc_o}{V}$. There is a lot of experimental scatter but it is possible to connect the results by a straight line through the origin. Taking the slope of this line as the derivative z_q, Fig. 4.29 shows this derivative plotted against incidence. There is no measurable difference between the derivatives for positive and negative rates of $\frac{qc_o}{V}$.

4.2.3.2 Variation of $C_{M.733c_o}$ with q and incidence

The variation of $C_{M.733c_o}$ with $\frac{qc_o}{V}$ (Fig.4.28) shows similar scatter to the normal force results. Once again, it is possible to connect these results by a straight line through the

origin. $\Delta \frac{C_{M.733c_o}}{\frac{qc_o}{V}}$ (Fig. 4.29) shows a slight shift between positive and negative rates of $\frac{qc_o}{V}$ but this is within the experimental scatter.

The q derivatives show less scatter than the other results because of the use of the high- gain amplifiers. This is encouraging because this is the manoeuvre which cannot normally be obtained in a wind tunnel. Consequently, there are no other experimental results for this type of wing to compare these derivatives with.

4.2.3.3 Initial transient

During the initial part of the run, when one follower was on the curved profile of the rail and the other on the horizontal part, the normal acceleration of the wing was exactly half that of the final normal acceleration.

Fig. 4.30 shows a comparison of the maximum increment in C_N during this initial acceleration and the product of the virtual mass from ref. 23 and the initial acceleration. There is a reasonable measure of agreement which lends support to the value of the virtual mass derived from the plunging manoeuvres.

4.2.4 Pitching manoeuvre

The pitching manoeuvre is the one normally performed in a wind tunnel oscillatory test and therefore provides an opportunity for a comparison of the derivatives measured by oscillatory methods with the technique used in this research. In addition, the cam rail was constructed from straight lengths of L section steel which meant that there were few irregularities in the rail. It can be seen from Fig. 4.31 that this resulted in a smooth trace. In addition, as there was no change in flight path angle there were fewer corrections to be applied to the results. It was hoped, as a result, that these factors would make these derivatives the most reliable.

Fig. 4.31 shows an example of a U/V recorder trace. The increased vibration at the start of the rotation was caused by the follower moving from the horizontal section of the rail onto the ramp. The mains ripple has been reduced by the addition of the low-pass filter. An example of the measurements from a pitching manoeuvre with corrections is shown in Table 4.03.

4.2.4.1 Variation of C_N with pitching rate and incidence

Figs. 4.32 to 4.35 show the variation of C_N during the run and demonstrate the difficulty of trying to measure a derivative which is the difference between two nearly equal large

quantities. It can be seen in Fig. 4.36 however, that the trend of the results is consistent even though the differences themselves are very small. The derivative $z_{\dot{\theta}}$ plotted in Fig. 4.37 is negative up to a fairly high angle of incidence, approximately 15°, and then becomes positive.

4.2.4.2 Variation of $C_{M.795c_o}$ with pitching rate and incidence

Figs. 4.38 to 4.41 show the values of ΔC_M to be much easier to measure than ΔC_N. When these values of ΔC_M are plotted against incidence, Fig. 4.42 the results for positive $\frac{\dot{\theta} c_o}{V}$ show much less scatter than for negative $\frac{\dot{\theta} c_o}{V}$. It is not clear why this should be so. Fig. 4.43 also illustrates this. A lot of the scatter is at the lowest rate however, and one run at the highest rate, 16° to 0°, was not very accurate. This run has been omitted from Fig. 4.43.

4.2.4.3 Effective camber theory

For aircraft with high aspect ratio wings and conventional tailplanes, the contribution of the wing to $m_{\dot{\theta}}$ is usually ignored and only the contribution of the tail is considered. This contribution is found by considering the tailplane as having an increased incidence due to the relative vertical velocity at the tail.

The increment in tailplane incidence is given by $\dot{\theta} l_T / V$ where l_T is the tail arm. It is therefore a quasi-static derivative. Ref. 1 explains how this concept can be extended to a low aspect ratio wing by considering the chordwise distribution of vertical velocity over the wing and equating this to the equivalent cambered wing.

Experimental measurements of the lift distribution on a low aspect ratio delta wing (ref. 25) were used to apply to this concept to the AGARD Model G planform. Fig.4.44 shows the lift distribution on the uncambered delta wing used in ref. 25. Although this wing has a delta planform, it was considered that the lift distribution for the model G planform would be similar. The effect of the parabolic tips on the model G planform is to flatten the peak of the lift distribution and move the centre of lift forward.

The detailed calculation of $z_{\dot{\theta}}$, $m_{\dot{\theta}}$ by this method is shown in Appendix 6. The technique was to superimpose a lift distribution due to the camber effect on the steady lift distribution. As the lift curve was non-linear the increment in lift due to the camber effect increased with incidence.

The results of this analogy are shown in Figs. 4.47 and 4.48. The theoretical $z_{\dot{\theta}}$ is

much less negative than the measured results and becomes more negative with increasing incidence, a trend in opposition to the behaviour of the measured results. The $m_{\dot{\theta}}$ derivative however, matches the measured results very closely. Although it has been stated that small differences in the lift distribution have a larger effect on the $z_{\dot{\theta}}$ derivative than the $m_{\dot{\theta}}$ derivative, this effect is not large enough to explain the difference, particularly the trend reversal.

4.2.5 Summation of normal force derivatives $z_{\dot{w}} + z_q$ and its comparison with $z_{\dot{\theta}}$

All the normal force derivatives have been collected together in Fig. 4.45. They are shown for both positive and negative rates. The $\dot{w}$ and $\dot{\theta}$ derivatives both show the same trend from negative at low incidence to positive at high incidence. The q derivative behaves quite differently, however, being negative at low incidence and becoming more negative as the incidence increases.

In an attempt to see whether the assumption of linearity holds true, i.e. whether $z_{\dot{\theta}} = z_{\dot{w}} + z_q$ the broken line on the $z_{\dot{\theta}}$ curves of Fig. 4.45 shows the sum of z_q and $z_{\dot{w}}$. This compares well with the measured value of $z_{\dot{\theta}}$, particularly for negative values of $\dot{\theta}$. There must be some reservations however, concerning the addition of

two derivatives with so much experimental scatter.

It is often assumed that the q derivative provides the major contribution to the derivative. Fig. 4.45 shows that this is not the case over the whole of the incidence range.

4.2.6 Summation of pitching moment derivatives $m_{\dot{w}} + m_q$ and its comparison with $m_{\dot{\theta}}$

The pitching moment derivatives were corrected to the pitching axis, $0.667c_o$, and are shown in Fig. 4.46. The derivatives are negative throughout the incidence range, becoming more negative with increasing incidence.

The sum of m_q and $m_{\dot{w}}$ compares well with $m_{\dot{\theta}}$ for positive $\dot{\theta}$ but at high incidences $m_q + m_{\dot{w}}$ is about 30% more negative than $m_{\dot{\theta}}$. Given the experimental scatter of the individual derivatives this is not altogether unexpected.

Within the overall accuracy of the results, Figs. 4.45 and 4.46 appear to confirm the assumption of linearity that $m_{\dot{w}} + m_q = m_{\dot{\theta}}$. However, any cross-coupling effects are likely to be of second order magnitude and therefore the accuracy of the results does not permit a more definite statement to be made.

4.2.7 Comparison of measured derivatives with those from other sources

Figs. 4.47 and 4.48 show the z and m derivatives together with results from other

experiments, which used wind tunnel oscillatory methods.

The only other results obtained for the model G planform came from experiments carried out at the RAE by Fail,(ref 21) which are at present unpublished.

The model used in ref. 21 had a centre line chord of 5ft (1.52m) and was mounted inthe RAE 13ft x 9ft (3.96m x 2.74m) tunnel. Wind speeds of 150ft/sec (45.6m/sec) and 200ft/sec (61m/sec) were used. The wing was pitched about an axis at $0.62c_o$ to measure the pitching derivatives $z_{\dot{\theta}}$ and $m_{\dot{\theta}}$. $m_{\dot{\theta}}$ from these tests was converted to $0.667c_o$ using the conversions given in Appendix 5.

The RAE results compare favourably with the present $m_{\dot{\theta}}$ derivative, particularly for negative $\dot{\theta}$. The $z_{\dot{\theta}}$ derivative does not correspond so well, however, the RAE derivative at zero incidence, being almost twice that found in the present tests. At high incidences the RAE $z_{\dot{\theta}}$ derivative does not become positive although it does become less negative.

The wind tunnel results do not distinguish between positive and negative pitch rates and the sinusoidal oscillation technique gives a continuously varying $\dot{\theta}$ throughout the cycle. The pitching frequency used was 3.6Hz which corresponded to a distance of about 6 chord lengths travelled

during one cycle. This is considered slow enough to eliminate the influence of transient effects on the derivatives and the use of two wind speeds confirmed there was no discernible effect of non-dimensional frequency on the derivative.

Cooper (ref. 26) employed a delta wing of aspect ratio 0.8 and root chord 6ft (1.83m) in an oscillatory test in a 7ft x 5ft (2.14m x 1.52m) tunnel. The wind speeds were 60 (18.3), 90 (27.4) and 100ft/sec (30.5m/sec) and frequencies from 0.5 to 3.0 Hz were used. Pitching axes were at $0.5c_o$ and $0.639c_o$.

Although the wing used in ref. 26 had a different planform, the aspect ratio was about the same as for model G so it would be expected that the derivatives would lie quite close to those measured here. The $z_{\dot{\theta}}$ derivative from ref. 26 compares well with the RAE value. The derivatives z_z and m_z which are effectively $z_{\dot{w}}$ and $m_{\dot{w}}$ were also measured in ref. 26. The $z_{\dot{w}}$ term is higher than that measured here but is of the same sign over most of the range of incidences covered. The $m_{\dot{w}}$ derivative measured by Cooper was attributed by him to contain a random error as it followed no set pattern. The use of such a large wing led to appreciable tunnel interference effects, corrections for which have not been applied to

the results quoted here. Ref. 26 states that wall constraints may reduce the derivatives by as much as 10%.

Some of the earliest results for slender wings were those obtained by Wright (ref. 12). He used a gothic wing of aspect ratio 0.75, 4ft (1.22m) root chord in a tunnel of cross-section 10ft x 12ft (3.05m x 3.66m). The wind speed was 150ft/sec (45.6m/sec) and the pitching frequency ranged from 1.3 to 5.6Hz.

His results compare well with the RAE results. Differences may be due to the different planform but are probably within the accuracy of the measurements.

In general, the measured $m_{\dot{\theta}}$ derivative compares favourably with the results mentioned above within the accuracy of the present results. The $z_{\dot{\theta}}$ derivative, however, does not agree very well with those from other sources and none of the other results show the change to a positive $z_{\dot{\theta}}$ at high incidence. There are no experimental measurements of the other derivatives except ref. 26 for the $\dot{w}$ derivatives, but Cooper believes that his measurements may be entirely due to experimental scatter.

It was not the purpose of this research to develop a theory to predict the longitudinal derivatives, It is useful however to compare the results with current theoretical predictions,

particularly for the q and $\dot{w}$ derivatives which have no other experimental results for comparison. Two theories are shown here for comparison:

(i) R.T. Jones slender wing theory (ref. 3). This classical theory is a linear one based on the concept of virtual mass and takes no account of the effect of the leading edge vortices or the effect of the trailing edge. For steady state lift however, it yields a lift slope which is very close to the measured value at zero lift (see Fig. 4.02).

The calculation of the derivatives is given in Appendix 4 and those for gothic and delta wings are shown for comparison. The derivatives are, of course, independent of incidence. The theoretical derivatives are shown on the vertical axes of Figs.4.47 and 4.48. They are shown to be of greater magnitude than any of the derivatives measured here or by any of the other experimenters. The fact that the leading edge vortices are not taken into account may be the reason for this. For instance, the $z_{\dot{w}}$ derivative is entirely due to the virtual mass term, no account being taken of the vortex lag.

(ii) A more advanced lifting surface theory by Garner (ref. 4) takes into account the trailing edge effect but still ignores the leading edge vortices. His theory is based

on the steady state lift distribution calculated from Multhopp's lifting surface theory (ref. 27). The values shown here were communicated to the author by Dr.A.J.Ross of the RAE. She used the theory to compare with some results gained from free flight model research at transonic speeds using the model G planform (refs. 10 and 28). The results of the model tests (refs. 10 & 28) showed good agreement with ref. 4 for $m_{\dot{\theta}}$ at transonic and supersonic speeds. The z derivatives given by ref. 4 can be seen in Fig. 4.47. The $z_{\dot{w}}$ and $z_{\dot{\theta}}$ derivatives at zero-lift can be seen to be higher than the values measured here but are in fair agreement with results from other sources. The z_q derivative is approximately the same as that given by slender wing theory, which is about twice the measured value.

The $m_{\dot{w}}$, m_q and $m_{\dot{\theta}}$ derivatives (Fig.4.48) on the other hand, show good agreement with the experimental results.

5. FLOW VISUALISATION

5.1 General

The experimental system provided a very good opportunity to use flow visualisation technique to indicate the position of the model wing leading edge vortices during unsteady manoeuvres. It was hoped that by measuring the position of the vortices, a correlation might be found with the normal force and pitching moment derivatives.

Several techniques of flow visualisation were tried to assess their suitability for this type of facility. They were:

(i) The injection of dye into the vortices.

(ii) The suspension of particles of nearly the same density as water.

(iii) The emission of hydrogen bubbles along the leading edge of the wing.

The tests are each described in the following sections.

5.1.1 Dye filament method

A small bore tube was led along the centre line of the wing and the open end turned through 180° to inject dye at the apex of the wing in the same direction as the free stream. The other end of the tube was led to a reservoir mounted on the trolley. The reservoir was filled with potassium permanganate dye and the outflow controlled by means of a tap.

The dye worked well in showing up the position of the vortex core. The major drawback

was the rapid discolouration of the water in the tank. The emptying and filling of the tank was quite a long process and it tended to initiate leaks. For this reason the technique was rejected.

5.1.2 Suspended polystyrene balls

Polystyrene balls of specific gravity slightly greater than 1 were tried in 2 different sizes, 0.04in (1.6mm) and 0.015in (0.6mm). As their density was slightly greater than water they sank slowly, the smaller balls having a slower rate of descent than the larger ones. The technique adopted was to release a handful of polystyrene balls into the water and then drive the wing through the 'cloud' of polystyrene balls. The polystyrene balls were illuminated by a 500w floodlight mounted on the trolley vertically above the wing. This arrangement gave the maximum amount of reflection from the balls at right angles to the direction of incident light.

It was found that the smallest balls gave the best results as they had a lower rate of descent and it was easier to obtain a dense, uniform 'cloud' with them. The definition of the vortex cores was not as good with method (i).

5.1.3 Electrolysis (hydrogen bubbles)

If two conductors are placed in water and connected to an electrical power supply, oxygen will be emitted at the anode and hydrogen at the

cathode. This fact is used in the electrolysis technique. The volume of hydrogen emitted is twice that of oxygen (there being two atoms of hydrogen to one of oxygen in each water molecule), and the amount of the gases given off depends on the size of the conductors, their proximity, the conductivity of the water and the voltage of the power supply.

Ref. 29 gives a good description of other experiments carried out using this technique. In most of these, rather sophisticated circuits have been used to give pulses of bubbles which can be observed in their subsequent passage through the fluid. In our case this was not necessary as a constant stream of bubbles was all that was required.

A simple test was set up using a fine copper wire (0.006in (0.15mm) dia) as the anode and the wing surface as a cathode. The anode wire was fixed to the surface of the wing with insulating tape which also insulated the wire from the wing. The anode wire ran round the perimeter of the wing and was supplied by a 30v adjustable d.c. power supply.

The results indicated that this was the most promising method. The bubbles showed up very well and were drawn into the vortex cores to give good definition. The circuit was very simple and convenient to use and there was no contamination of the water. As a result this method was adopted. The experimental apparatus

is described in the following section.

5.2 Apparatus for hydrogen bubble technique

As described in the introduction, the technique required two conductors to act as an anode and a cathode and a power supply to provide a potential difference between them. The choice of anode material, size, etc. was mainly based on ref.29. The wire diameter was chosen as a result of studying Figs. 5.01, 5.02, 5.03 taken from ref. 29 which are reproduced here. The anode consisted of a fine wire (0.003in (0.075mm) dia) attached to the leading edge of the wing and the cathode was a thin flat metal plate attached to the undersurface of the wing. Wires were led along the sting to a power supply. The model wing and a scale used to measure the position of the vortices can be seen in Figs. 5.04 and 5.05. A schematic diagram of the wing and circuit is shown in Fig. 5.06.

Platinum was chosen for the anode as it could be cleaned by reversing the polarity. Other metals corrode when this is done. The cathode was made from stainless steel plate. The wing itself was made from a formica laminate to the model G planform. The 0.003in (0.075mm) dia platinum wire was attached to the leading edge with cyanoacrylate adhesive. This type of adhesive requires only a very thin film and provides instant contact adhesion. The small diameter of

the wire meant that a sharp leading edge was maintained.

Some tests were done to find the optimum supply voltage. At low voltages the supply of bubbles was inadequate. The volume of bubbles increased with increasing voltage but a point was reached where the wire rapidly became contaminated and the supply of bubbles diminished. Because of uneven contamination these bubbles also collected into irregularly spaced larger bubbles. A compromise between the bubble supply and speed of contamination of the wire was reached with a voltage of about 15v. To clean the wire between runs, the polarity was simply reversed. The platinum wire was lacquered on the trailing edge and one leading edge so that a clear picture of a single leading edge vortex could be obtained.

5.3 Recording of flow patterns

Three methods of recording were used:

(i) Closed circuit television (CCTV) with video tape recorder (VTR).

(ii) Cine camera.

(iii) Still camera.

It was originally intended to carry the camera on an arm extended from the vertical slide over the side of the trolley and thus able to move with the wing. It was found, however, that the cameras were too heavy for this and so they were fixed on a frame

mounted on the trolley. The camera was then able to move with the trolley but not move in elevation with the wing. This did not prove to be a very big drawback. The frame to carry the camera is shown in Fig. 5.07.

In all cases a black background was used and the wing was lit from above using a 500w floodlamp. The flow pattern was filmed from the side of the tank at right angles to the direction of the incident light.

To aid in the measurement of the vortex position a scale was attached to the sting shield and travelled with the wing.

5.3.1 CCTV and VTR

This proved to be very useful for initial testing and qualitative analysis. Without the use of CCTV it would have been very difficult to establish the best values of current density, trolley speed etc. as the wing was small and was moving relative to the observer. Equally, the time interval involved in processing film made the use of still or cine cameras unattractive for initial testing. CCTV gave good magnification onto a 21in (54cm) screen and provided instant playback facility with the use of a VTR. The contrast could be adjusted to give good definition of the vortices and best results were obtained when the contrasts were reversed to show the

vortices black on a white background.

Although this method proved excellent for initial testing and qualitative assessment (and later for demonstration purposes) it was found unsuitable for quantitative analysis. The main limitation was the distortion of the image on the television screen. This became worse towards the edges of the screen. Another difficulty was that one frame could be held for about 20 seconds only and was not very steady during this time. These drawbacks could have been removed by the use of more sophisticated equipment. The cost of suitable equipment is much higher, however, and was far outside the budget of this research project.

A videotape recording was retained for demonstration purposes.

5.3.2 Cine camera

A Bolex 16mm cine camera running at 64 frames/sec was used to record several complete runs. It provided the most complete record of a run and demonstrated the build up of vorticity when the wing started from rest. It was considered that this was the best method for detailed analysis of the whole run. In our case, however, where time was limited, it was thought that the volume of information yielded by this method would have been a disadvantage. It was

decided that the use of a still camera to record a few specific points during a run would be the best solution in the time available.

5.3.3 Still camera

A Nikkormat camera was used with a Pan F(AS A 40) film, a shutter speed of 1/30th sec and aperture set at f8. An electronic flash was used to illuminate the wing. The camera was triggered using a cable release operated by a cam as shown in Fig. 5.07. The position of the wing was recorded on the film by locating the wing with lines drawn on the tank side.

A total of 24 pictures were taken covering examples of steady runs, plunging, constant q and pitching. These were taken at different incidences and at different stages in the run, but all unsteady pictures were taken at a non dimensional rate of 0.0525.

5.4 Results

A selection of the still photographs of the vortices is shown in Figs. 5.08, 5.09. The positions of the vortices measured on these photograps have been plotted in Figs. 5.10, 5.11. They were all taken at the same incidence, 18°, except for the constant q one , which was at $17^{\circ}20'$.

The conditions were:

18°	constant	positive $\dot{w}$
18°	constant	negative $\dot{w}$
17°20′	constant	negative q
18°	constant	positive $\dot{\theta}$
18°	constant	negative $\dot{\theta}$

On inspection, it can be seen that there is very little difference in the position of the vortices. The quality of the pictures is not as good as was achieved in some of the early tests. There is some irregularity in the path of the vortex core where previous work (ref. 30) has shown it to be a smooth line. It is thought that this was due to some unevenness in the wire attached to the leading edge. This would not only lead to uneven flow separation but also uneven contamination of the wire causing localised concentrations of hydrogen bubbles.

The use of the measuring scale tended to obscure the vortex. Fig. 5.10 shows the position of the vortex cores over a range of incidences measured from the steady results. No correction has been made for parallax error but as they are only intended for comparative purposes, this should not affect any broad conclusions which may be drawn from the results. The vortex core follows a straight line from the apex of the wing for most of the wing chord. Near the trailing edge the vortex core begins to curve away from the wing as it forms the trailing vortex. As the incidence is

increased the slope of the vortex core, relative to the wing, increases. These features have been well established in other research (ref. 30).

Fig. 5.11 shows a similar treatment of the paths of the vortex cores in unsteady flow. The constant $\dot{\theta}$ runs (pitching) show a difference in the position of the vortex for positive and negative $\dot{\theta}$ at the same incidence. Their positions are consistent with a lag effect, the vortex remaining at the position of a slightly higher incidence as the incidence was reduced and remaining at a slightly lower incidence as the incidence was increased. The difference was too small, however, to measure at this scale and draw any firm conclusions.

The $\dot{w}$ and q runs were only successful at either positive or negative rates so no comparison could be made. These do, however, lie very close to the steady positions.

6. CONCLUSIONS

The system has demonstrated its ability to provide the complete set of unsteady longitudinal derivatives $z_{\dot{w}}$, z_q, $z_{\dot{\theta}}$, $m_{\dot{w}}$, m_q, $m_{\dot{\theta}}$ for a sharp-edged slender wing over an incidence range from 0° to 24°. In doing so, it has been able to provide the pure pitching derivatives (rotation at constant incidence) z_q and m_q, for the first time under laboratory conditions.

The system was simple in not having to be designed to withstand large cyclic forces. Also the instrumentation did not have to discriminate the small phase angles of these large cyclic forces. The inertia forces due to the model wing were small in relation to the aerodynamic forces, which eliminated one of the major sources of error in oscillatory tests.

The main failure of the system was in the amount of mechanical noise transmitted from the wheels of the trolley and the followers to the output signal. This noise was the main reason for the scatter in the results.

The steady motion measurements of C_N and C_M show good agreement with existing values from other sources when account is taken of tunnel blockage and wall constraint. The repeatability of the results provided a basis which could be used with confidence for comparison with the unsteady motion results.

The unsteady motion results show a lot of experimental scatter but it has been possible to

extract the basic derivatives. The experimental scatter was more for the normal force derivatives than for the pitching moment derivatives because the ratio $\frac{\Delta C_M}{C_M}$ was greater than $\frac{\Delta C_N}{C_N}$. It is encouraging that the z_q and m_q derivatives, which are normally unobtainable in wind tunnel experiments, show the least experimental scatter because high-gain amplifiers were used to measure them.

The derivatives appear to be linear with rate within the accuracy of measurement. They do show a difference for positive and negative rates, however. The summations of the $\dot{w}$ and q derivatives show close agreement with the $\dot{\theta}$ derivatives but reservations must be held concerning the addition of two derivatives containing so much experimental scatter.

The derivatives are shown to be dependent on the incidence of the wing and for the pitching moment derivatives the trend corresponds with that measured in oscillatory tests. The normal force derivatives $z_{\dot{\theta}}$ and $z_{\dot{w}}$ show a change in sign at high angles of incidence which has not been shown in oscillatory tests. This trend corresponds with the concept of the derivative being comprised of two effects - the virtual mass and the vortex lag.

The results used for comparison (refs. 12,21,26) have been shown to be independent of non-dimensional frequency over a limited range but because of the experimental scatter in the results of this experiment

it is not possible to say whether the difference in the derivatives was due to frequency effect.

The transient response at the beginning of the test run is potentially very interesting since this could provide a more detailed knowledge of the effect of the continuously varying acceleration and speed in an oscillatory test. A good correlation was obtained between the amplitude of the transient impulse and the virtual mass but separate experiments with more accurate cam rails would be necessary to investigate the transient properly.

The flow visualisation experiments did not produce photographs good enough for quantitative analysis but it is thought the hydrogen bubble technique offers enough scope for improvement to make this possible. The still photographs show a small movement in the position of the vortices for positive and negative pitching rates. The cine and television films provided a good opportunity to see the build-up in vorticity for a wing starting from rest.

Whilst the system has demonstrated its ability to measure the longitudinal derivatives, much more work needs to be done to improve its accuracy, particularly by removing the mechanical noise, and reducing electrical interference.

7. RECOMMENDATIONS FOR FURTHER WORK

The main area requiring further work is in the reduction of the experimental scatter. Significant improvements in this respect could be achieved by:

(i) Running the trolley on air bearings to eliminate vibrations transmitted from the main wheels.

(ii) A more accurate cam rail profile, possibly machined from a single piece of metal and paying particular attention to the transformation from the straight section to the curved section of rail. This would have the further benefit of making it possible to study the transient behaviour at the start of a manoeuvre.

(iii) Stiffening the sting to raise its natural frequency and enable the vibration at the natural frequency to be filtered out more easily. In addition, the sting could be damped by having a split sting or fitting a close tolerance ring on it.

(iv) To compensate for the reduction in strain with a stiffer sting, semiconductor strain gauges which have a higher gauge factor could be used. The drift associated with this type of strain gauge would not be a problem over the duration of a test run.

To enable the increments in C_N and C_M in plunging and pitching manoeuvres to be amplified, the strain gauge output signal could be compared to an analogue signal simulating the quasi-steady

variation in C_N and C_M. The difference between the two signals could then be amplified in a similar fashion to the constant q manoeuvres.

The original intention of performing test runs at constant forward accderation was not carried out and this is an important area for further work to complete the measurement of the fundamental unsteady longitudinal derivatives.

The present system is only applicable to slender wings since the Reynolds number is unrepresentative of real flight conditions. To achieve a significant increase in Reynolds number, say to 10^6, would require a combination of increasing the model size and speed of the trolley. These increases would probably be beyond the resources of a small University laboratory experiment.

ACKNOWLEDGEMENTS

I should like to record my appreciation of the assistance I have received over the $4\frac{1}{2}$ years of work which have led to the production of this thesis. In particular, the guidance and help of Dr. J.F. Henderson and Mr. P.J. Wingham have enabled me to steer a course through the considerable technical problems which have arisen in the experimental work and the writing of this thesis.

The implementation of the experiment would not have been possible without the University workshop staff who built the system, and I should like to thank particularly Mr. R. Cole, Mr. A.F. Morris and Mr. T. Keston for producing the hardware. I should also like to thank Mr. G. Jones for his assistance in the collection and analysis of the experimental data.

I should like to thank MOD(PE) for sponsoring the research and the SRC for providing financial support. The assistance of Mr. R. Fail of MOD(PE) has been greatly appreciated.

Last, but by no means least, I wish to thank my wife, Linda, for typing this thesis and providing moral support during a period which was probably more difficult for her than for me.

APPENDIX 1

Design of stings and calculation of theoretical strain gauge outputs

Sting no. 1 was made from commercial grade aluminium alloy, and sting no. 2 was made from HE30 aluminium alloy. Both had a value of Youngs modulus E of approximately 10×10^6. The dimensions of both stings were nominally the same and are given in Fig. A.1.1. The deflection and end slope of the sting are shown in Fig. A.1.2 for a 0.6 lbf (2.7N) load applied at the aerodynamic centre. There was s deflection at the aerodynamic centre of 0.12in (3.07mm) per lbf of normal force and a slope of 0.021 rad per lbf. The model itself weighed 0.055 lbf (0.244N). The maximum normal force of 0.6 lbf (2.7N) therefore produced a deflection of0.073in (1.85mm) and a slope of 0.0125 rads. With this load the strains at the measuring stations were:

M_1 = 0.016%

L_1 = 0.018%

L_2 = 0.027%

M_2 = 0.020%

The gauges had a resistance of 120 ohms and a gauge factor of 2.05. The outputs from the strain gauge bridges are given by

(i) Normal force bridge circuit

Consider the model producing positive normal force and pitching moment. The strain gauges on the upper surface are under compression. The strain gauges on the lower surface are under tension. (Fig.A.1.1)

Resistance N_1 lower $= R + \delta R_{12}$

N_2 lower $= R + \delta R_{14}$

P.D. across 2.4 $= \delta R_{12} - \delta R_{14}\left(\frac{V}{2R}\right)$

now $\frac{\delta R_{12} - \delta R_{14}}{R} = \left(\varepsilon_{12} - \varepsilon_{14}\right)$ x gauge factor

$$= \left(\frac{\text{Moment}_1\, y_1}{EI_1} - \frac{\text{Moment}_2\, y_2}{EI_2}\right) \text{x gauge factor}$$

now $\left(\frac{y}{EI}\right)_1 = \left(\frac{y}{EI}\right)_2$

and $\text{Moment}_1 - \text{Moment}_2 = (\text{Normal force} \times l_1 + PM) - (\text{Normal force} \times l_2 + \text{pitching moment})$

$= \text{Normal force} \times (l_1 - l_2)$

$\therefore$ Output $=$ Normal force x $(l_1 - l_2)\left(\frac{y}{EI}\right)_{N_1, N_2}\left(\frac{v}{2}\right)$ x gauge factor

Substituting values, Output = Normal force x 180 x Vmicrovolts

(ii) Pitching Moment Bridge

Again consider the model producing positive normal force and pitching moment (Fig. A.1.1)

Reistance M_1 lower $= R + \delta R_{56}$

M_2 lower $= R + \delta R_{58}$

$\therefore$ PD across 6-8 $= \delta R_{56} - \delta R_{58}\left(\frac{V}{2R}\right)$

now $\frac{\delta R_{56} - \delta R_{58}}{R} = (\varepsilon_{56} - \varepsilon_{58})$ x gauge factor

$$= \left(\text{Moment}_1 \left(\frac{y}{EI}\right)_{m_1} - \text{Moment}_2 \left(\frac{y}{EI}\right)_{m_2}\right) \text{x gauge factor}$$

Now if $\left(\frac{y}{EI}\right)_{m_1} = n \times \left(\frac{y}{EI}\right)_{m_2}$

and $m_2 N_2 = n\, m_1 N_1$

then the normal force cancels and

$$\delta R_{56} - \delta R_{58} = \text{P.M.} \times \left((n\ 1) \times \left(\frac{y}{EI}\right)_{m_2} \right) \times \text{gauge factor}$$

$$\therefore \text{Output} = \text{P.M.} \times (n-1)\left(\frac{y}{EI}\right)_{m_1} \times \left(\frac{V}{2}\right) \times \text{gauge factor}$$

Substituting values, Output = Pitching moment x 70xVmicrovolts

Therefore for a load of 0.6lbf (2.7N) and a bridge voltage of 6v the output from the lift bridge was 650μV and with the pitching moment focus at 0.733co, the output from the pitching moment bridge was 250μV.

At first sight it appears that no amplification of the signal was necessary for the lift bridge using C.40 galvanometers (with a sensitivity of 0.067 V/cm), and a gain of only about 2.5 was necessary for the pitching moment bridge. It was necessary, however, to amplify the signal and put a resistor in series with the galvanometer in order to protect the galvanometer should a short circuit occur that would apply the whole bridge voltage across the galvanometer

APPENDIX 2.

Reduction of noise using filters

A noise signal appeared on the output traces due to vibration of the sting. The main cause of this noise was vibration in the vertical mode with some cross-coupling from lateral vibration. The strain gauges were symmetrically placed along the neutral axis of bending in the lateral plane, so that any lateral bending should not produce any signal. This was not quite true in practice, but the lateral bending contribution to the vibration was small.

If the wing and sting are considered as a simple mass-spring system, the natural frequency of vibration is between 44Hz (including the mass of the sting) and 49Hz (ignoring the mass of the sting) in air. This was confirmed by tapping the wing-sting combination in air and measuring the frequency of the resulting vibration on the U/V recorder. Repeating this in water, it was found that the frequency was reduced to 17.5Hz. It was also noticed that other vibrations occurred at a much higher frequency, presumably a harmonic of the first natural frequency.

To remove the noise signal a notch filter was used to remove the first natural frequency and a low-pass filter to remove the higher frequencies. The circuit diagrams of the two filters are shown in Fig. A.2.1.

A.2.1 Output signal from notch filter

A notch filter is a second order system whose

transfer function is

$$\frac{Vout}{Vin} = \frac{1+(Ts)^2}{1+4Ts+(Ts)^2}$$

which produces a gain and phase lag in the system. The input to the filter is a signal from the strain gauge proportional to the normal force or pitching moment, which varies in the form:

$V_{in} = at^2 + bt$ where t = time and a and b are constants

Solving the differential equation using the D-operator the full equation is:

$(D^2 + 2\zeta w_n D + w_n^2)\, V out = (D^2 + w_n^2)\, V in$

The solution to this equation is:

$$V_{out} = \underbrace{Ae^{-\zeta+\sqrt{\zeta^2-1}} + Be^{-\zeta-\sqrt{\zeta^2-1}}}_{\text{Complementary function}} + \underbrace{a(t-2\zeta/\omega_n)^2 + b(t-2\zeta/\omega_n) + 4a(\zeta/\omega_n)^2}_{\text{Particular integral}}$$

Where the complementary function describes the transient and the Particular integral describes the steady state response. In this case $\zeta = 2$ and $w_n = 110$rad/sec. For an electrical system with capacitance in the circuit the conditions at $t = 0$ are $V = 0$ and $\frac{dV}{dt} = 0$

Solving we get $V_{out} = (14\times10^{-6}a + 2.33 \times 10^{-3}b)e^{-410t}$
$+ (-2.64\times10^{-3}a + 34\times10^{-3}b)e^{-29.5t} + a(t-0.0364)^2 + b(t-0.0364)$
$+ 1.32\times10^{-3}a$

The response to a ramp input is shown in Fig.A.2.1 for two plunging and pitching rates.

A.2.2 Output signal from low-pass filter

A low-pass filter is a first order system

whose transfer function is

$$\frac{Vout}{Vin} = \frac{1}{1+Ts}$$

The input is of the form

$$Vin = at^2+bt$$

The differential equation is therefore

$$(D+w_n)\ Vout = w_n Vin$$

The Complementary Function is:

$$Vout = Ae^{-\omega_n t}$$

And the Particular Integral is:

$$Vout = a(t-\frac{1}{w_n})^2 + b(t-\frac{1}{w_n}) + \frac{3a}{w_n^2}$$

The complete solution is then:

$$Vout = Ae^{-\omega_n t} + a(t-\frac{1}{w_n})^2 + b(t-\frac{1}{w_n}) + \frac{3a}{w_n^2}$$

In this case $w_n = 88$rad/sec and putting V=0 when T=0

$$Vout = (0.01136b-0.00052a)e^{-88t} + a(t-0.0114)^2+b(t-0.0114)+0.00039a$$

The response to a ramp input is shown in Fig.A.2.2

A.2.3 Output signal from galvanometer

A galvanometer is a second order system whose transfer function is

$$\frac{Vout}{Vin} = \frac{1}{1+2\zeta Ts+(Ts)^2}$$

The input is of the form

$$Vin = at^2+bt$$

The differential equation is then:

$$(D^2+2\zeta w_n D+w_n^2)\ Vout = w_n^2 Vin$$

The complementary function in this case, where $\zeta = 0.64$, is:

$$Vout = e^{-\zeta\omega_n t}(A\cos\sqrt{\zeta^2-1}\,w_n t + B\sin\sqrt{\zeta^2-1}\,w_n t)$$

And the Particular Integral is

$V_{out} = a(t-2\zeta/w_n)^2 + b(t-2\zeta/w_n) - 2a/w_n^2 + 8a(\zeta/w_n)^2$

The complete solution is then:

$$V_{out} = e^{-\zeta\omega_n t}(A\cos\sqrt{\zeta^2-1}\,\omega_n t + B\sin\sqrt{\zeta^2-1}\,\omega_n t) + a(t-2\zeta/\omega_n)^2 + b(t-2\zeta/\omega_n) - 2a/\omega_n^2 + 8a(\zeta/\omega_n)^2$$

In this case $\zeta = 0.64$ and $w_n = 251$ rad/sec and putting

$V = 0$ when $t=0$ we obtain

$$V_{out} = (0.005b - 0.000046a)e^{-160t}\cos 102t + a(t-0.005)^2 + b(t-0.005) + 0.0002a$$

The response to a ramp input is shown in Fig. A.2.3.

APPENDIX 3

Virtual Mass

When a body is accelerated through a fluid, the fluid around the body must also be accelerated to maintain the flow field around the body. The extra force needed to do this must be supplied by the force moving the body. This makes the body appear to have a bigger mass and for this reason the extra mass of the fluid is sometimes called the 'virtual mass'. The associated inertia is called the 'virtual inertia'.

It is fairly easy to calculate the virtual mass from potential flow for most simple bodies. It is given by

$$m = -\rho \int l \left(\frac{\partial \phi}{\partial V}\right) ds$$

where ϕ is the velocity potential
V is the freestream velocity

The derivation of this equation is given in ref. 23.

For a flat plate of chord b and infinite span this equation yields the result (see, for example, ref.23)

$$m = \pi \rho \frac{b^2}{4} \text{ per unit span}$$

For wings of finite span, a correction can be applied to this equation. Ref.23 describes a series of tests which were made to determine this correction for a variety of plates.

To apply this equation to a slender wing, the wing was divided into chordwise strips and the virtual mass integrated along the span. This gave a loading which fell to zero at the tips. This overcame the difficulty of applying results in ref. 23 which applies to rectangular and elliptical wings. For the model G

planform used in this experiment the virtual mass was:

$m = 0.0152$ slugs (0.21 Kg)

As previously stated, this value is based on potential flow theory. The flow round a slender wing differs considerably from "ideal flow" having large regions of separated flow, and therefore the virtual mass was thought likely to differ considerably. To see if this was the case, a simple experiment was set up.

A.3.1 Experimental method for measuring the virtual mass

The experimental arrangement is shown in Fig.A.3.1. The wing and supporting sting were removed from their normal positions and fixed in a vertical position. An additional shield was a attached to the sting shield which extended to very close to the trailing edge of the wing and had the same span as the wing. This was used to prevent any significant flow separation at the trailing edge so approximating to the flow about the wing in forward motion. The wing was towed through water in this position at constant speed to measure the 'drag' coefficient. The trolley was disconnected from the winch and attached to a weight via a string passing over a pulley at the end of the tank. Releasing the weights gave the trolley a nearly constant acceleration. Runs were performed in air to measure the inertia effect of the model which was subtracted from the inertia measured in water. The reed switch markers on the U/V trace were used to measure the acceleration and the normal force and pitching moment measured during the

test run. Runs were performed using a range of weights to give a range of accelerations. Further runs were performed with the model wing at different angles of attack.

A.3.1.1 Measured virtual mass

The drag coefficient and pitching moment coefficient of the wing normal to the flow and at an angle of up to 20° to the normal are shown in Fig.A.3.2. These were used in the analysis of the accelerating runs.

In the analysis the acceleration was assumed constant between the reed switches. The acceleration was then calculated by measuring the time interval between the reed switches and an average speed was calculated. The drag force was then found for this average speed and subtracted from the measured load on the model wing. A correction was made for the inertia of the model wing itself. The resulting normal force and pitching moment on the wing were then assumed to be due to the acceleration of the virtual mass. The virtual mass thus measured was approximately 0.040 slugs (0.56Kg).

The values of C_N measured at the beginning of each run for the $\dot{w}$ and q manoeuvres were plotted against incidence as shown in Figs.4.17, 4.18, 4.30. These were compared with values of C_N obtained by the product of the normal acceleration and the virtual mass.

It is evident from Figs. 4.17,4.18, 4.30 that the experimental value is much larger

than the values obtained during the $\dot{w}$ and q manoeuvres, which are much closer to the potential flow values. It was concluded that the flow over the wing when it was treated as a flat plate normal to a viscous stream was even less representative of the true flow field than the potential flow case. Fig. A.3.3 shows a comparison of the three types of flow field.

APPENDIX 4

Slender wing theory

One of the earliest attempts to predict the lift curve slope of slender wings was the theory due to Jones (ref. 3). This theory was based on the concept of virtual mass in potential flow. Although it gave a linear lift curve, it showed good agreement with the lift curve slope at zero lift where the flow is attached. Ref. 31 shows this theory applied to unsteady longitudinal motion, giving the following equation:
The lift per unit length in the streamwise direction,

$$\bar{l} = \pi\rho s^2\left(\frac{\partial^2 z}{\partial t^2} + 2V\frac{\partial^2 z}{\partial x \partial t} + V^2\frac{\partial^2 z}{\partial x^2}\right) + 2\pi\rho V s\frac{ds}{dx}\left(\frac{\partial z}{\partial t} + V\frac{\partial z}{\partial x}\right)$$

where

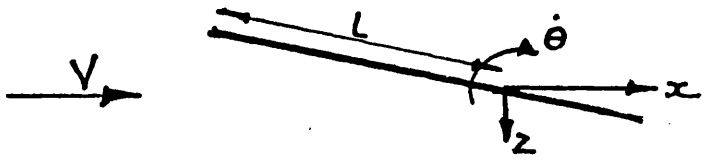

For the case with positive $\dot{\theta}$, no vertical translation (pitching):

$$\frac{\partial z}{\partial t} = -\dot{\theta}(l-x) \qquad \frac{\partial z}{\partial x} = +\theta$$

$$\frac{\partial^2 z}{\partial x \partial t} = +\dot{\theta} \qquad \frac{\partial^2 z}{\partial x \partial t} = +\dot{\theta}$$

$$\frac{\partial^2 z}{\partial t^2} = 0 \qquad \frac{\partial^2 z}{\partial x^2} = 0$$

$$\bar{l} = \pi\rho s^2(2\dot{\theta}V) + 2\pi\rho V s\frac{ds}{dx}(-\dot{\theta}l + \dot{\theta}x + V\theta)$$

$$m = \int_0^{t.e.} \bar{l}(l-x)\,dx$$

For the case with constant vertical acceleration and zero $\dot{\theta}$(plunging):

$$\frac{\partial z}{\partial t} = \omega \qquad \frac{\partial z}{\partial x} = +\theta$$

$$\frac{\partial^2 z}{\partial x \partial t} = 0 \qquad \frac{\partial^2 z}{\partial x \partial t} = 0$$

$$\frac{\partial^2 z}{\partial t^2} = \dot{\omega} \qquad \frac{\partial^2 z}{\partial x^2} = 0$$

$$\bar{L} = \pi\rho s^2(\dot{\omega}) + 2\pi\rho V s \frac{ds}{dx}(\omega + V\theta)$$

For the case with positive $\dot{\theta}$, positive $\dot{w}$ (constant q)

$$\frac{\partial z}{\partial t} = -\dot{\theta}(l-x)+\omega \qquad \frac{\partial z}{\partial x} = \theta$$

$$\frac{\partial^2 z}{\partial x \partial t} = \dot{\theta} \qquad \frac{\partial^2 z}{\partial x \partial t} = \dot{\theta}$$

$$\frac{\partial^2 z}{\partial t^2} = \dot{\omega} \qquad \frac{\partial^2 z}{\partial x^2} = 0$$

$$\bar{L} = \pi\rho s^2(\dot{\omega} + 2V\dot{\theta}) + 2\pi\rho V s \frac{ds}{dx}(-\dot{\theta}(l-x) + \omega + V\theta)$$

For no change of incidence

$$-\dot{\theta}(l-x) + \omega + V\theta = \text{constant}$$

The derivatives have been non-dimensionalised as follows:

$$Z_{\dot{\omega}} = \frac{Z}{\frac{1}{2}\rho V^2 S \cdot \frac{\dot{\omega} c_0}{V^2}} \qquad M_{\dot{\omega}} = \frac{M}{\frac{1}{2}\rho V^2 S c_0 \cdot \frac{\dot{\omega} c_0}{V^2}}$$

$$Z_q = \frac{Z}{\frac{1}{2}\rho V^2 S \cdot \frac{q c_0}{V}} \qquad M_q = \frac{M}{\frac{1}{2}\rho V^2 S c_0 \cdot \frac{q c_0}{V}}$$

$$Z_{\dot{\theta}} = \frac{Z}{\frac{1}{2}\rho V^2 S \cdot \frac{\dot{\theta} c_0}{V}} \qquad M_{\dot{\theta}} = \frac{M}{\frac{1}{2}\rho V^2 S c_0 \cdot \frac{\dot{\theta} c_0}{V}}$$

A.4.1 Theoretical longitudinal derivatives for a wing of aspect ratio 0.865 with different planforms

The derivatives have been calculated for the AGARD model G planform and for delta and gothic planforms of the same aspect ratio. The three planforms are shown in Fig. A.4.1. The complete set of derivatives is shown in Table A.4.1 and plotted against pitching axis position in Fig.A.4.2.

APPENDIX 5

Transfer of axes for measuring derivatives

In oscillatory tests, the unsteady derivatives are measured about two axes in order to be able to separate the plunging and pitching derivatives. It is also necessary to be able to convert the derivatives measured about a pitching axis to another pitching axis to compare with other experimental results.

In the following analysis it is assumed that pitching about an axis $x+x'$ is equivalent to pitching about an axis x with a plunging component superimposed at x. The following conversions have been used to transfer results from other sources to the pitching axis, $0.667c_o$, used in this experiment:

Consider a wing pitching about two axes at x and x+x' respectively, the normal force and pitching moment being measured for body axes:

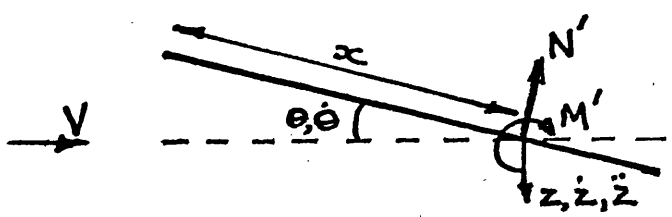

$$M' = M_\theta\theta + M_{\dot\theta}\dot\theta + M_z z + M_{\dot z}\dot z + M_{\ddot z}\ddot z$$

$$N' = N_\theta\theta + N_{\dot\theta}\dot\theta + N_z z + N_{\dot z}\dot z + N_{\ddot z}\ddot z$$

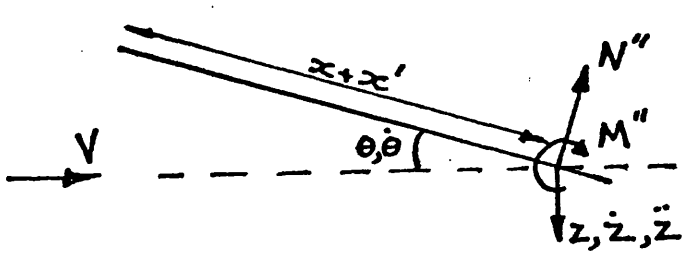

For small θ:

$$M'' = M_\theta\theta + M_{\dot\theta}\dot\theta + M_z(z-x'\theta) + M_{\dot z}(\dot z - x'\dot\theta) + M_{\ddot z}\ddot z$$
$$+ N_\theta\theta x' + N_{\dot\theta}\dot\theta x' + N_z(z-x'\theta)x' + N_{\dot z}(\dot z - x'\dot\theta)x' + N_{\ddot z}\ddot z x'$$
$$= \underline{(M_\theta + x'(N_\theta - M_z) - x'^2 N_z)\theta + (M_{\dot\theta} + x'(N_{\dot\theta} - M_{\dot z}) - x'^2 N_{\dot z})\dot\theta}$$
$$\underline{+ (M_z + N_z x')z + (M_{\dot z} + N_{\dot z}x')\dot z + (M_{\ddot z} + N_{\ddot z}x')\ddot z}$$

$$N'' = N_\theta\theta + N_{\dot\theta}\dot\theta + N_z(z-x'\theta) + N_{\dot z}(\dot z - x'\dot\theta) + N_{\ddot z}\ddot z$$
$$= \underline{(N_\theta - x'N_z)\theta + (N_{\dot\theta} - x'N_{\dot z})\dot\theta + N_z z + N_{\dot z}\dot z + N_{\ddot z}\ddot z}$$

In all cases there are no stiffness derivatives:

$$M'' = \underline{(M_\theta + x'N_\theta)\theta + (M_{\dot\theta} + x'(N_{\dot\theta} - M_{\dot z}) - x'^2 N_{\dot z})\dot\theta}$$
$$\underline{+ (M_{\dot z} + N_{\dot z}x')\dot z + (M_{\ddot z} + N_{\ddot z}x')\ddot z}$$

$$N'' = \underline{N_\theta\theta + (N_{\dot\theta} - x'N_{\dot z})\dot\theta + N_{\dot z}\dot z + N_{\ddot z}\ddot z}$$

(i) Plunging manoeuvre (constant $\dot w$)

θ = initial attitude

$\dot\theta = 0$

$$M'' = (M_\theta + x'N_\theta)\theta + (M_{\dot z} + N_{\dot z}x')\dot z + (M_{\ddot z} + N_{\ddot z}x')\ddot z$$

$$N'' = N_\theta\theta + N_{\dot z}\dot z + N_{\ddot z}\ddot z$$

(ii) Constant q manoeuvre

$$M'' = (M_\theta + x'N_\theta)\theta + (M_{\dot\theta} + x'(N_{\dot\theta} - M_{\dot z}) - x'^2 N_{\dot z})\dot\theta$$
$$+ (M_{\dot z} + N_{\dot z}x')\dot z + (M_{\ddot z} + N_{\ddot z}x')\ddot z$$

$$N'' = N_\theta\theta + (N_{\dot\theta} - x'N_{\dot z})\dot\theta + N_{\dot z}\dot z + N_{\ddot z}\ddot z$$

(iii) Pitching manoeuvre (constant $\dot\theta$)

$\dot\omega = \ddot z = 0$

$$M'' = (M_\theta + x'N_\theta)\theta + (M_{\dot\theta} + x'(N_{\dot\theta} - M_{\dot z}) - x'^2 N_{\dot z})\dot\theta$$
$$+ (M_{\dot z} + N_{\dot z}x')\dot z$$

$$N'' = N_\theta\theta + (N_{\dot\theta} - x'N_{\dot z})\dot\theta$$

APPENDIX 6

'Effective camber' theory

Fig. 4.44 is taken from ref. 25 and shows the chordwise loading distribution on a wing of aspect ratio 1.0. Now, in the case of the model G wing, the normal force on the wing can be expressed as:

$$C_N = a\alpha + b\alpha^2$$

If a load distribution due to the rotation of the wing is superimposed on the steady load distribution shown in Fig. 4.44, this can be expressed as a function of the effective incidence distribution caused by the rotation.

If the increment in incidence at any point is then:

$$\Delta C_N = a\Delta\alpha + b\Delta\alpha^2 + 2b\alpha\Delta\alpha$$

To calculate ΔC_N and ΔC_M the wing was divided into spanwise strips and the increment in incidence at each strip calculated for a pitching rate, $\frac{\dot{\theta} c_0}{V} = 0.07$ about $0.667c_0$. The total increment in C_N was then given by:

$$\Delta C_N = \sum_0^n \left(\frac{C_{N_{local}}}{C_N} a\Delta\alpha_{local} + b\Delta\alpha^2_{local} + 2b\alpha\Delta\alpha_{local}\right)$$

It was assumed that

$$\frac{C_{N_{local}}}{C_N} = \frac{C_{L_{local}}}{C_L}$$

Similarly

$$\Delta C_M = \sum_0^n \left(\frac{C_{N_{local}}}{C_N} a\Delta\alpha_{local} + b\Delta\alpha^2_{local} + 2b\alpha\Delta\alpha_{local}\right)\left(0.667 - \frac{x}{c_0}\right)$$

The results of these calculations are shown in Table A.6.1 for $\alpha = 7.5^\circ$. Dividing by $\frac{\dot{\theta} c_0}{V}$ gave the derivatives:

$$\underline{z_{\dot{\theta}} = 0.11} \qquad \underline{m_{\dot{\theta}} = 0.10}$$

Similar treatment for $\alpha = 22^\circ$ gives:

$$\underline{z_{\dot{\theta}} = 0.23} \qquad \underline{m_{\dot{\theta}} = 0.18}$$

REFERENCES

1. B. Etkin — Dynamics of atmospheric flight. J. Wiley & Sons New York 1971

2. P.L. Bisgood — Stability and Control tests on a slender wing research aircraft. RAE Techmemo Aero 1311 April 1971

3. R.T. Jones — Properties of low aspect ratio pointed wings at speeds below and above the speed of sound. NACA report 835

4. H.C. Garner — Multhopp's lifting-surface theory of wings in slow pitching oscillations. ARC R & M 2885 1952

5. W.E. Watkins, H.L. Runyan, D.S. Woolston — On the kernal function of the integral equation relating the lift and downwash distributions of oscillating finite wings in subsonic flow. NACA report 1234 1955

6. M. Tobak — On the use of the indicial function concept in the analysis of unsteady motions of wings and wing-tail combinations. NACA report 1188 1954

7. Doris E.Lehrian, H.C. Garner — Theoretical calculation of generalised forces and load distribution on wings oscillating at general frequency in a subsonic stream. RAE TR 71147 July 1971

8. D.G. Randall — Oscillating slender wings in the presence of leading edge separation. RAE TR Structures 286 April 1963

9. C.E. Brown, W.H. Michael — On slender delta wings with leading edge separation. J.Ae.S Vol. 21 October 1954

10. K.J. Turner, A.Jean Ross, Geraldine Edwards — The dynamic stability derivatives of a slender wing, a comparison of theory with free flight model tests at near zero lift, M=0.8 to 2.4. RAE TR 66170 June 1966.

11. J.B. Bratt — Wind tunnel techniques for the measurement of oscillatory derivatives.
ARC R & M 3319 Aug. 1960

12. J.G. Wright — Low speed wind tunnel measurements of the oscillatory longitudinal derivatives of a gothic wing of aspect ratio 0.75.
ARC S & T memo 1/62 April 1962.

13. J.S.Thompson, R.A.Fail, J.V.Inglesby — Low speed wind tunnel measurements of the oscillatory lateral stability derivatives for a model of a slender aircraft (HP115) including the effects of frequency parameter.
ARC CP 1097 Feb. 1969.

14. A.W.Babister — Aircraft Stability & Control. Chapter 14.
Pergamon Press London 1961.

15. Irving C.Statler, Orren B. Tufts, Walter J. Hirtreiter — A new capability for measuring dynamic air loads in a wind tunnel.
AIAA paper no. 66-15

16. P.J. Wingham — A research proposal for studying the behaviour of slender wings in unsteady motion under incompressible flow conditions.
Bath University Report No.176 Sept.1970.

17. D.H. Perry — The airborne path during take-off for constant rate-of-pitch manoeuvres.
RAE TR 68071 1968.

18. W. Griffel — Handbook of formulae for stress and strain.
F. Ungar

19. S.B. Berndt — Wind tunnel interference due to lift for delta wings of small aspect ratio.
K.T.H. - Aero TN 19 Stockholm 1950.

20. A. Pope — Wind tunnel testing.
J. Wiley & Sons New York 1964.

21. R. Fail — Unpublished results of oscillatory tests on model G. planform.

22. ESDU Item No. 7106 — Low speed longitudinal characteristics of slender wings. ESDU London

23. W. Gracey — The additional-mass effect of plates as determined by experiments. NACA Report No. 707

24. N.C.Lambourne, D.W. Bryer, J.F.M.Maybrey — The behaviour of the leading-edge vortices over a delta wing following a sudden change of incidence. ARC 31056 March 1969.

25. R.K. Nangia, G.J. Hancock — Delta wings with longitudinal camber at low speed. ARC C.P. No. 1129

26. R.K.Cooper — Low speed wind tunnel measurements of the oscillatory longitudinal derivatives of a delta wing of AR 0.8. Aero TN 7105 University of Sydney Dec.1971.

27. H. Multhopp — Methods for calculating the lift distribution of wings (subsonic lifting-surface theory). ARC R & M 2884 Jan 1950.

28. A.Jean Ross, Geraldine F. Edwards, A.P. Waterfall — The dynamic stability derivatives of a slender wing at zero and moderate lift.

29. A.C. Tory — The hydrogen bubble technique Symposium of flow visualisation techniques and applications at the Borough Polytechnic Borough Road, London SE1. June 1970.

30. R.L. Maltby, P.B. Engler, R.F.A. Keating — Some exploratory measurements of leading edge vortex positions on a delta wing oscillating in heave. ARC R & M 3410 July 1963.

31. I.E. Garrick — Some research on high speed flutter. Anglo-American Aeronautical Conference, Brighton 1951.

CORRECTION	STEADY RUN	MANOEUVRE		
		$\dot{\omega}$	q	$\dot{\theta}$
CHANGE IN WEIGHT COMPONENT DUE TO CHANGE IN ATTITUDE			✓	✓
MODEL WING AND STING INERTIA		✓	✓	
DEFLECTION OF STING UNDER AERODYNAMIC LOAD	✓	✓	✓	✓
CHANGE IN DYNAMIC PRESSURE		✓	✓	
INSTRUMENT LAG		✓	✓	✓
WALL CONSTRAINT	✓	✓	✓	✓
CHANGE IN WALL CONSTRAINT		✓	✓	

TABLE 3.01 CORRECTIONS APPLIED TO EXPERIMENTAL MEASUREMENTS

LOAD lbf	SLOPE AT END OF STING	
	THEORY	MEASURED
0.5	0.6 DEG	0.4 DEG
1.0	1.2	1.0
1.5	1.8	1.7
2.0	2.4	2.2

TABLE 3.02 DEFLECTION OF STING UNDER AERODYNAMIC LOAD

TABLE 4.01

$\frac{x}{c_0}$	INSTR. LAG $\Delta\frac{x}{c_0}$	$\frac{x}{c_0}$	α_{NOM} DEG	$\Delta\alpha_{LOAD}$ DEG	α DEG	N FROM U/V TRACE cm	N lbf	$\frac{\frac{1}{2}\rho V^2}{\frac{1}{2}\rho V^2_{HORIZ}}$	C_N
0	0	0	0	'0	0	0	0	1	0
0.5	0.22	0.28	1.56	0.03	1.59	0.65	0.029	1	0.054
1.0	0.22	0.78	3.56	0.06	3.62	1.3	0.059	1	0.108
1.5	0.22	1.28	5.56	0.09	5.65	1.9	0.086	1.01	0.156
2.0	0.22	1.78	7.56	0.12	7.68	2.7	0.123	1.02	0.220
2.5	0.22	2.28	9.56	0.16	9.72	3.7	0.164	1.03	0.291
3.0	0.22	2.78	11.56	0.21	11.77	4.7	0.214	1.045	0.374
3.5	0.22	3.28	13.56	0.26	13.82	5.8	0.264	1.06	0.455
4.0	0.22	3.78	15.56	0.31	15.87	6.9	0.314	1.08	0.532
STEADY	0	—	16	0.34	16.34	7.5	0.341	1.08	0.578

NORMAL FORCE

$\frac{x}{c_0}$	INSTR. LAG SEC	$\frac{x}{c_0}$	α_{NOM} DEG.	$\Delta\alpha_{LOAD}$ DEG	α DEG	M FROM U/V TRACE cm.	M lbf in	$\frac{\frac{1}{2}\rho V^2}{\frac{1}{2}\rho V^2_{HORIZ}}$	C_M
0	0	0	0	0	0	0	0	1	0
0.5	0.22	0.28	1.56	0.03	1.59	0.3	0.016	1	.0049
1.0	0.22	0.78	3.56	0.06	3.62	0.9	0.048	1	.0146
1.5	0.22	1.28	5.56	0.09	5.65	1.4	0.075	1.01	.0226
2.0	0.22	1.78	7.56	0.12	7.68	2.0	0.107	1.02	.0320
2.5	0.22	2.28	9.56	0.16	9.72	2.65	0.142	1.03	.0420
3.0	0.22	2.58	11.56	0.21	11.77	3.5	0.188	1.045	.0547
3.5	0.22	3.28	13.56	0.26	13.82	4.4	0.2360	1.06	.0680
4.0	0.22	3.58	15.56	0.31	15.87	5.5	0.295	1.08	.0833
STEADY	0	—	16	0.34	16.34	6.15	0.330	1.08	.0932

PITCHING MOMENT

TABLE 4.01 RESULTS FOR PLUNGING MANOEUVRE FOR $\frac{\dot{w}c_0}{V^2} = +0.07$ AND $\alpha_0 = 0$

TABLE 4.01

$\frac{x}{c_0}$	γ DEG	θ DEG	N FROM U/V TRACE cm.	ΔN DUE TO CHANGE IN θ	N cm	N lbf	$\frac{1/2\rho V^2}{1/2\rho V^2_{HOVER}}$	ΔN DUE TO CHANGE IN V^2	N lbf	C_N	C_N CORRECTED FOR ZERO ERROR
0	0	22	0	0	0	0	1	0	0	0	0
1.0	1	21	+2.8	0	+2.8	+0.015	1	0	+0.015	+0.027	+0.020
1.8	4.5	17.5	-3.2	+0.2	-3.0	-0.017	1.006	-0.003	-0.020	-0.037	-0.044
2.0	4.5	17.5	-2.3	+0.2	-2.1	-0.012	1.006	-0.003	-0.015	-0.027	-0.034
2.5	6.5	15.5	-0.5	+0.3	-0.2	-0.001	1.015	-0.008	-0.009	-0.016	-0.023
3.0	8.5	13.5	+0.7	+0.4	+1.1	+0.006	1.022	-0.011	-0.005	-0.009	-0.016
3.5	10.5	11.5	+1.0	+04	+1.4	+0.008	1.034	-0.018	-0.010	-0.018	-0.025
4.0	12.5	9.5	+2.4	+0.5	+2.9	+0.017	1.048	-0.025	-0.008	-0.015	-0.022
5.0	15.5	6.5	+3.7	+0.6	+4.3	+0.025	1.072	-0.037	-0.012	-0.022	-0.029
6.0	16	6	+8.3	+0.6	+8.9	+0.051	1.032	-0.043	+0008	+0.015	0

NORMAL FORCE

$\frac{x}{c_0}$	γ DEG	θ DEG	M FROM U/V TRACE cm	ΔM DUE TO CHANGE IN θ cm	M cm	M lbf in	$\frac{1/2\rho V^2}{1/2\rho V^2_{HOVER}}$	ΔM DUE TO CHANGE IN V^2 lbf in	M lbf in	C_M	C_M CORRECTED FOR ZERO ERROR
0	0	22	0	0	0	0	1	0	0	0	0
1.4	2.5	19.5	+5.0	-0.1	+4.9	+0.040	1	0	+0.040	+0.012	+0.0124
2.0	4.5	17.5	+2.6	-0.2	+2.4	+0.020	1.006	-0.003	+0.017	+0.0052	+0.0046
2.5	6.5	15.5	+3.4	-0.3	+3.1	+0.026	1.015	-0.007	+0.019	+0.0058	+0.0052
3.0	8.5	13.5	+4.7	-0.3	+4.4	+0.037	1.022	-0.011	+0.026	+0.0080	+0.0074
3.5	10.5	11.5	+5.6	-0.4	+5.2	+0.044	1.034	-0.016	+0.028	+0.0085	+0.0079
4.0	12.5	9.5	+6.1	-0.4	+5.7	+0.048	1.048	-0.023	+0.025	+0.0076	+0.0070
5.0	15.5	6.5	+4.1	-0.5	+3.6	+0.030	1.072	-0.035	-0.005	-0.0015	-0.0021
6.0	16.0	6.0	+5.7	-0.5	+5.2	+0.044	1.082	-0.040	+0.004	+0.0012	0

PITCHING MOMENT MEASURED ABOUT 0.733 c_0

TABLE 4.02 RESULTS FOR CONSTANT q MANOEUVRE FOR $\frac{q c_0}{V} = -0.07$ FOR $\alpha_0 = 22°$

$\frac{x}{c_0}$	INSTR. LAG $\Delta x/c_0$	$\frac{x}{c_0}$	α DEG.	$\Delta\alpha_{LOAD}$ DEG	α DEG	N FROM U/V TRACE cm	N lbf	ΔN DUE CHANGE IN θ lbf	N lbf	C_N
0	0	0	0	0	0	0	0	0	0	0
0.5	0.25	0.25	1	0.03	1.03	0.65	0.028	0	0.028	0.051
1.0	0.25	0.75	3	0.05	3.05	1.4	0.060	0	0.060	0.110
1.5	0.25	1.25	5	0.08	5.08	2.05	0.087	0.0003	0.087	0.159
2.0	0.25	1.75	7	0.12	7.12	2.9	0.124	0.0005	0.125	0.225
2.5	0.25	2.25	9	0.16	9.16	3.8	0.162	0.0008	0.163	0.294
3.0	0.25	2.75	11	0.21	11.21	4.8	0.204	0.0011	0.205	0.371
3.5	0.25	3.25	13	0.25	13.25	5.9	0.251	0.0016	0.253	0.455
4.0	0.25	3.75	15	0.30	15.30	7.0	0.298	0.0020	0.300	0.541
STEADY	0	—	16	0.32	16.32	7.5	0.320	0.0024	0.322	0.581

NORMAL FORCE

$\frac{x}{c_0}$	INSTR LAG $\Delta x/c_0$	$\frac{x}{c_0}$	α DEG	$\Delta\alpha_{LOAD}$ DEG	α DEG	N FROM U/V TRACE cm	M lbf in	ΔM DUE TO CHANGE IN θ lbf in	M lbf in	C_M
0	0	0	0	0	0	0	0	0	0	0
0.5	0.25	0.25	1	0.03	1.03	0	0	0	0	0
1.0	0.25	0.75	3	0.05	3.05	0.85	0.05	0	0.050	0.015
1.5	0.25	1.25	5	0.08	5.08	1.5	0.089	0	0.089	0.027
2.0	0.25	1.75	7	0.12	7.12	2.15	0.127	0.0003	0.127	0.039
2.5	0.25	2.25	9	0.16	9.16	2.9	0.171	0.0006	0.172	0.052
3.0	0.25	2.75	11	0.21	11.21	3.7	0.219	0.0009	0.220	0.067
3.5	0.25	3.25	13	0.25	13.25	4.6	0.272	0.0013	0.273	0.083
4.0	0.25	3.75	15	0.30	15.30	5.8	0.343	0.0018	0.345	0.105
STEADY	0	—	16	0.32	16.32	6.9	0.408	0.0020	0.410	0.125

PITCHING MOMENT MEASURED ABOUT 0.795c_0

TABLE 4.03 RESULTS FOR PITCHING MANOEUVRE FOR $\frac{\dot{\theta} c_0}{V} = +0.07$ AND $\alpha_0 = 0$

TABLE A6.1

			A	B				
DIST. FROM APEX x/c_0	$\frac{C_{N_{local}}}{C_N}$	$\Delta\alpha$ DEG	$a\Delta\alpha + b\Delta\alpha^2$	$2b\alpha\Delta\alpha$	A+B	$\Delta C_{N_{local}}$	$0.667-\frac{x}{c_0}$	$\Delta C_{M_{local}}$
0	0	-2.67	-0.061	-0.033	-0.094			
						-0.010	0.62	0.0062
0.1	0.23	-2.27	-0.051	-0.028	-0.079			
						-0.025	0.52	0.0130
0.2	0.45	-1.87	-0.042	-0.023	-0.065			
						-0.034	0.42	0.0143
0.3	0.70	-1.47	-0.033	-0.018	-0.051			
						-0.036	0.32	0.0115
0.4	0.95	-1.07	-0.024	-0.013	-0.037			
						-0.032	0.12	0.0070
0.5	1.20	-0.67	-0.015	-0.008	-0.023			
						-0.021	0.02	0.0025
0.6	1.42	-0.27	-0.006	-0.003	-0.009			
						-0.003	-0.08	0
0.7	1.62	+0.13	+0.003	+0.002	+0.005			
						+0.019	-0.18	0.0015
0.8	1.65	+0.53	+0.012	+0.007	+0.019			
						+0.039	-0.28	0.0070
0.9	1.36	+0.93	+0.021	+0.012	+0.033			
						+0.027	-0.38	0.0076
1.0	0	+1.33	+0.030	+0.017	+0.047			
TOTALS						-0.076		-0.0706

TABLE A6.1 CALCULATION OF PITCHING DERIVATIVES USING 'EFFECTIVE CAMBER' THEORY

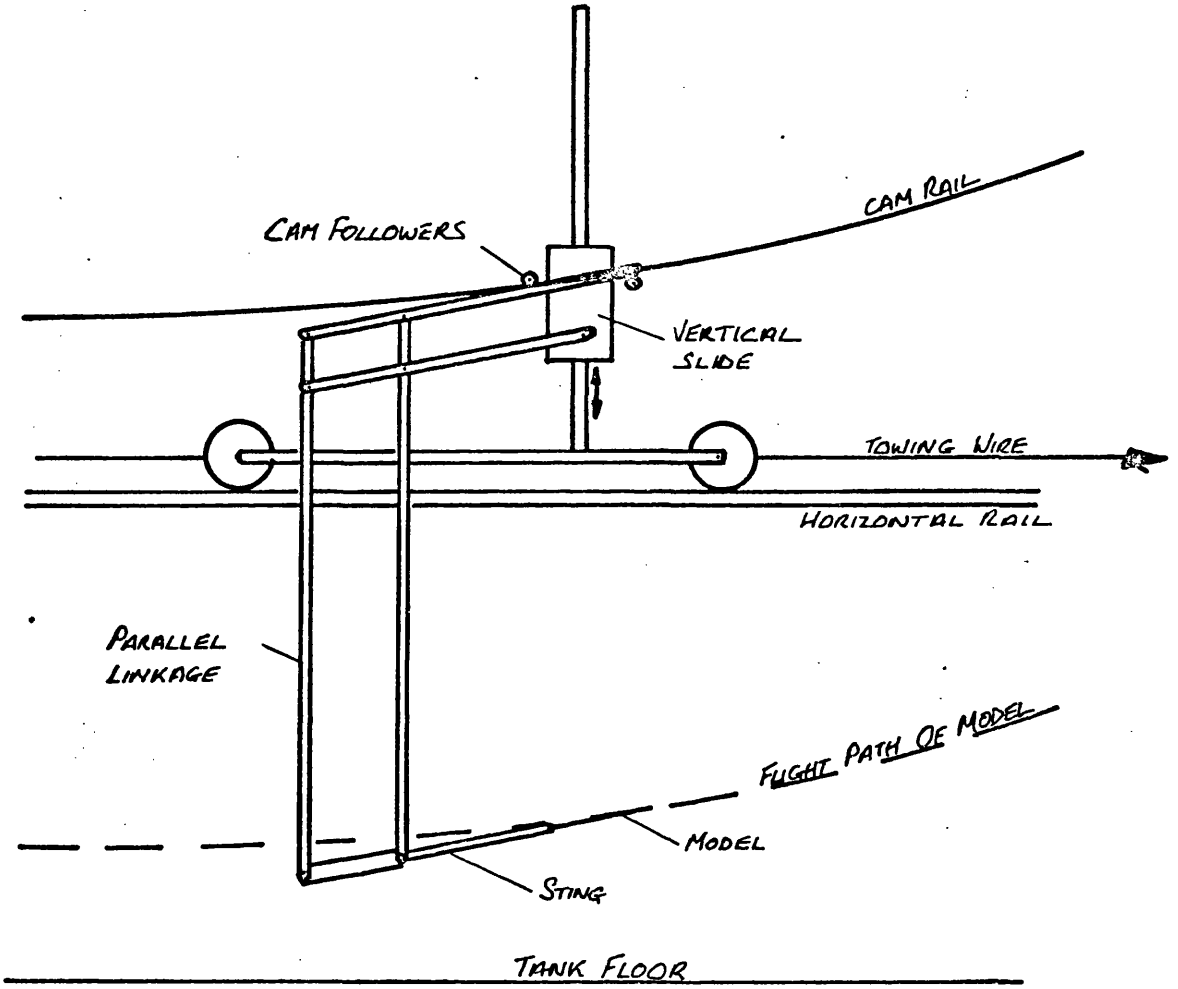

FIG 2.01 SCHEMATIC DIAGRAM SHOWING PRINCIPLES OF THE EXPERIMENT

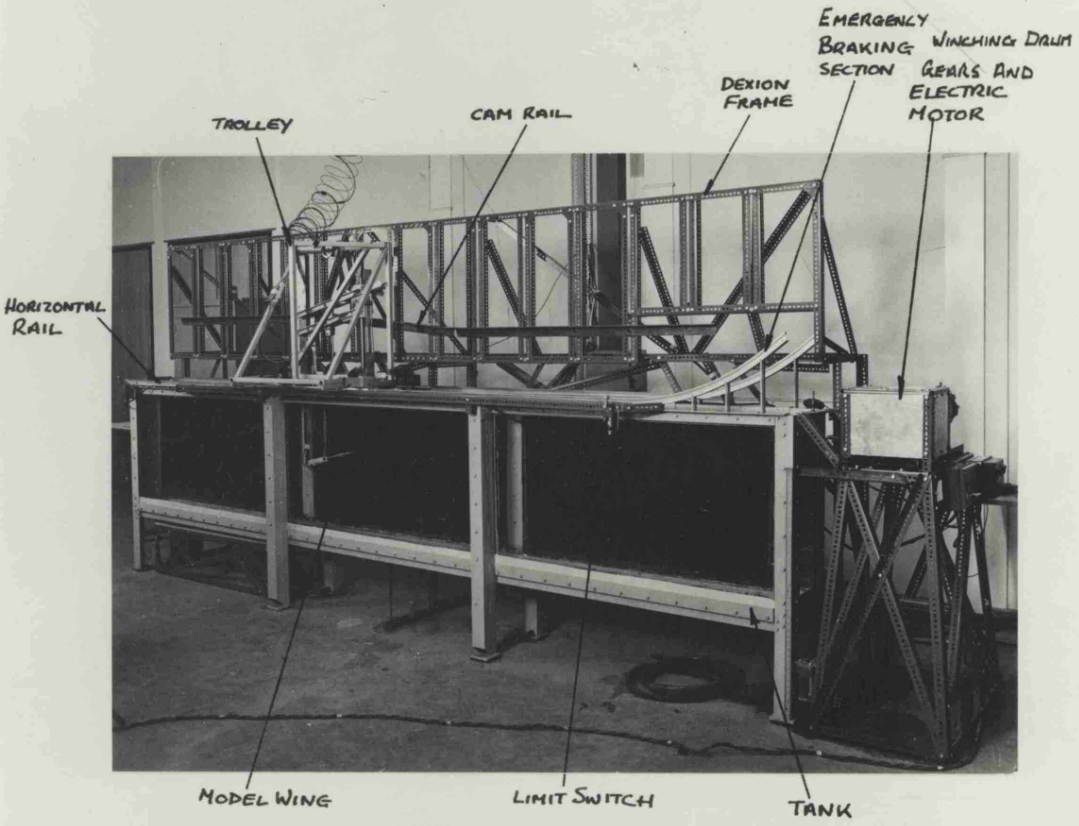

FIG 2.03 GENERAL VIEW OF EXPERIMENTAL SYSTEM SHOWING TANK, TROLLEY, CAM RAIL AND WINCHING MOTOR

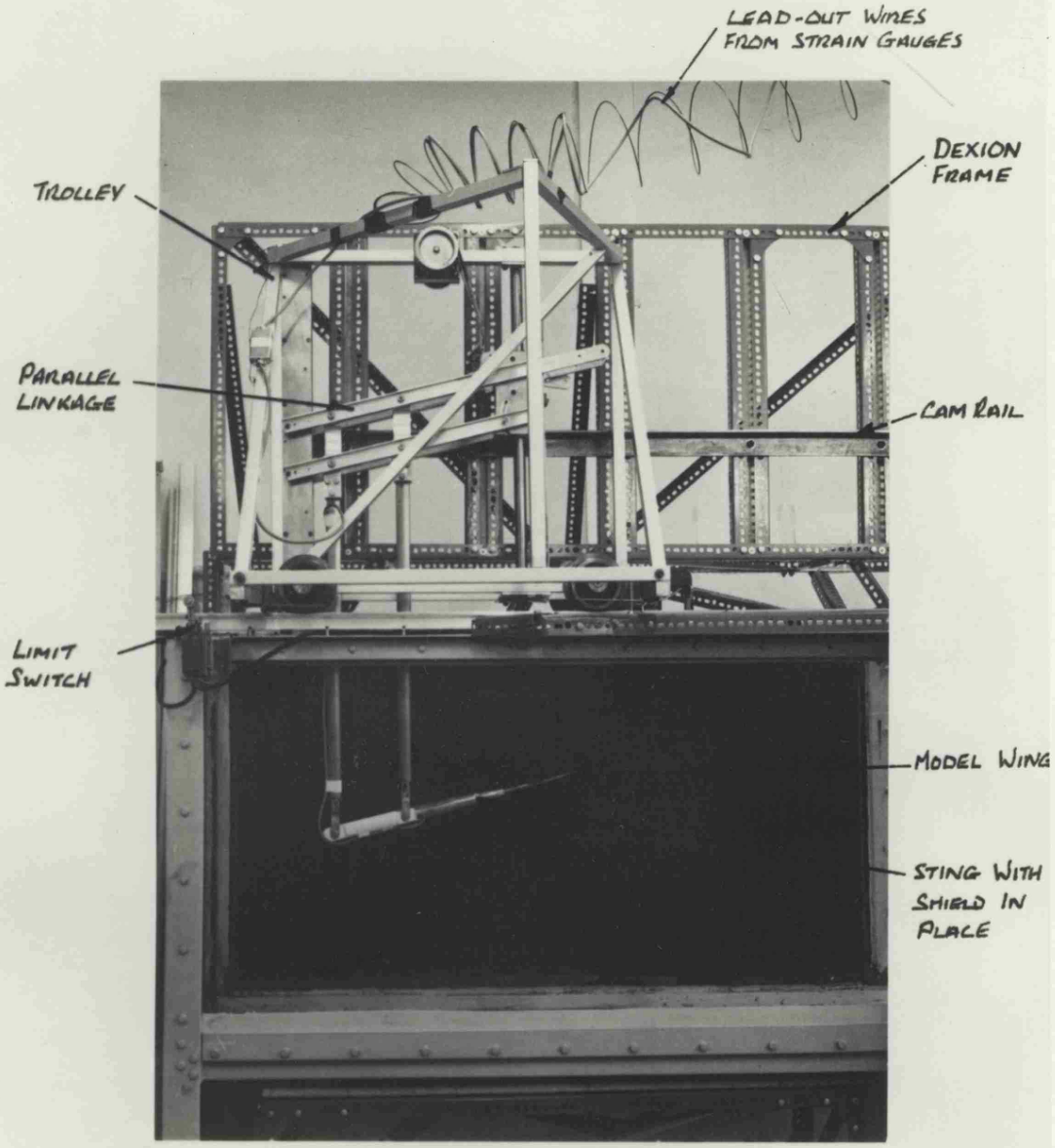

FIG 2.04 VIEW OF SYSTEM SHOWING TROLLEY, PARALLEL LINKAGE AND STING

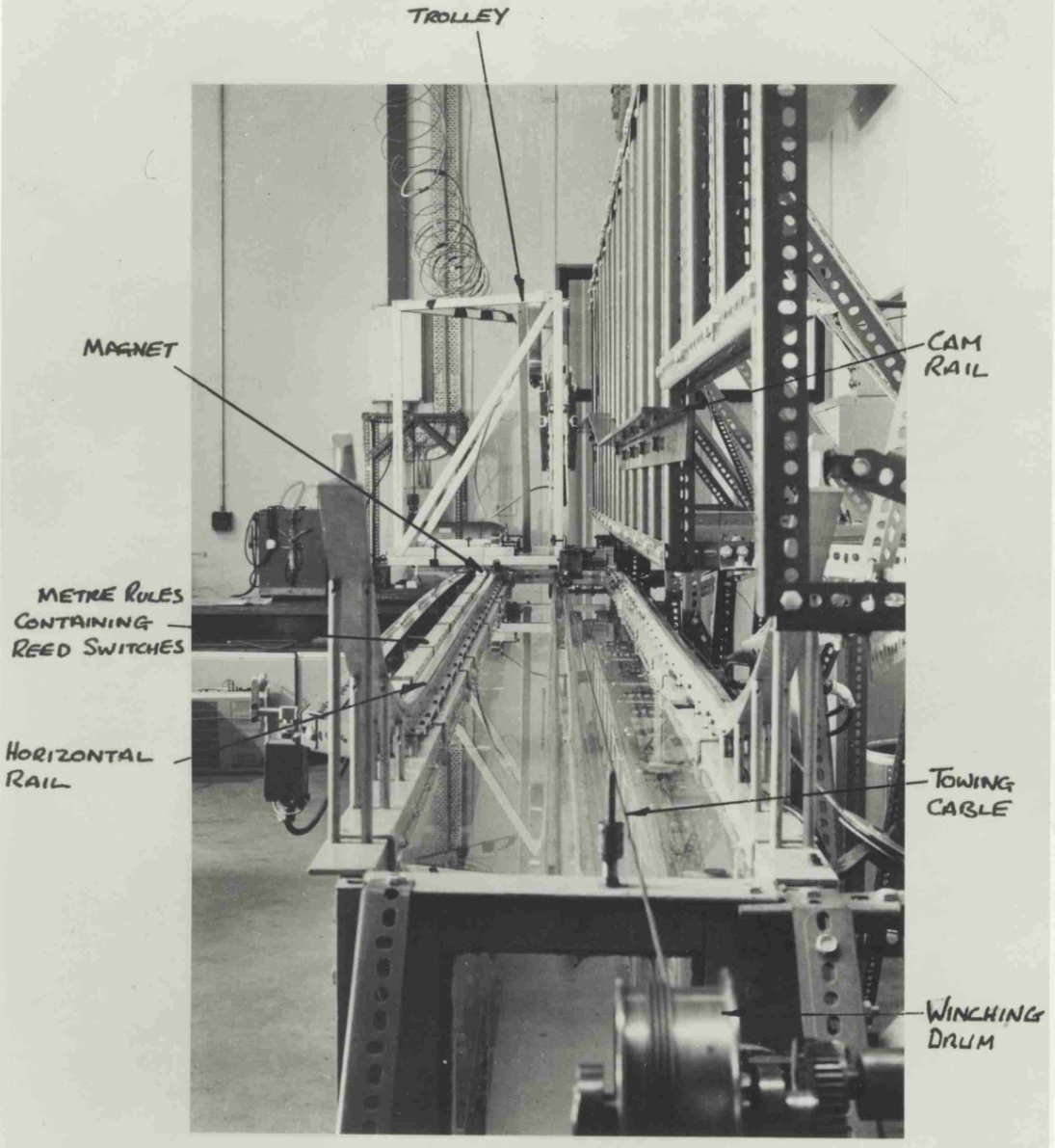

FIG 2.05 VIEW ALONG TOP OF TANK SHOWING TOWING CABLE AND POSITION OF REED SWITCHES

FIGS 2.06a
AND 2.06b

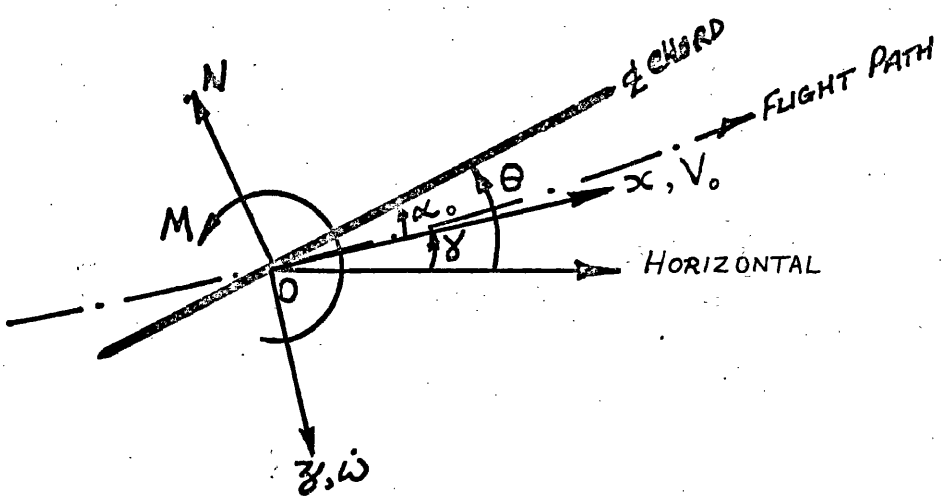

FIG 2.06a CO-ORDINATE SYSTEM WITH WIND AXES AT TIME $t = 0$

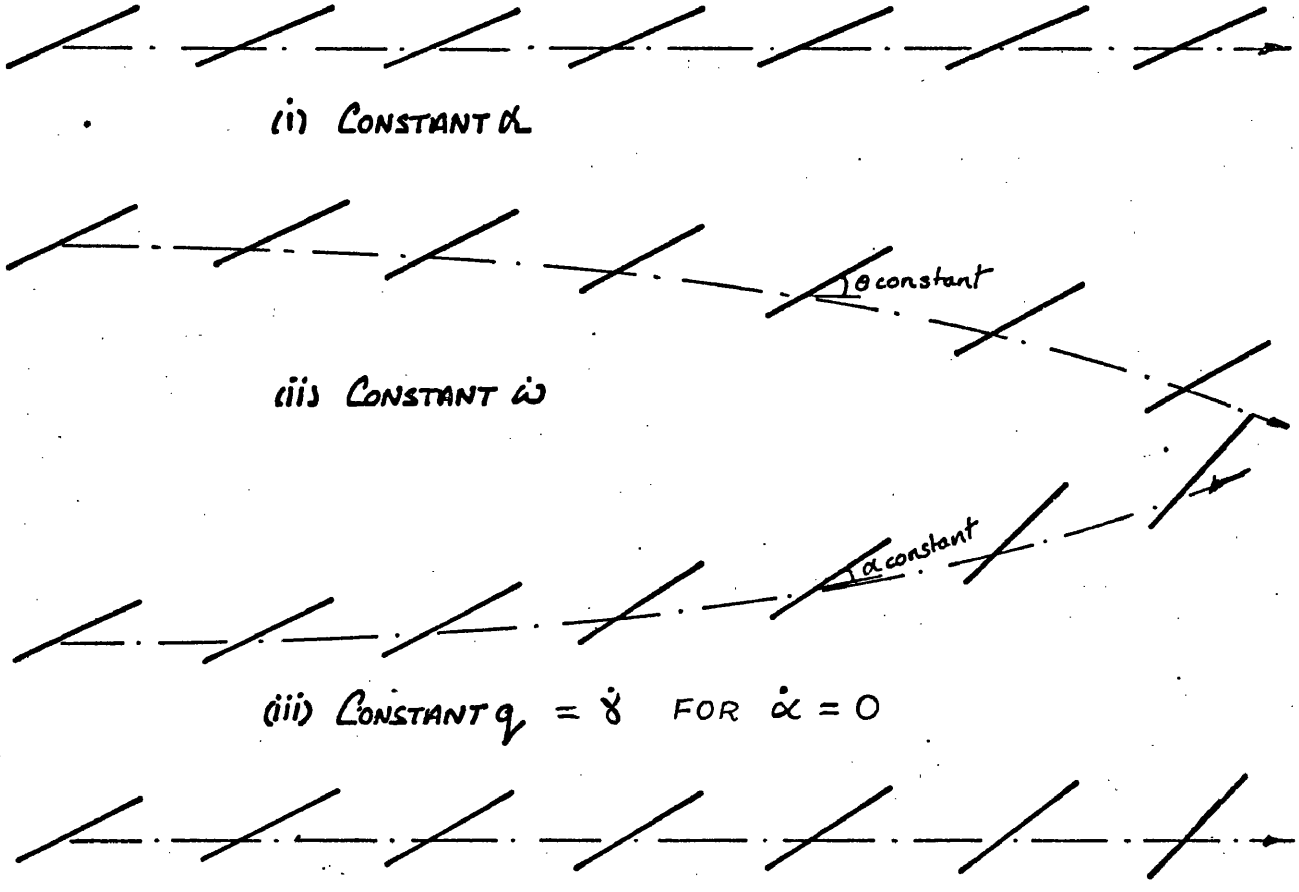

FIG 2.06b FLIGHT PATHS OF SIMULATED MANOEUVRES

FIG 2.07

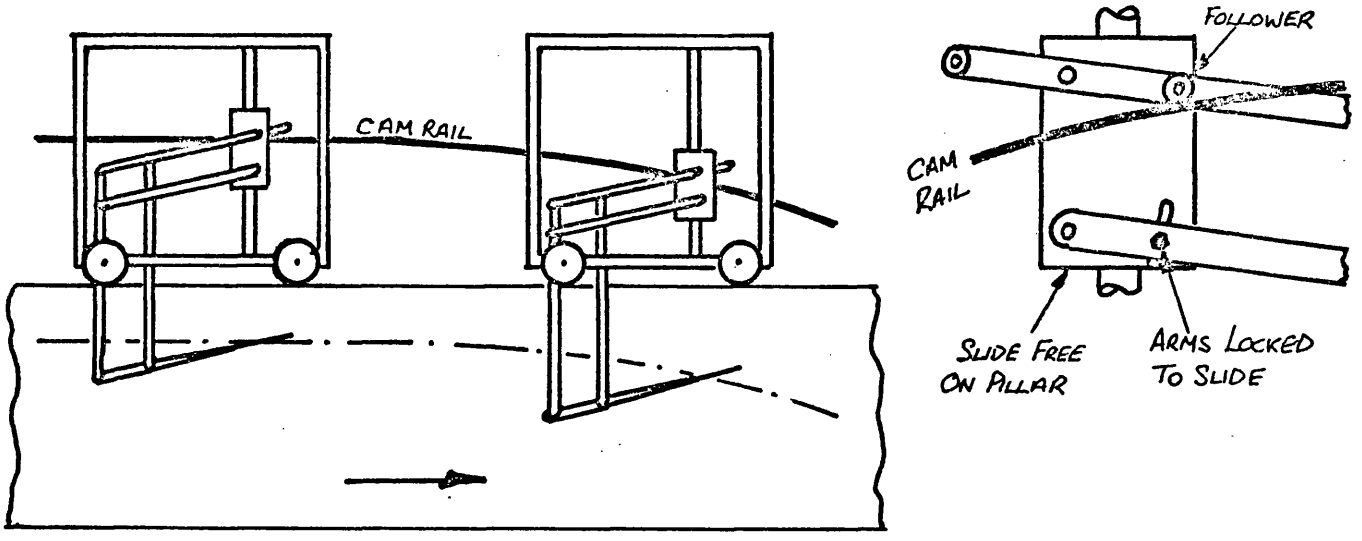

(a) CONSTANT $\dot{\omega}$ MANOEUVRE (PLUNGING)

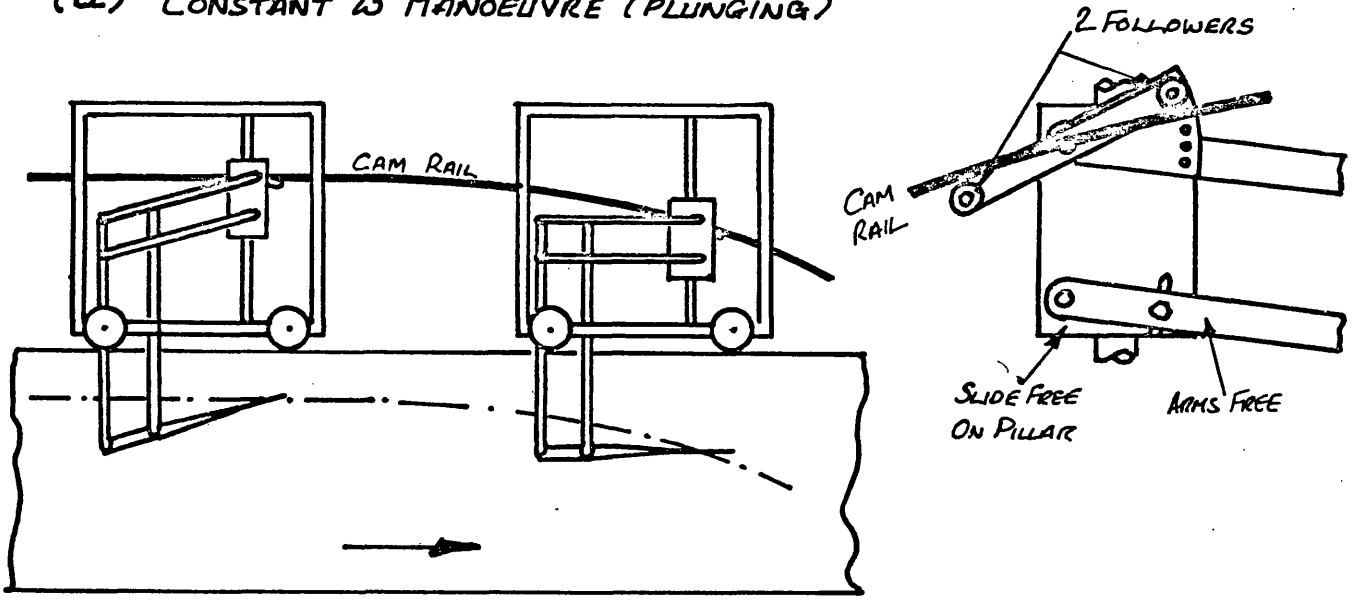

(b) CONSTANT q MANOEUVRE

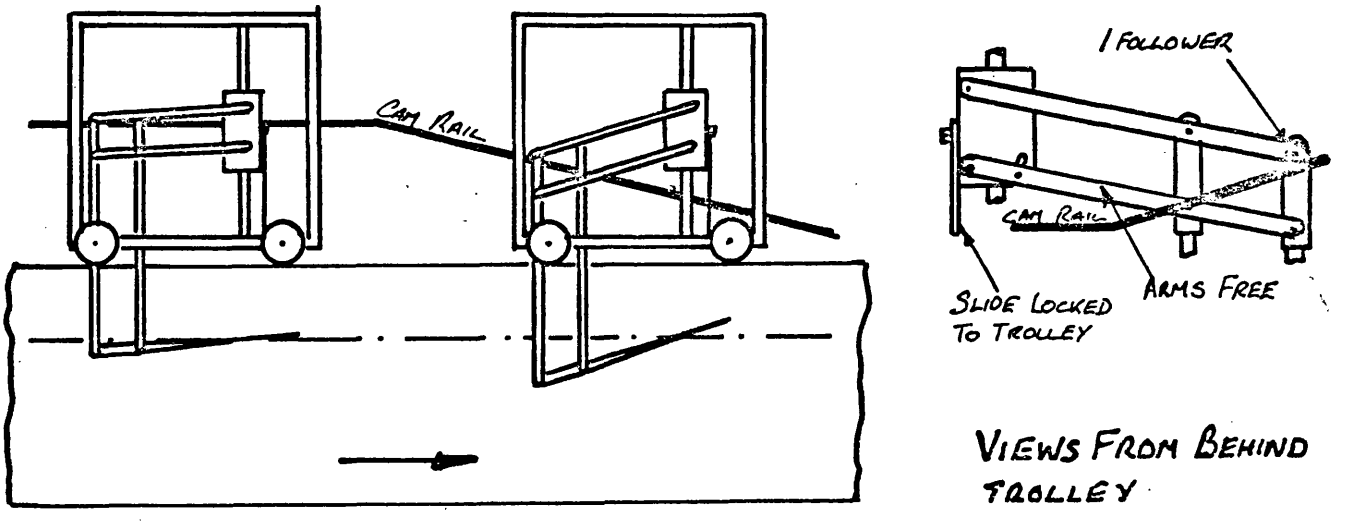

VIEWS FROM BEHIND TROLLEY

(c) CONSTANT $\dot{\theta}$ MANOEUVRE (PITCHING)

FIG 2.07 ARRANGEMENT OF FOLLOWERS FOR UNSTEADY MANOEUVRES

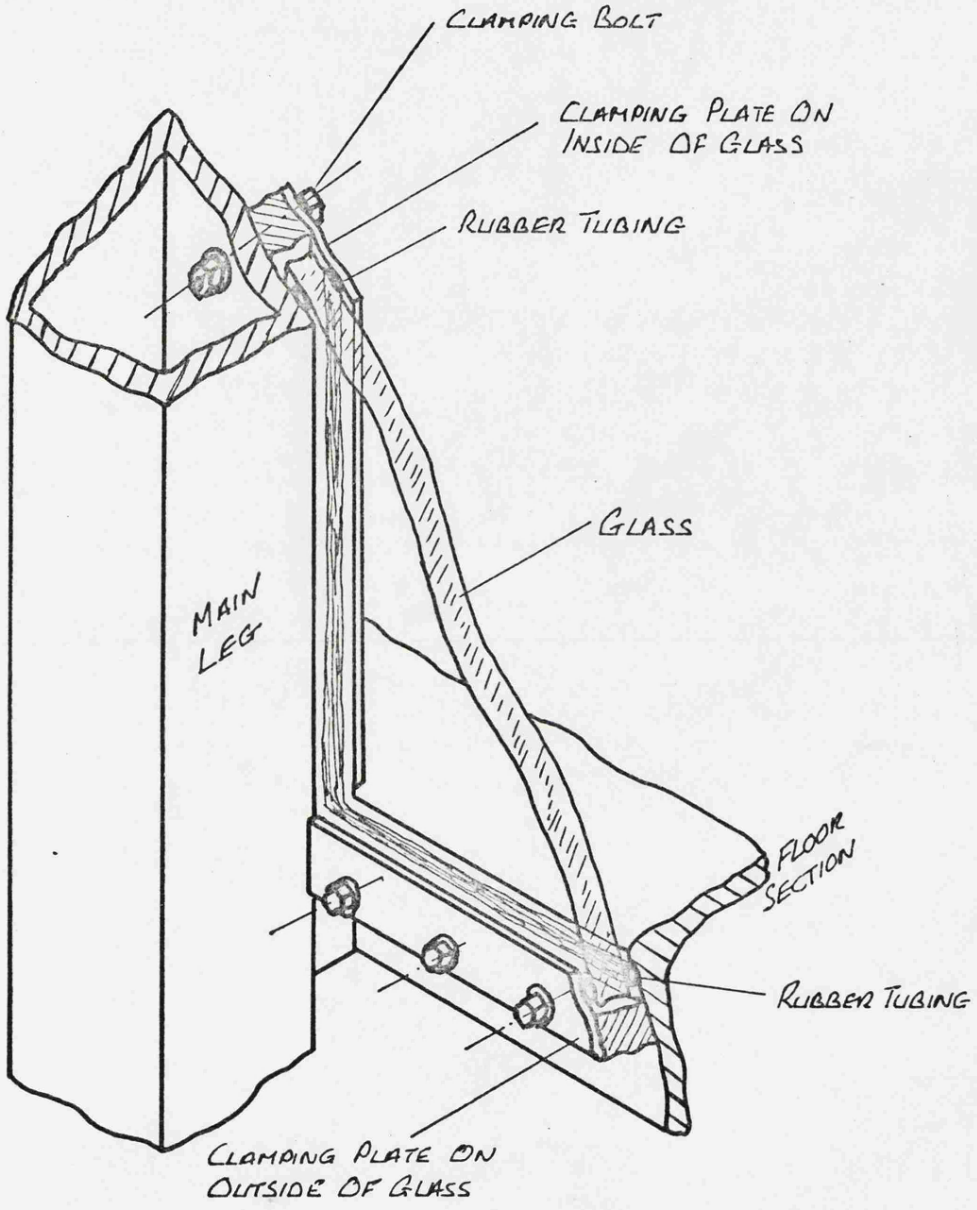

FIG 2.08 DETAIL OF GLASS MOUNTING

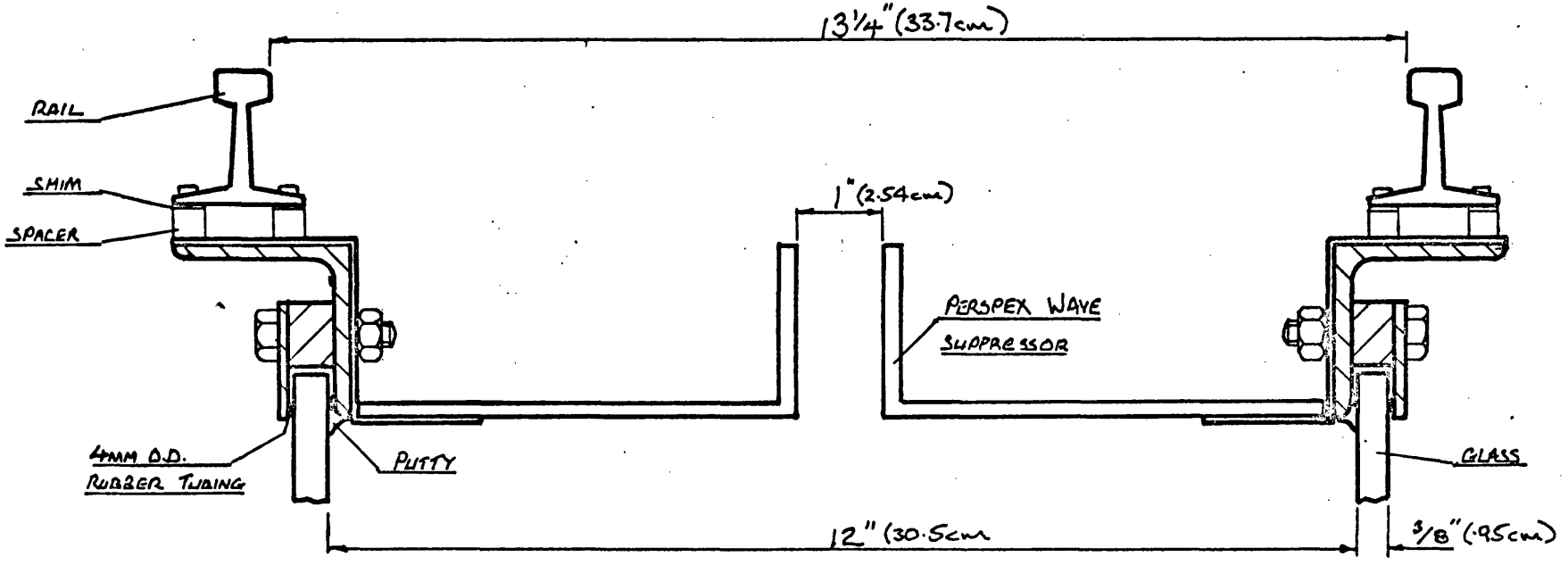

FIG 2.09 SECTION ACROSS TOP OF TANK

SCALE 1:2

FIG 2.09

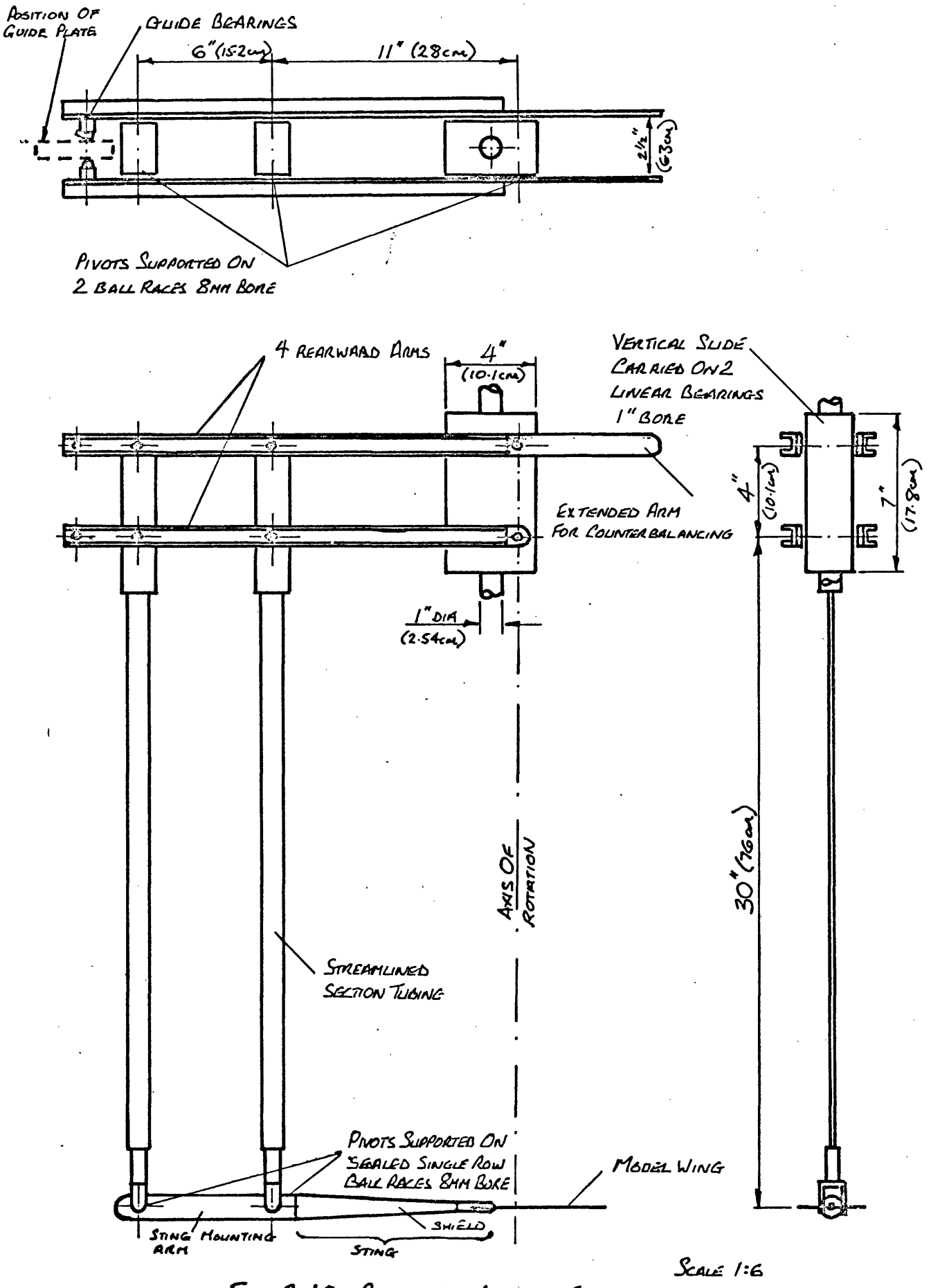

FIG 2.10 PARALLEL LINKAGE

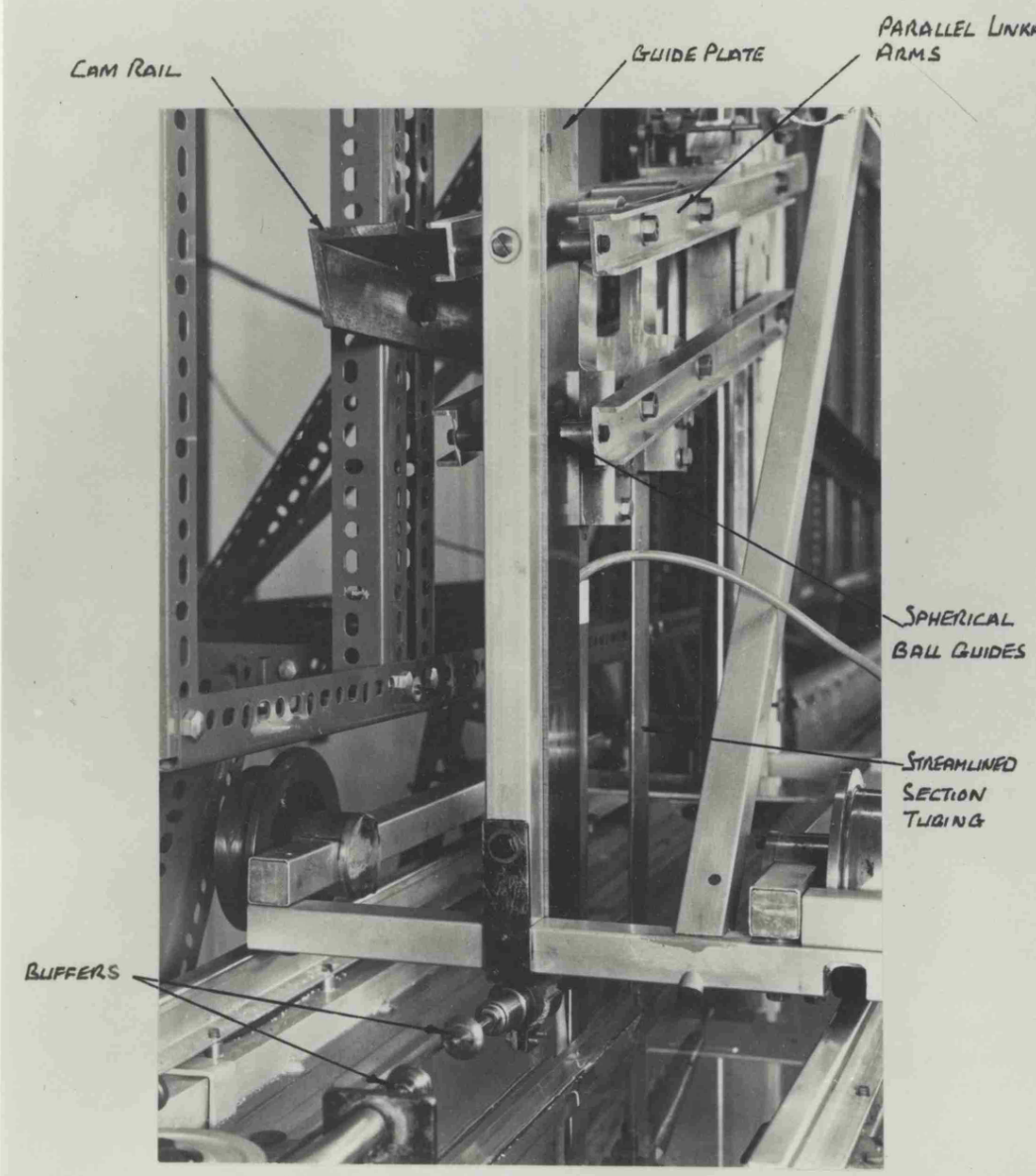

FIG 2.11 VIEW FROM REAR OF TROLLEY SHOWING SPHERICAL BALL GUIDES, PARALLEL LINKAGE ARMS AND BUFFER

FIGS 2.12
& 2.13

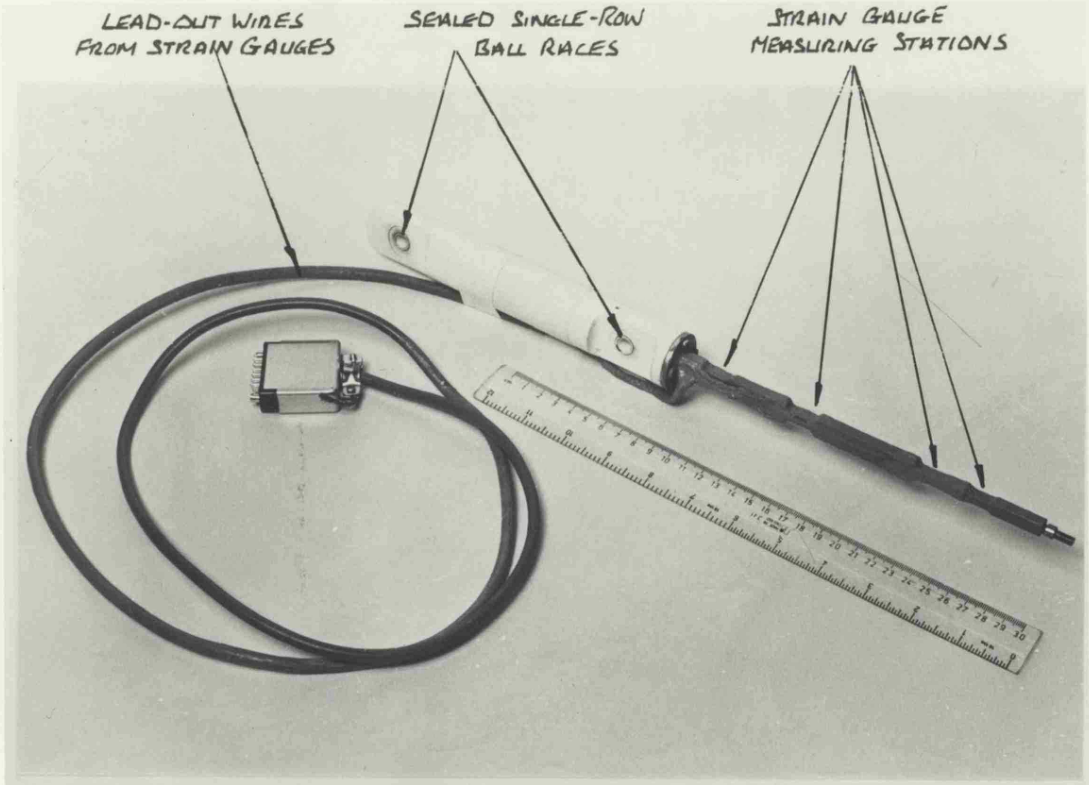

FIG 2.12 STING SHOWING STRAIN GAUGE MEASURING STATIONS AND WATERPROOF COATING

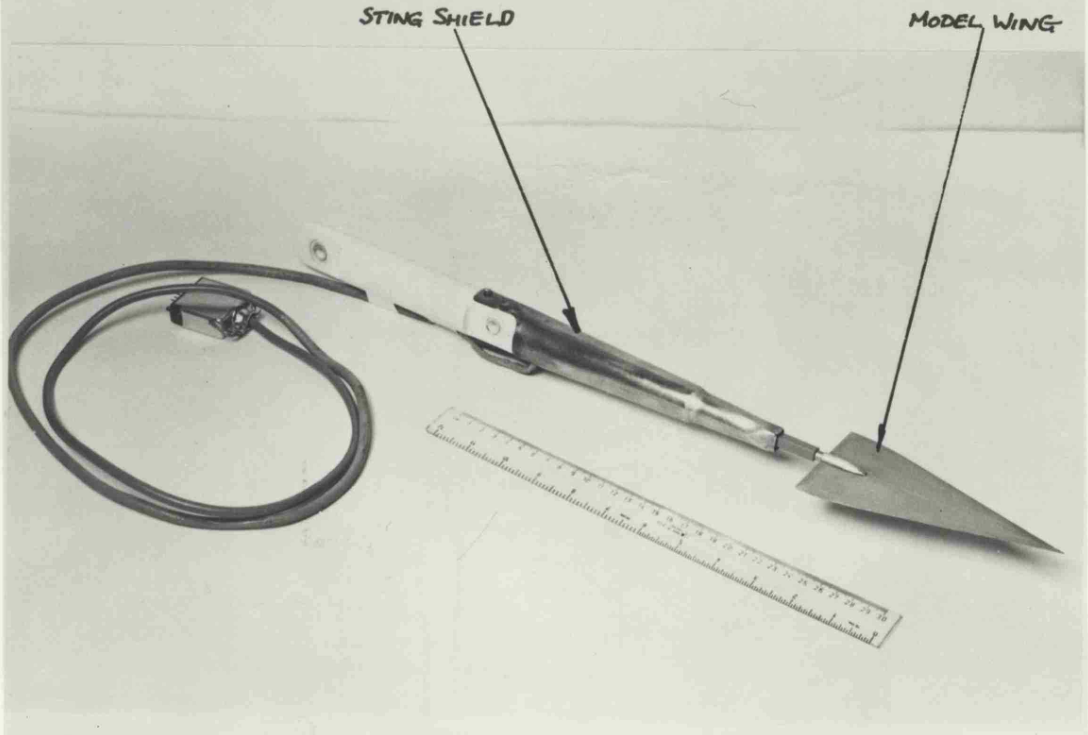

FIG 2.13 STING WITH MODEL WING AND SHIELD ATTACHED

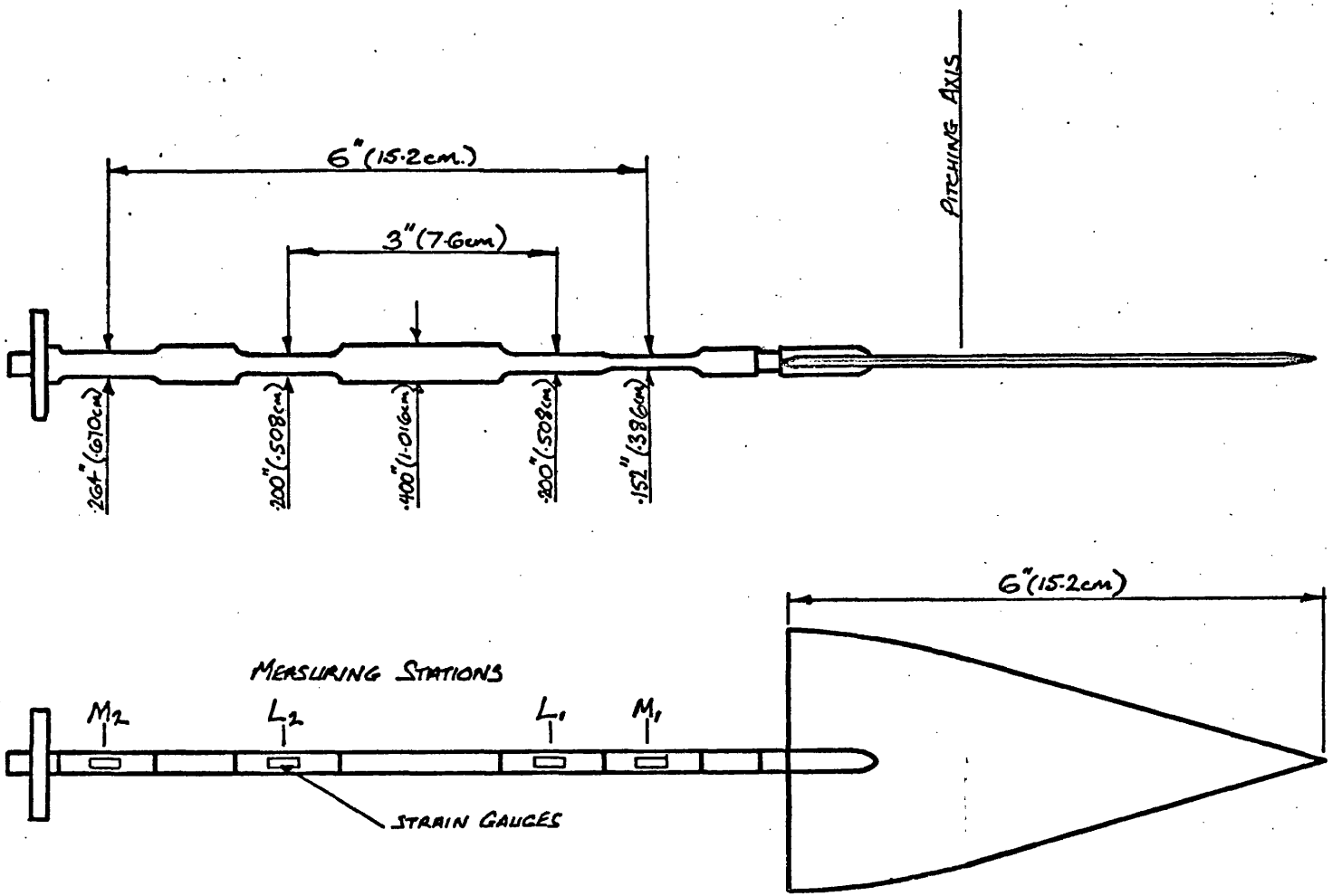

STATION	I in^4	y/I in^{-3}
M_1	73×10^{-6}	1039×10^{3}
L_1	167×10^{-6}	6×10^{3}
L_2	167×10^{-6}	6×10^{3}
M_2	384×10^{-6}	349×10^{3}

FIG 2.14 STING AND MODEL, MAIN DIMENSIONS
(SEE ALSO FIGS 2.15 & A.1.1)

FIG 2.14

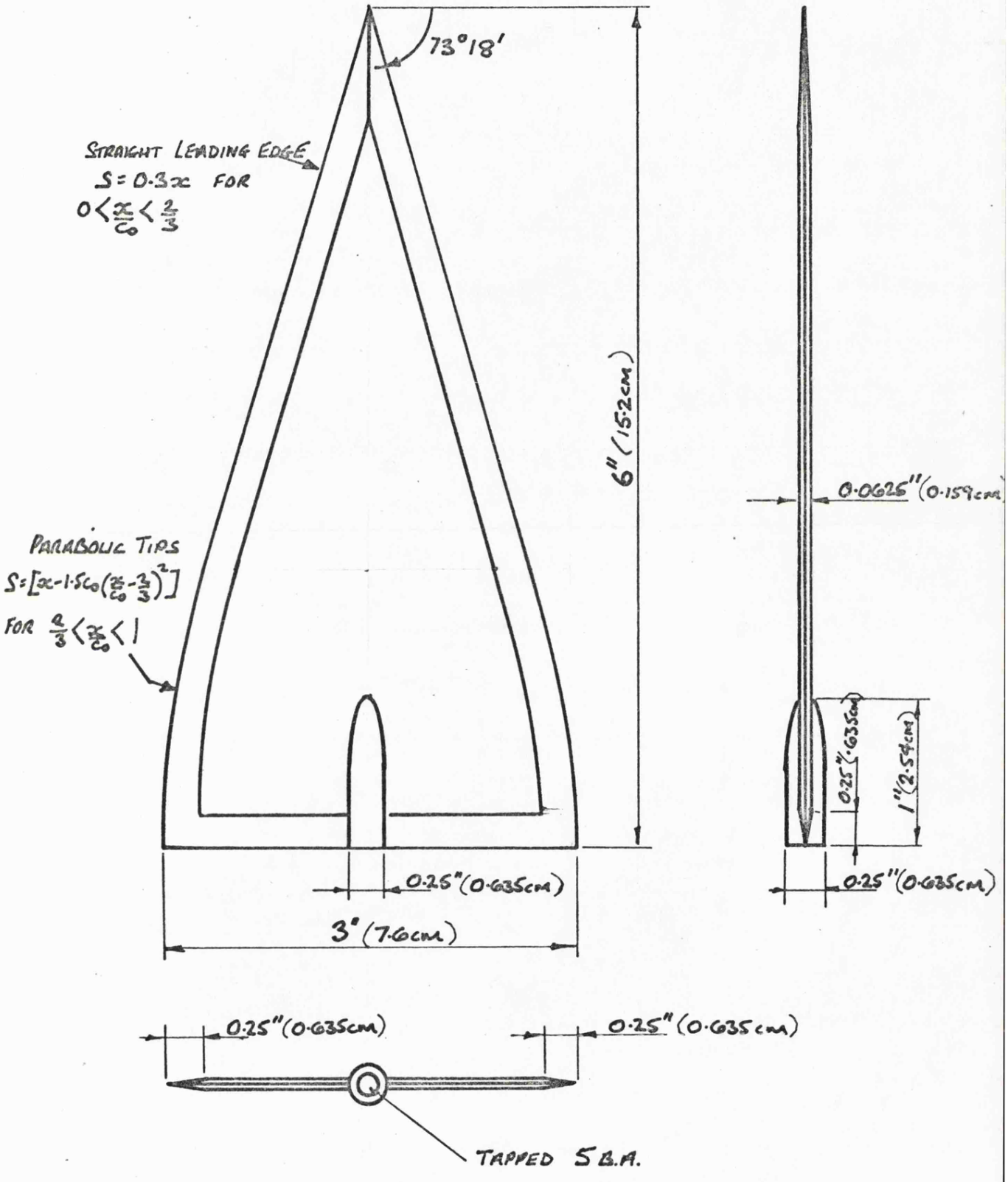

FIG 2.15 MODEL WING WITH AGARD MODEL G PLANFORM

FIGS 2.16 & 2.17

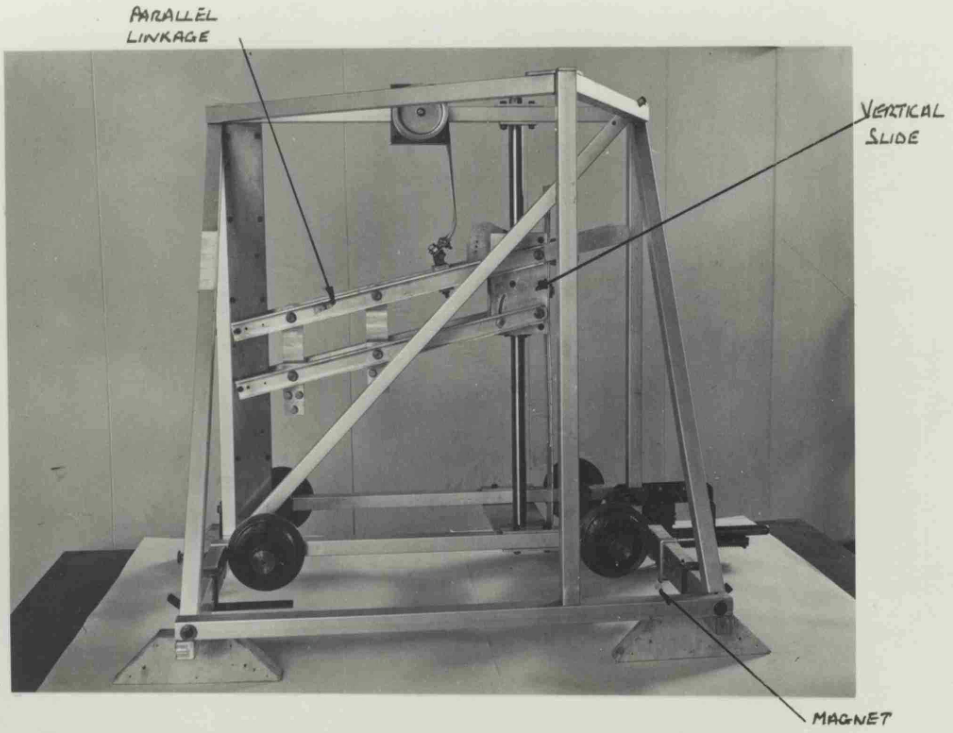

FIG 2.16 TROLLEY VIEWED FROM FRONT OF TANK

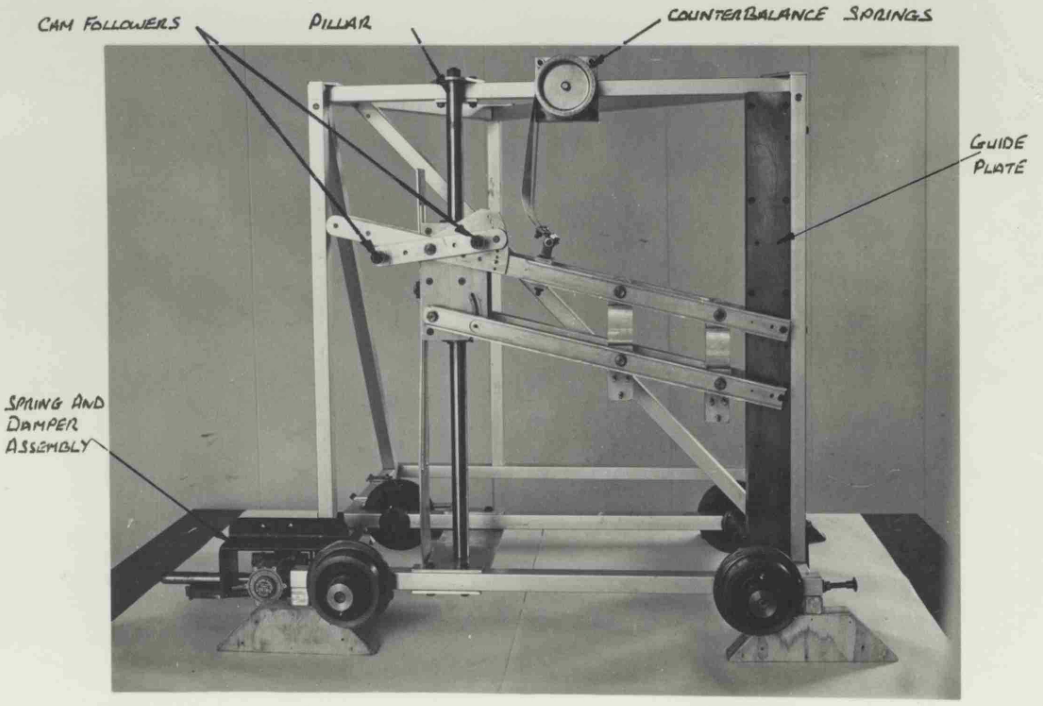

FIG 2.17 TROLLEY VIEWED FROM REAR OF TANK

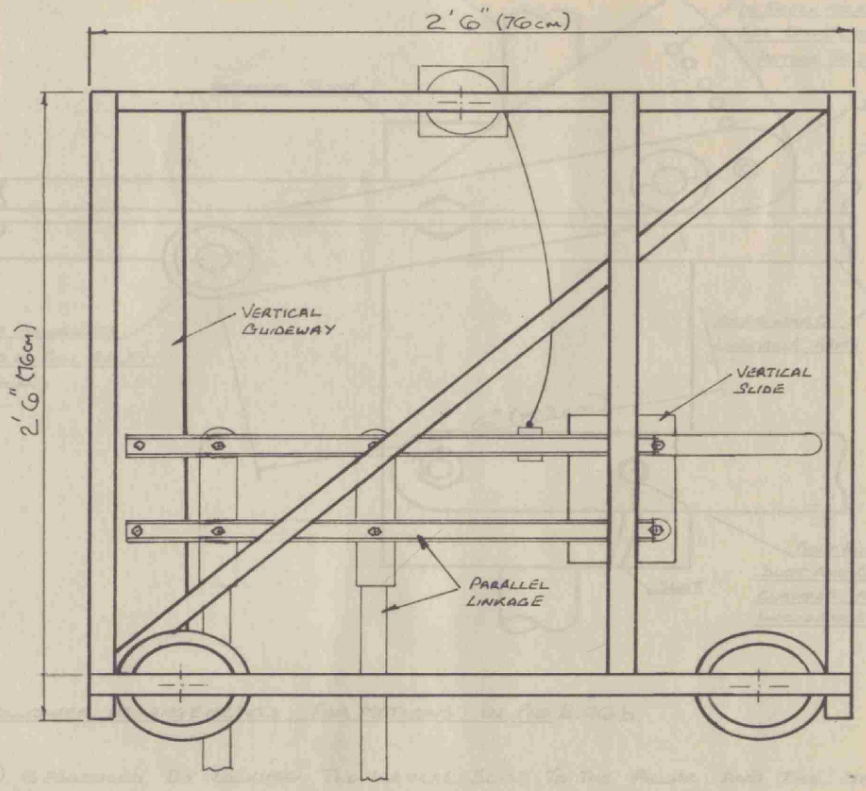

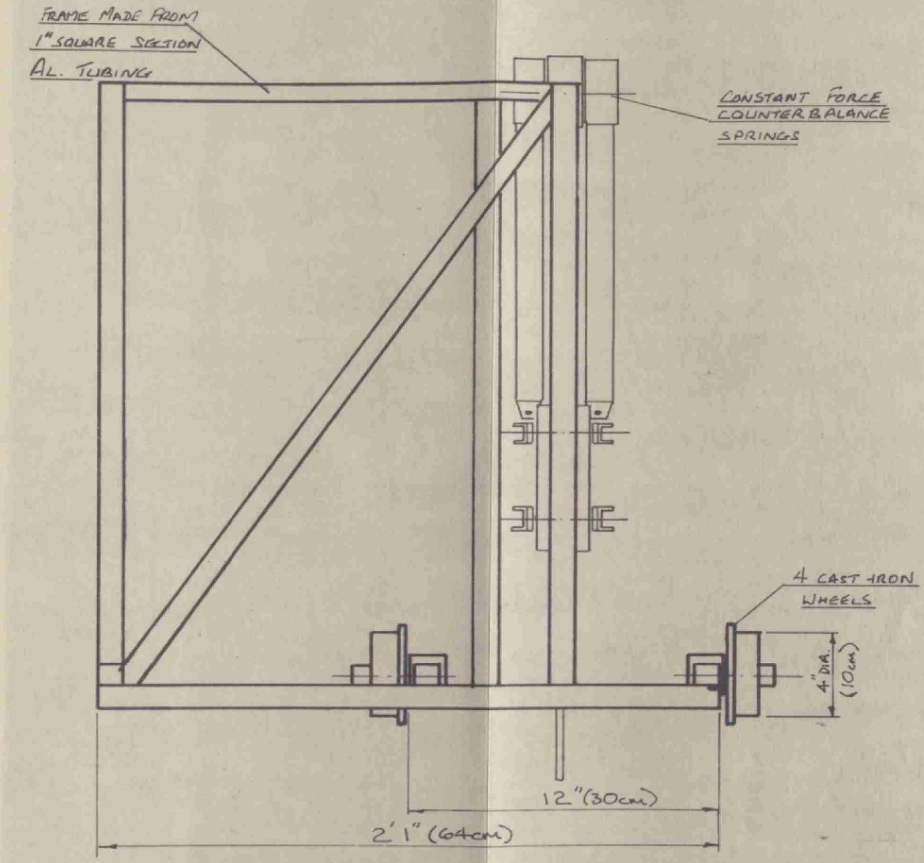

FIG 2.18 TROLLEY AND PARALLEL LINKAGE

SCALE 1:6

FIG 2.19

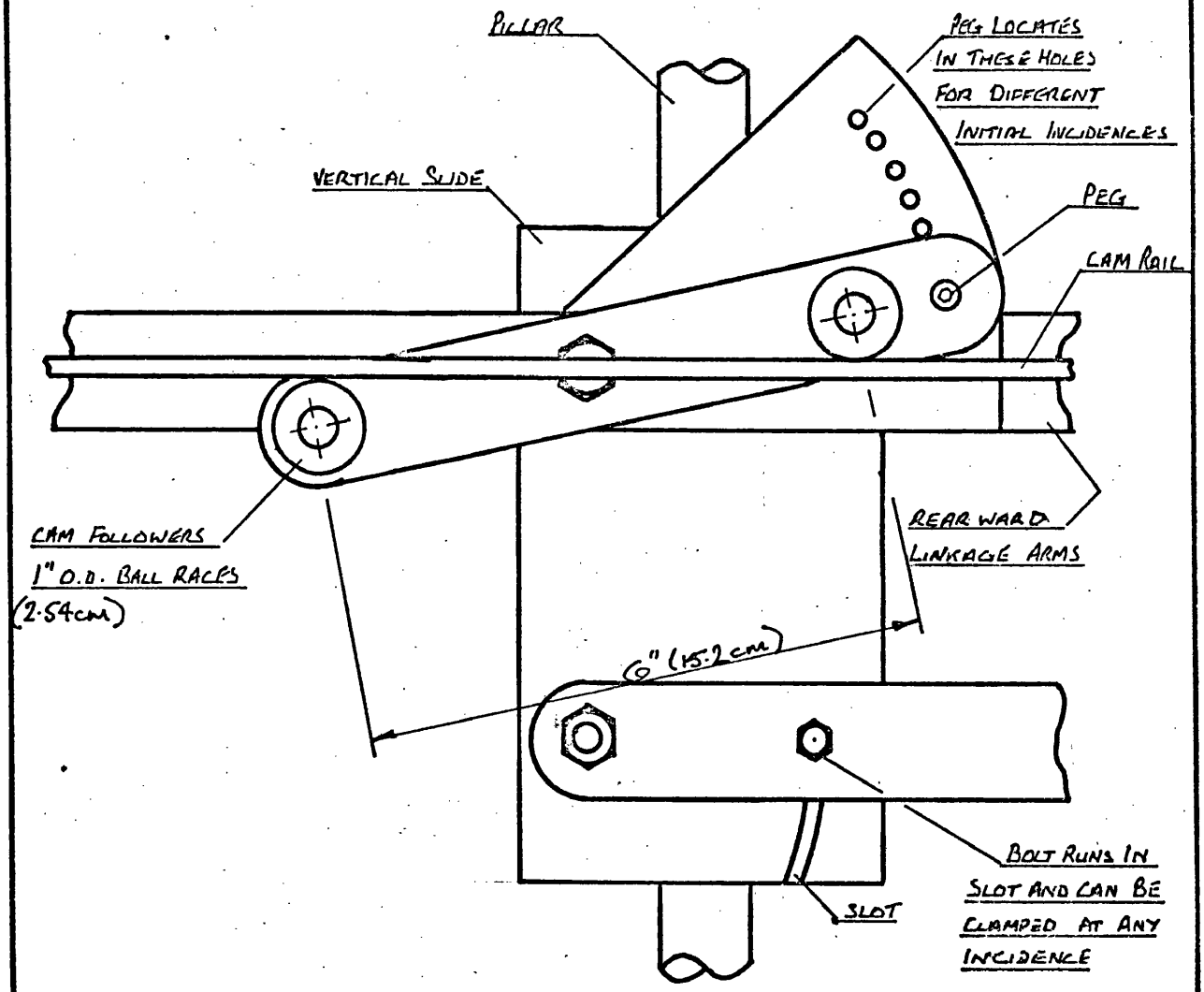

FOLLOWER ARRANGEMENTS FOR MOTIONS IN FIG 2.06b

A) IS PRODUCED BY LOCKING THE VERTICAL SLIDE TO THE PILLAR AND THE LINKAGE ARMS TO THE SLIDE

B) IS PRODUCED BY LOCKING THE ARMS AT A GIVEN ATTITUDE AND USING ONE FOLLOWER

C) IS PRODUCED BY USING BOTH FOLLOWERS WITH THE ARMS AND VERTICAL SLIDE FREE

D) IS PRODUCED BY LOCKING THE VERTICAL SLIDE AND USING ONE FOLLOWER.

FIG 2.19 VERTICAL SLIDE AND CAM FOLLOWER ARRANGEMENTS

SCALE 1:2

FIGS 2.20
& 2.21

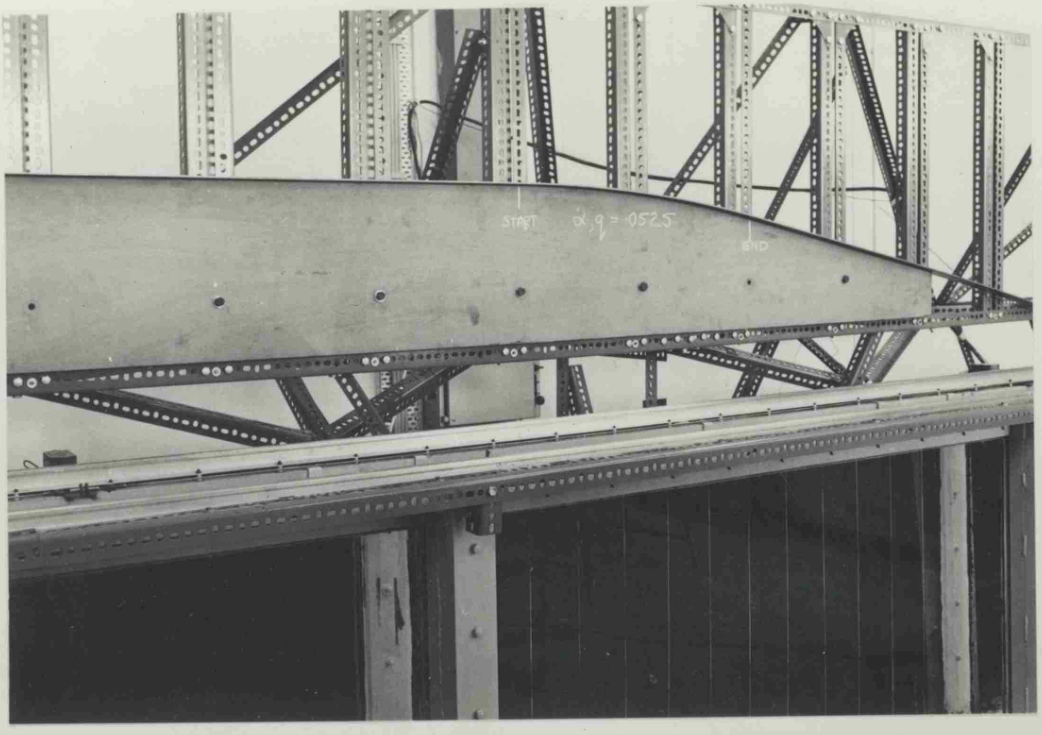

FIG 2.20 CAM RAIL USED FOR PLUNGING (CONSTANT $\dot{\omega}$) AND CONSTANT q MANOEUVRES FOR $\frac{\dot{\omega}c_0}{V^2}$, $\frac{qc_0}{V} = 0.0525$

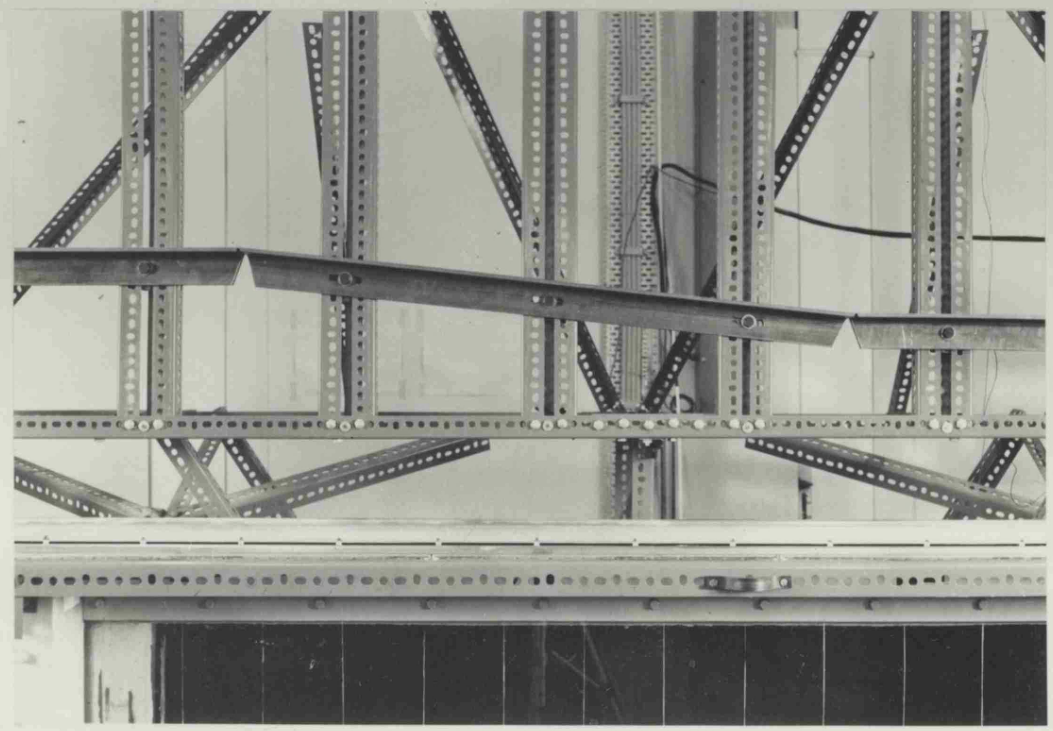

FIG 2.21 CAM RAIL USED FOR PITCHING (CONSTANT $\dot{\theta}$) MANOEUVRE FOR $\frac{\dot{\theta}c_0}{V^2} = 0.035$

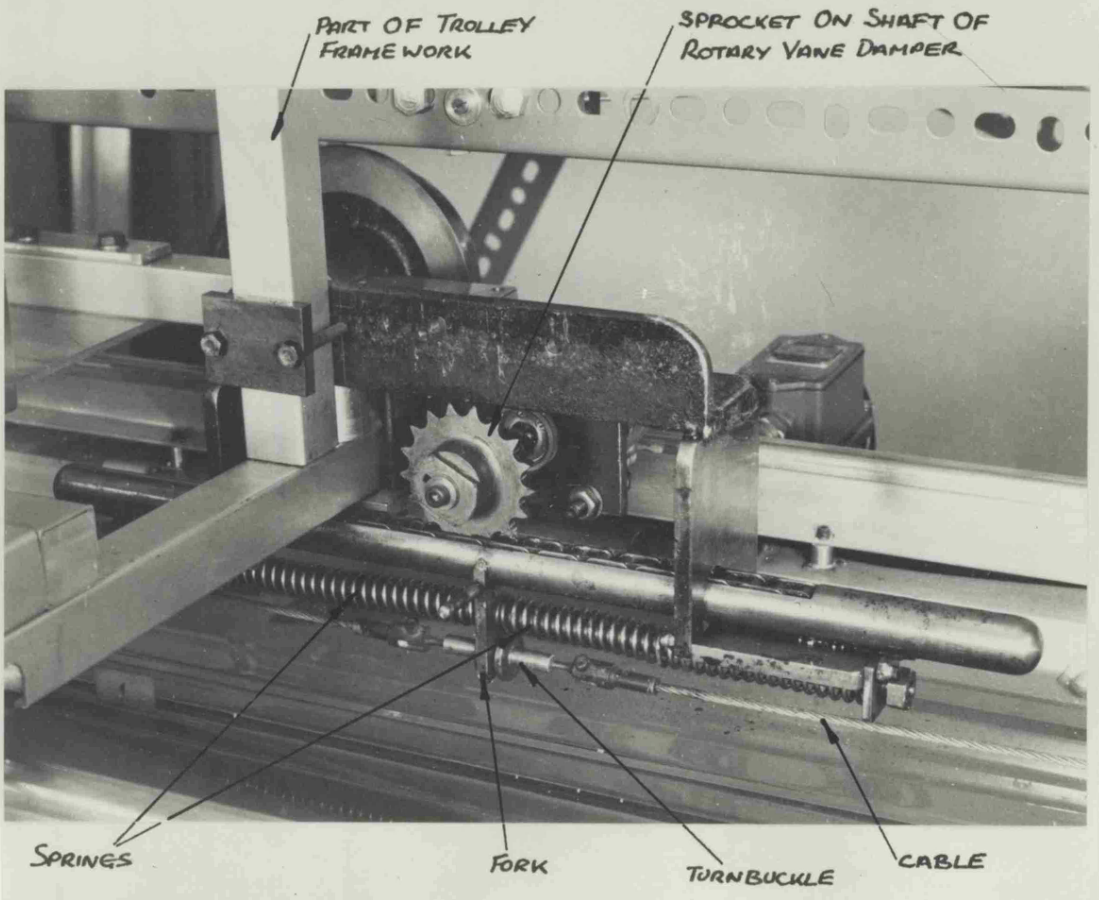

FIG 2.22 SPRING AND DAMPER UNIT FOR ABSORBING STARTING SHOCK BETWEEN TOWING CABLE AND TROLLEY

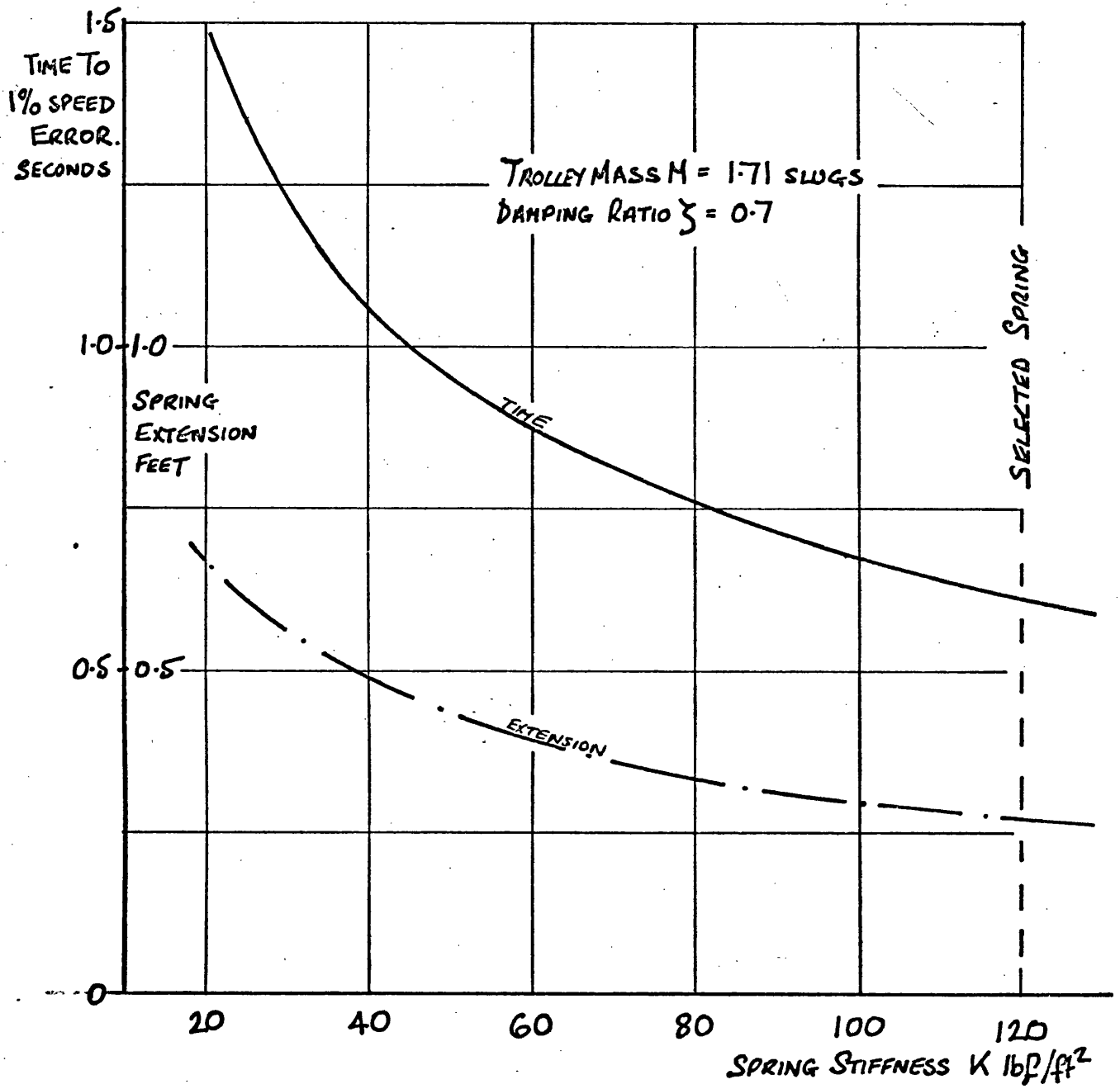

FIG 2.23 PERFORMANCE OF SPRING AND DAMPER

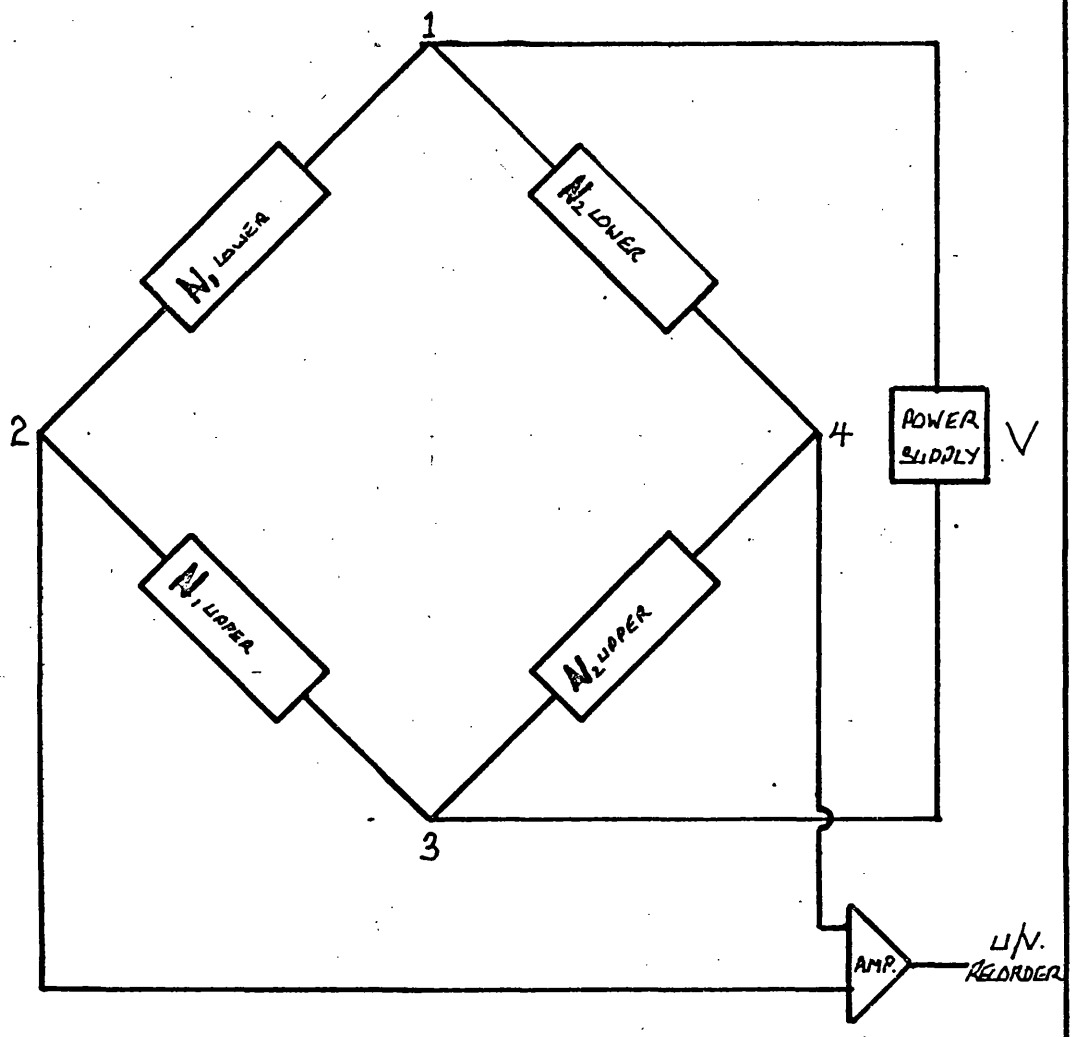

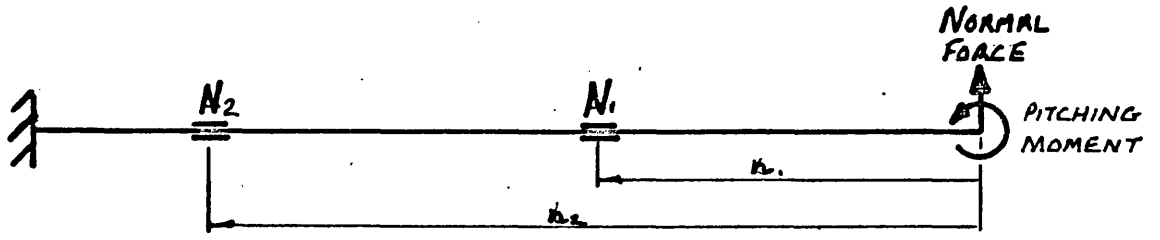

NOW IF $\left(\frac{y}{EI}\right)_{N_1} = \left(\frac{y}{EI}\right)_{N_2}$

THEN BRIDGE OUTPUT = $\underset{\text{FORCE}}{\text{NORMAL}} \times (h_2 - h_1)\left(\frac{y}{EI}\right)_{N_1,N_2}\left(\frac{V}{2}\right) \times$ GAUGE FACTOR VOLTS

(APP1)

FIG. 2.24 NORMAL FORCE BRIDGE CIRCUIT

FIG 2.25

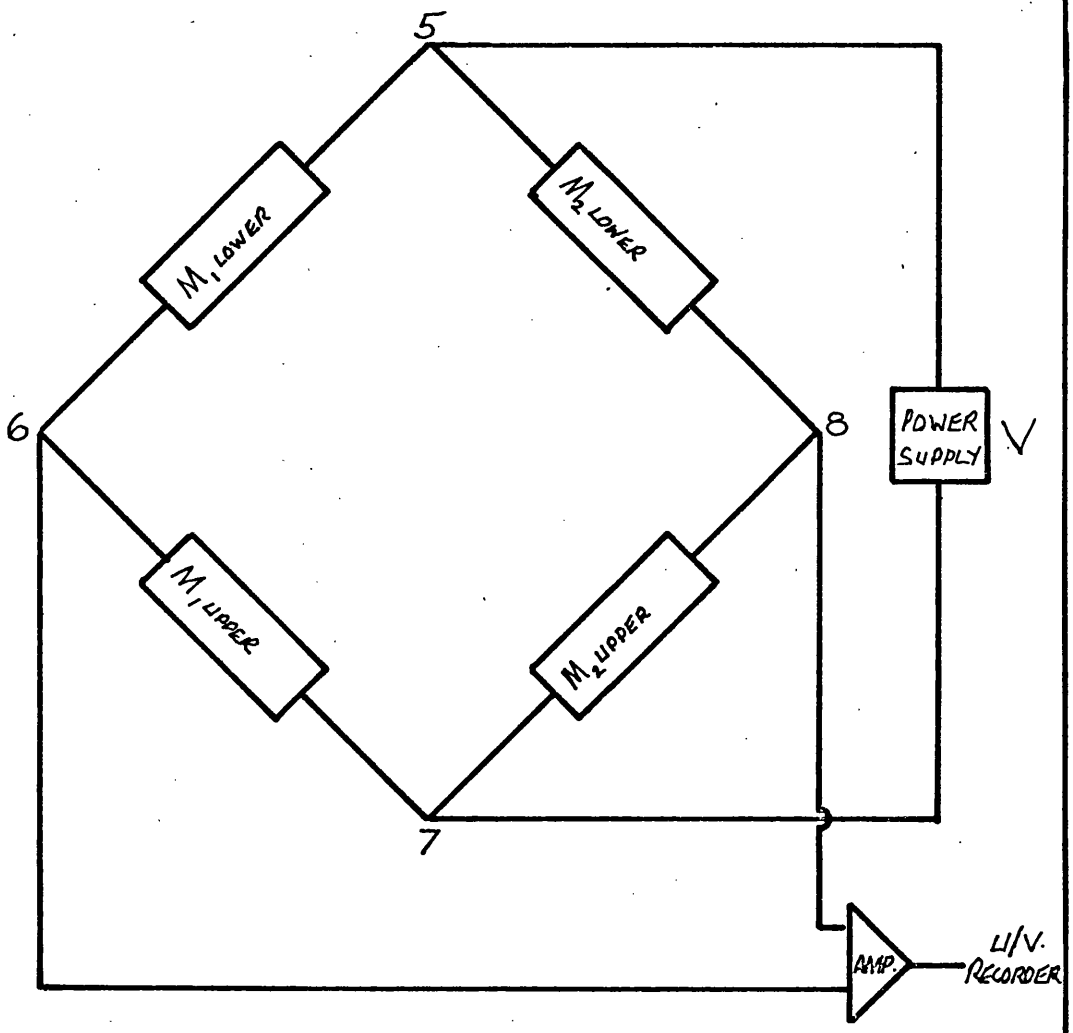

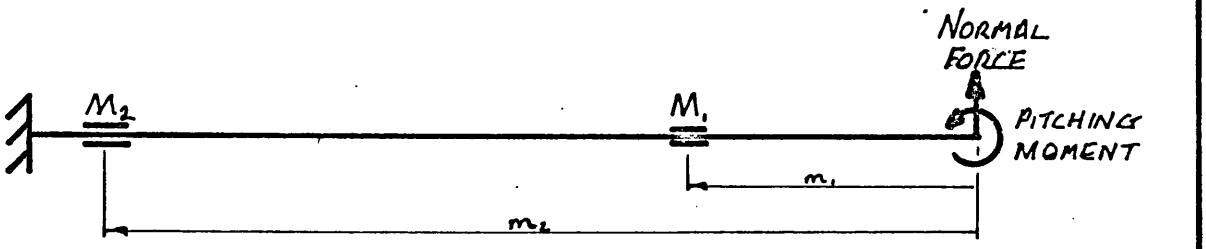

NOW IF $m_2 = n \times m_1$

AND $\left(\frac{y}{EI}\right)_{M_1} = n \times \left(\frac{y}{EI}\right)_{M_2}$

THEN BRIDGE OUTPUT = $P.M. \times \left[\left(\frac{y}{EI}\right)_{M_1} - \left(\frac{y}{EI}\right)_{M_2}\right]\left(\frac{V}{2}\right) \times$ GAUGE FACTOR VOLTS

(APP. 1)

FIG 2.25 PITCHING MOMENT BRIDGE CIRCUIT

FIGS 2.26
& 2.27

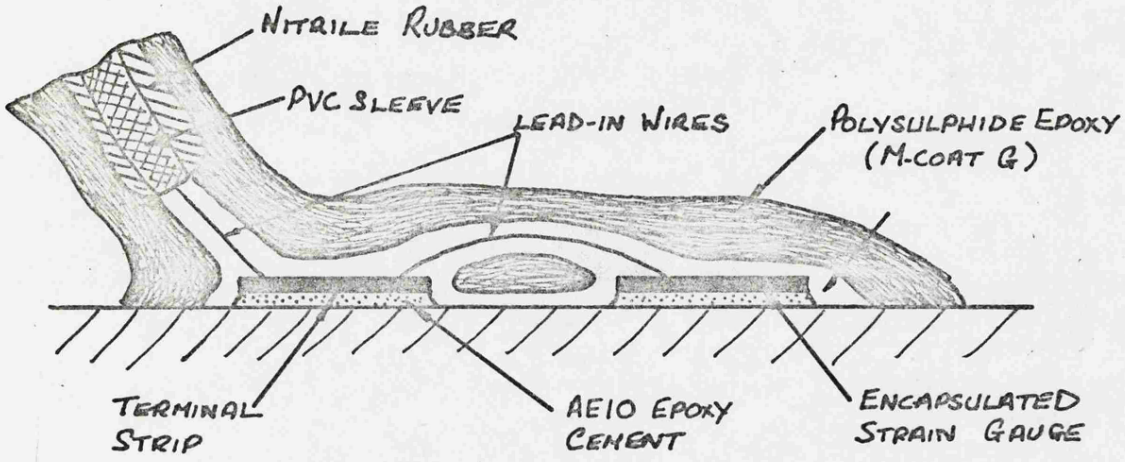

FIG 2.26 STRAIN GAUGE INSTALLATION AND WATERPROOFING

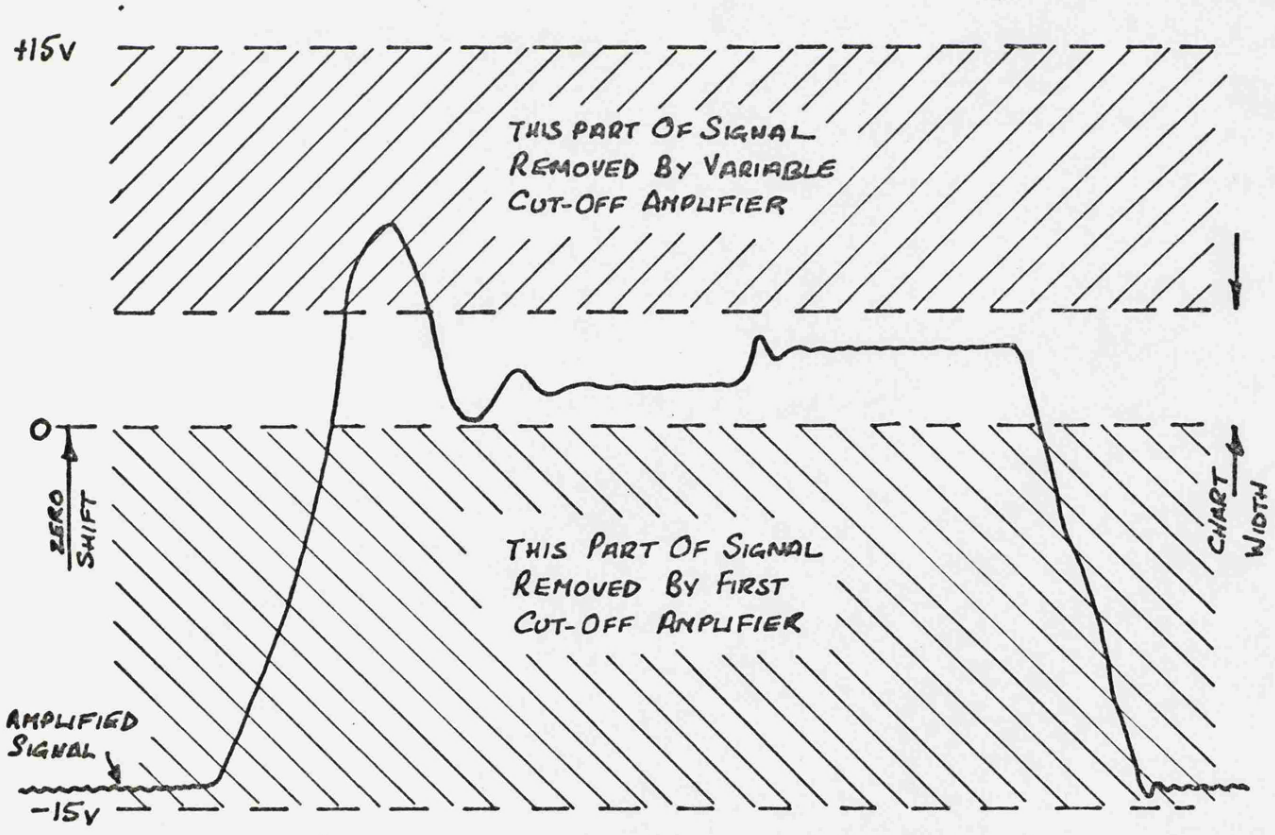

FIG 2.27 EFFECT OF HIGH GAIN AMPLIFIER AND CUT-OFF ON
STRAIN GAUGE OUTPUT SIGNAL

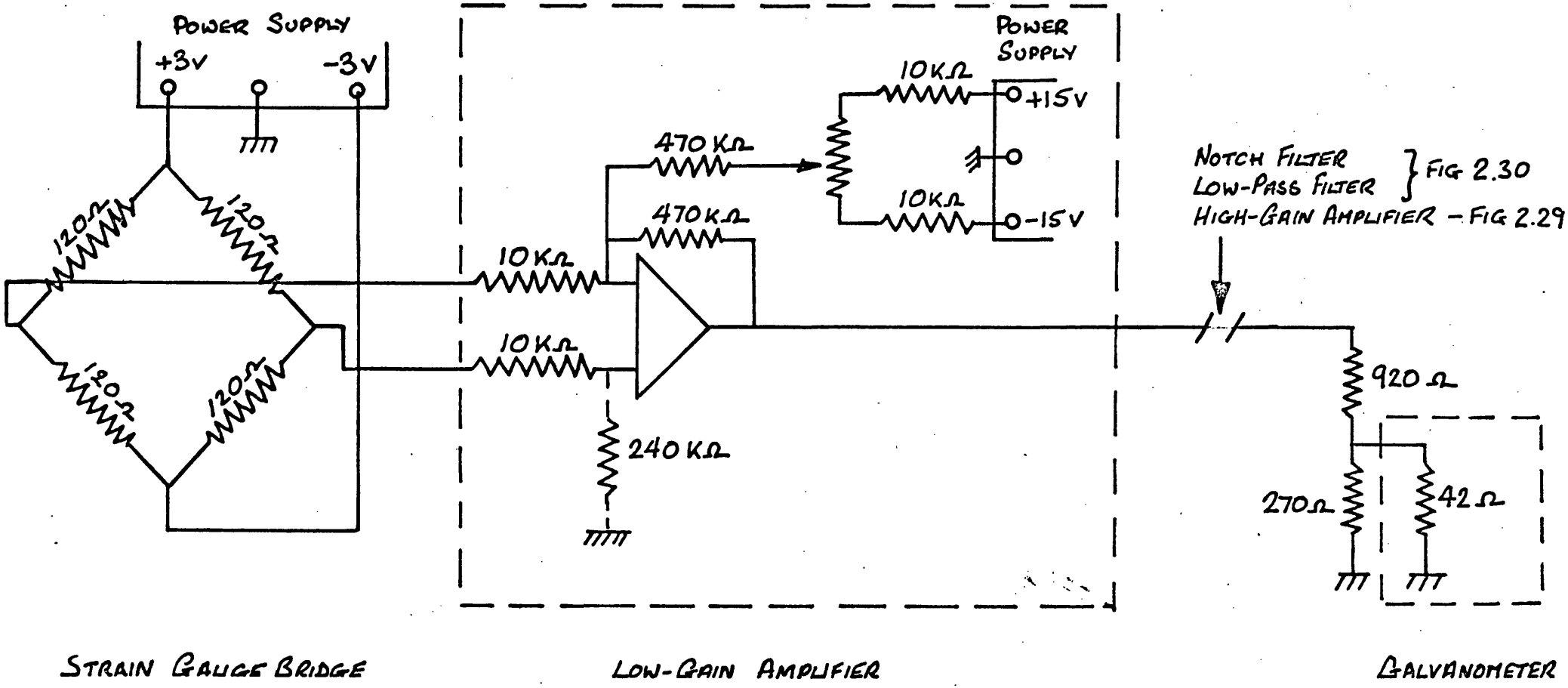

FIG 2.28 NORMAL FORCE AND PITCHING MOMENT CIRCUITS

FIG 2.28

FIG 2.29

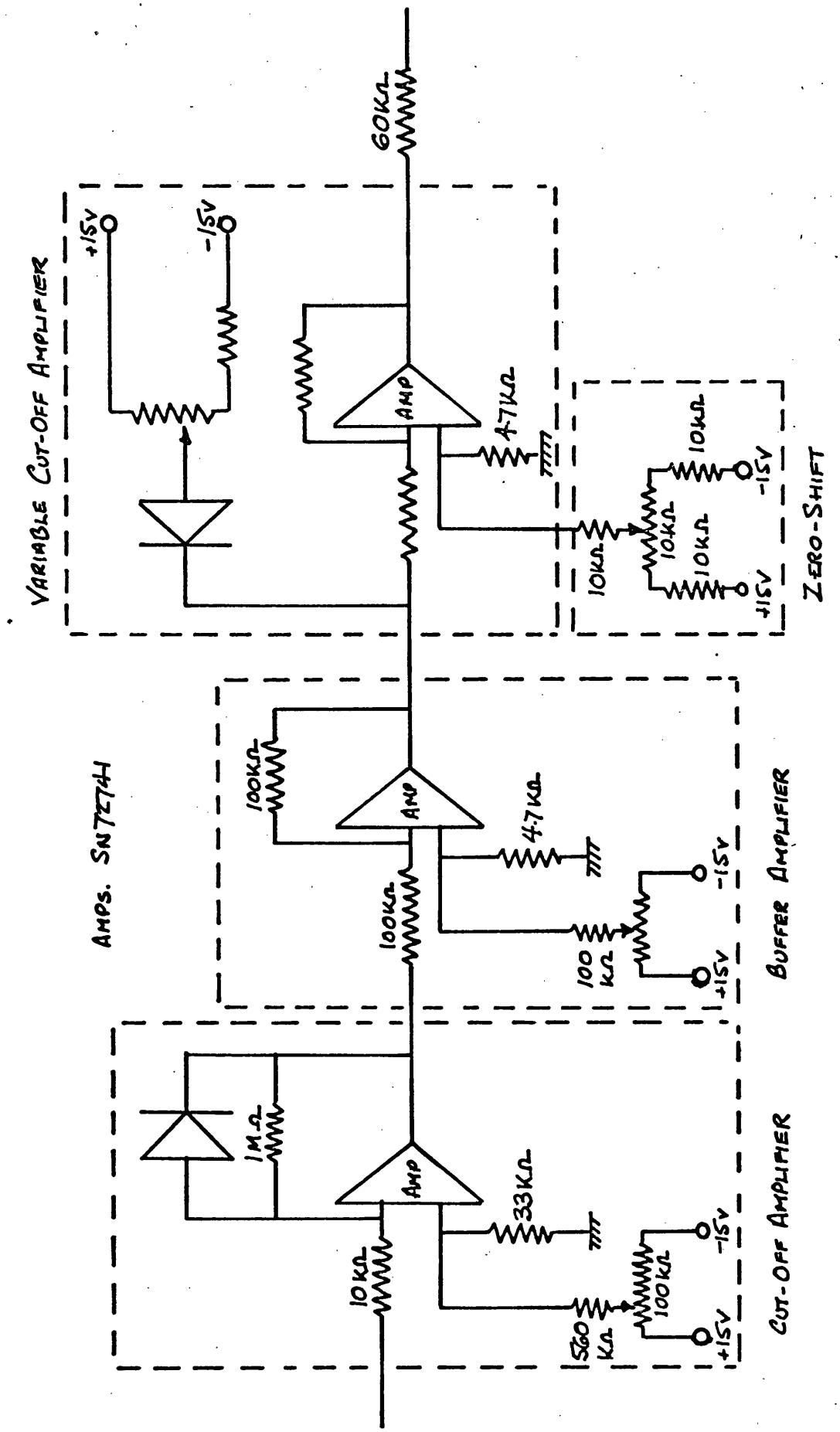

FIG 2.29 HIGH-GAIN AMPLIFIER CIRCUIT

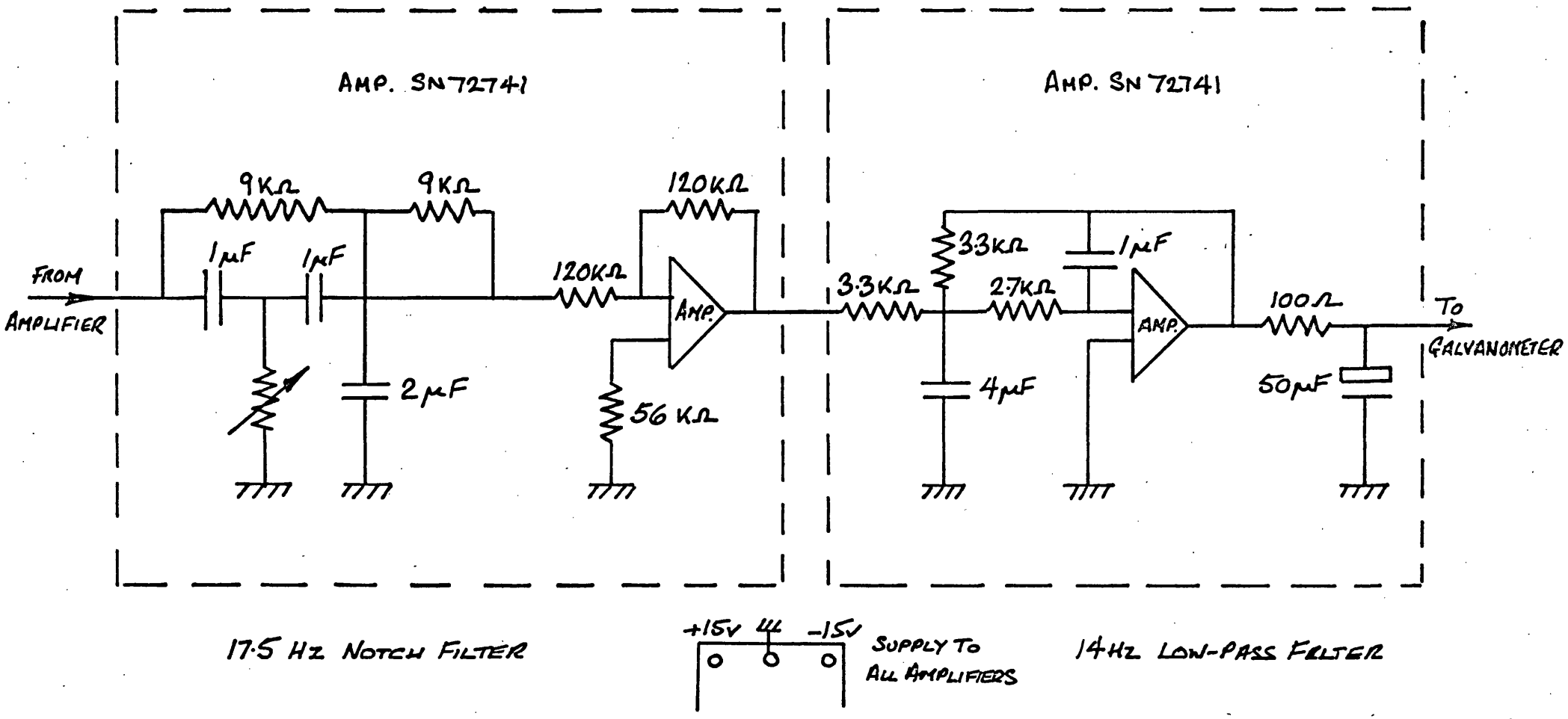

FIG. 2.30

FIG 2.30 STRAIN GAUGE OUTPUT SIGNAL FILTER CIRCUITS

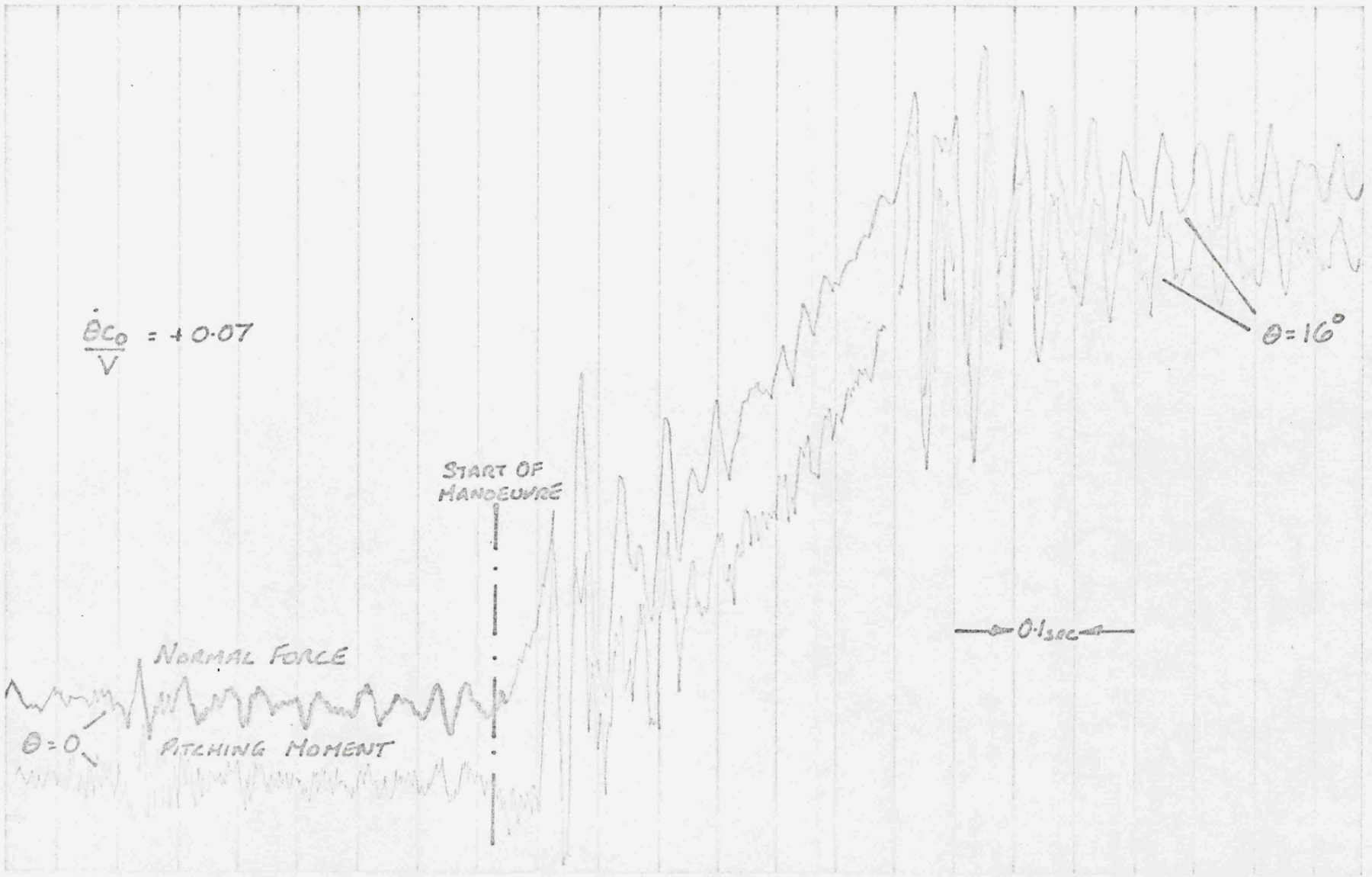

FIG 2.31 U/V TRACE OF RUN AT CONSTANT $\dot{\theta}$ USING NO FILTERS

FIG 2.31

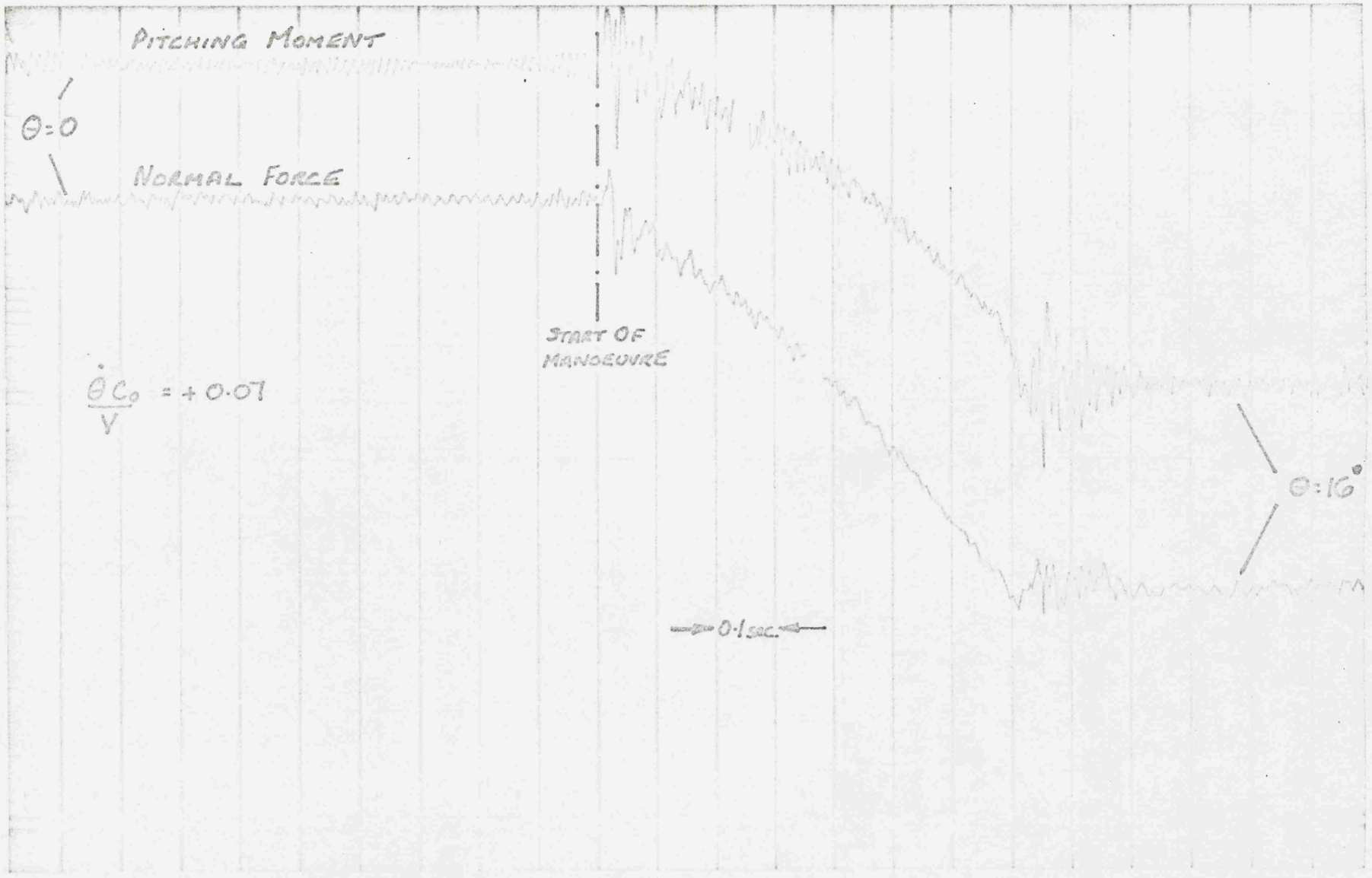

FIG 2.32 L/V TRACE OF RUN AT CONSTANT $\dot{\theta}$ USING NOTCH FILTER

FIG 2.32

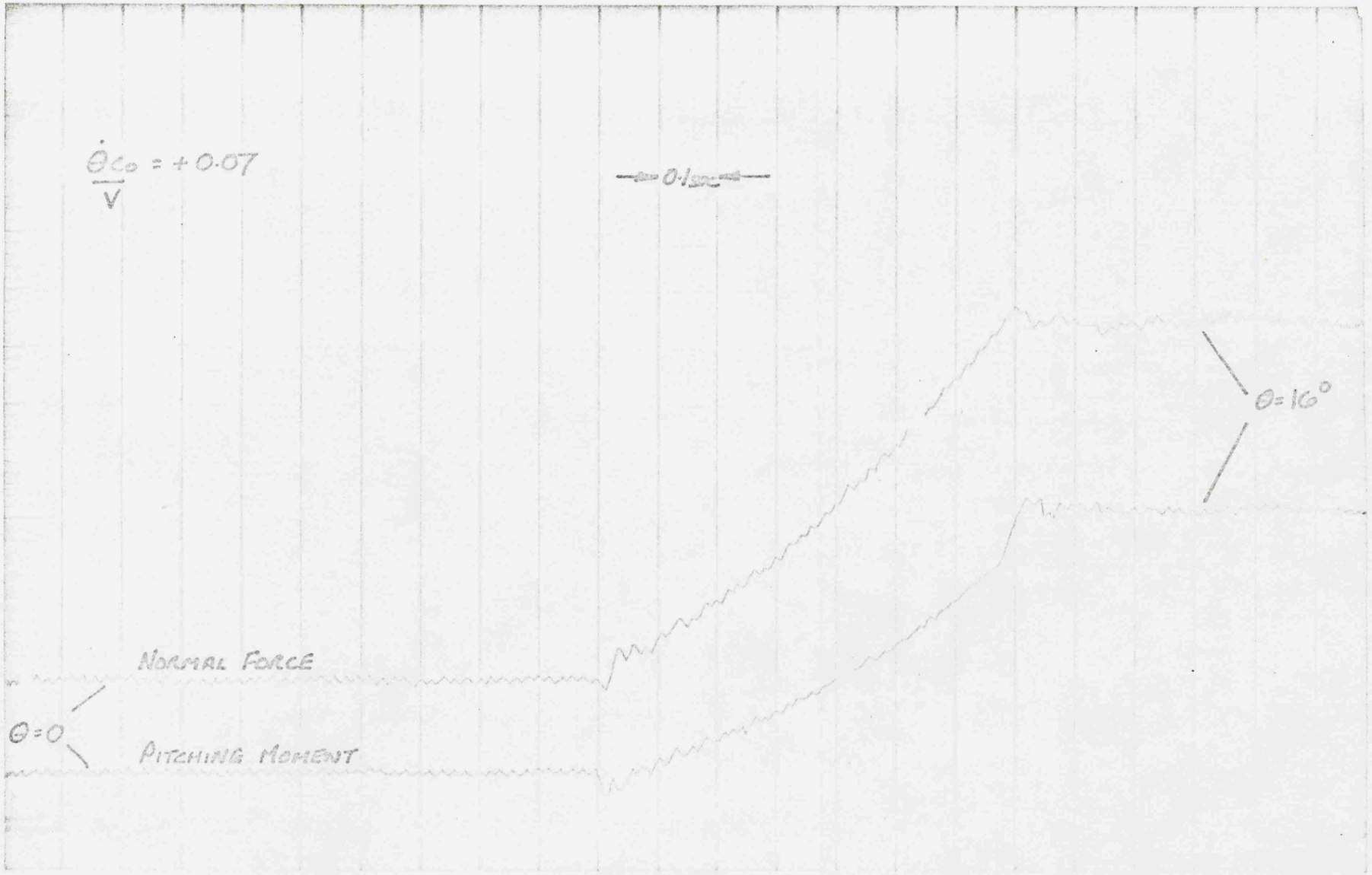

FIG 2.33 L/V TRACE OF RUN AT CONSTANT $\dot{\theta}$ USING NOTCH FILTER AND LOW-PASS FILTER

FIG 2.33

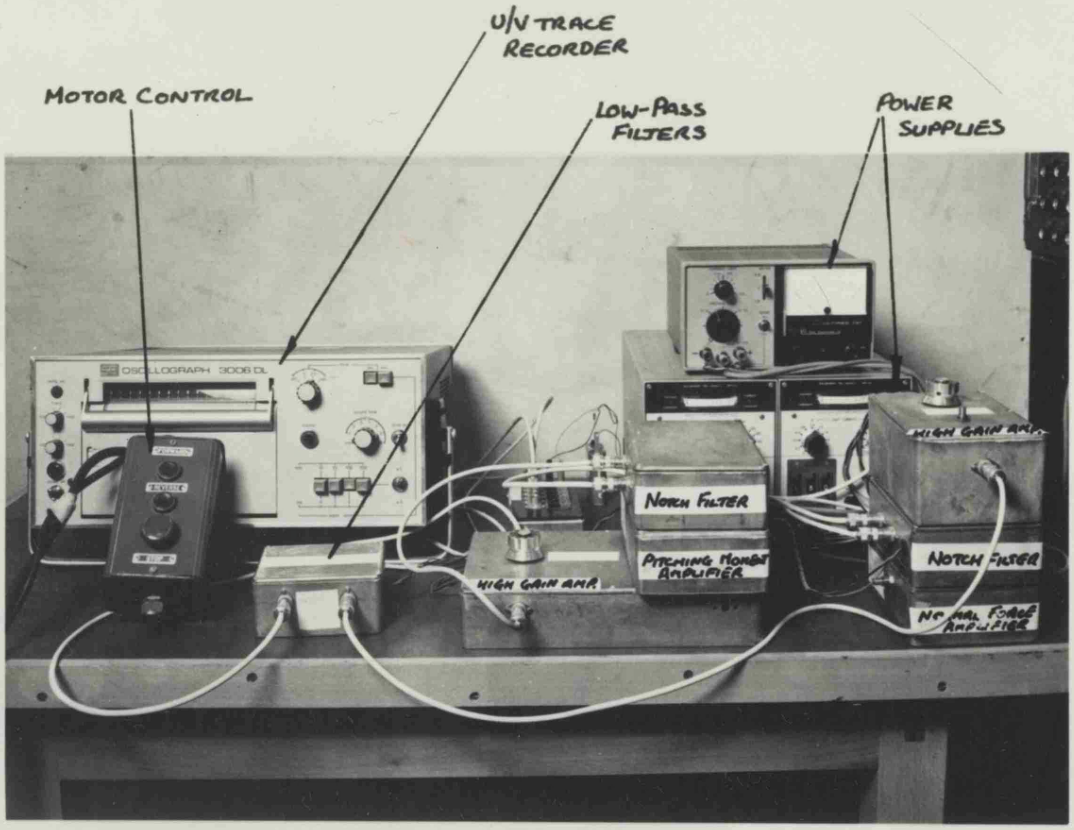

FIG 2.34 INSTRUMENTATION SHOWING STRAIN GAUGE CIRCUIT AMPLIFIERS AND FILTERS, U/V TRACE RECORDER AND MOTOR SPEED CONTROL

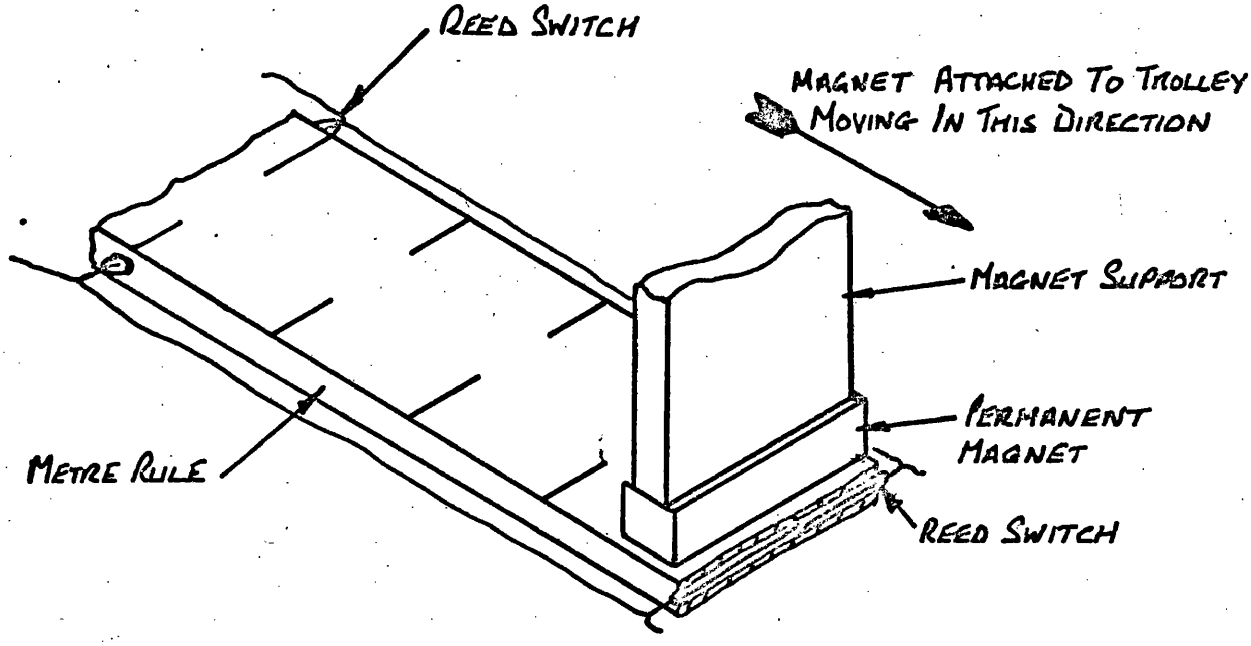

FIG 2.35 ARRANGEMENT OF REED SWITCHES AND MAGNET FOR MEASURING HORIZONTAL DISTANCE TRAVELLED (x)

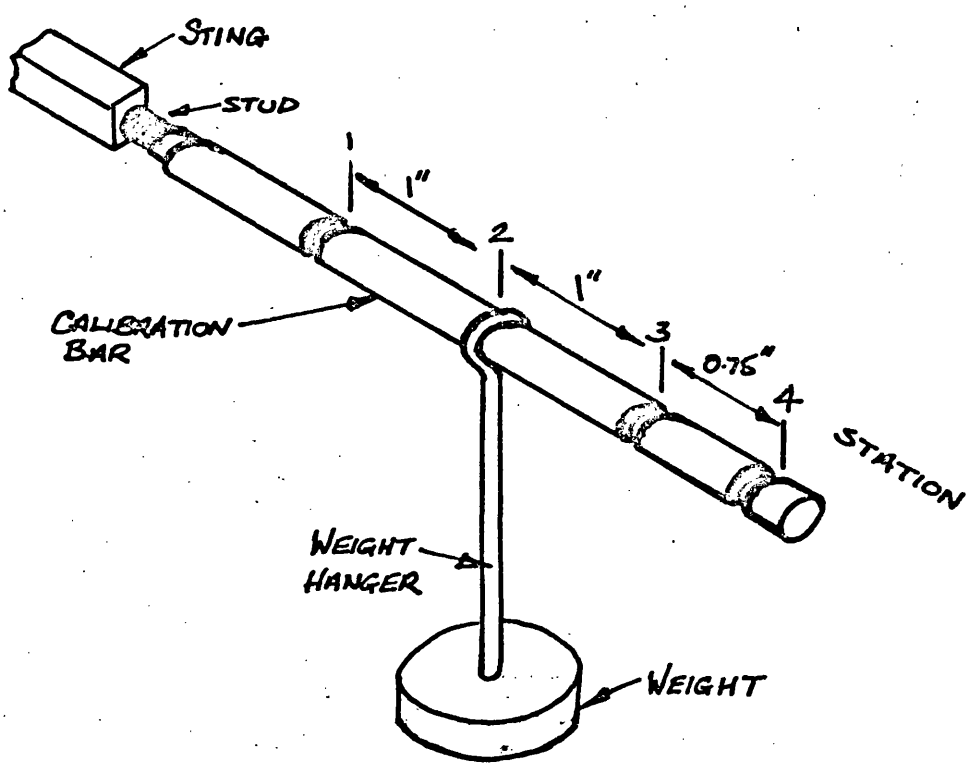

FIG3.01 STING CALIBRATION BAR WITH WEIGHT

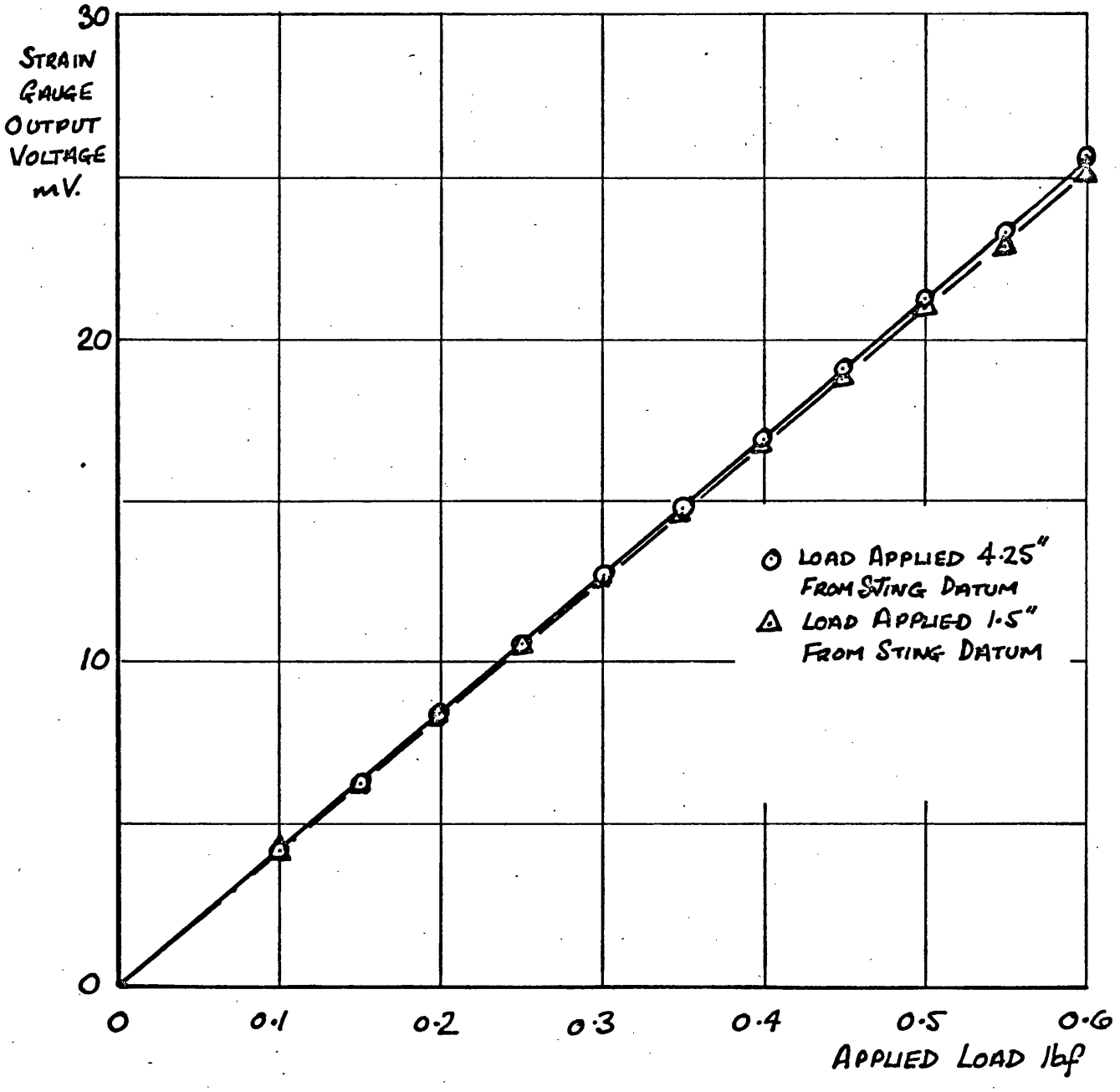

FIG 3.02 CALIBRATION OF NORMAL FORCE BRIDGE USING DVM TO FIND PITCHING MOMENT INTERFERENCE

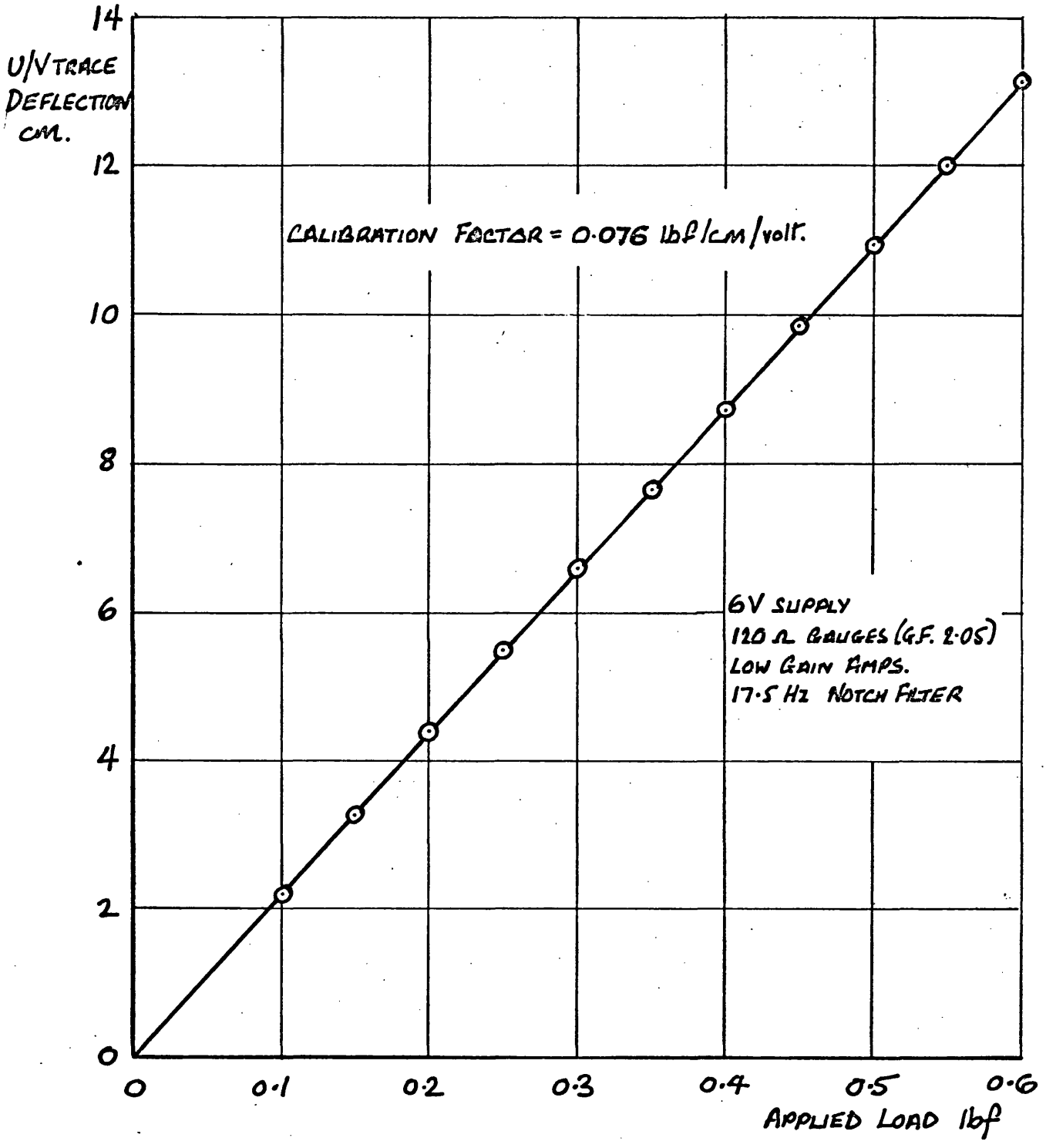

FIG. 3.03 CALIBRATION OF NORMAL FORCE BRIDGE OF STING No.2 FOR STEADY RESULTS AND PLUNGING RESULTS

FIG 3.04

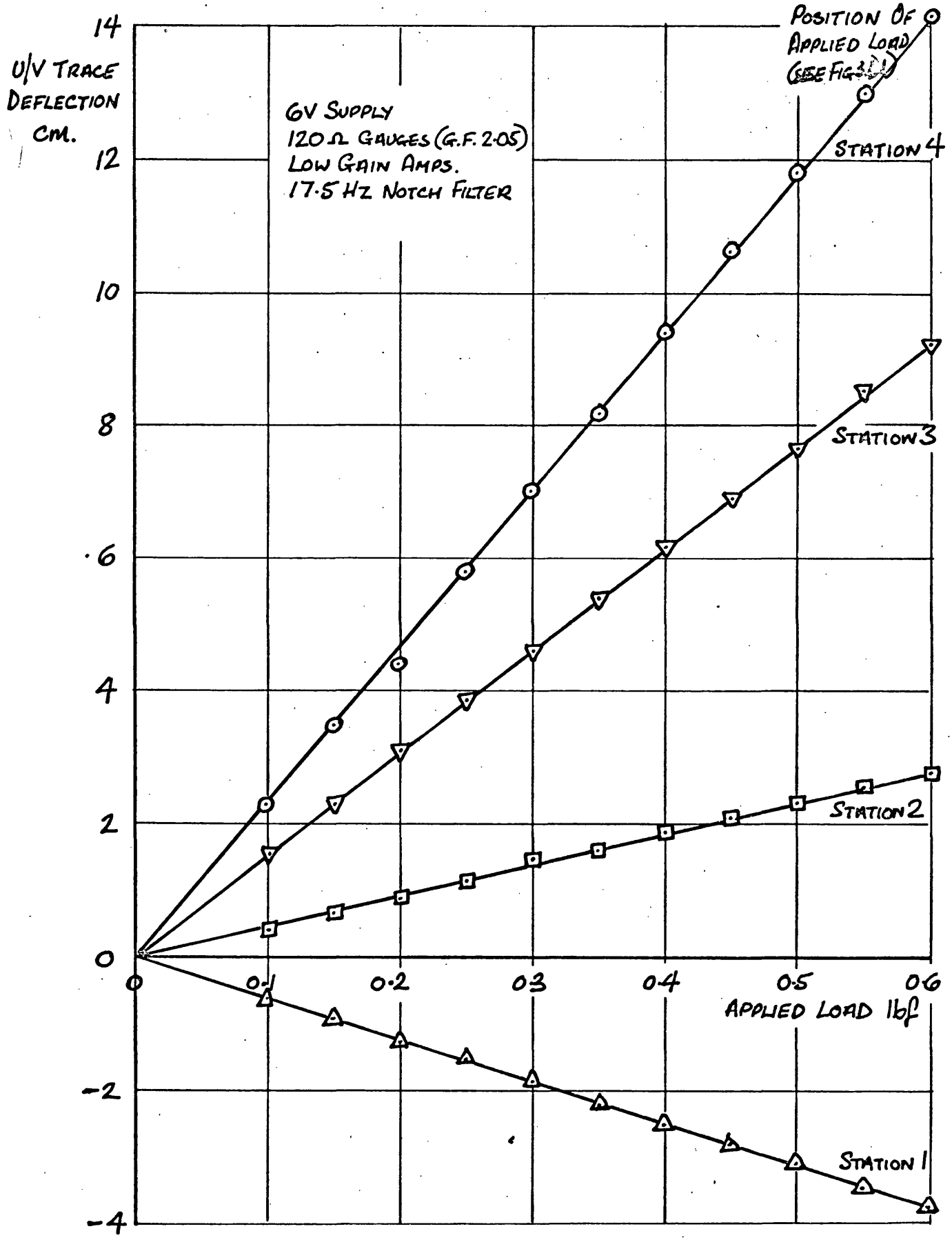

FIG 3.04 CALIBRATION OF PITCHING MOMENT BRIDGE OF STING NO.2 FOR STEADY RESULTS AND PLUNGING RESULTS

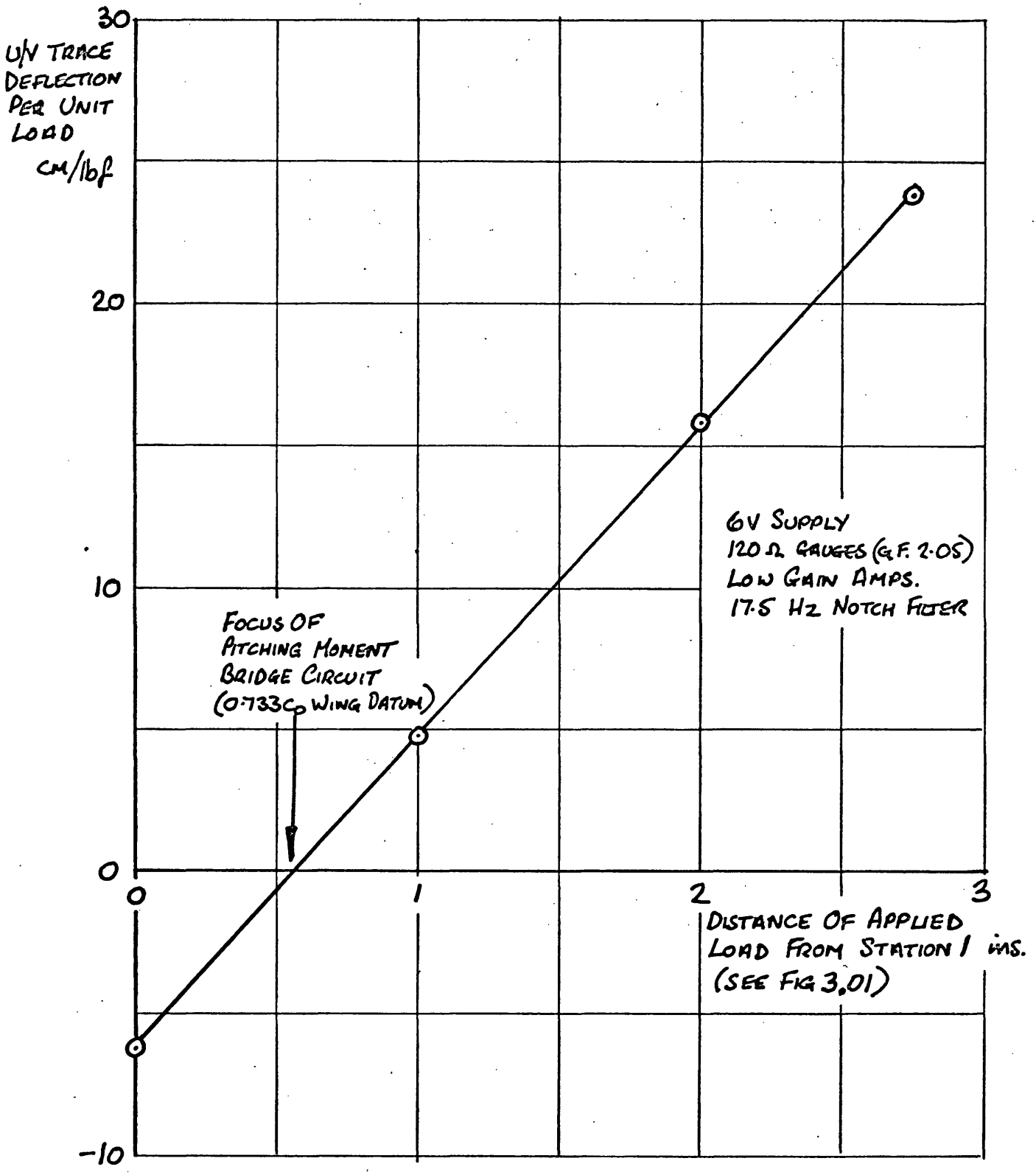

FIG 3.05 DETERMINATION OF FOCUS OF PITCHING MOMENT BRIDGE OF STING No. 2 FOR STEADY RESULTS AND PLUNGING RESULTS

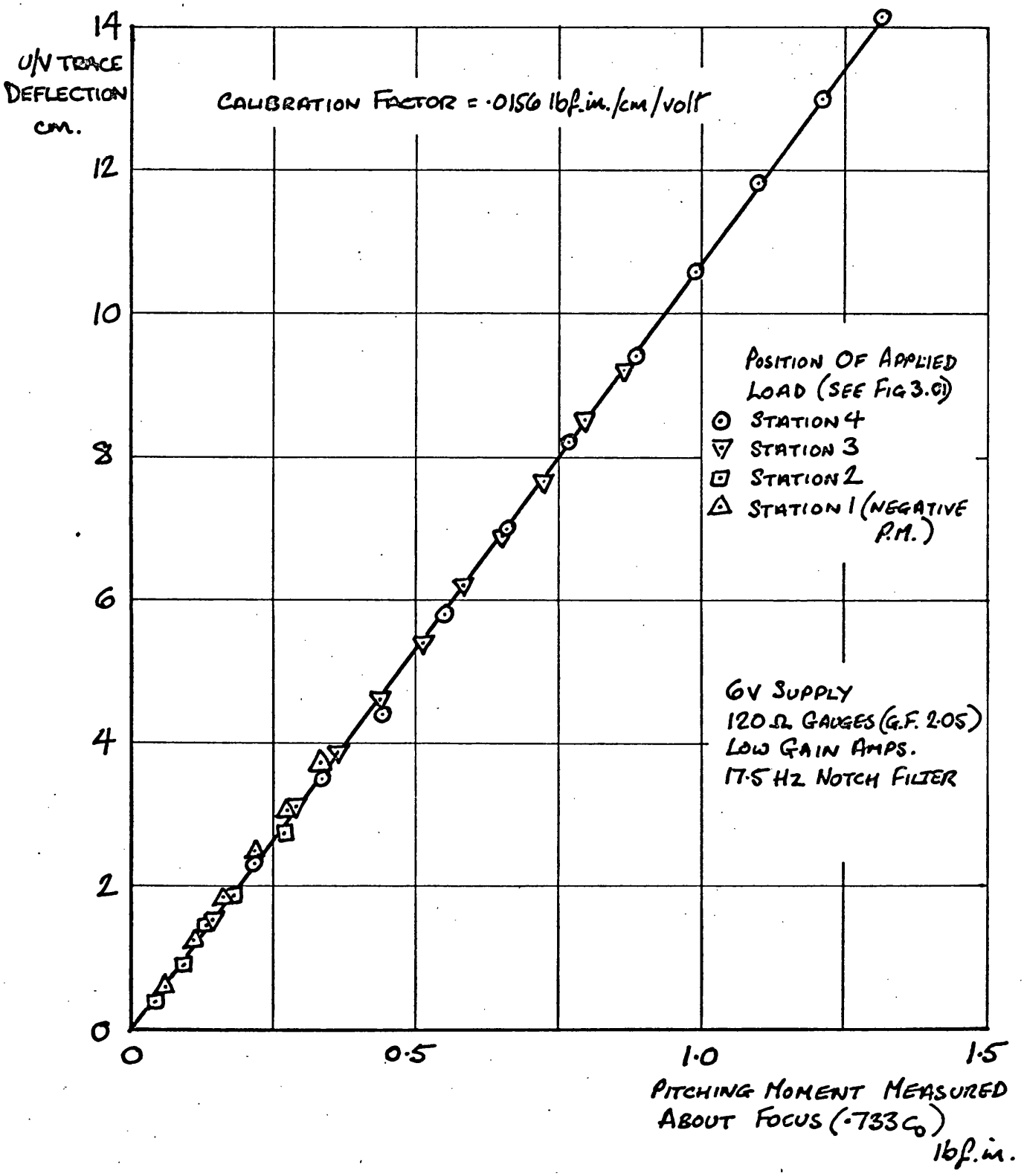

FIG 3.06 CALIBRATION OF PITCHING MOMENT BRIDGE OF STING No.2 FOR STEADY RESULTS AND PLUNGING RESULTS

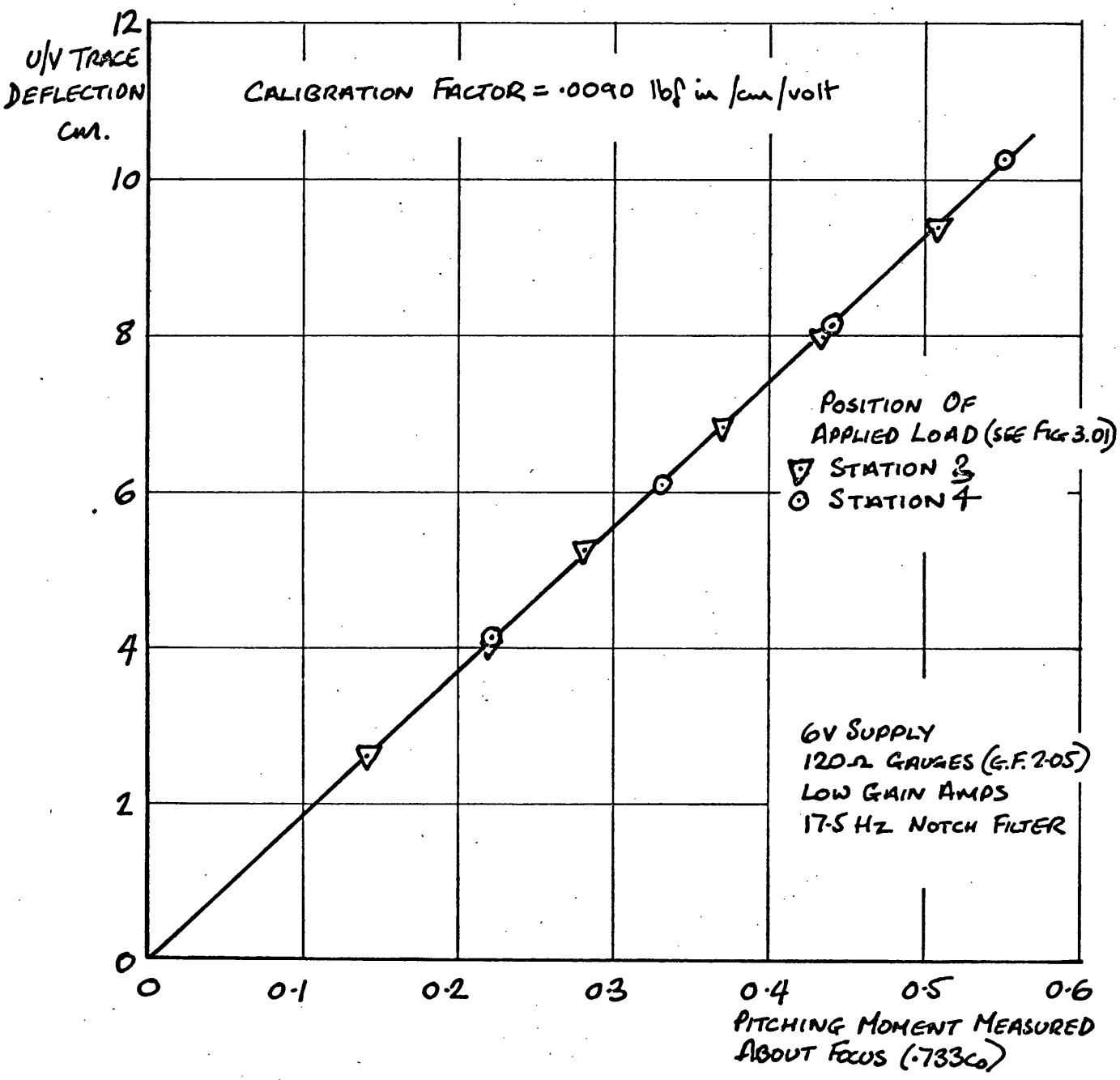

FIG 3.07 CALIBRATION OF PITCHING MOMENT BRIDGE OF STING NO2 WITH INCREASED SENSITIVITY FOR STEADY RESULTS AND PLUNGING RESULTS

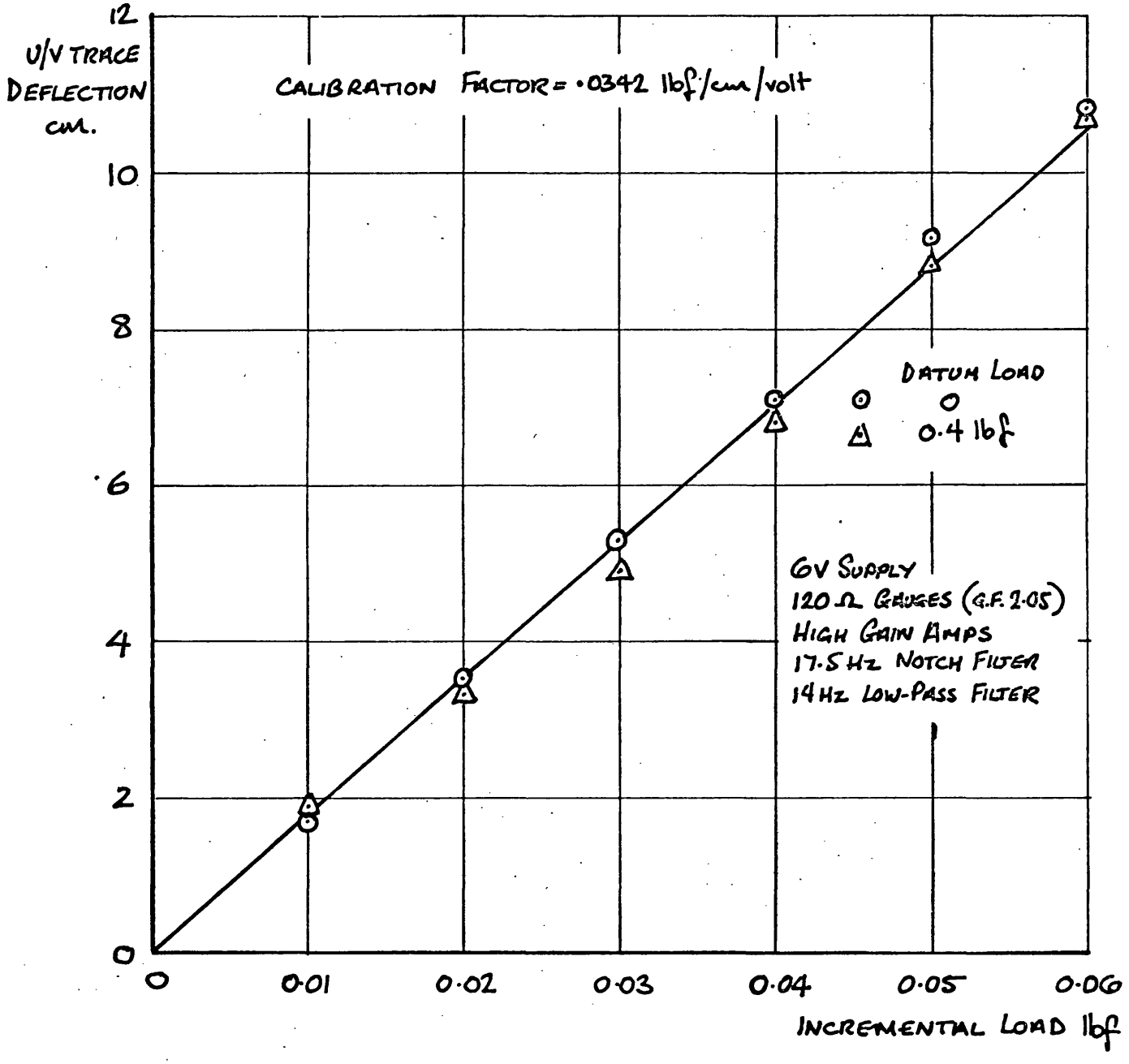

FIG 3.08 CALIBRATION OF NORMAL FORCE BRIDGE OF STING No.2 WITH HIGH GAIN AMPLIFIERS FOR CONSTANT q RESULTS

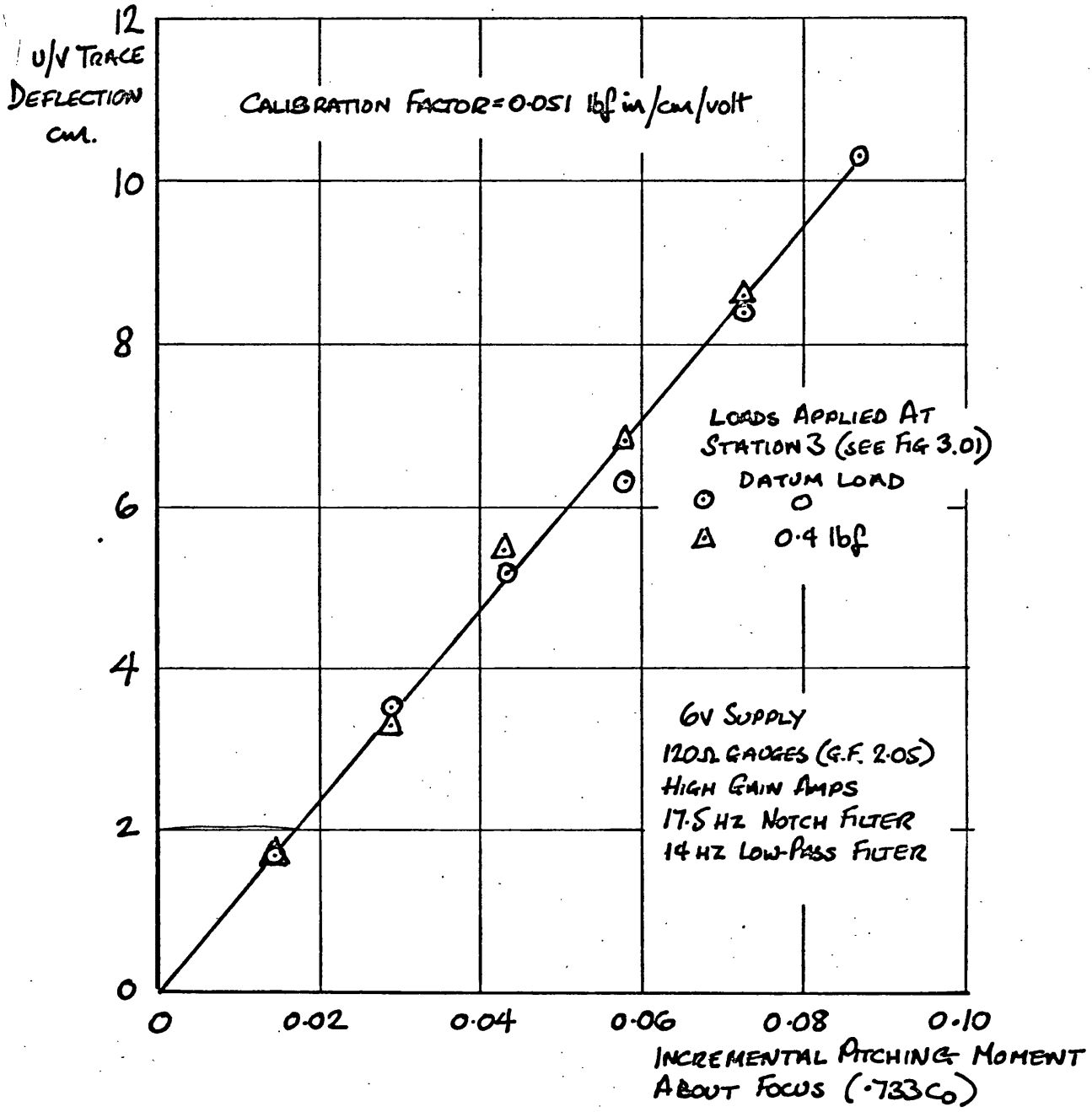

FIG 3.09 CALIBRATION OF PITCHING MOMENT BRIDGE OF STING NO 2. WITH HIGH GAIN AMPLIFIERS FOR CONSTANT q RESULTS

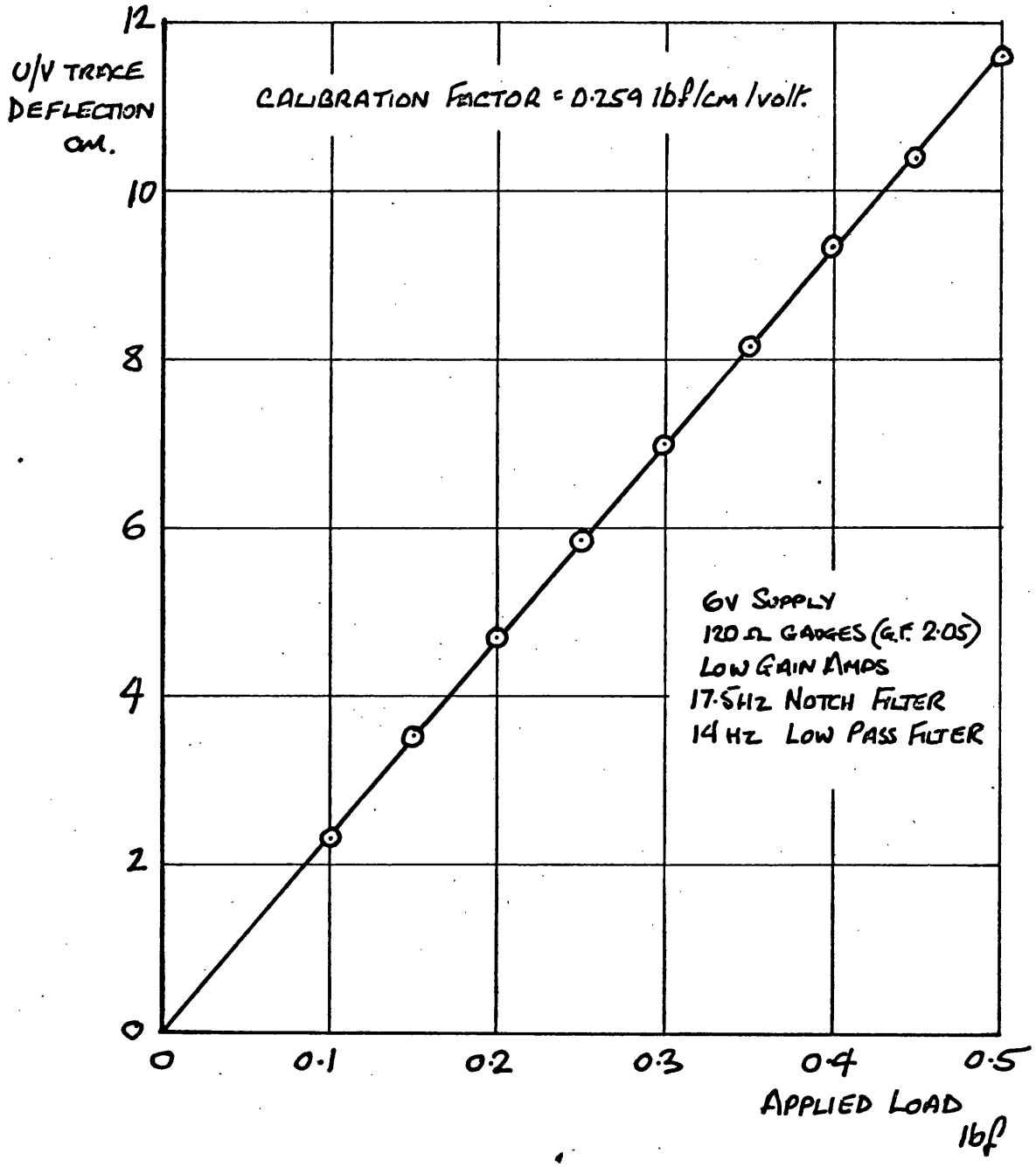

FIG. 3.10 CALIBRATION OF NORMAL FORCE BRIDGE OF STING NO.1 FOR PITCHING RESULTS

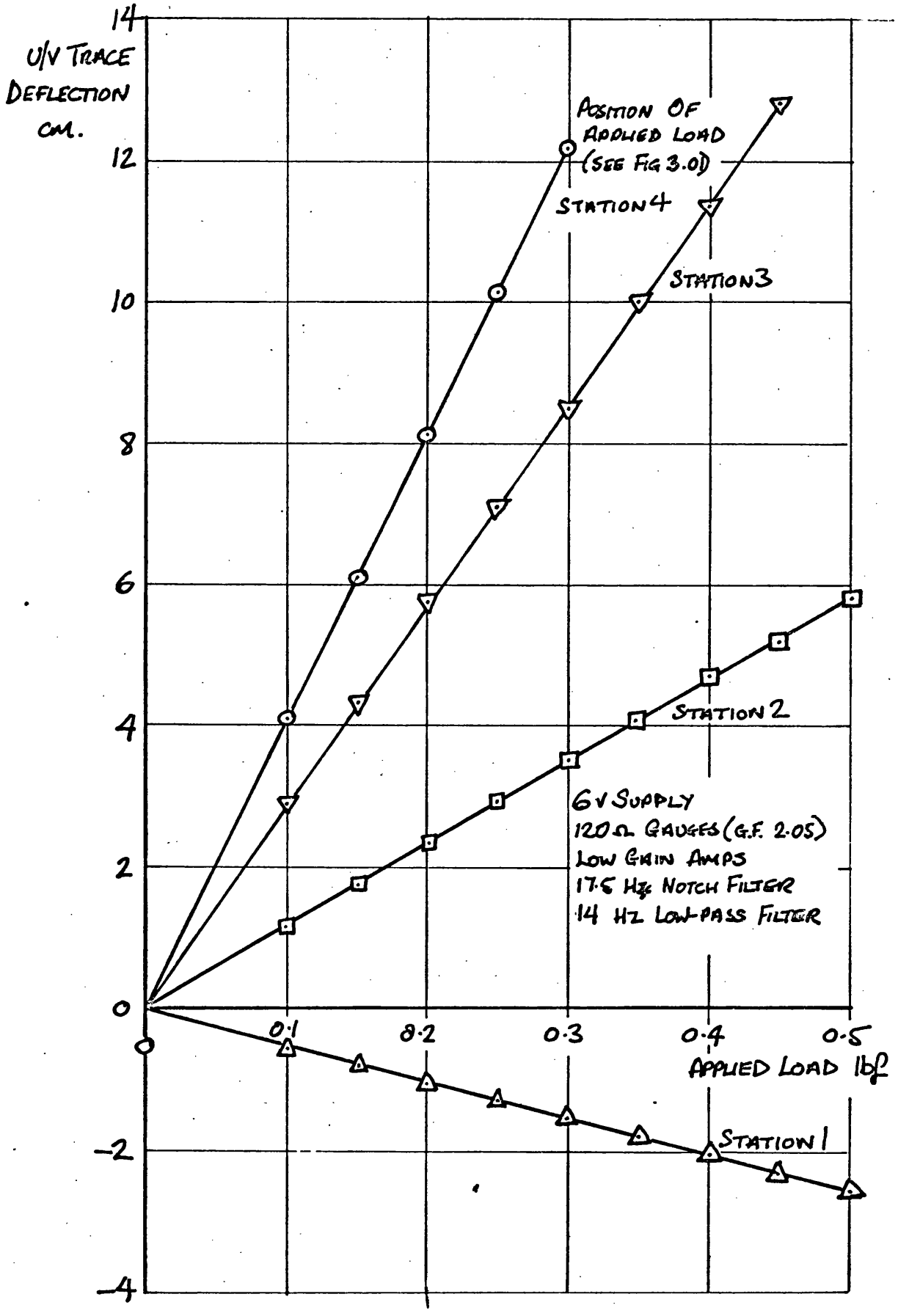

FIG 3.11 CALIBRATION OF PITCHING MOMENT BRIDGE OF STING No.1 FOR PITCHING RESULTS

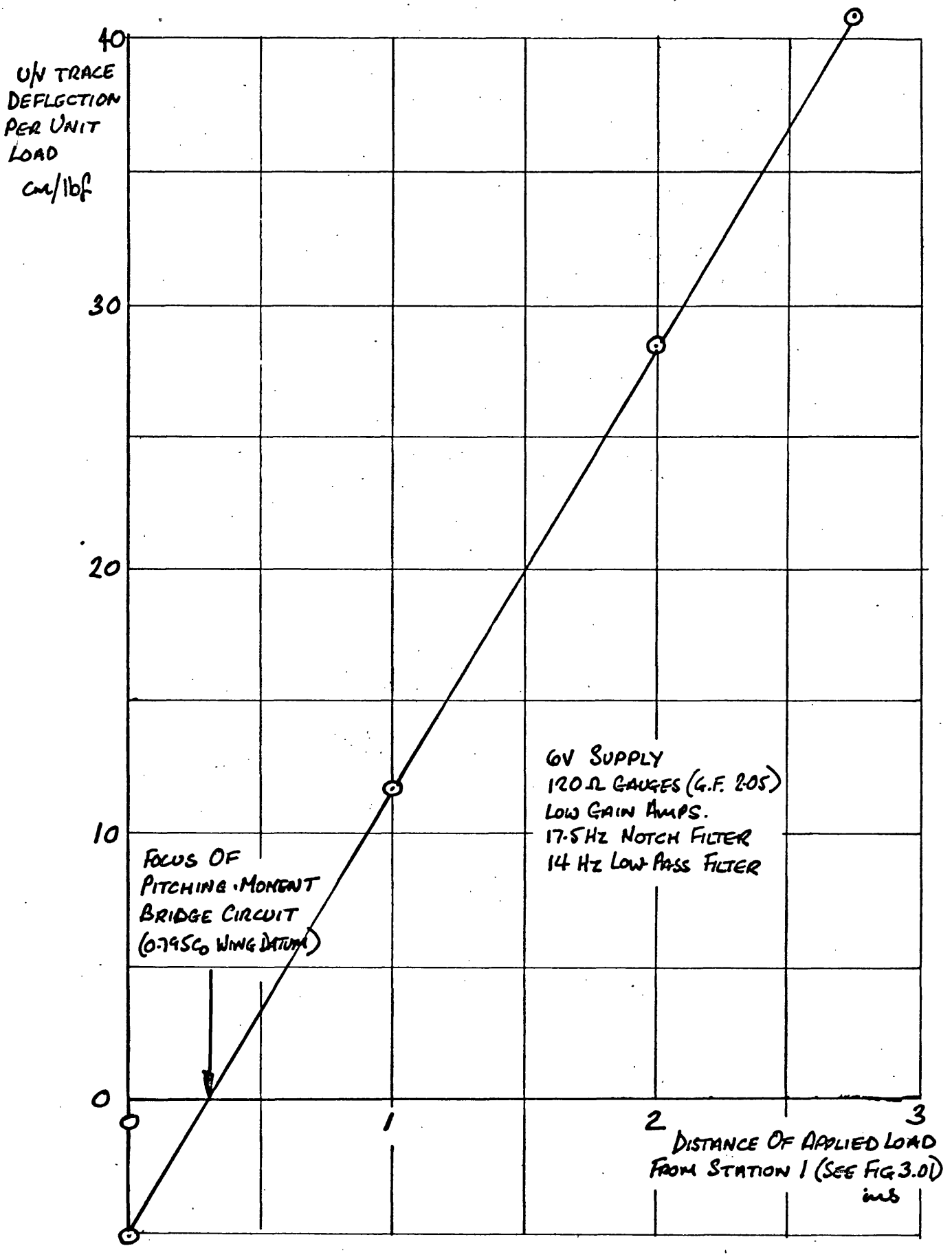

FIG. 3.12 DETERMINATION OF FOCUS OF PITCHING MOMENT BRIDGE OF STING NO. 1 FOR PITCHING RESULTS

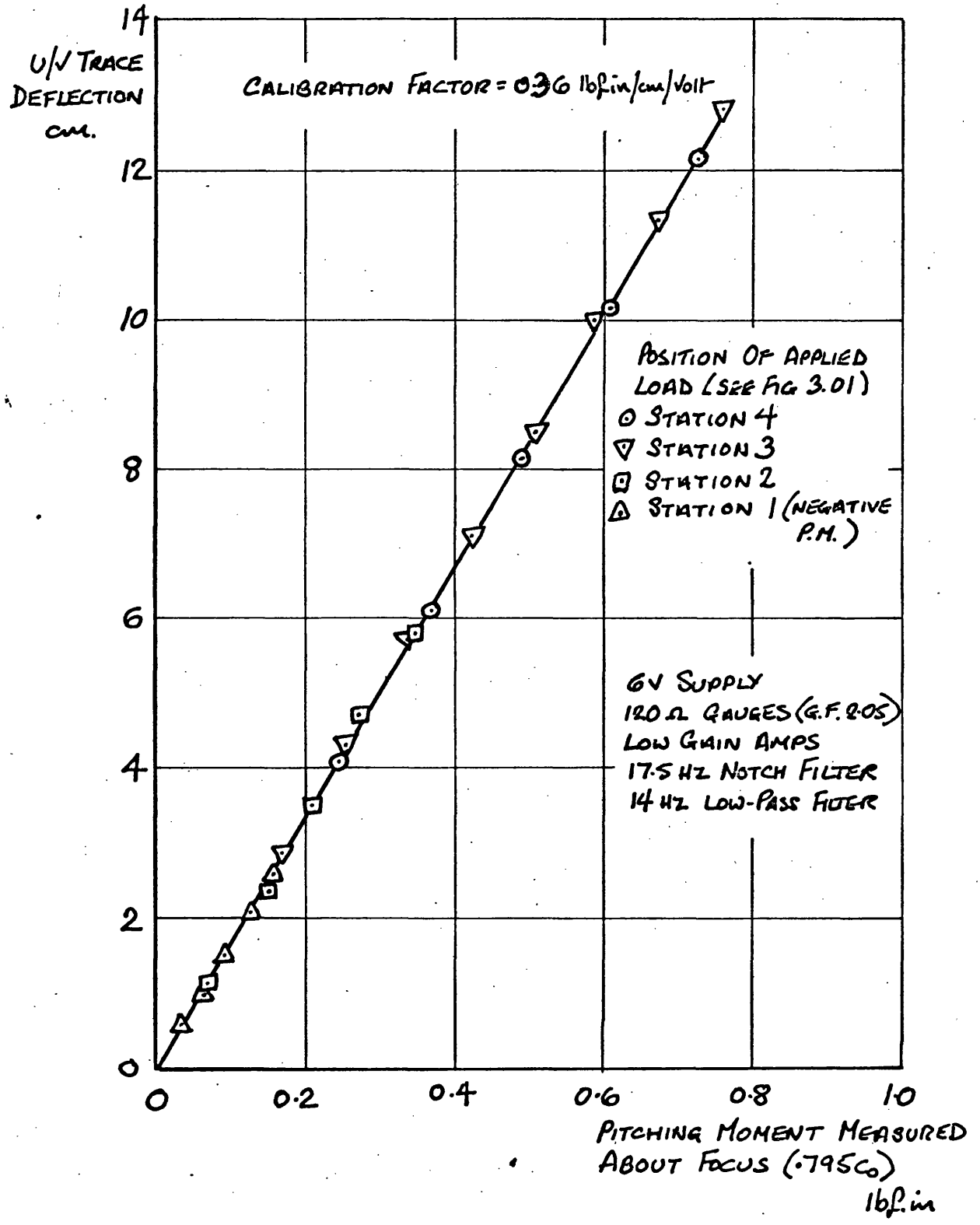

FIG 3.13 CALIBRATION OF PITCHING MOMENT BRIDGE OF STING NO.1 FOR PITCHING RESULTS

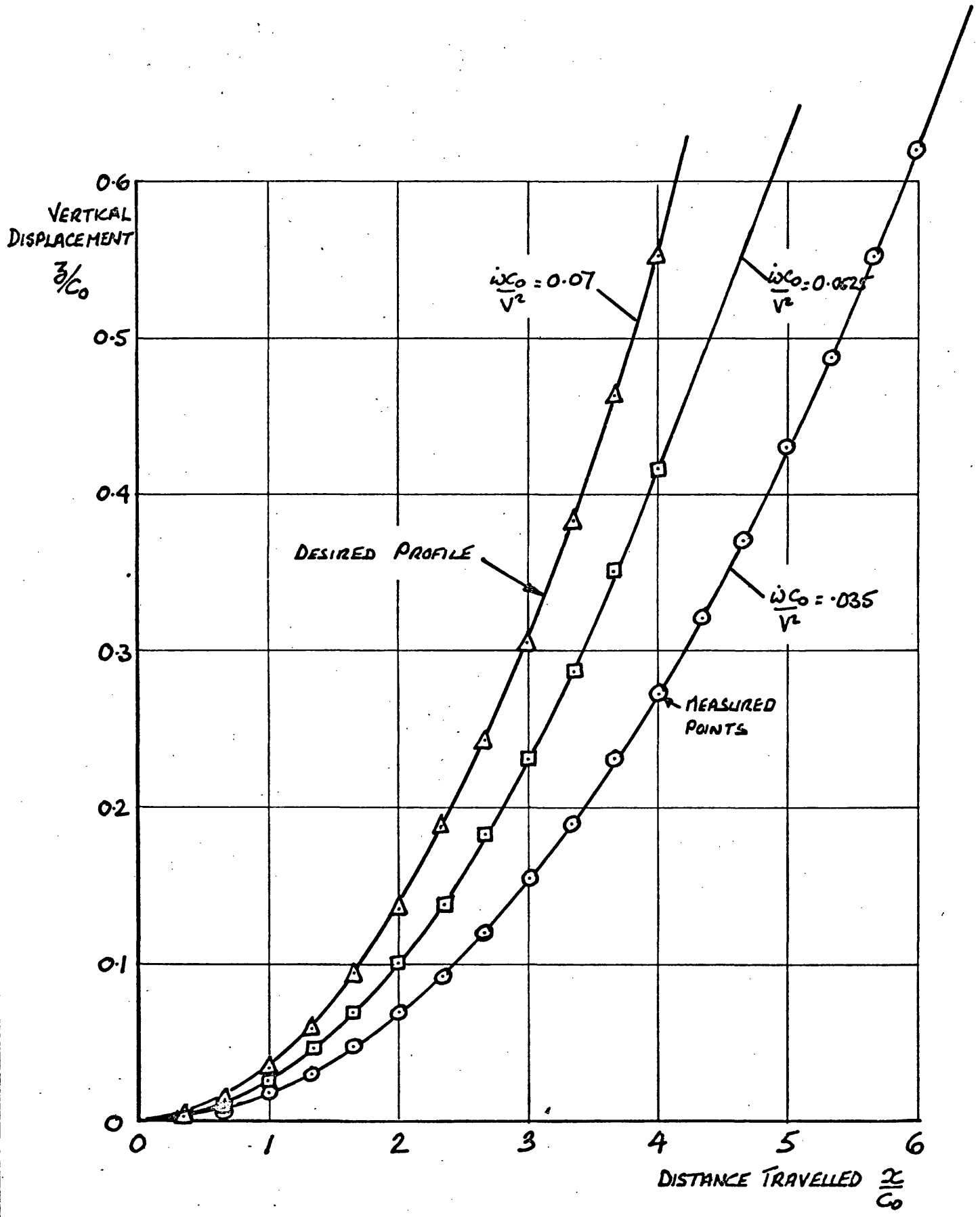

FIG 3.14 COMPARISON OF CAM RAIL PROFILE WITH DESIRED PROFILE FOR PLUNGING MANOEUVRE

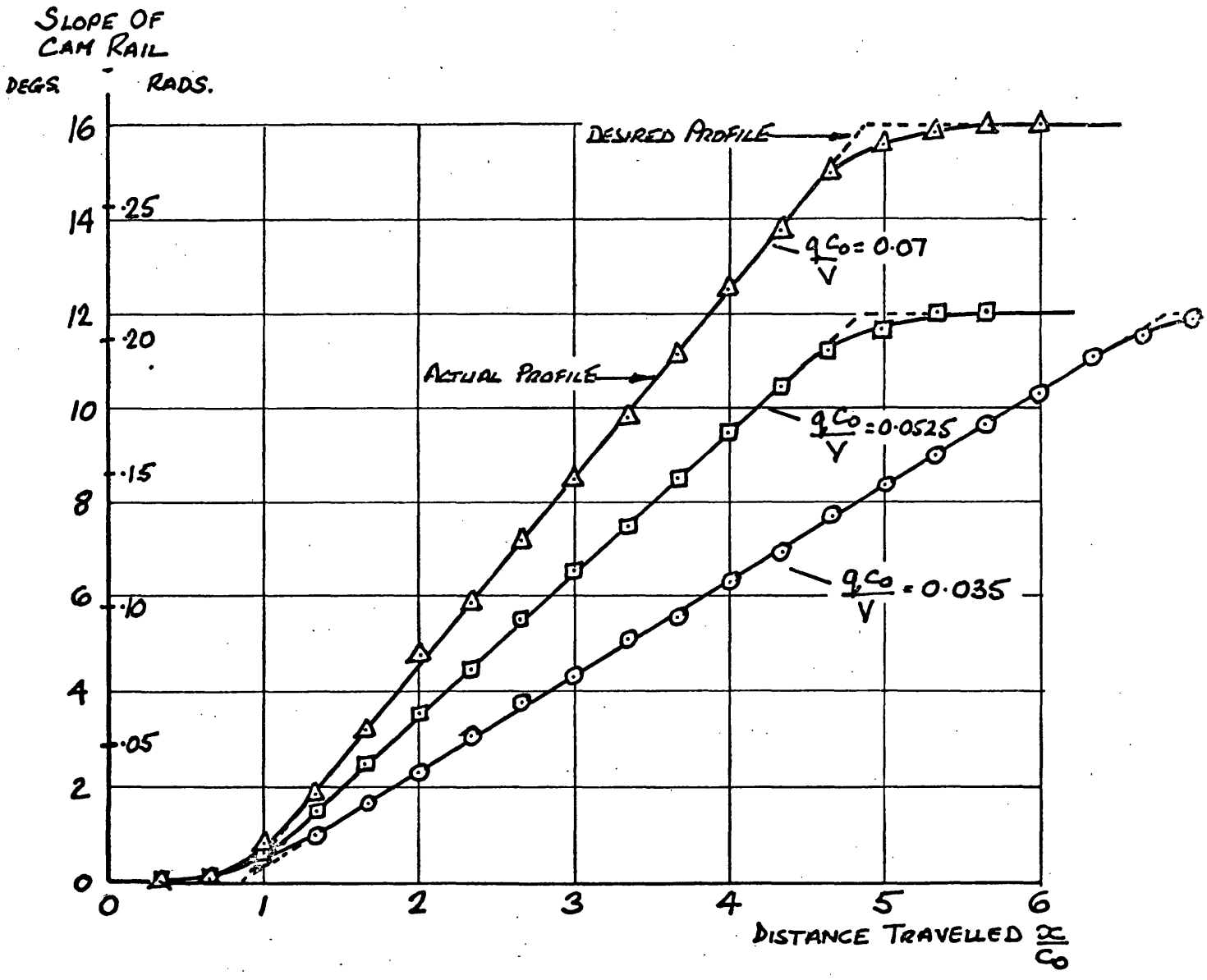

FIG 3.15 COMPARISON OF CAM RAIL PROFILE WITH DESIRED PROFILE FOR CONSTANT q MANOEUVRE

FIGS 3.16 & 3.17

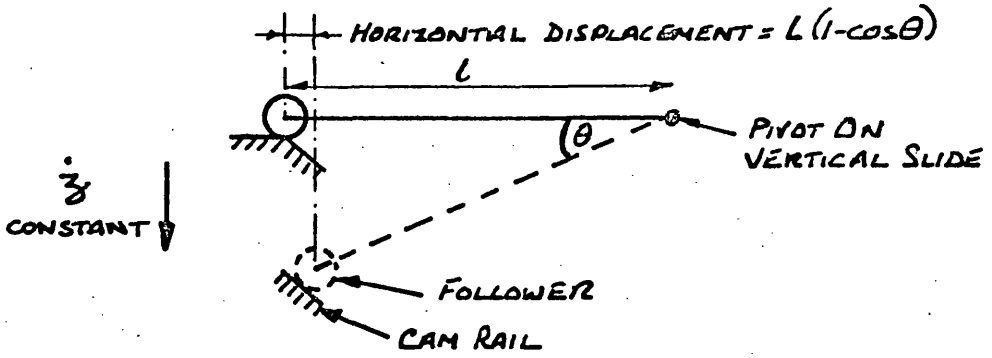

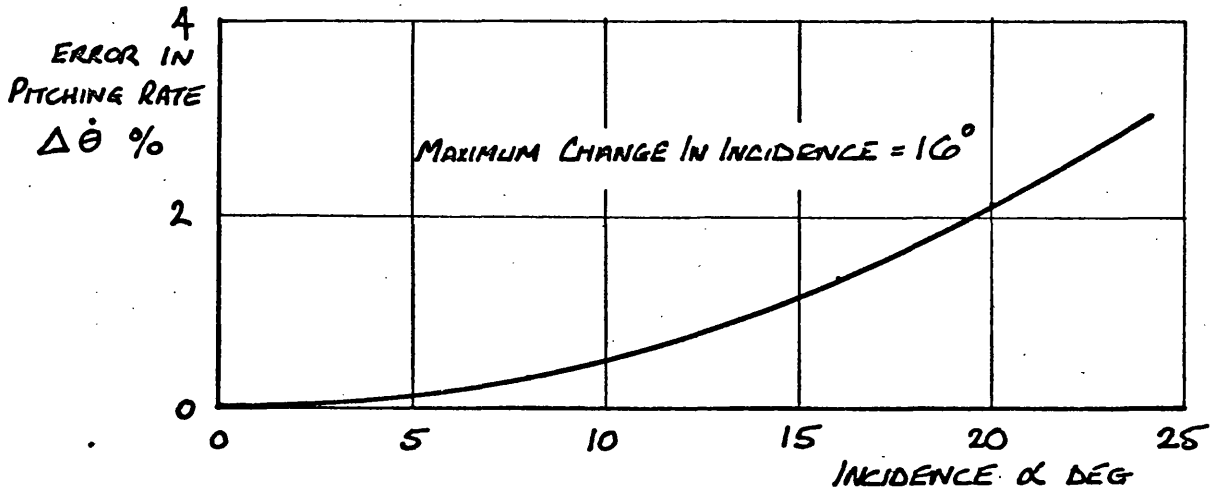

FIG 3.16 CORRECTION TO PITCHING RATE DUE TO USING A STRAIGHT RAMP CAM RAIL INSTEAD OF A SINE CURVE

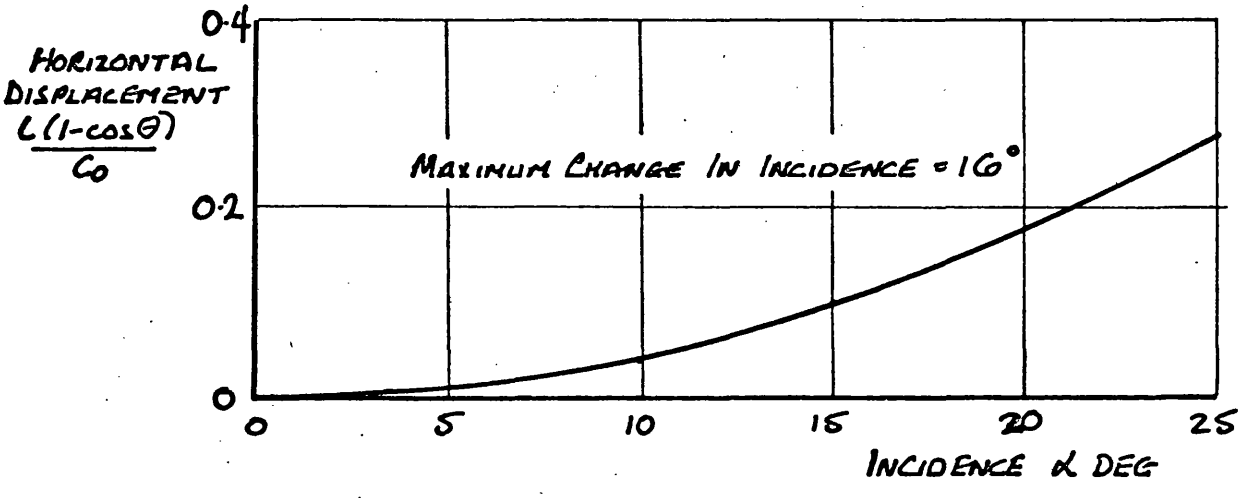

FIG 3.17 CORRECTION TO DISTANCE TRAVELLED DUE TO HORIZONTAL DISPLACEMENT OF FOLLOWER DURING ROTATION

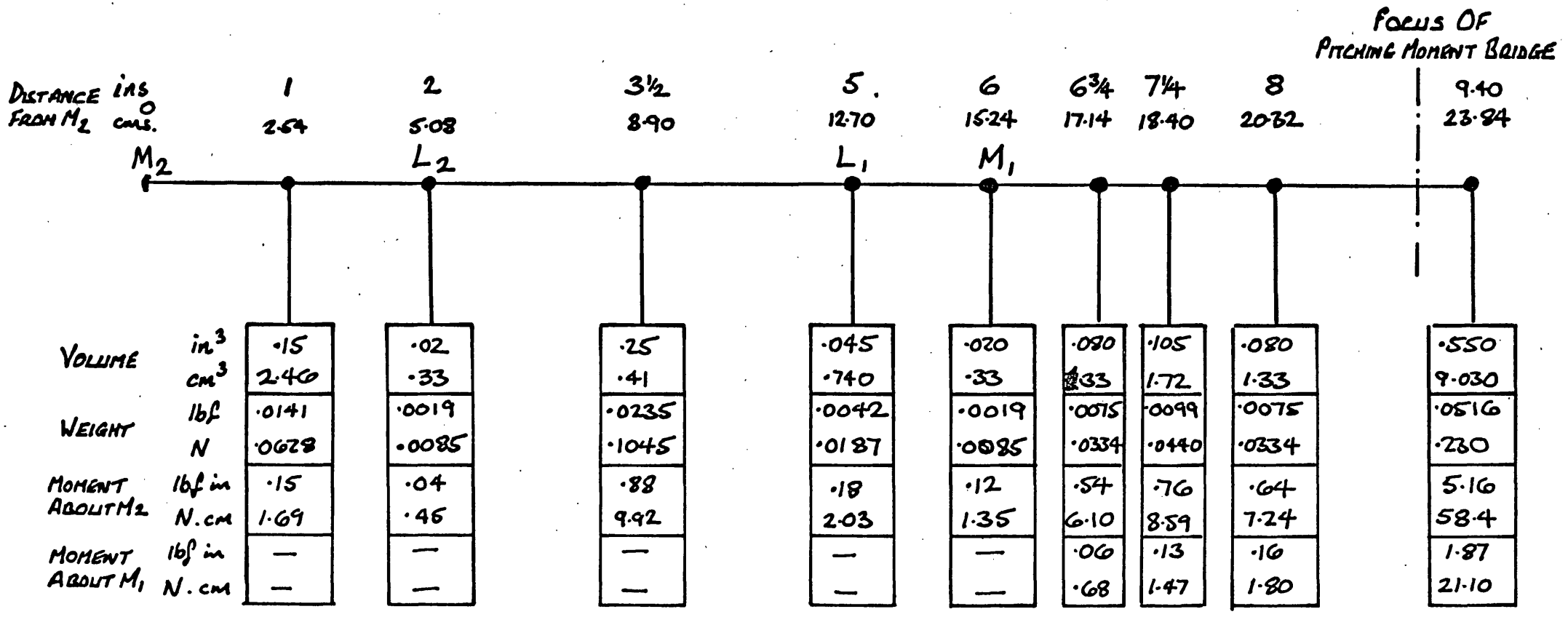

WEIGHT OF WING + STING IN AIR = ·098 lbf (·436N)
C.G. OF WING + STING = 6·4 ins (16·3cm) FROM M2
MOMENT ABOUT PITCHING MOMENT FOCUS (·733c_0) = −·0525 lbf.in. (·593 N.cm)

FIG. 3.18 CALCULATION OF WEIGHT, C.G AND MOMENT OF MODEL WING AND STING TO FIND THEIR EFFECT ON MEASURED NORMAL FORCE AND PITCHING MOMENT

FIG 3.18

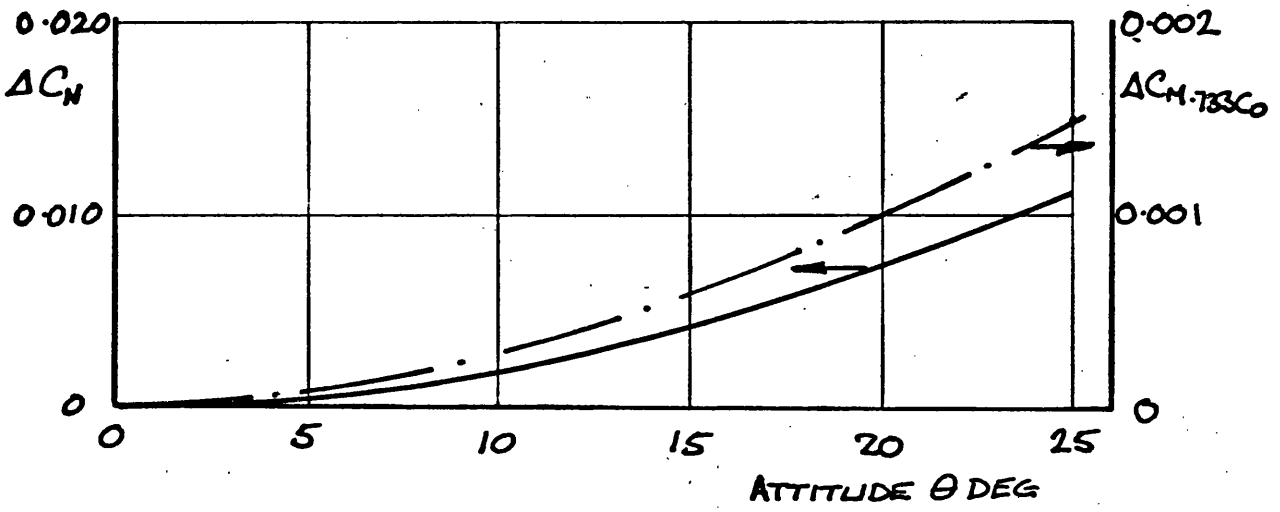

FIG 3.19 CORRECTION TO NORMAL FORCE AND PITCHING MOMENT DUE TO CHANGE IN ATTITUDE OF WING AND STING IN WATER ALLOWING FOR BUOYANCY

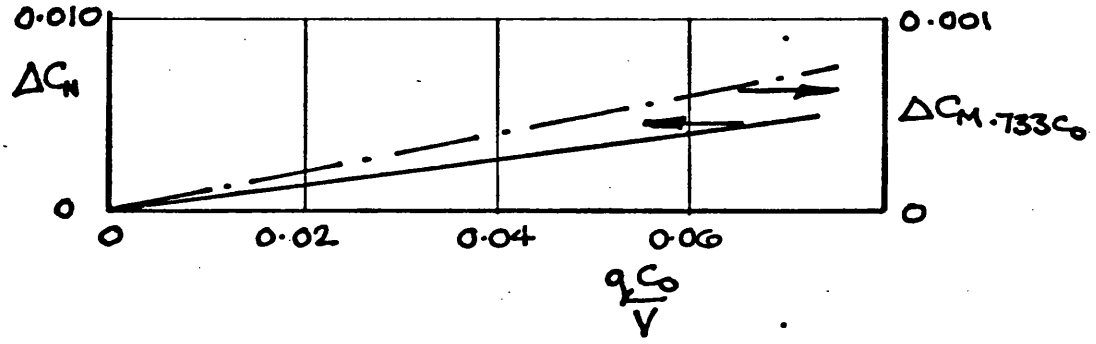

FIG 3.20 CORRECTION TO NORMAL FORCE AND PITCHING MOMENT DUE TO INERTIA OF WING AND STING IN WATER ALLOWING FOR BUOYANCY

FIGS 3.21
& 3.22

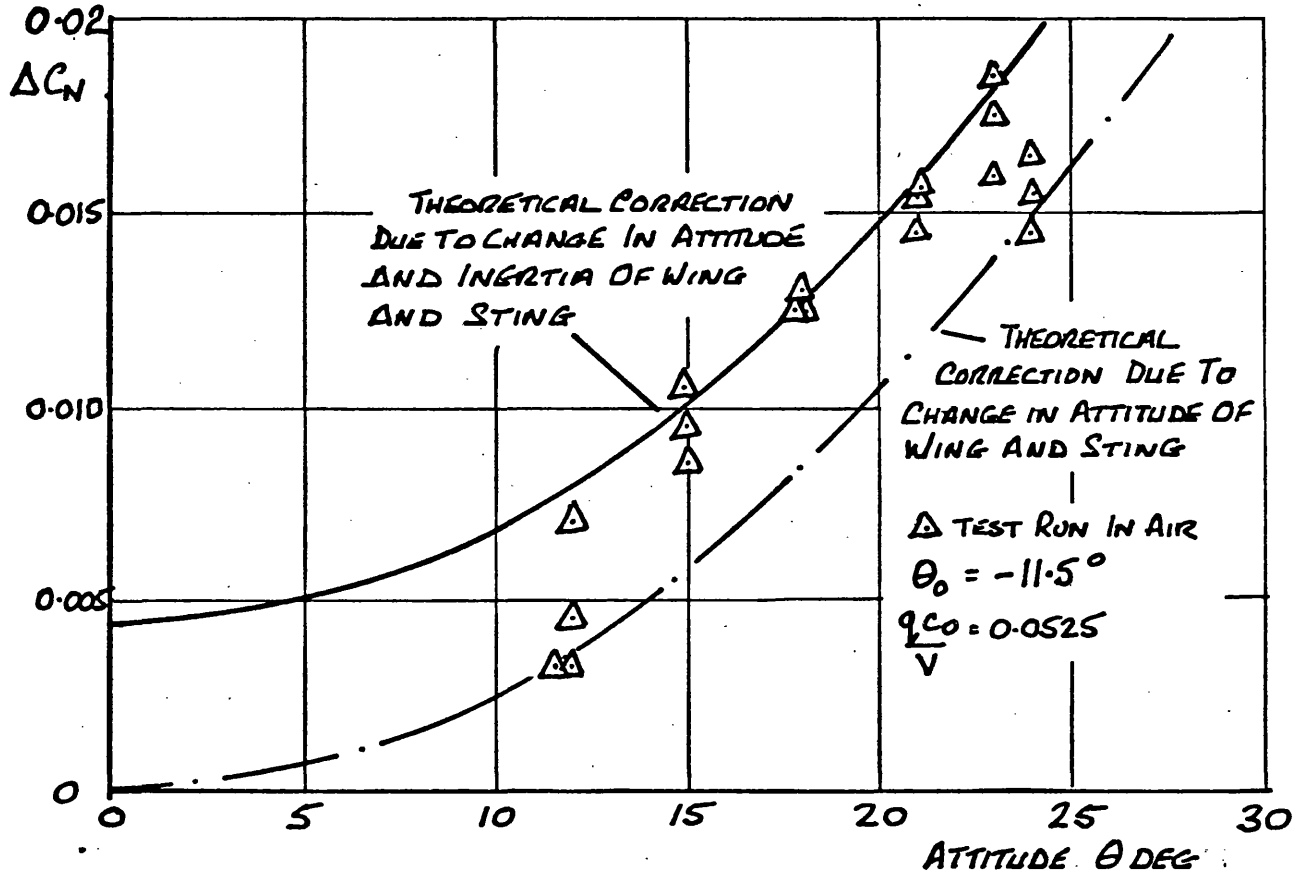

FIG 3.21 CORRECTION DUE TO CHANGE IN ATTITUDE AND INERTIA OF WING AND STING

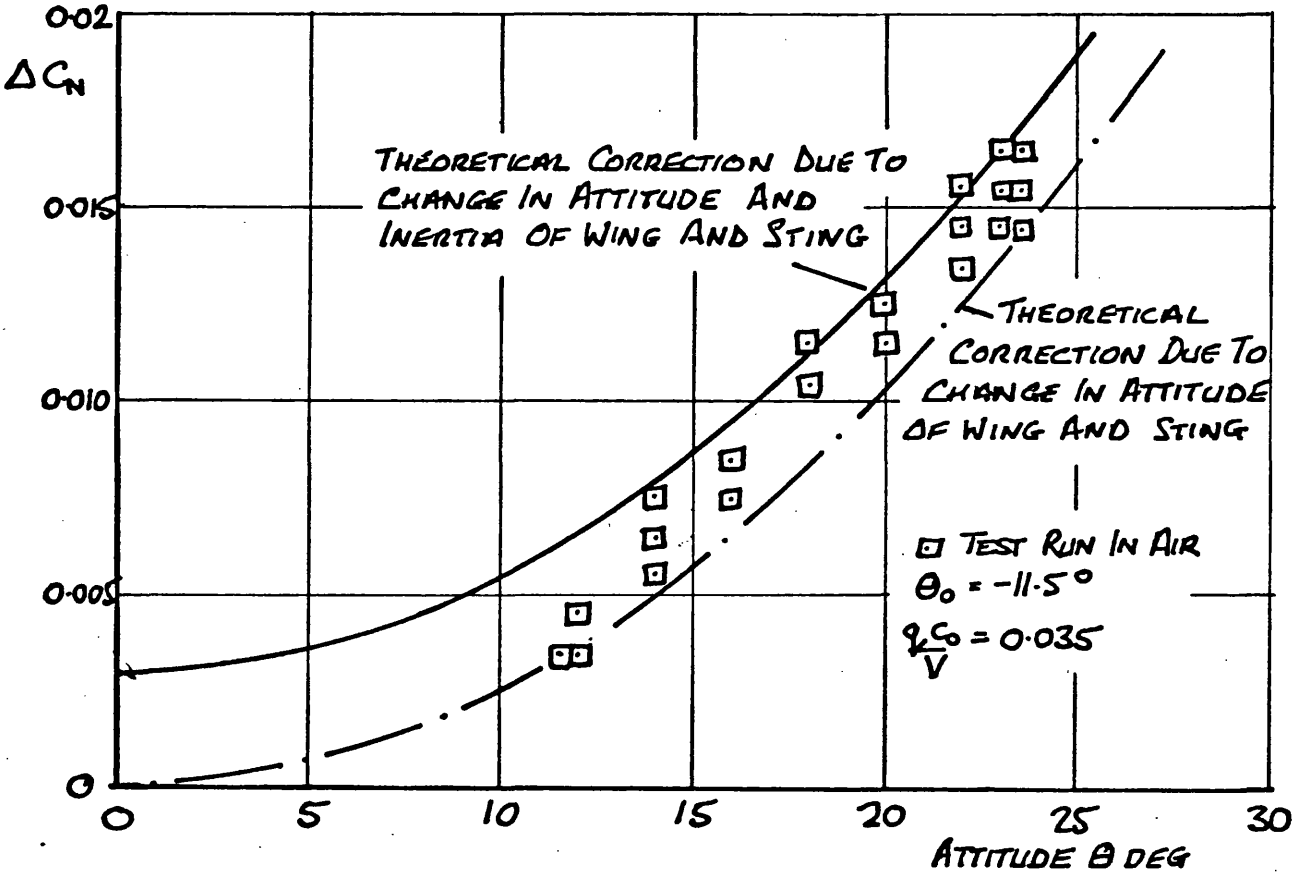

FIG 3.22 CORRECTION TO NORMAL FORCE DUE TO CHANGE IN ATTITUDE AND INERTIA OF WING AND STING

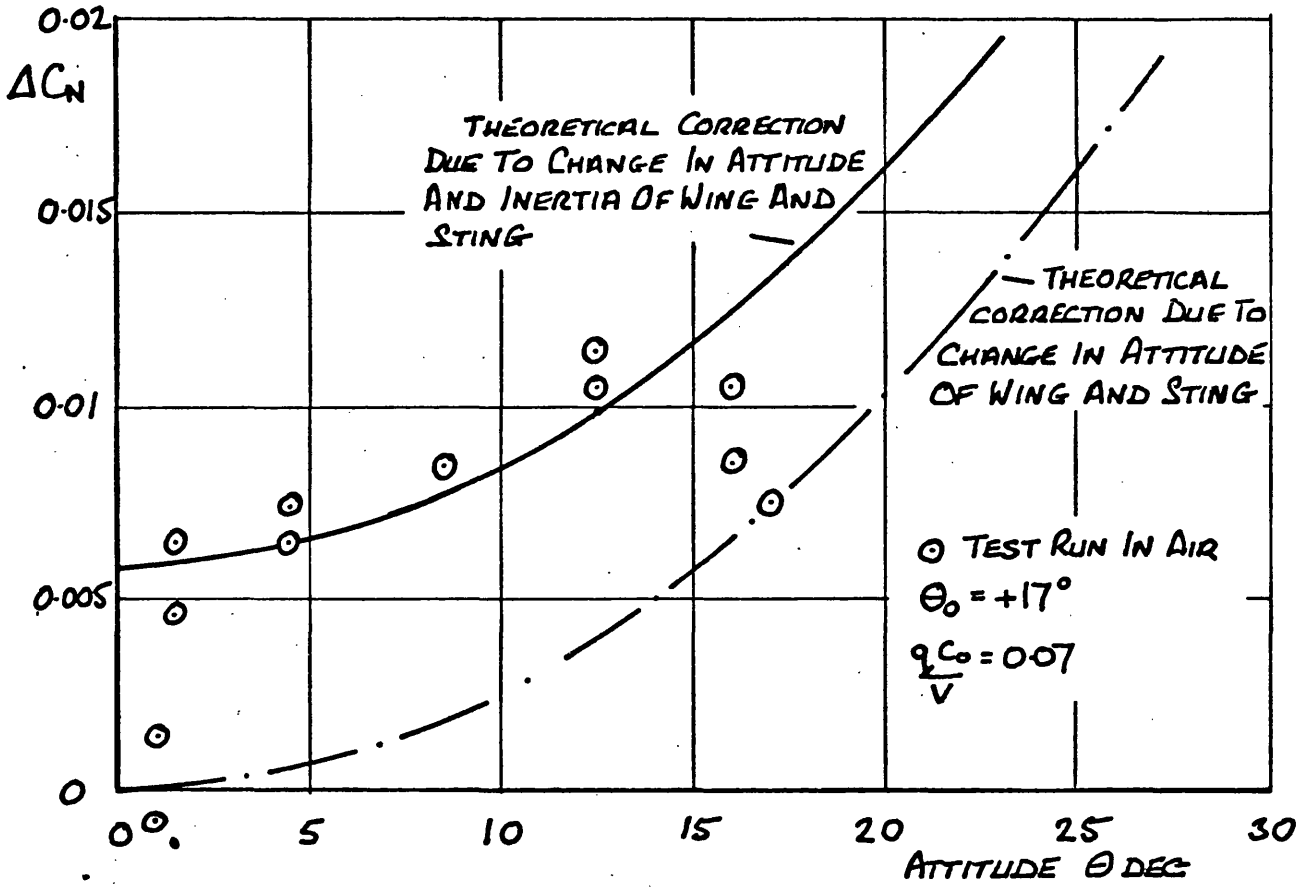

FIG 3.23 CORRECTION TO NORMAL FORCE DUE TO CHANGE IN ATTITUDE AND INERTIA OF WING AND STING

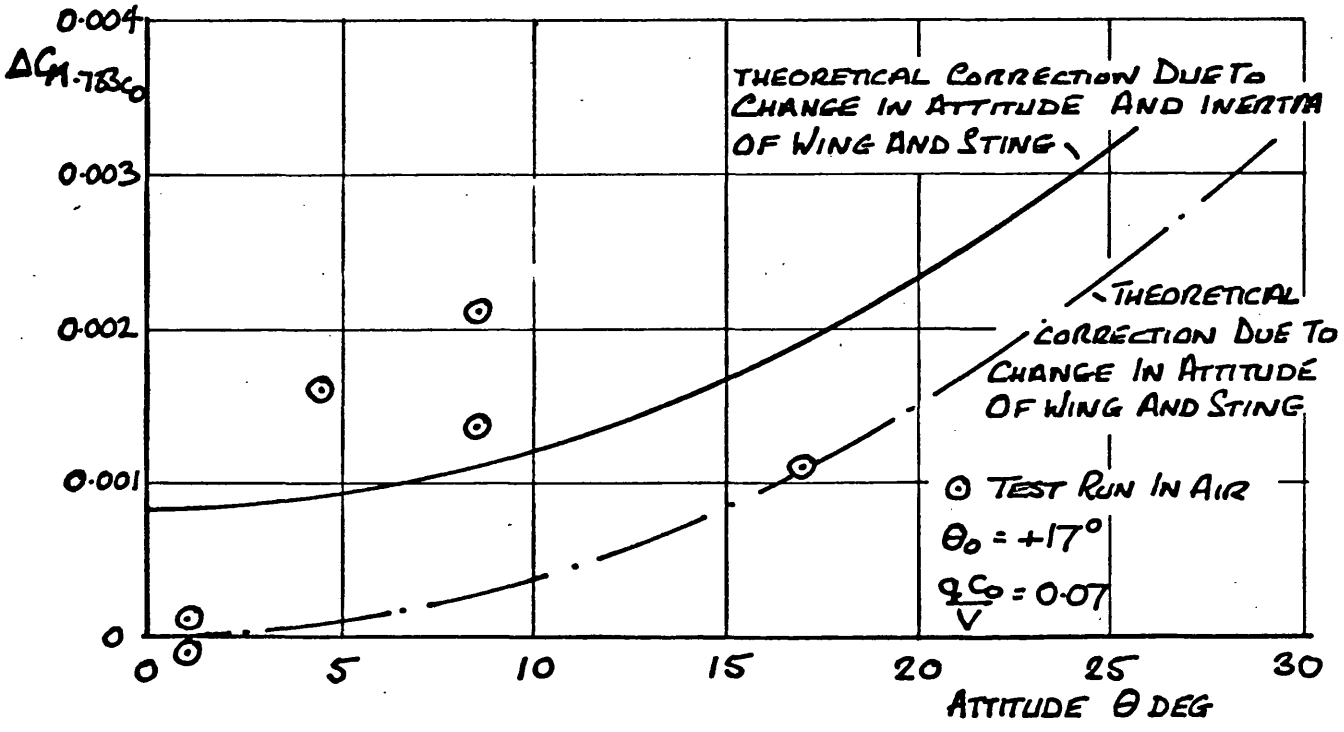

FIG 3.24 CORRECTION TO PITCHING MOMENT DUE TO CHANGE IN ATTITUDE AND INERTIA OF WING AND STING

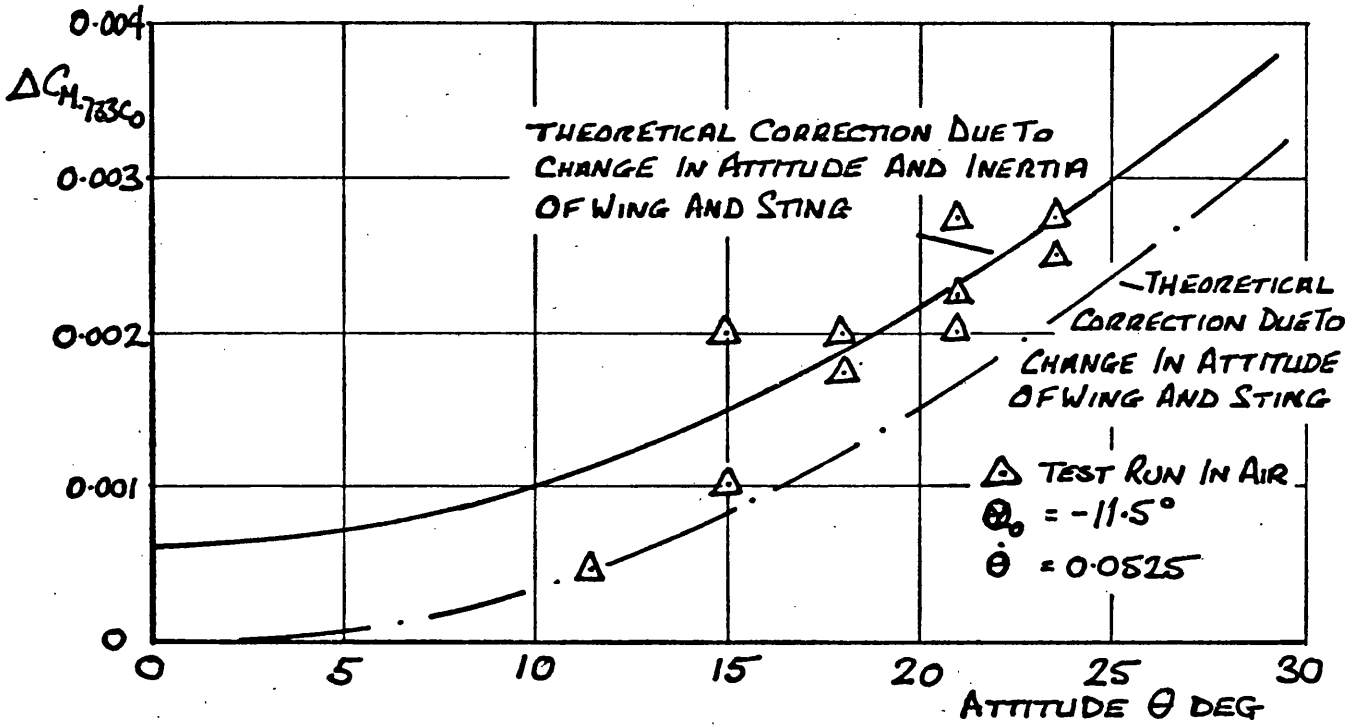

FIG 3.25 CORRECTION TO PITCHING MOMENT DUE TO CHANGE IN ATTITUDE AND INERTIA OF WING AND STING

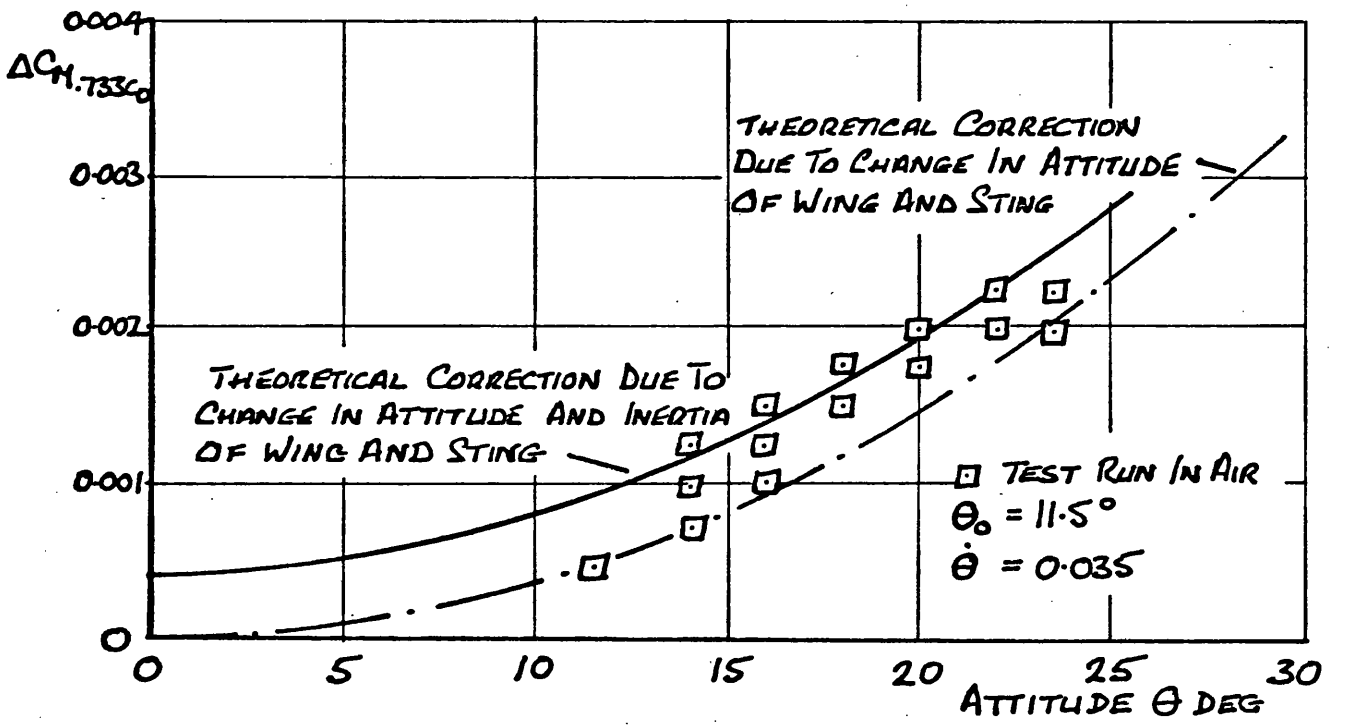

FIG 3.26 CORRECTION TO PITCHING MOMENT DUE TO CHANGE IN ATTITUDE AND INERTIA OF WING AND STING

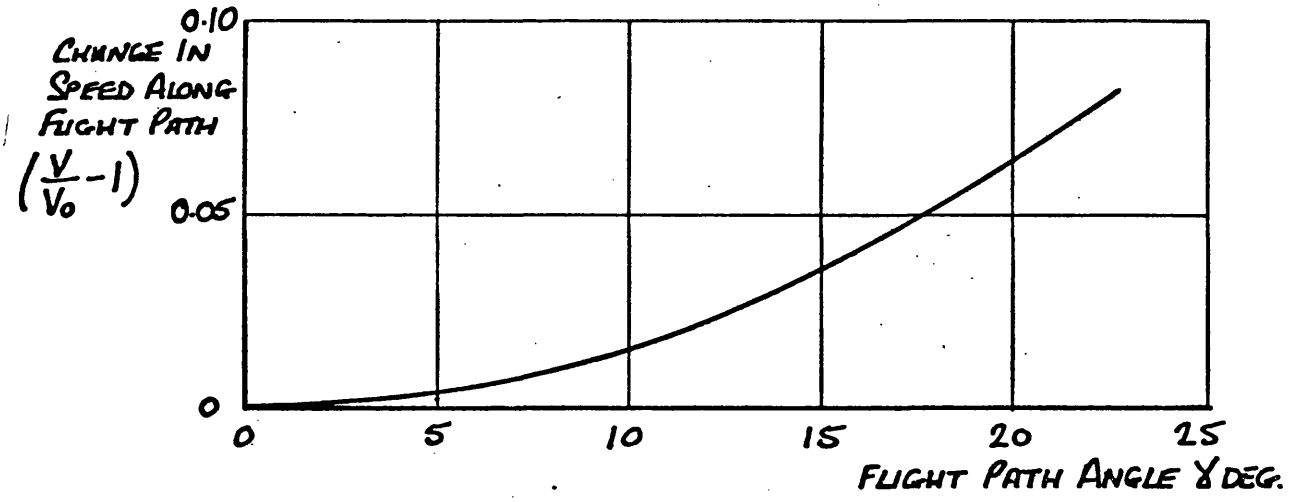

FIG 3.27 CORRECTION FOR CHANGE IN SPEED ALONG FLIGHT PATH DURING PLUNGING AND CONSTANT q MANOEUVRES

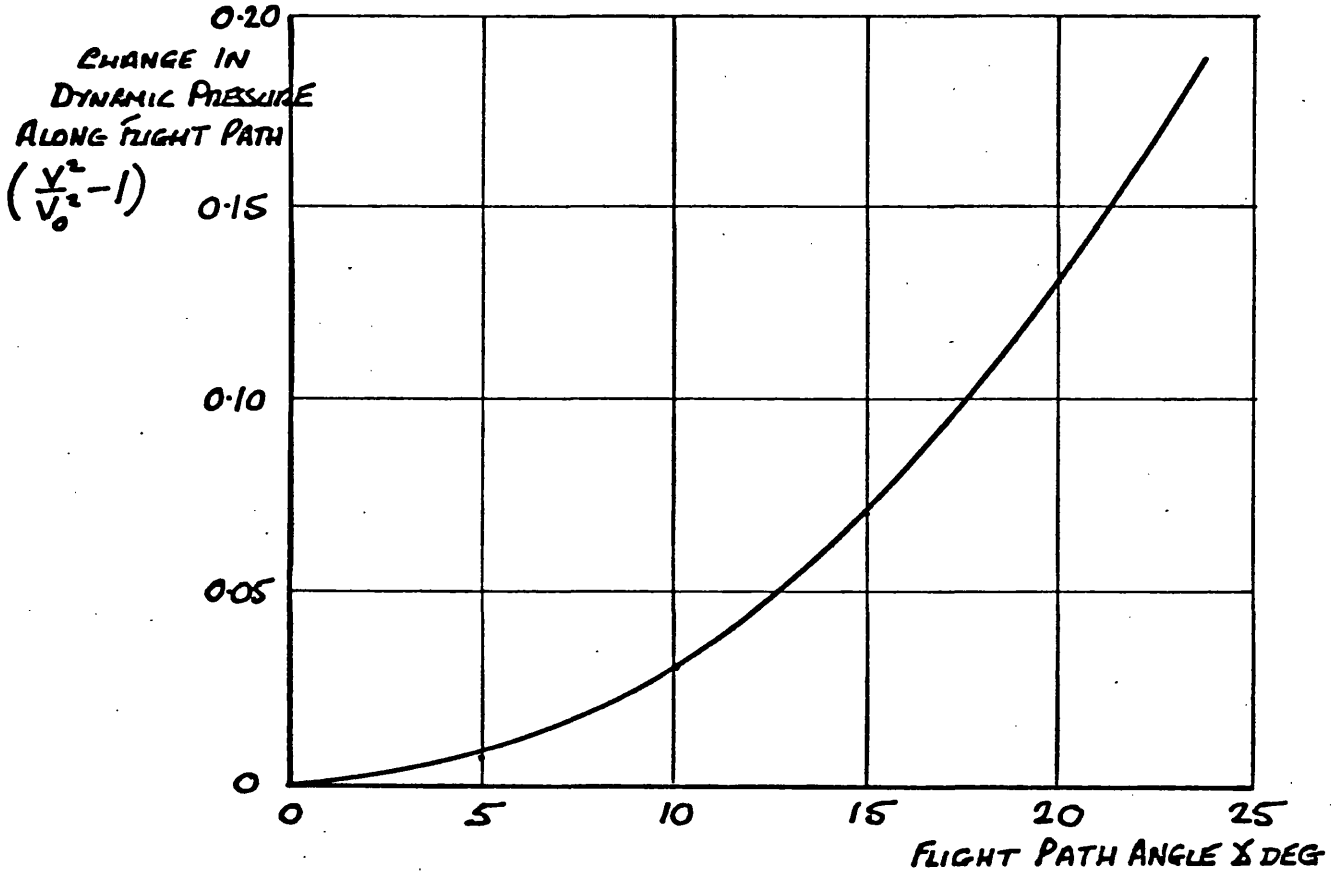

FIG 3.28 CORRECTION FOR CHANGE IN DYNAMIC PRESSURE ALONG FLIGHT PATH DURING PLUNGING AND CONSTANT q MANOEUVRES

FIGS 3.29
& 3.30

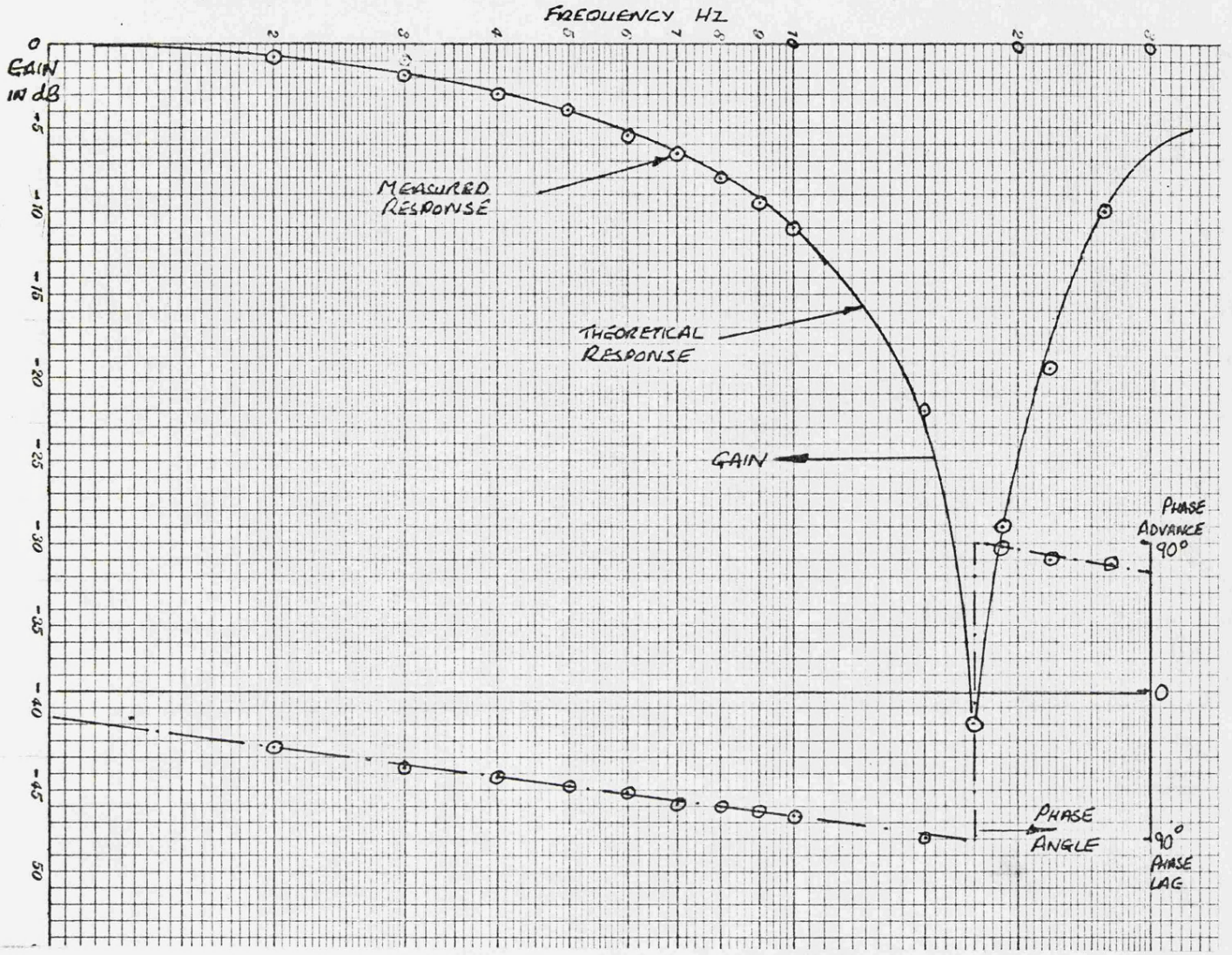

FIG 3.29 FREQUENCY RESPONSE OF 17.5 Hz NOTCH FILTER

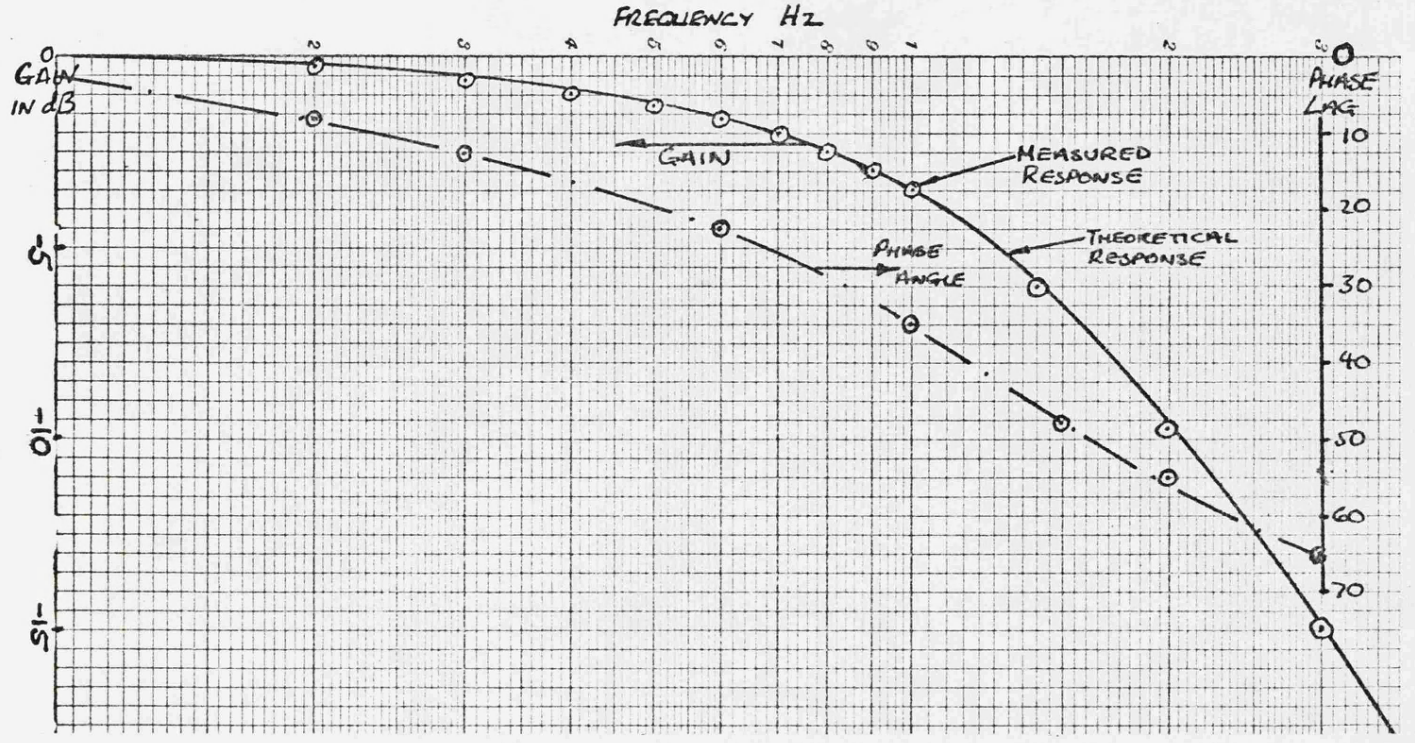

FIG 3.30 FREQUENCY RESPONSE OF 14 Hz LOW-PASS FILTER

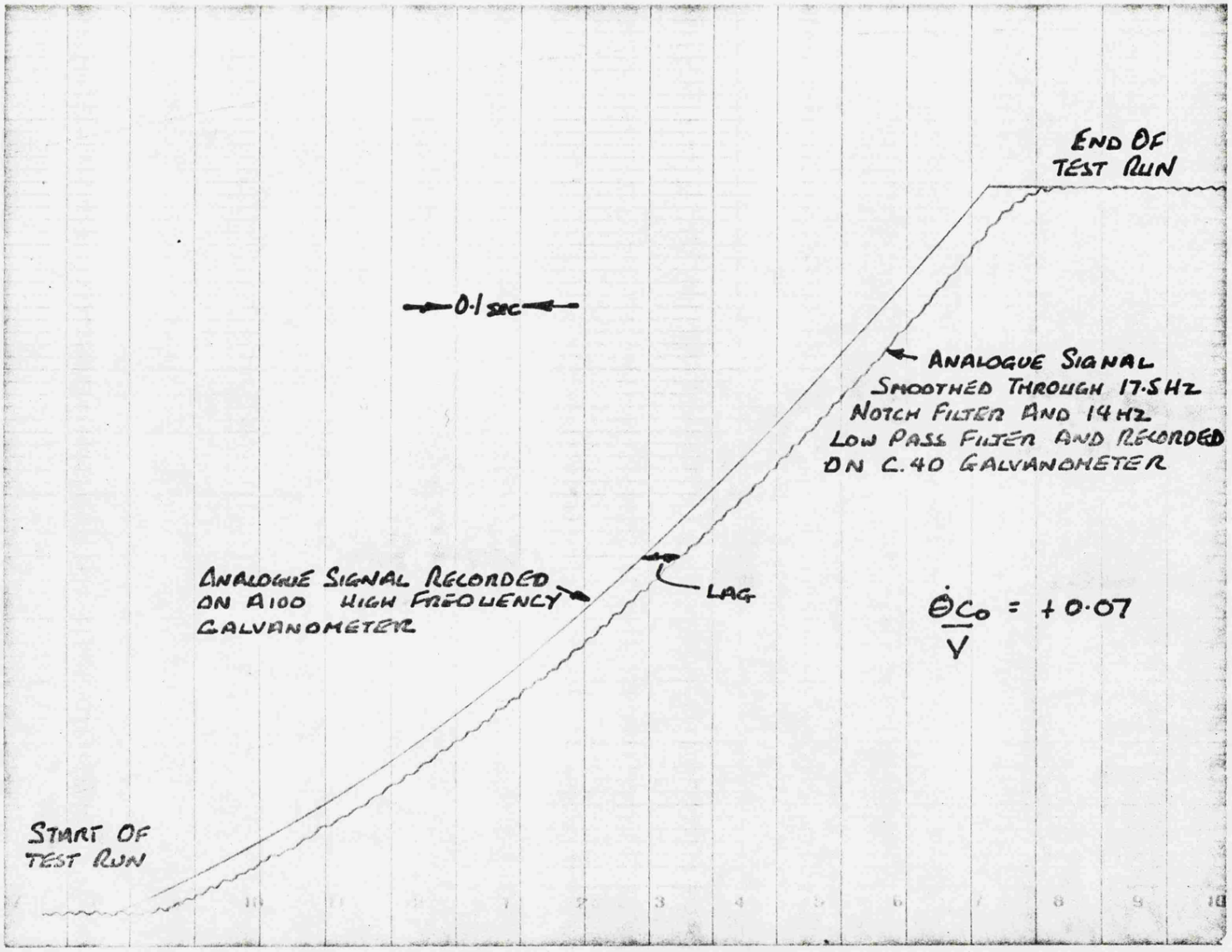

FIG 3.31 PHASE LAG PRODUCED BY 17·5Hz NOTCH FILTER AND 14Hz LOW-PASS FILTER

FIG 3.31

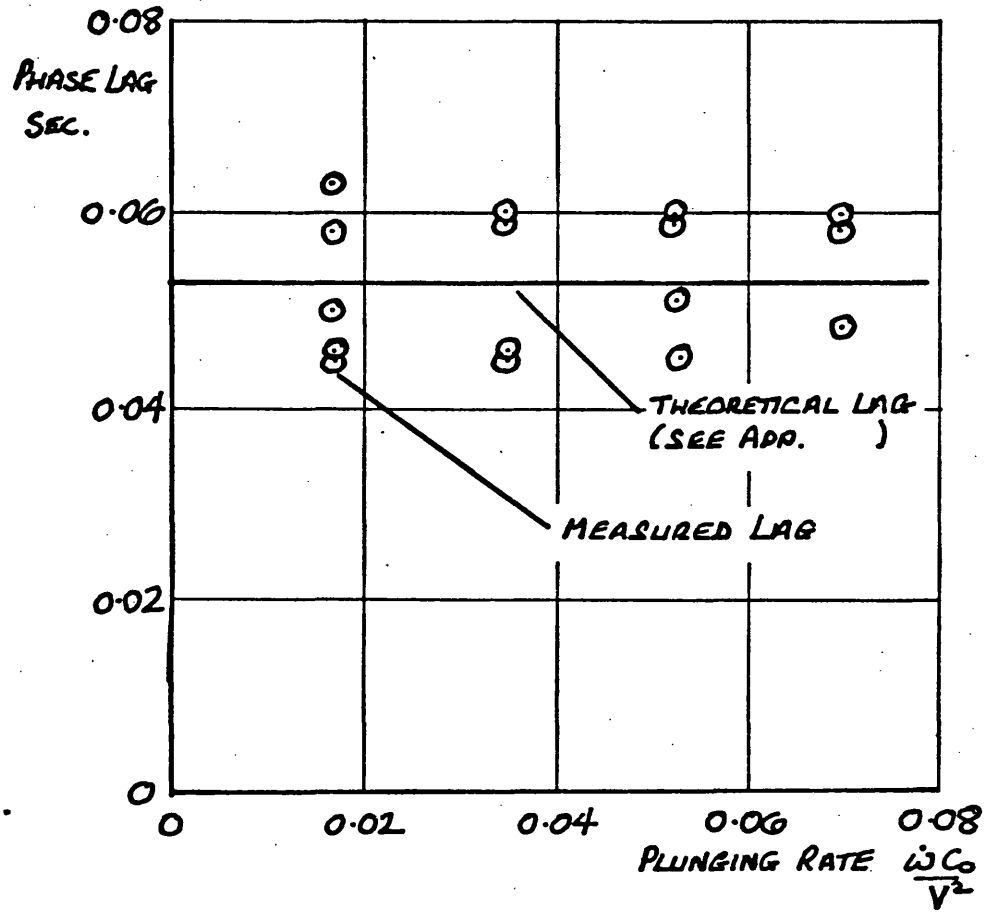

FIG 3.32 PHASE LAG OF CIRCUIT CONTAINING 17.5 Hz NOTCH FILTER + 14 Hz LOW-PASS FILTER + C.40 GALVANOMETER

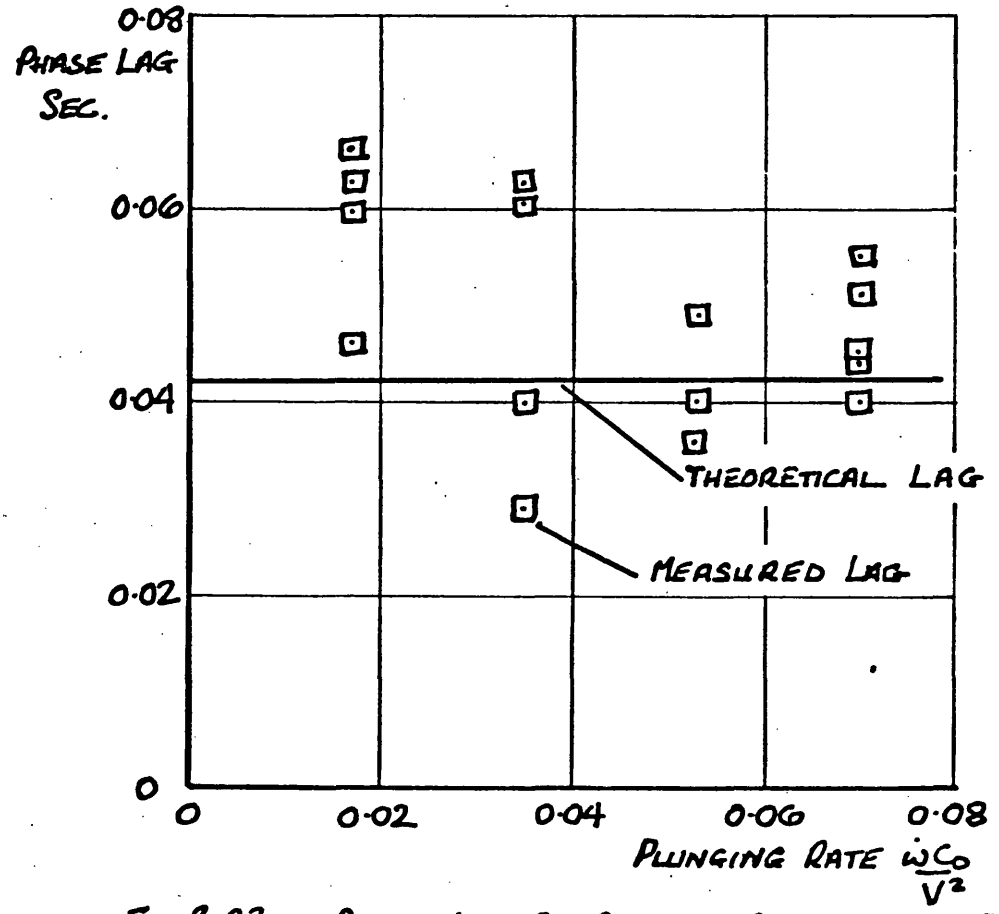

FIG 3.33 PHASE LAG OF CIRCUIT CONTAINING 17·5 Hz NOTCH FILTER + C.40 GALVANOMETER

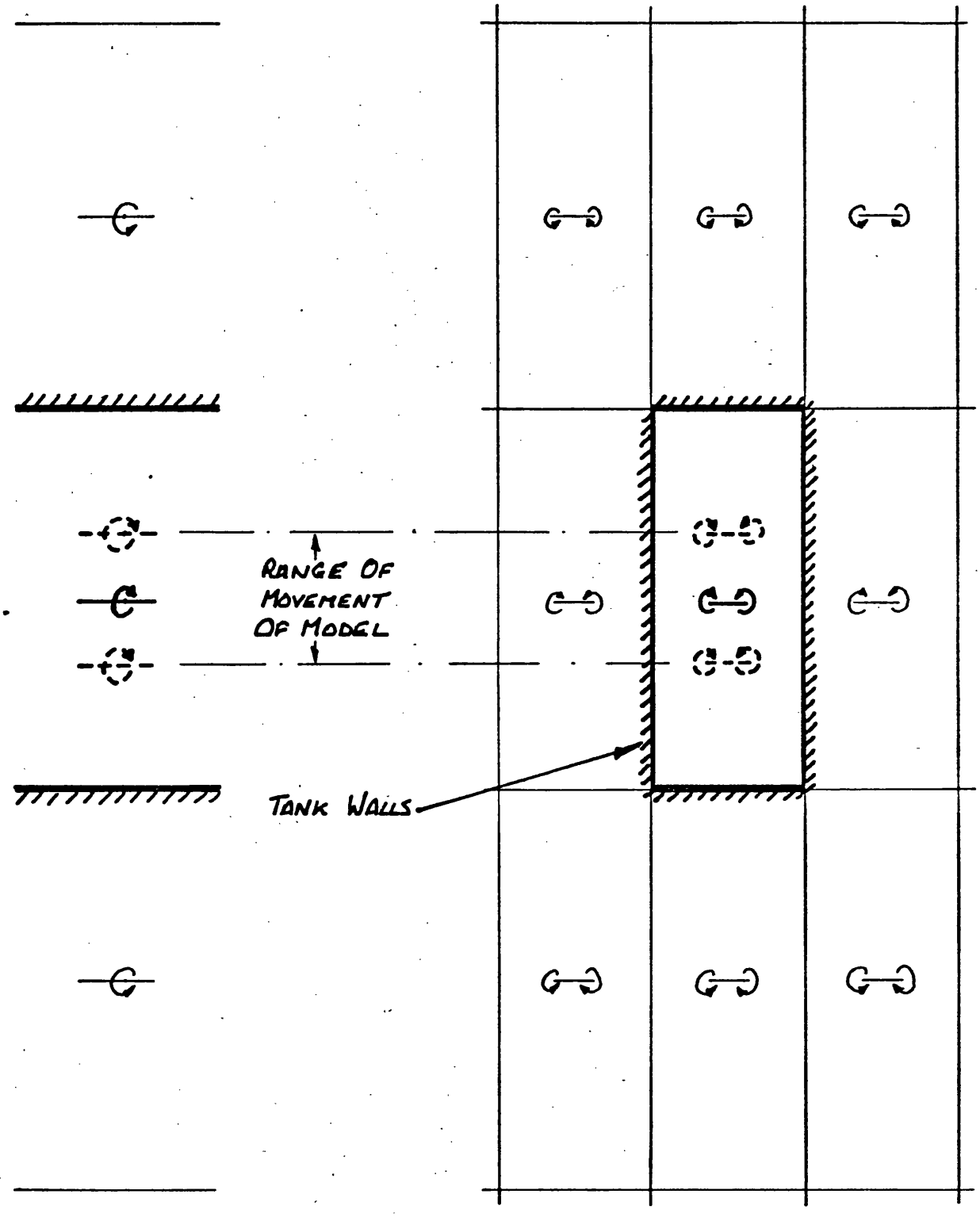

FIG 3.34 PART OF VORTEX IMAGE SYSTEM USED FOR WALL CONSTRAINT CALCULATION

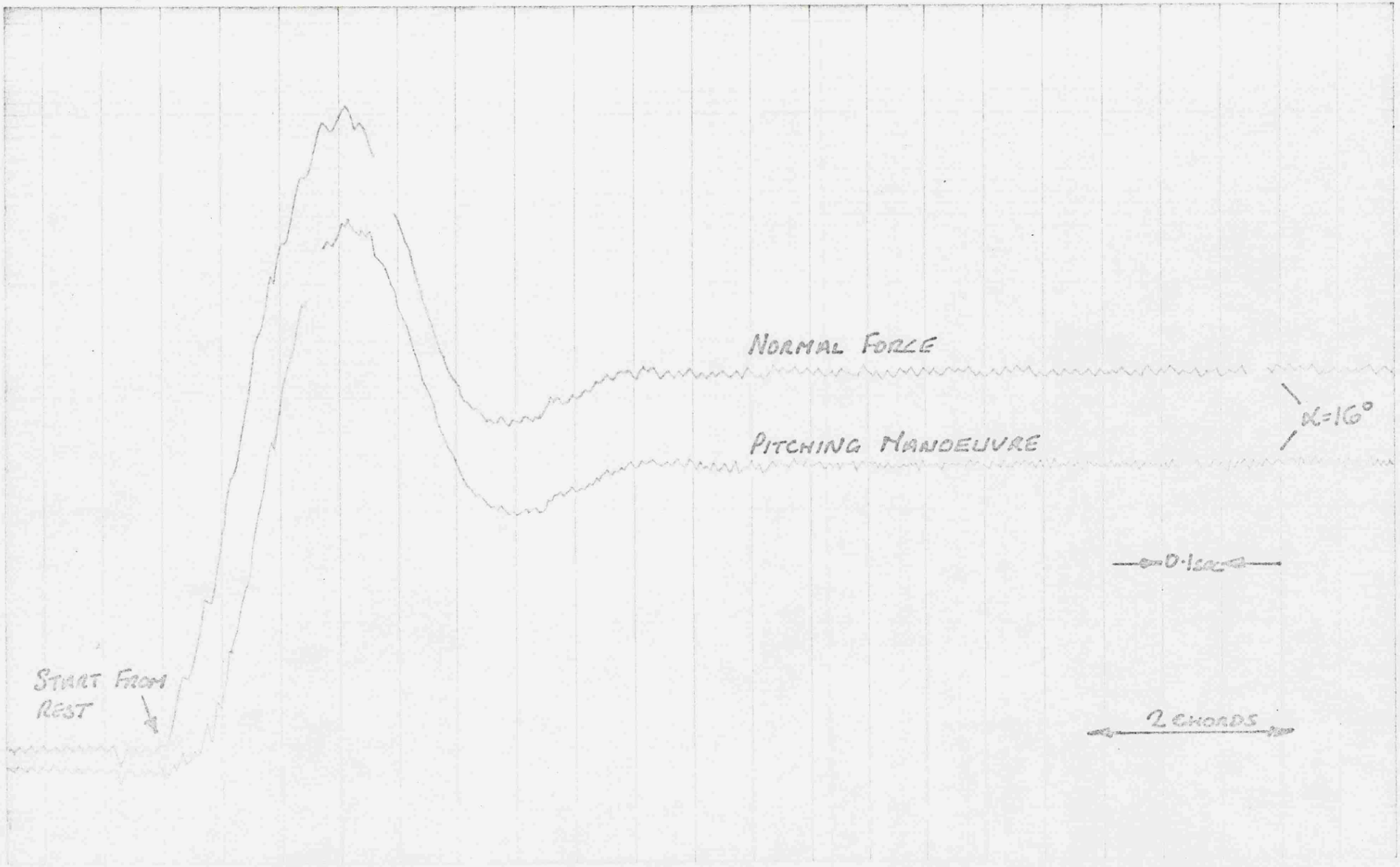

FIG 4.01

FIG 4.01 A TYPICAL L/V TRACE FOR A STEADY RUN AT CONSTANT INCIDENCE α

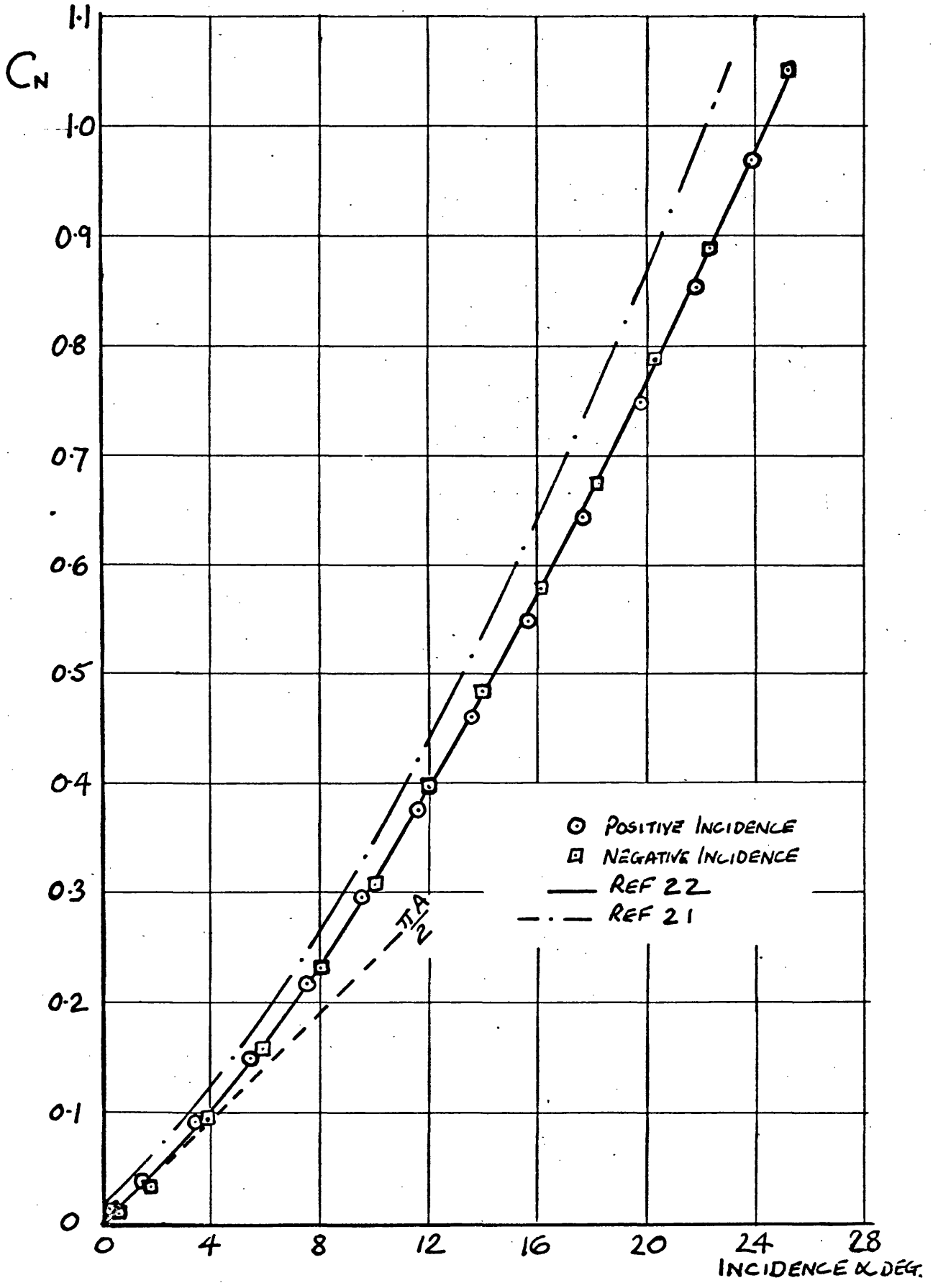

FIG 4.02 VARIATION OF NORMAL FORCE COEFFICIENT C_N WITH INCIDENCE α DEG.

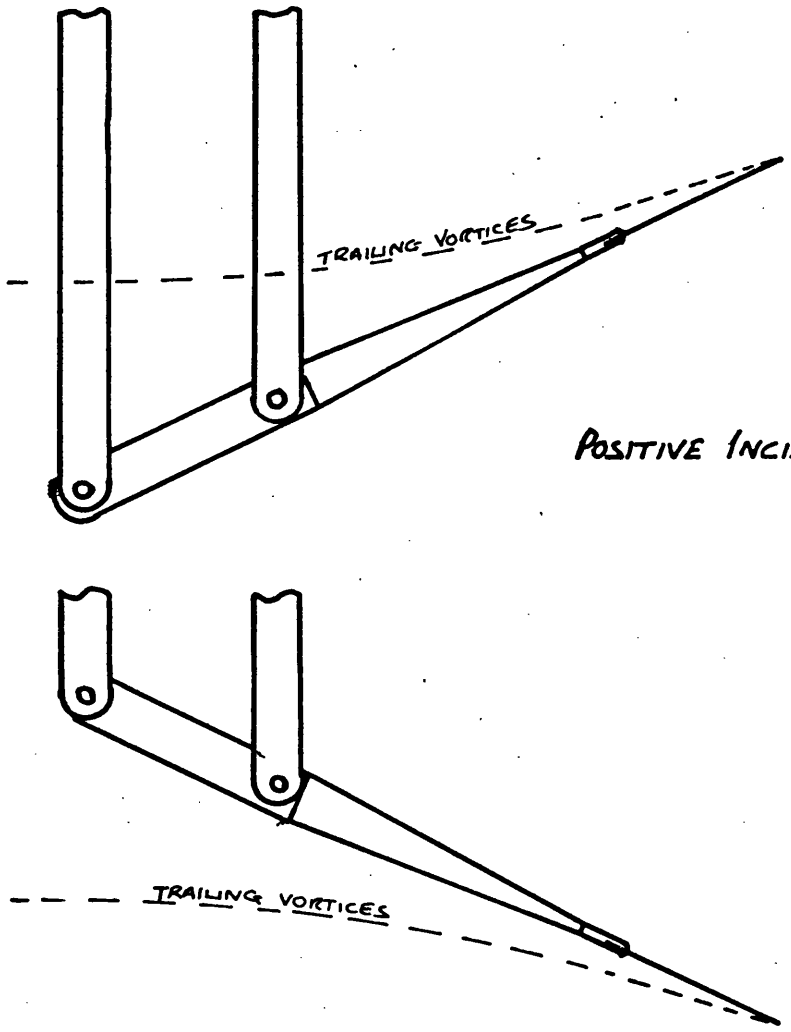

FIG 4.03 POSSIBLE ASYMMETRIC EFFECT OF SUPPORTING STRUCTURE ON TRAILING VORTICES

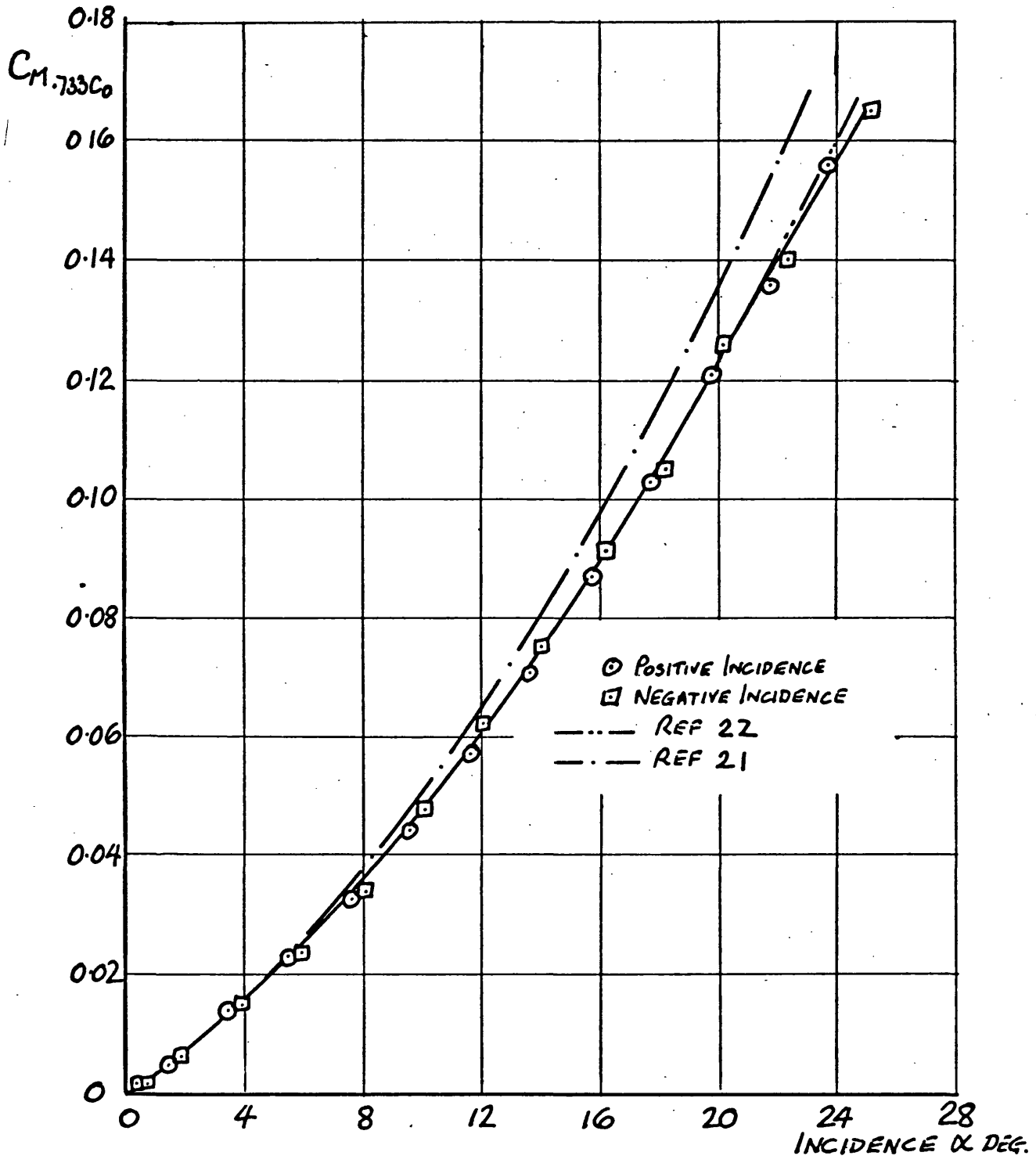

FIG 4.04 VARIATION OF PITCHING MOMENT COEFFICIENT $C_{M.733C_0}$ WITH INCIDENCE α DEG.

FIG 4.05

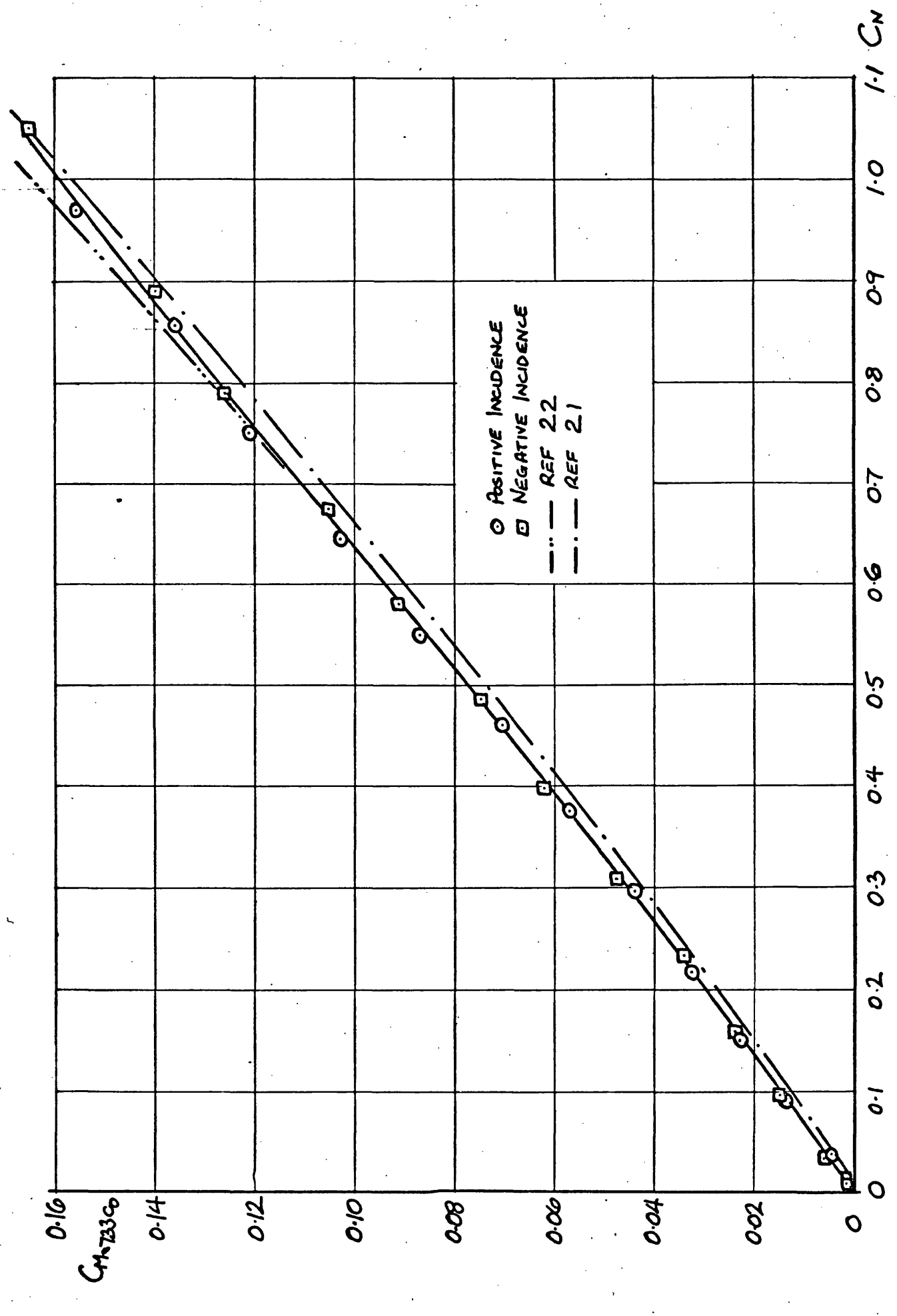

FIG 4.05 VARIATION OF PITCHING MOMENT COEFFICIENT $C_{M_{.733c}}$ WITH NORMAL FORCE COEFFICIENT C_N

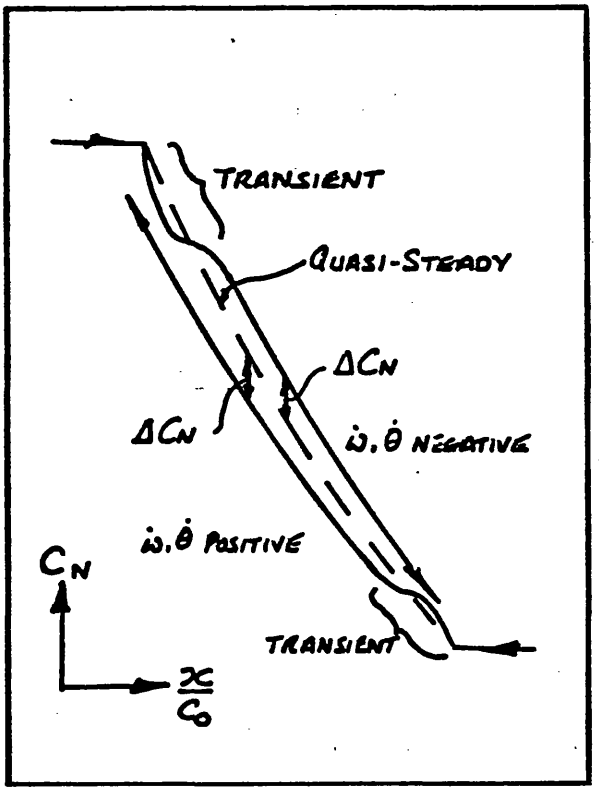

(a)

ΔCN FOR $\frac{x}{c_0} > 1$

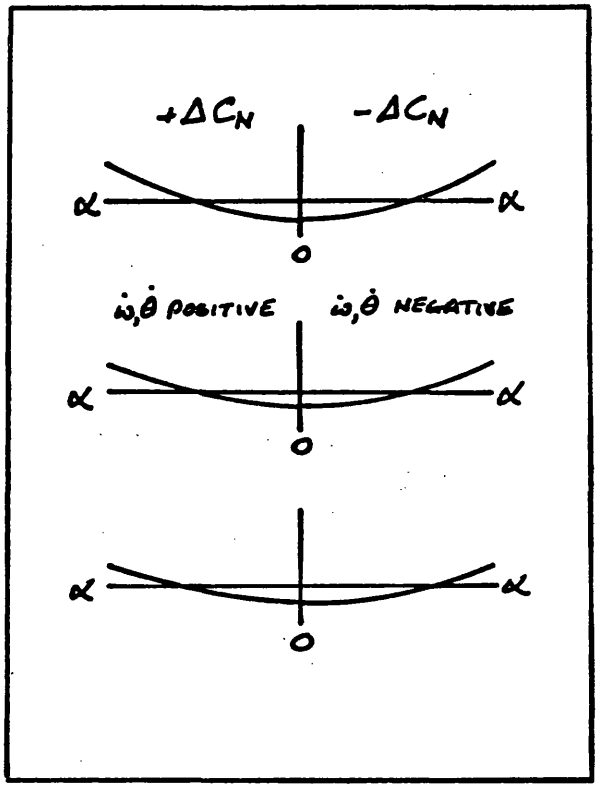

(b)

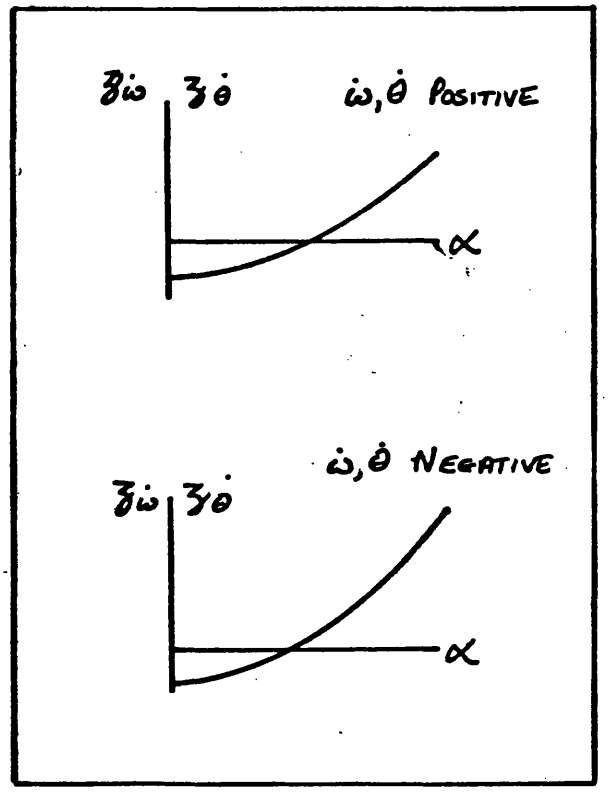

(c)

$$z_{\dot{\omega}} = -\frac{\Delta C_N \cos\alpha}{\frac{\dot{\omega} c_0}{V^2}}$$

$$z_{\dot{\theta}} = -\frac{\Delta C_N \cos\alpha}{\frac{\dot{\theta} c_0}{V^2}}$$

FIG 4.06 ILLUSTRATION OF METHOD OF PRESENTATION OF PLUNGING AND PITCHING RESULTS AND SEQUENCE OF ANALYSIS

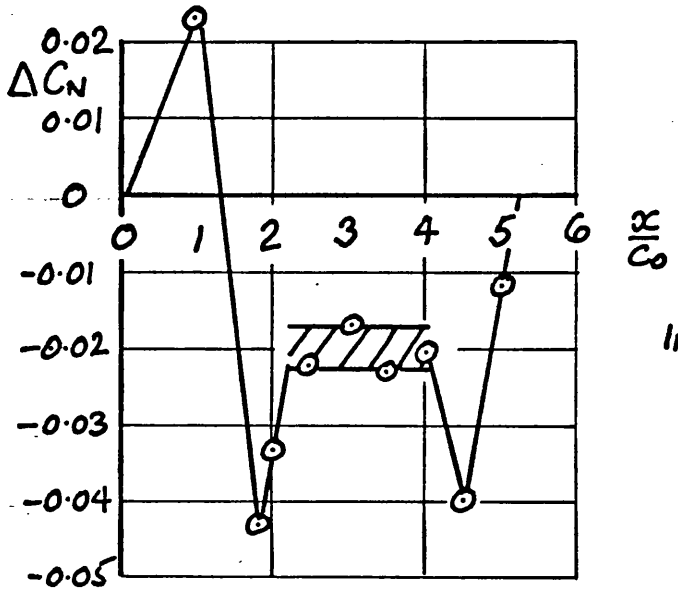

INCIDENCE $\alpha = 22°52'$

$\frac{\dot{q}c_0}{V} = -0.07$

PITCHING AXIS AT ·667 c_0

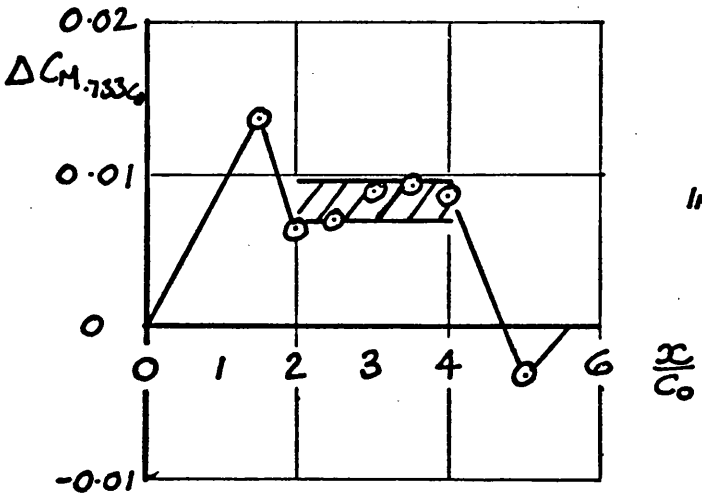

INCIDENCE $\alpha = 22°52'$

$\frac{\dot{q}c_0}{V} = -0.07$

FIG 4.07 EXAMPLES OF VARIATION OF C_N AND $C_{M.733c_0}$ DURING CONSTANT q MANOEUVRE AFTER CORRECTIONS HAVE BEEN APPLIED

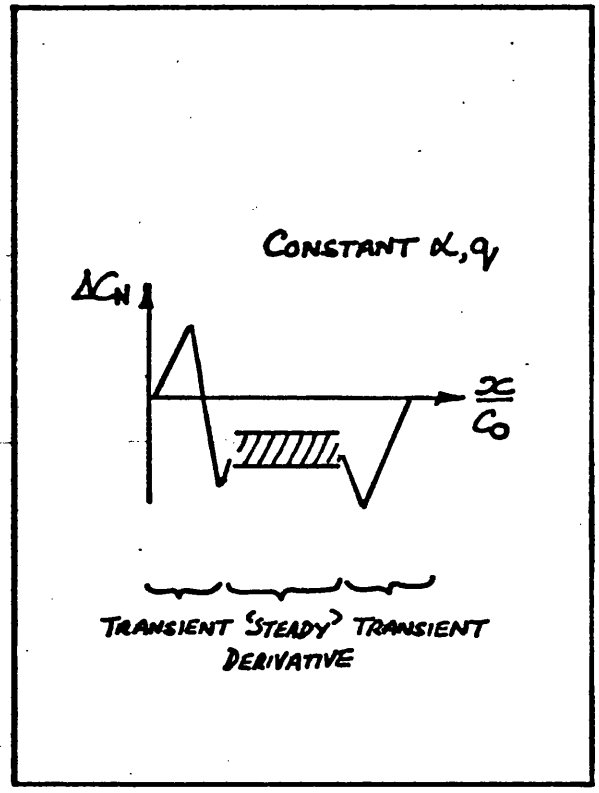

(a)

'STEADY' ΔC_N

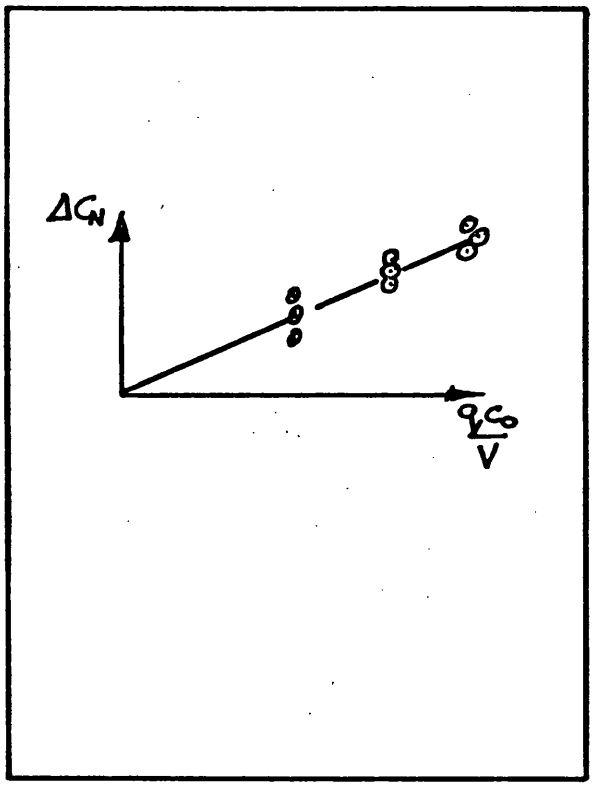

(b)

$z_q = -\frac{\Delta C_N}{\frac{qc_0}{V}}$

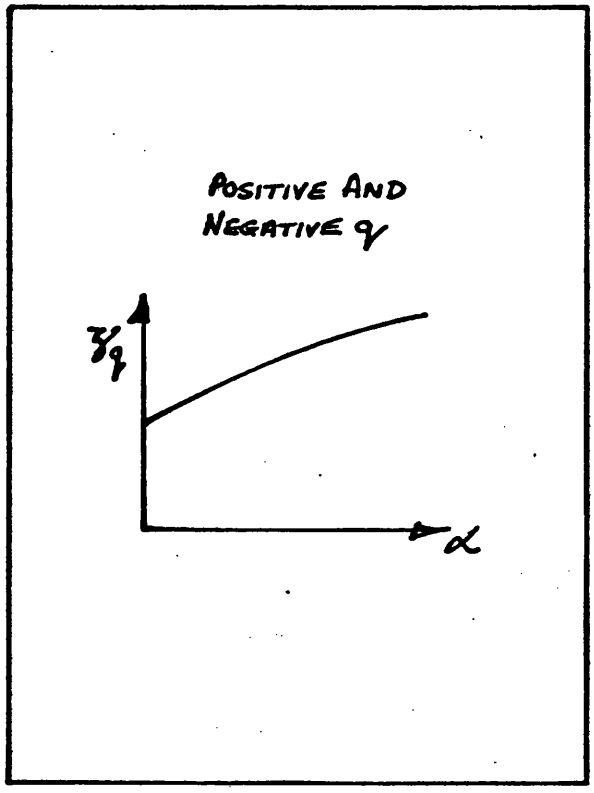

(c)

FIG 4.08 ILLUSTRATION OF METHOD OF PRESENTATION OF CONSTANT q RESULTS AND SEQUENCE OF ANALYSIS

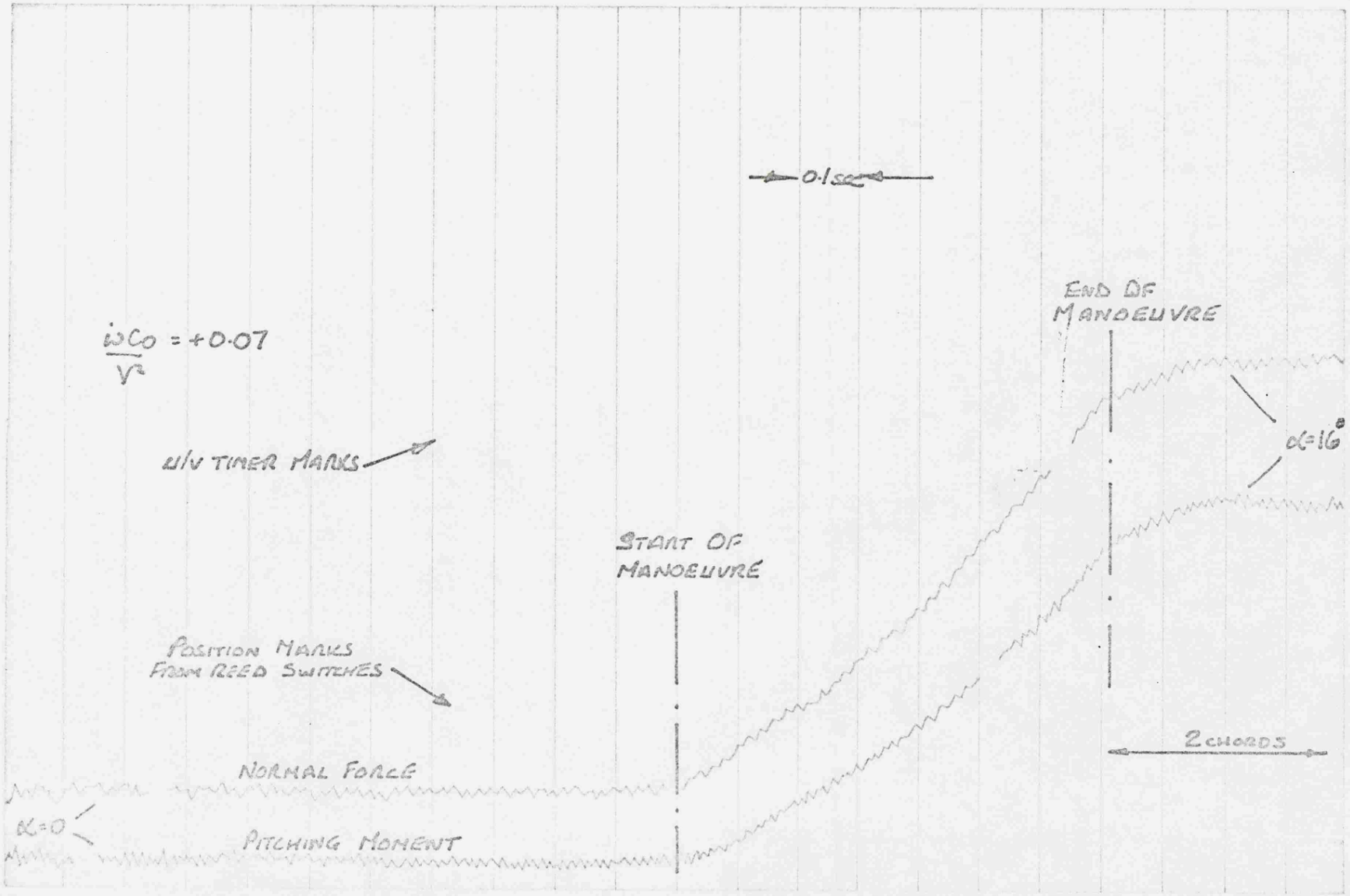

FIG 4.09 A TYPICAL U/V TRACE FOR A PLUNGING MANOEUVRE (CONSTANT $\dot{\omega}$)

FIG 4.09

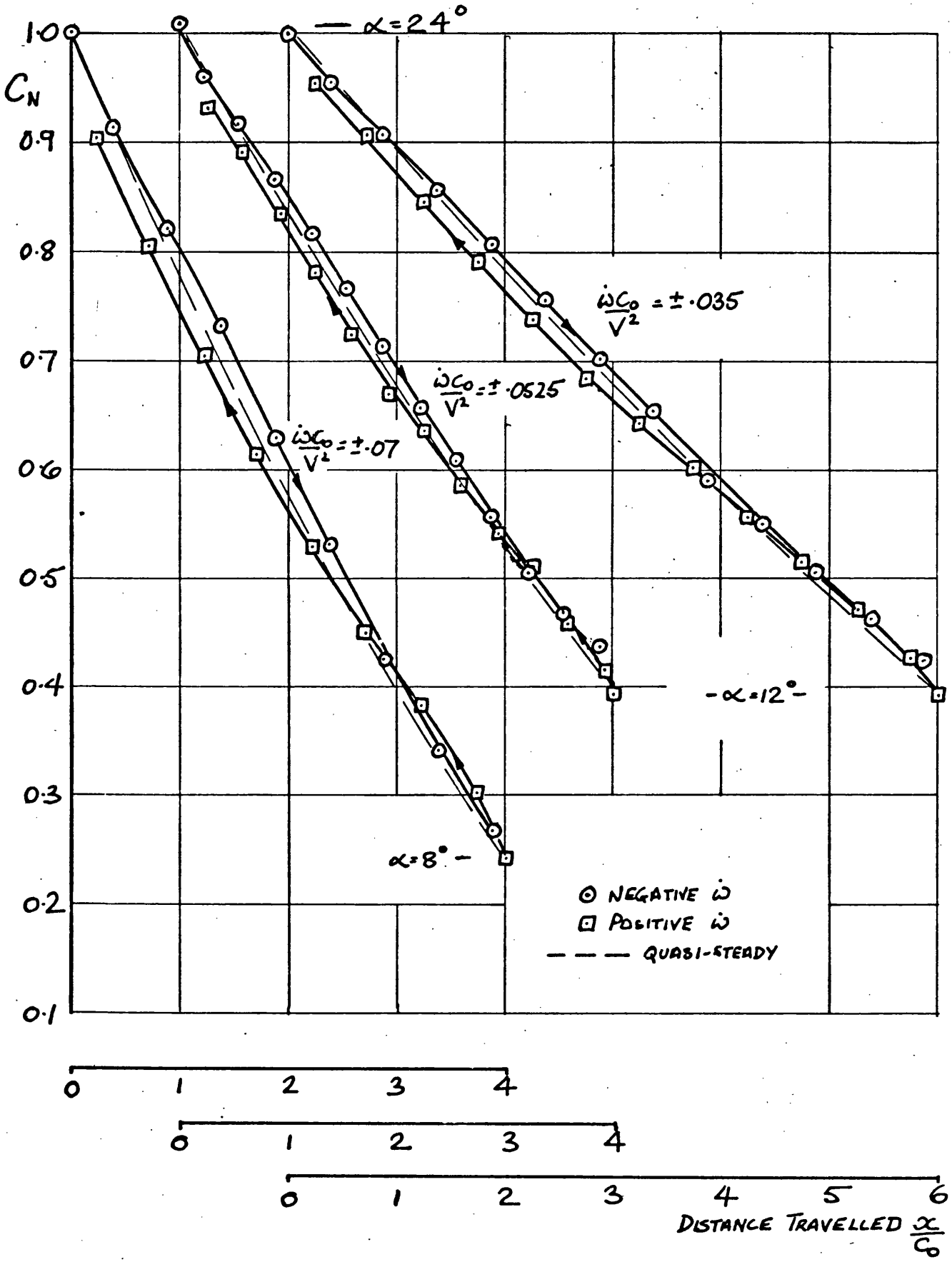

FIG 4.10 VARIATION OF C_N DURING PLUNGING MANOEUVRE (CONSTANT $\dot{\omega}$) WITH INITIAL INCIDENCE 24° AND FOR THREE PLUNGING RATES

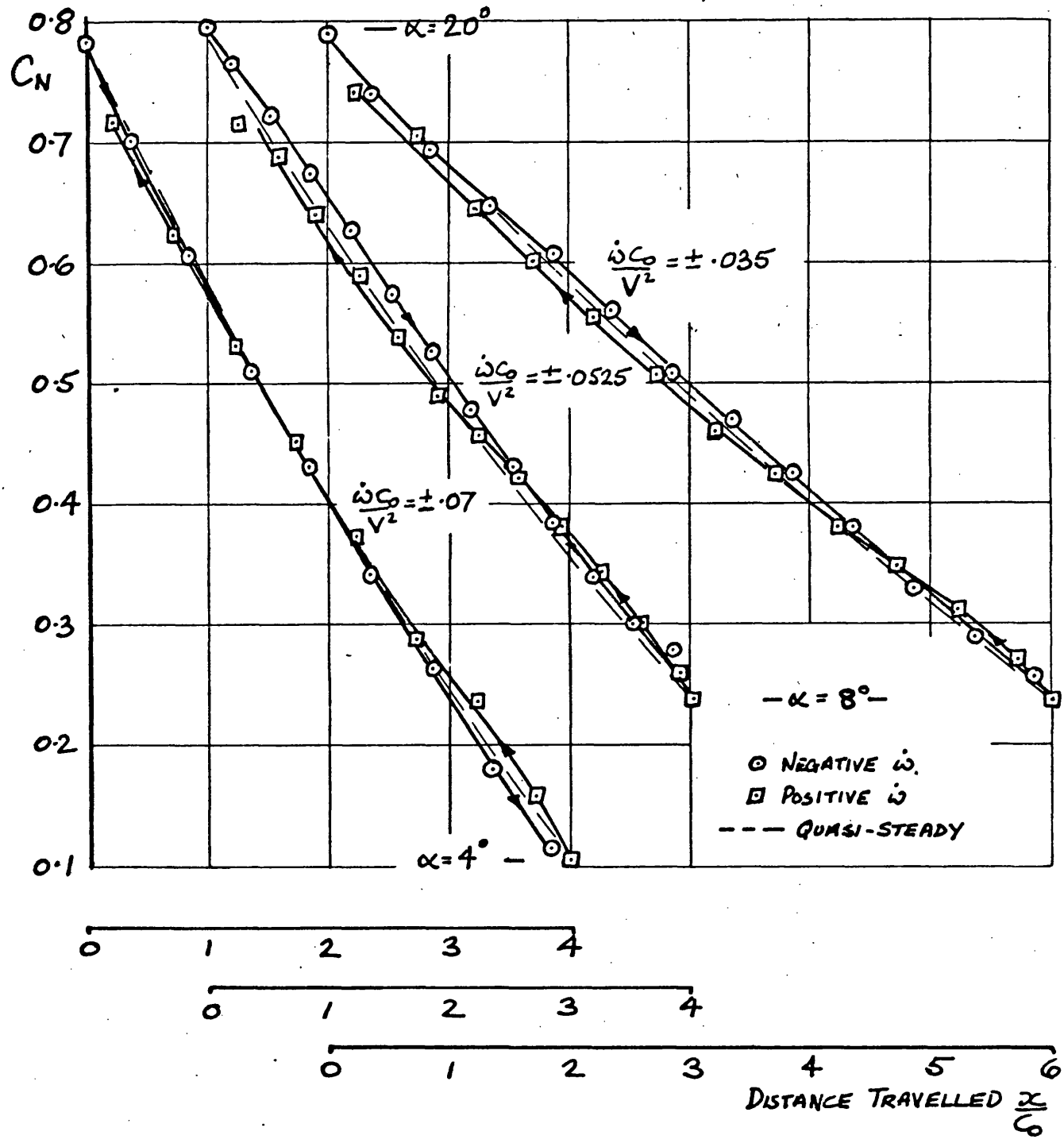

FIG 4.11 VARIATION OF C_N DURING PLUNGING MANOEUVRE (CONSTANT $\dot{\omega}$) WITH INITIAL INCIDENCE 20° AND FOR 3 PLUNGING RATES

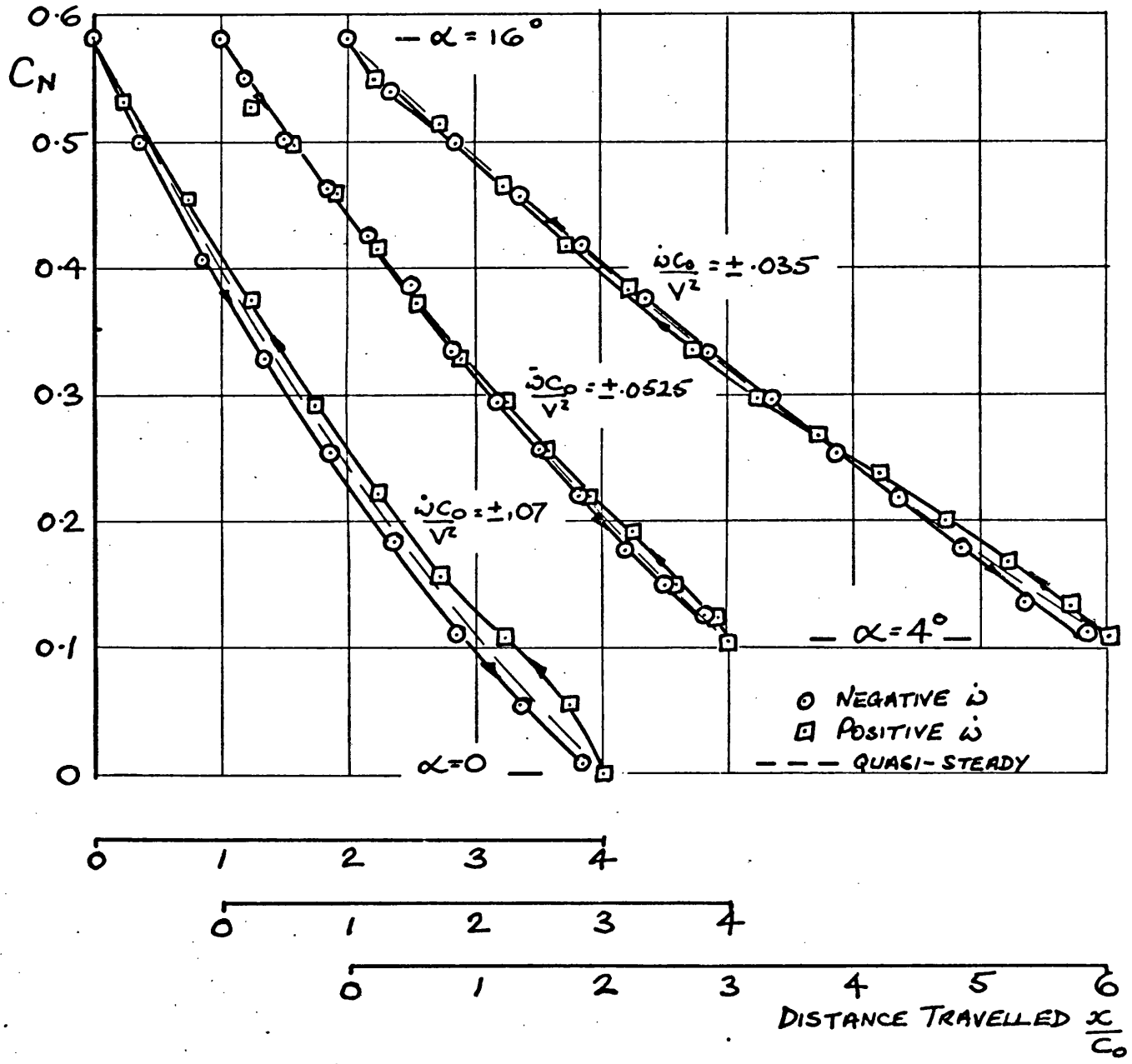

FIG 4.12 VARIATION OF C_N DURING PLUNGING MANOEUVRE (CONSTANT $\dot{\omega}$) WITH INITIAL INCIDENCE 16° AND FOR 3 PLUNGING RATES

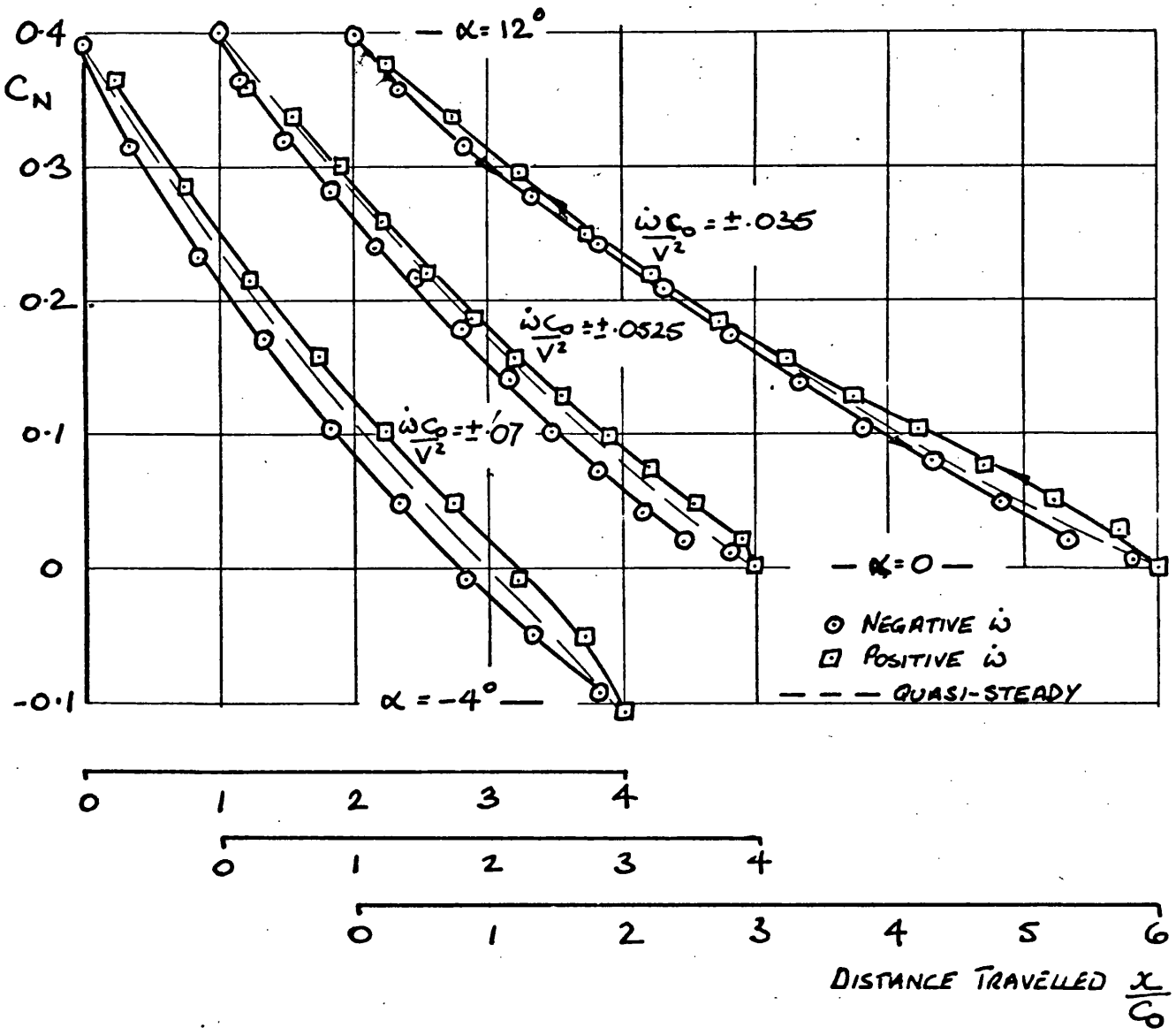

FIG 4.13 VARIATION OF C_N DURING PLUNGING MANOEUVRE (CONSTANT ω) WITH INITIAL INCIDENCE 12° AND FOR 3 PLUNGING RATES

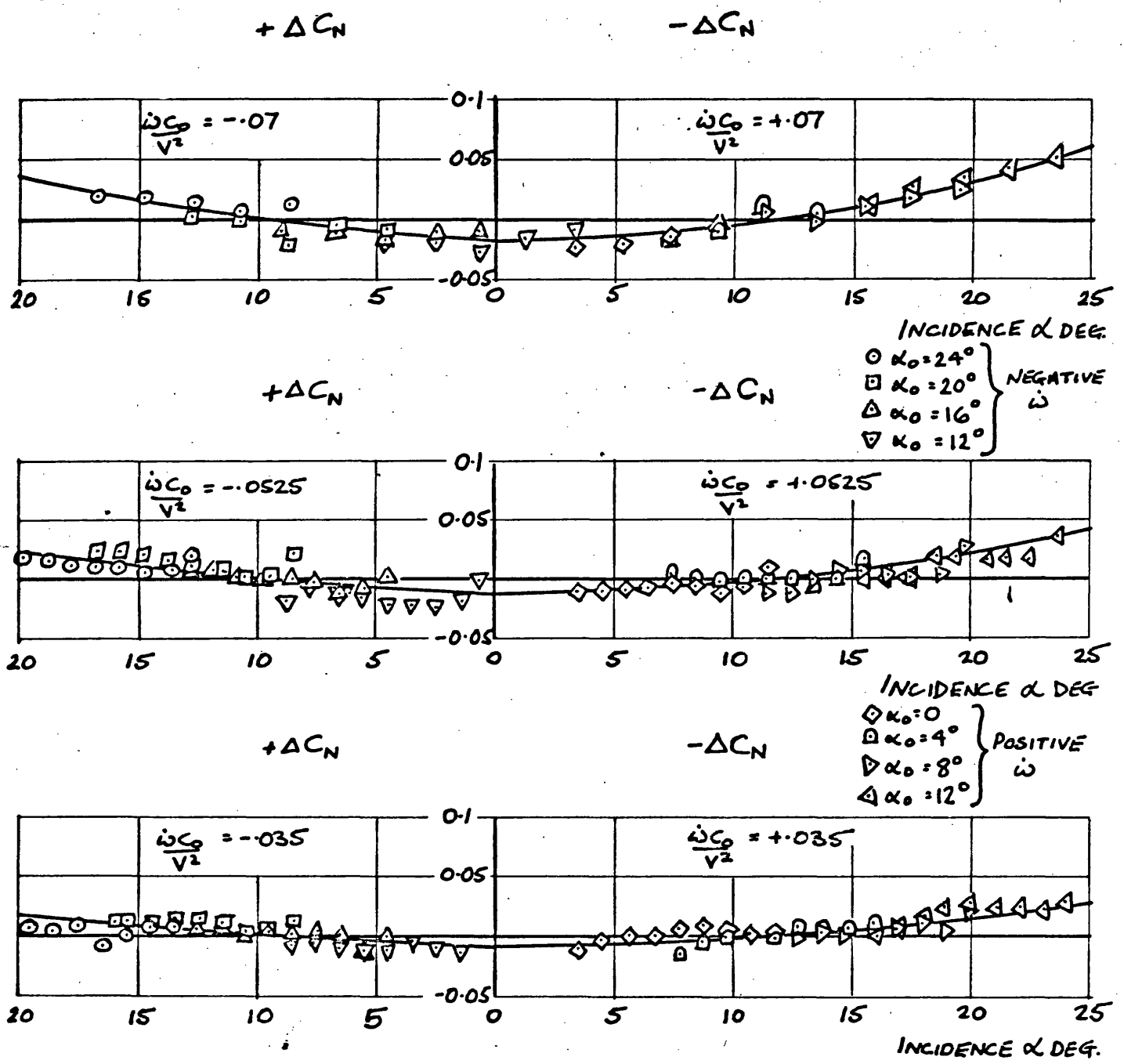

FIG 4.14 VARIATION OF ΔC_N WITH INCIDENCE α DURING PLUNGING MANOEUVRE (EXCLUDING TRANSIENT) FOR 3 PLUNGING RATES

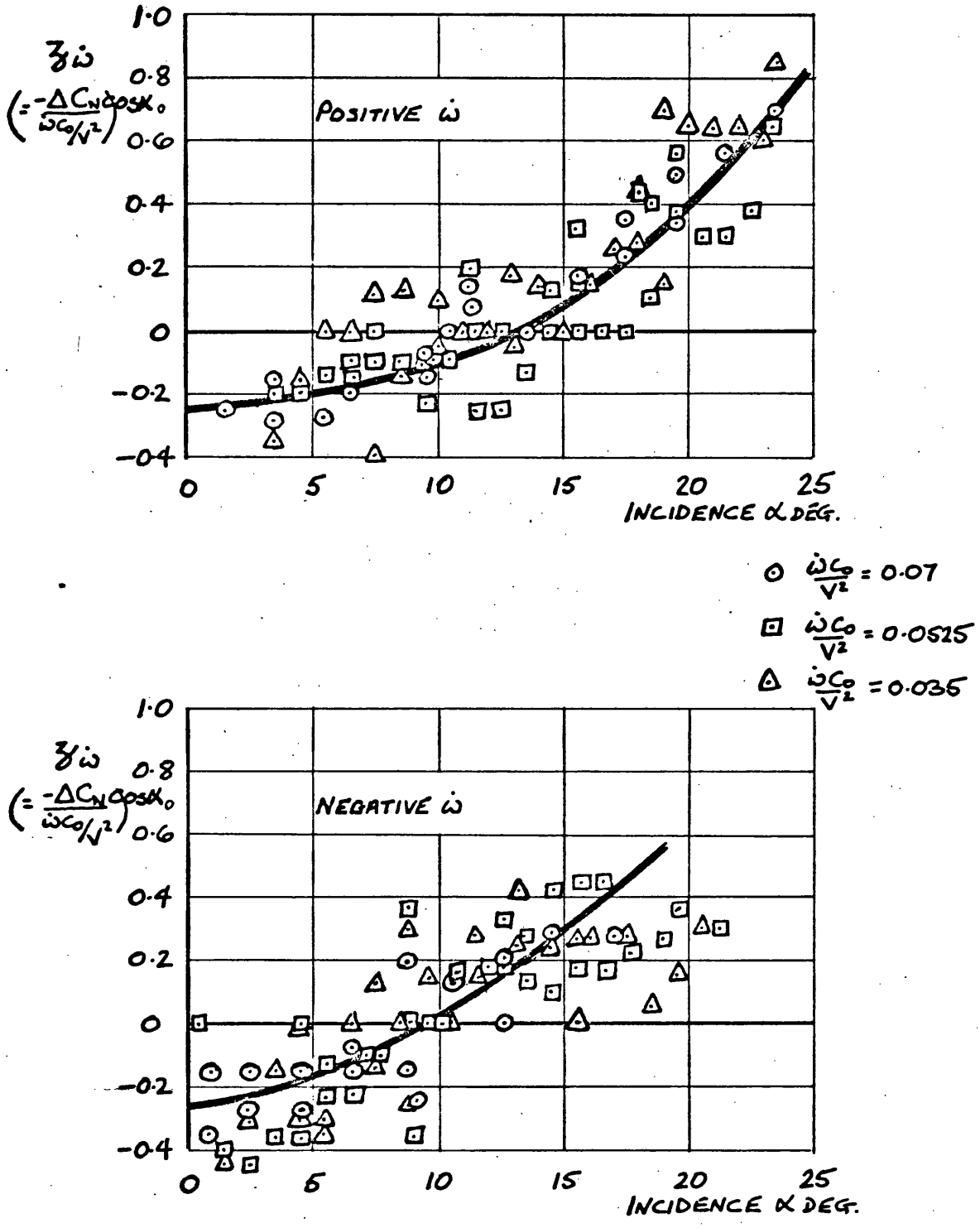

FIG 4.15 NORMAL FORCE DERIVATIVE $z_{\dot{\omega}}$ FOR POSITIVE AND NEGATIVE RATES OF $\dot{\omega}$

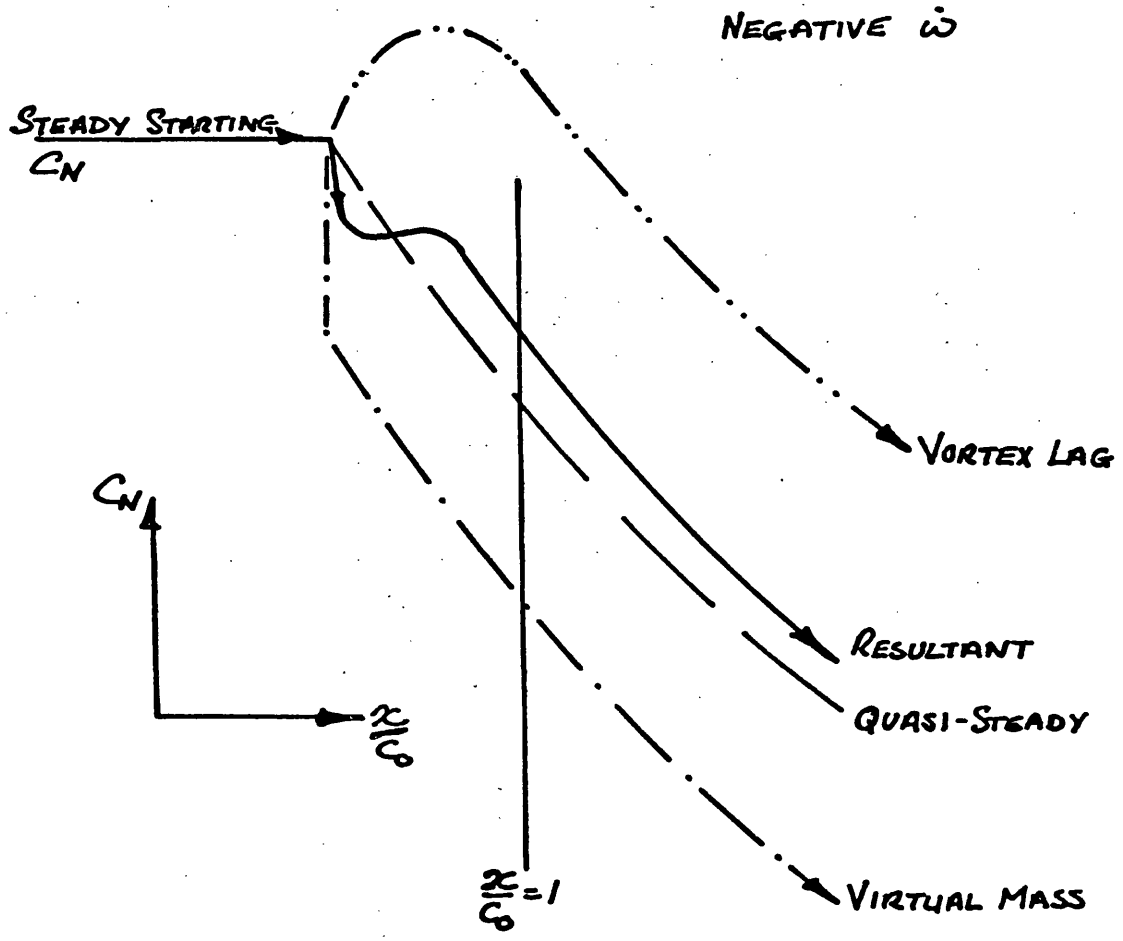

FIG 4.16 BEHAVIOUR OF NORMAL FORCE AT START OF PLUNGING MANOEUVRE FOR NEGATIVE PLUNGING RATE AS PREDICTED BY 'VIRTUAL MASS + VORTEX LAG' THEORY

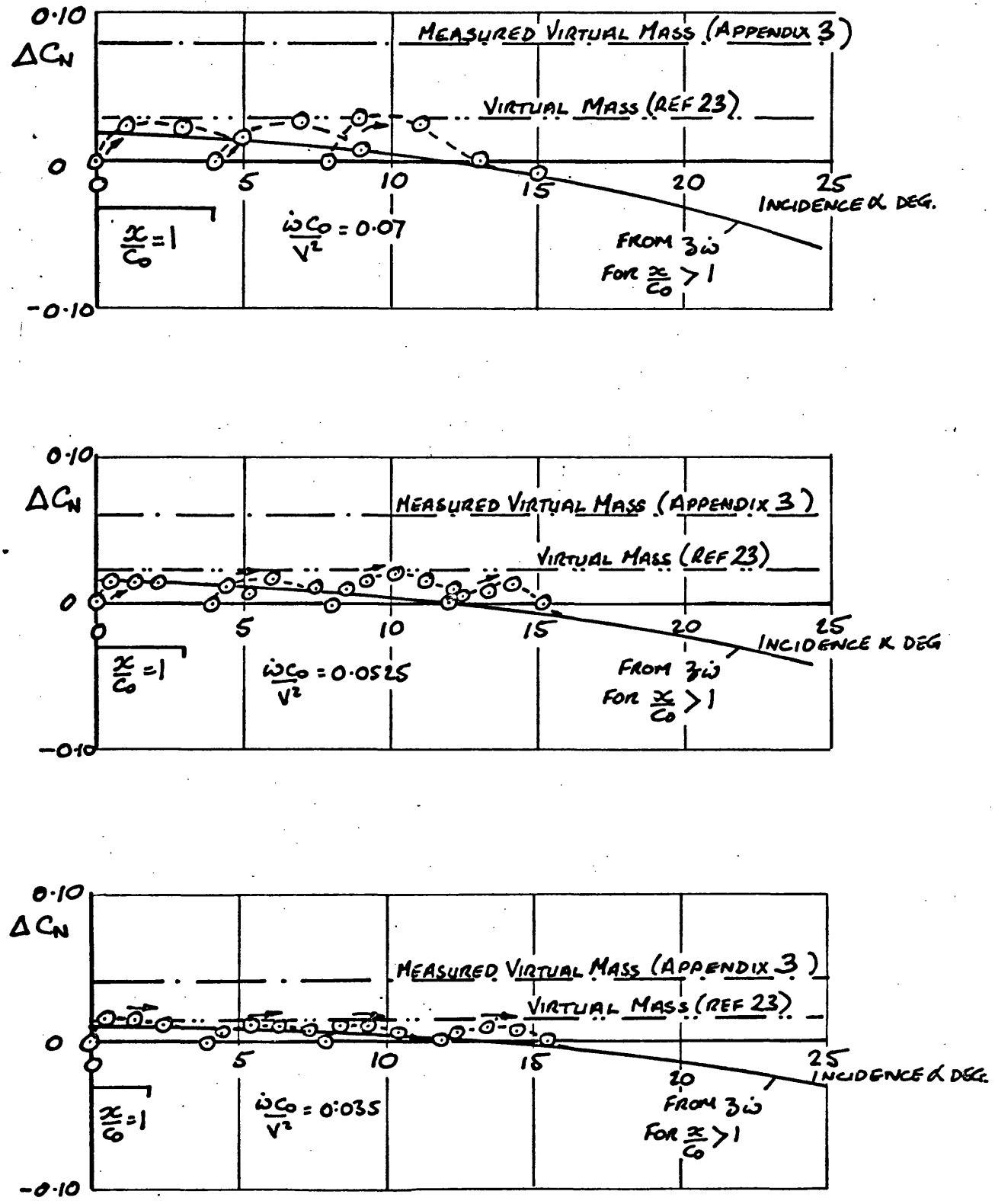

FIG 4.17 TRANSIENT BEHAVIOUR OF NORMAL FORCE AT START OF PLUNGING MANOEUVRE AND ITS COMPARISON WITH THE VIRTUAL MASS

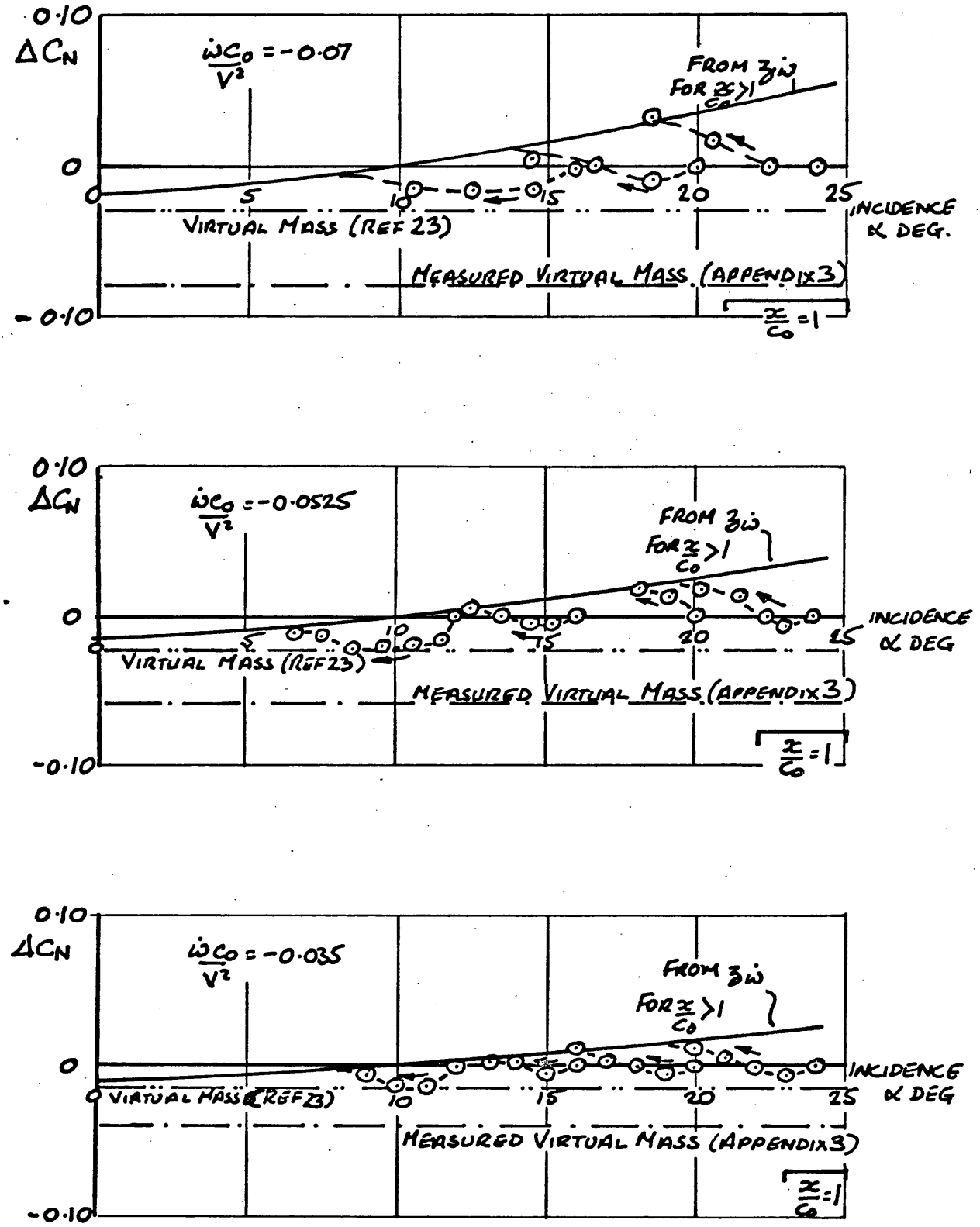

FIG 4.18 TRANSIENT BEHAVIOUR OF NORMAL FORCE AT START OF PLUNGING MANOEUVRE AND ITS COMPARISON WITH THE VIRTUAL MASS

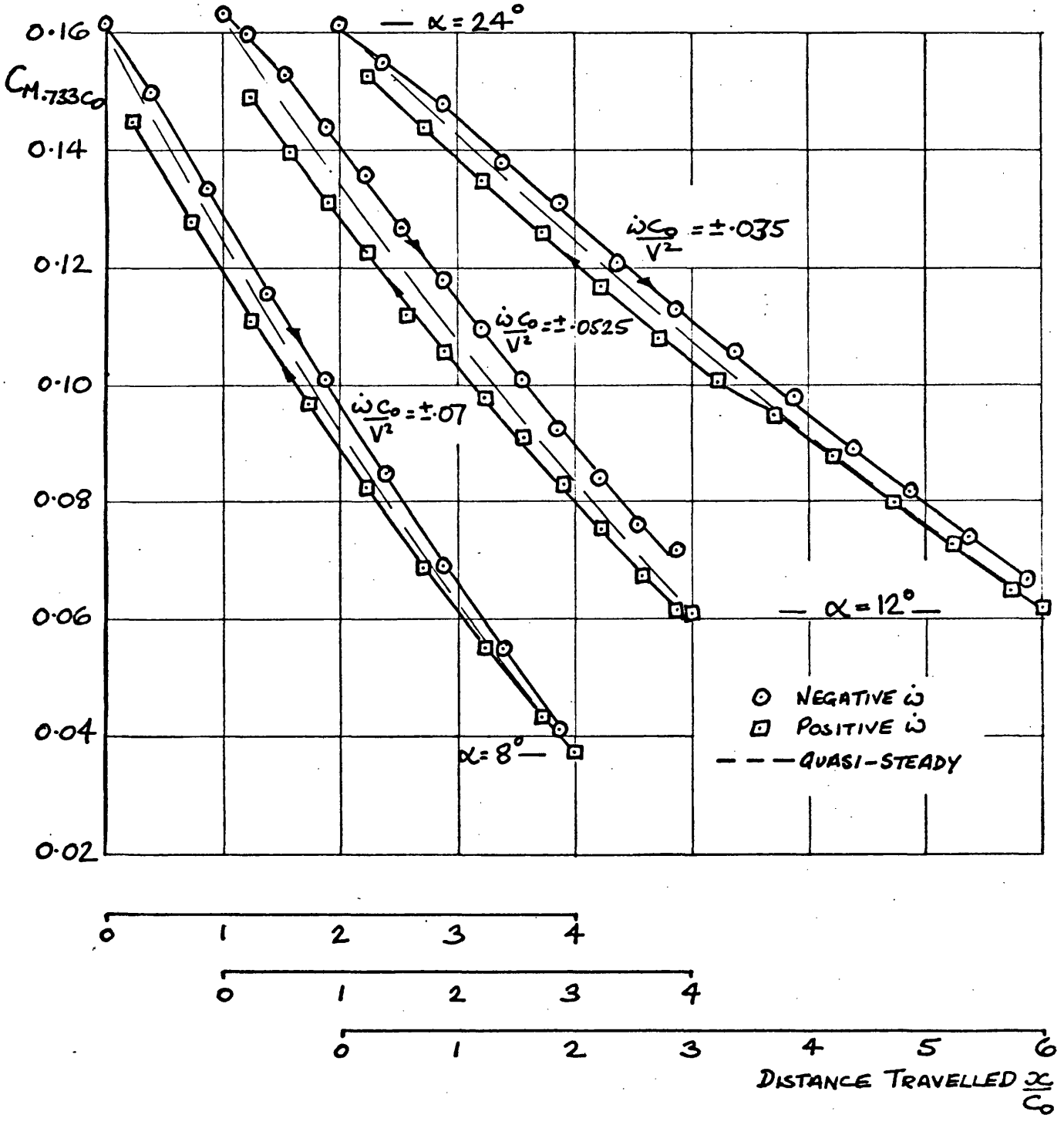

FIG 4.19 VARIATION OF $C_{M\cdot733c_0}$ DURING PLUNGING MANOEUVRE (CONSTANT $\dot{\omega}$) WITH INITIAL INCIDENCE 24° AND FOR 3 PLUNGING RATES

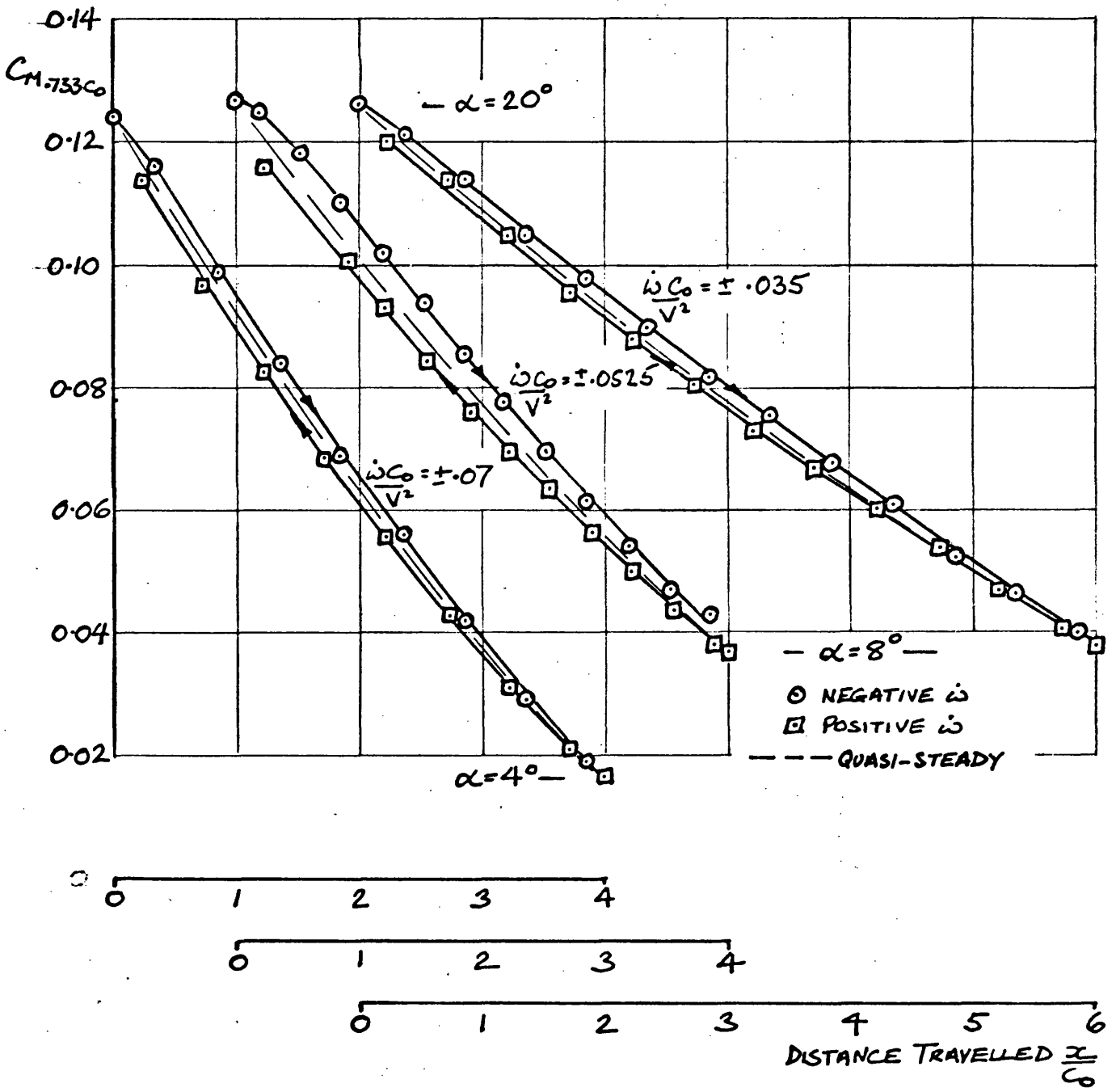

FIG 4.20 VARIATION OF $C_{M\cdot733c_0}$ DURING PLUNGING MANOEUVRE (CONSTANT $\dot{\omega}$) WITH INITIAL INCIDENCE 20° AND FOR 3 PLUNGING RATES

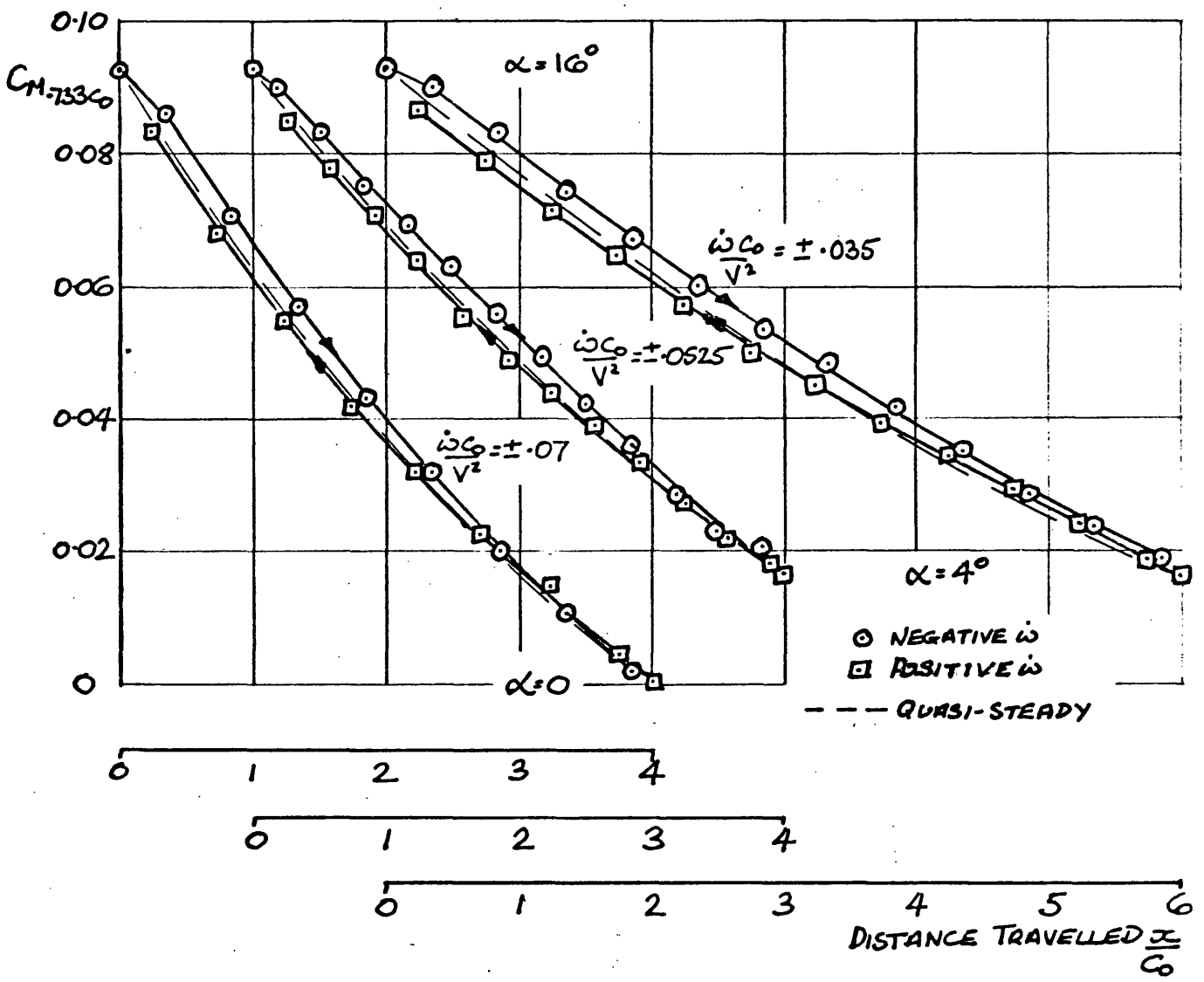

FIG 4.21 VARIATION OF $C_{M\cdot 733c_0}$ DURING PLUNGING MANOEUVRE (CONSTANT $\dot{\omega}$) WITH INITIAL INCIDENCE 16° AND FOR 3 PLUNGING RATES

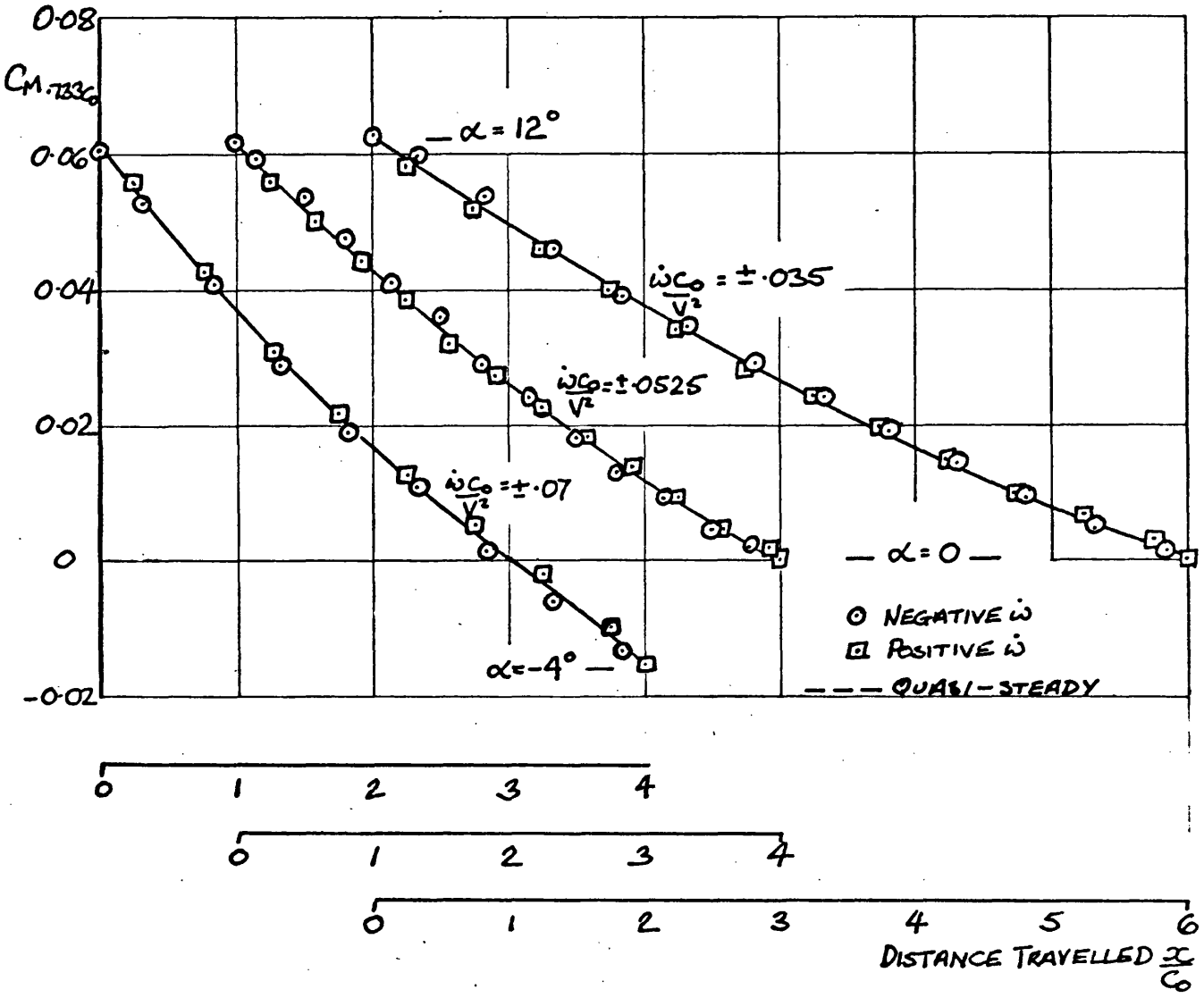

FIG 4.22 VARIATION OF $C_{M\cdot 733c_0}$ DURING PLUNGING MANOEUVRE (CONSTANT $\dot{\omega}$) WITH INITIAL INCIDENCE 12° AND FOR 3 PLUNGING RATES

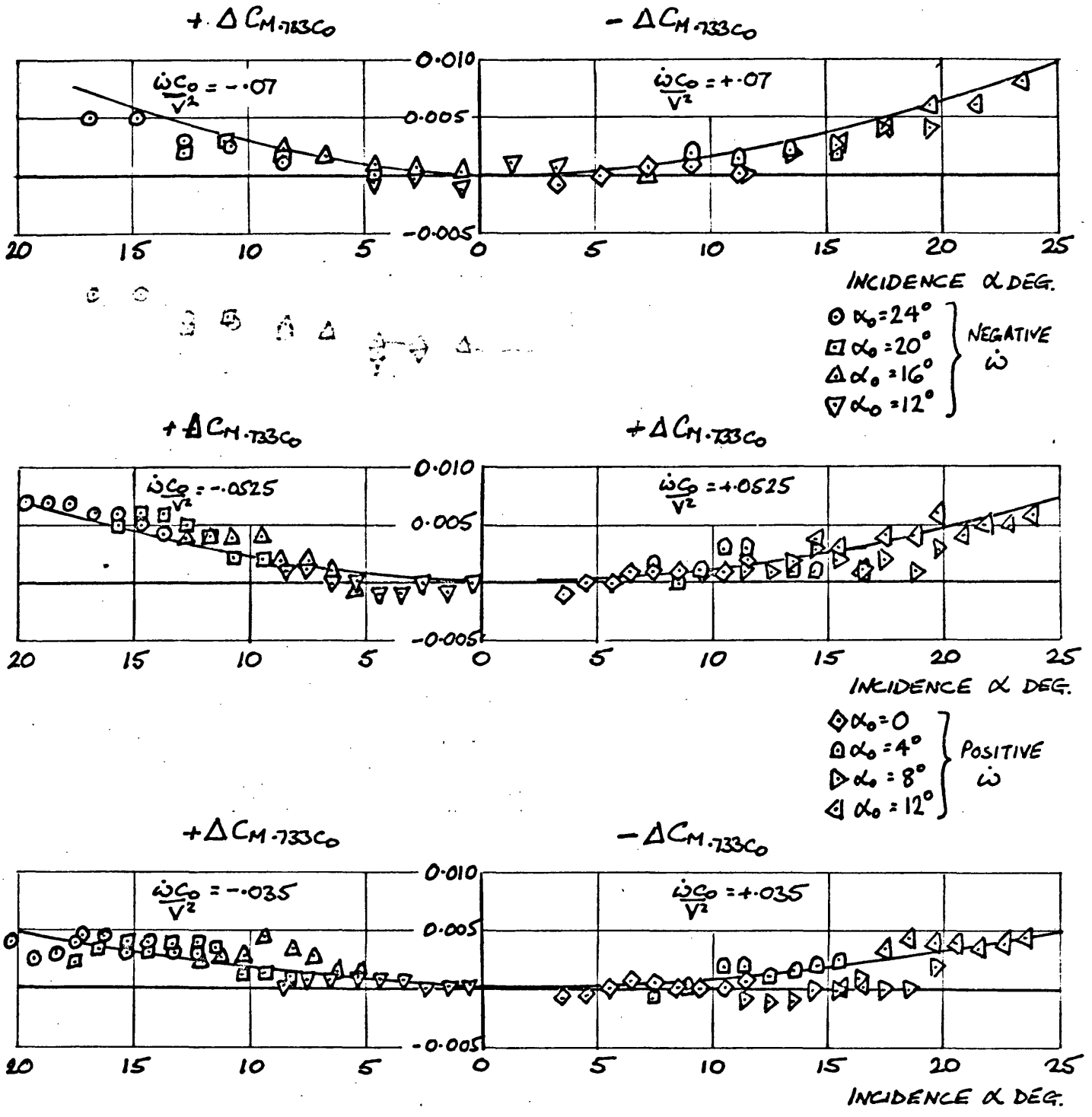

FIG 4.23 VARIATION OF $\Delta C_{M\cdot733C_0}$ WITH INCIDENCE DURING PLUNGING MANOEUVRE (EXCLUDING TRANSIENT) FOR 3 PLUNGING RATES

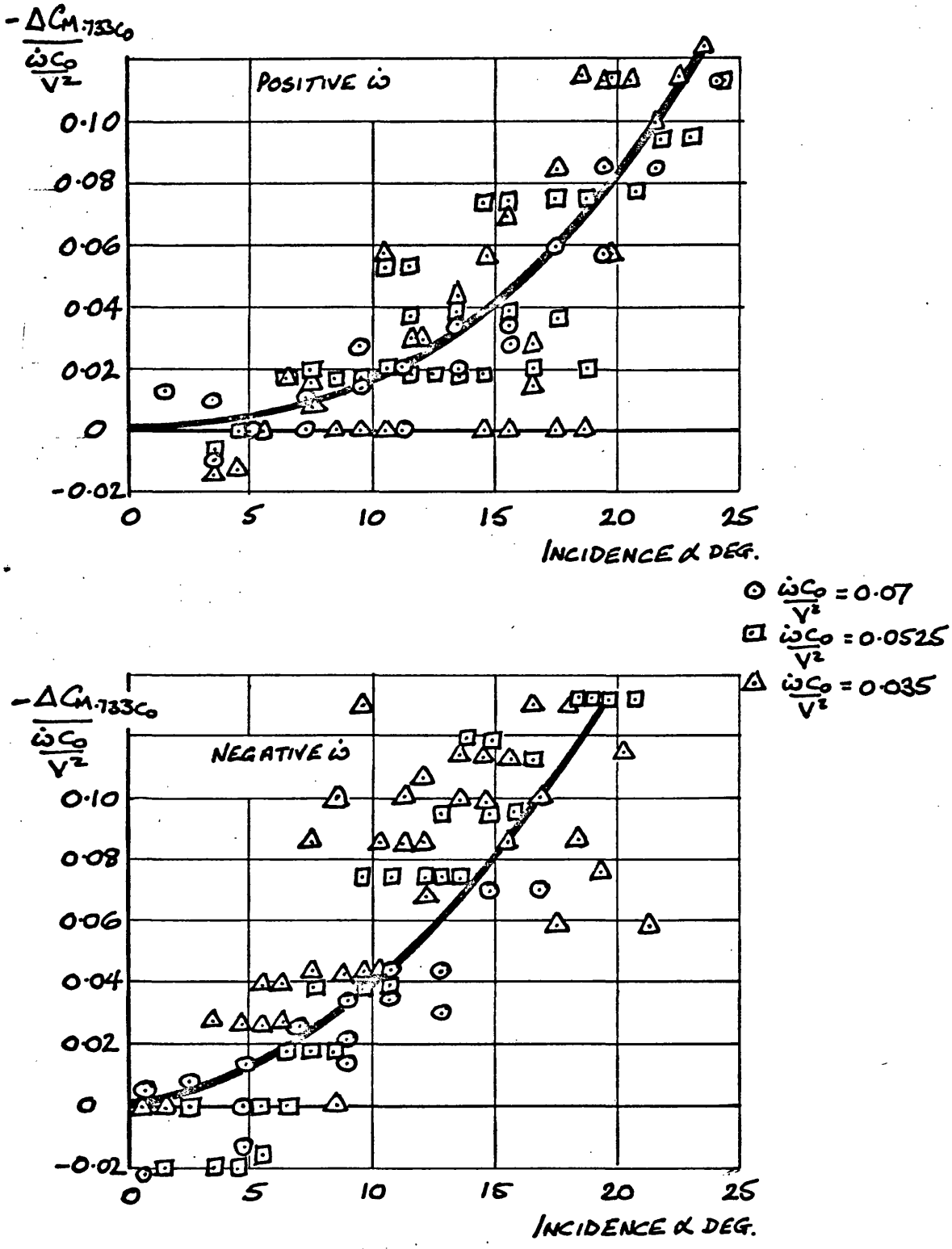

FIG 4.24 PITCHING MOMENT DERIVATIVE $\frac{\Delta C_{M\cdot 733 C_0}}{\frac{\dot{\omega} C_0}{V^2}}$ FOR POSITIVE AND NEGATIVE PLUNGING RATES

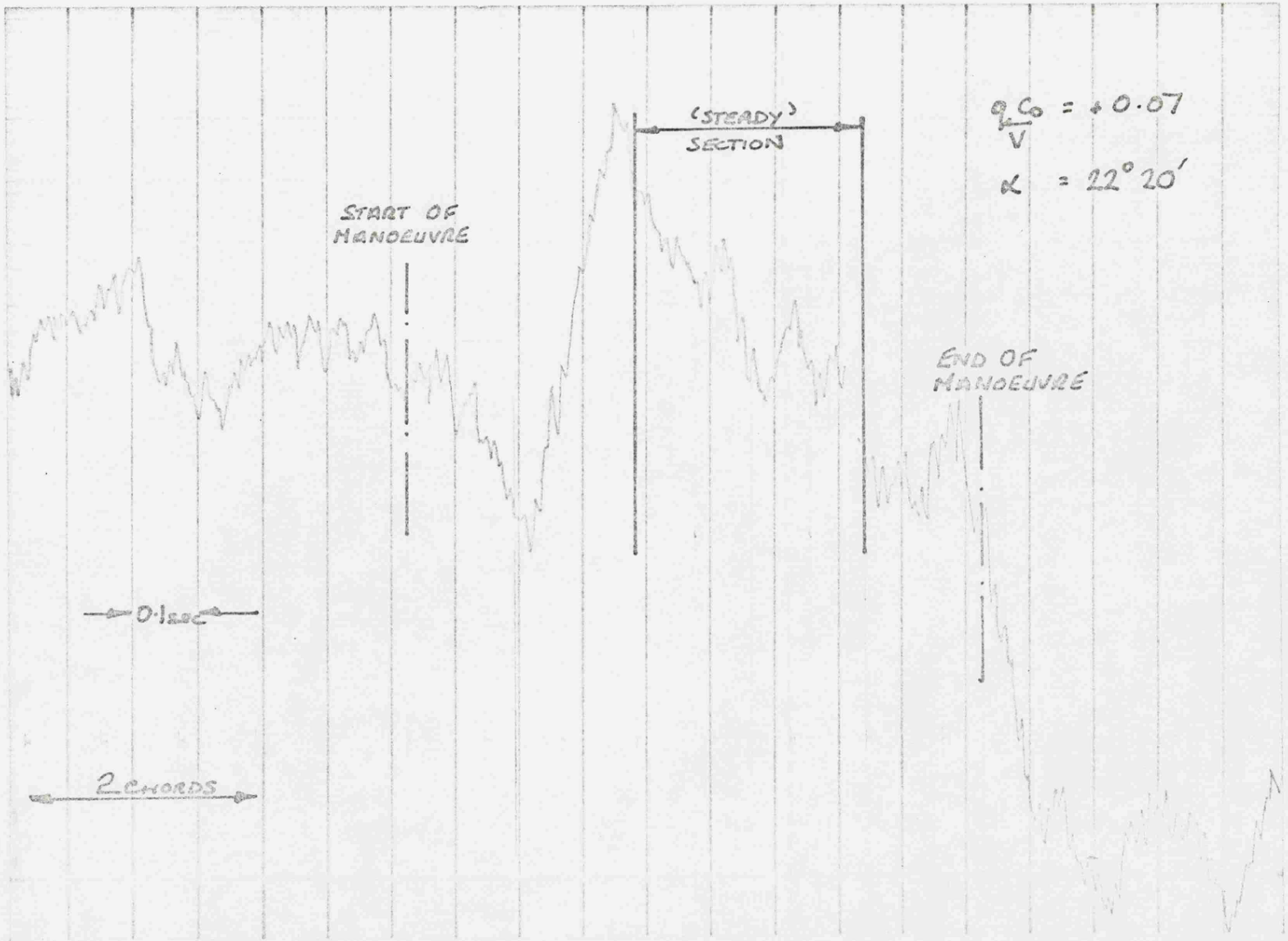

FIG 4.25 A TYPICAL U/V TRACE FOR A CONSTANT q MANOEUVRE (NORMAL FORCE)

FIG 4.25

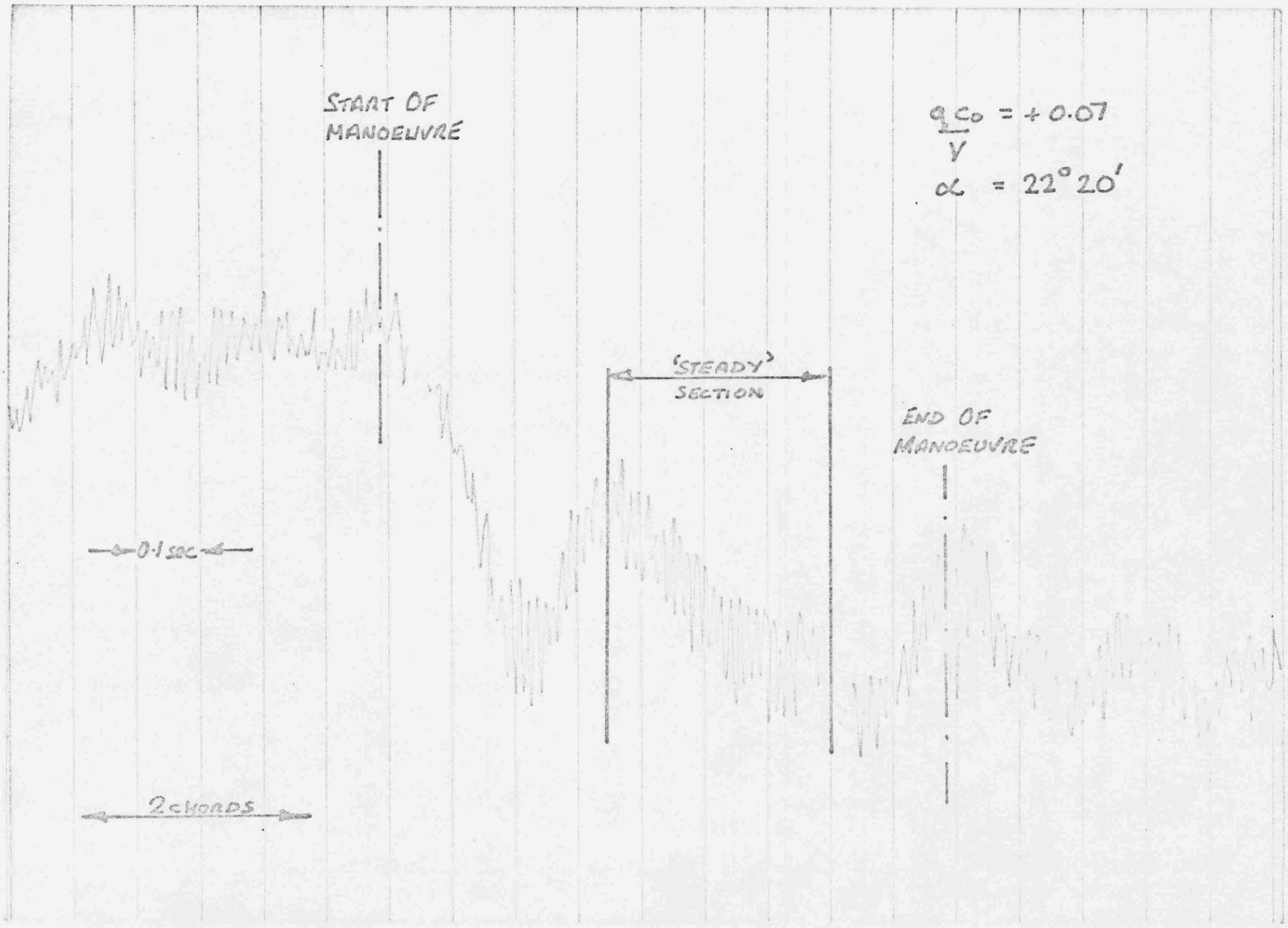

FIG 4.26 A TYPICAL TRACE FOR A CONSTANT q_1 MANOEUVRE (PITCHING MOMENT)

FIG 4.26

Fig 4.27

PITCHING AXIS AT ·667 C_o

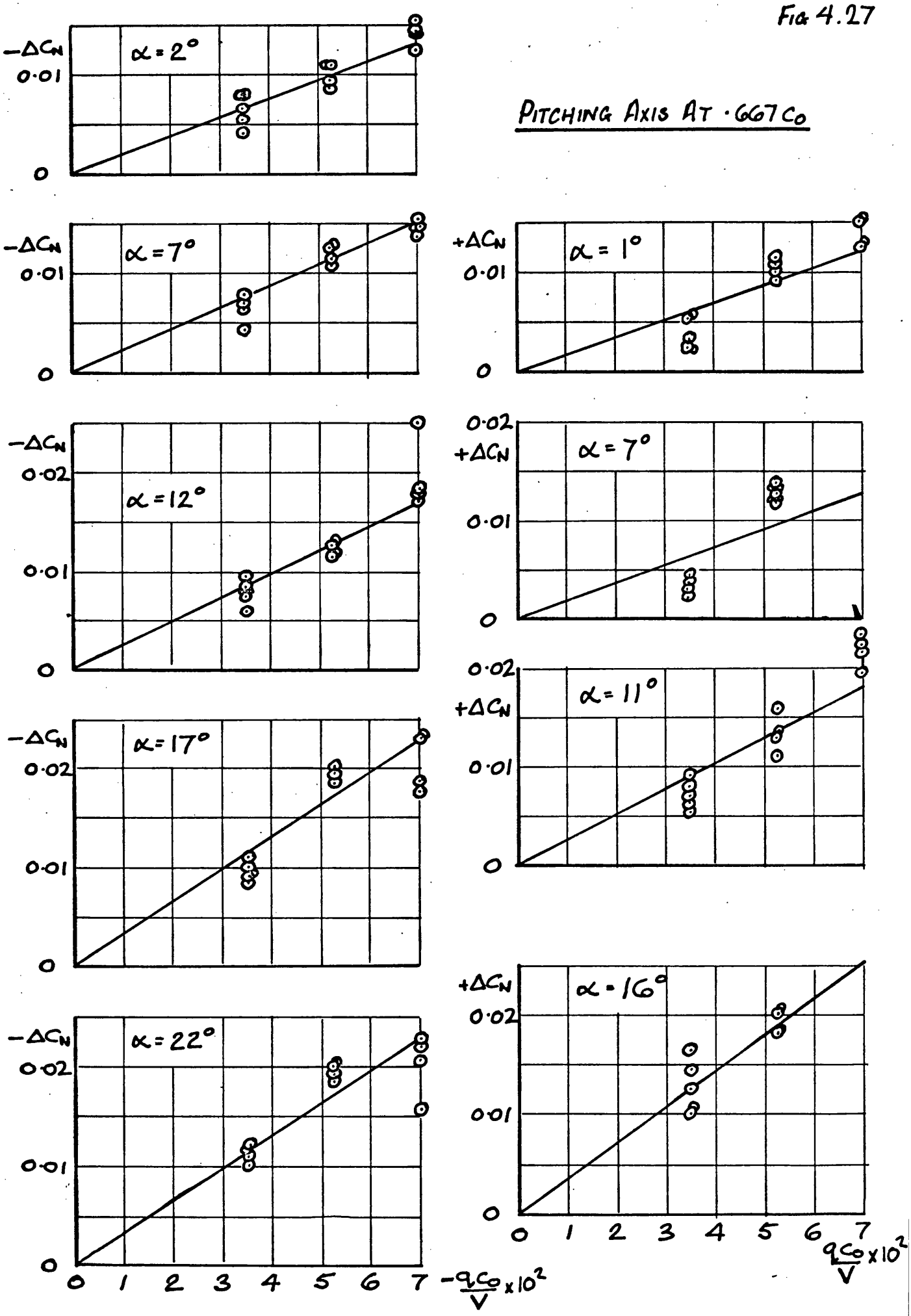

FIG 4.27 STEADY INCREMENT IN C_N DURING CONSTANT q MANOEUVRE PLOTTED AGAINST q TO FIND DERIVATIVE

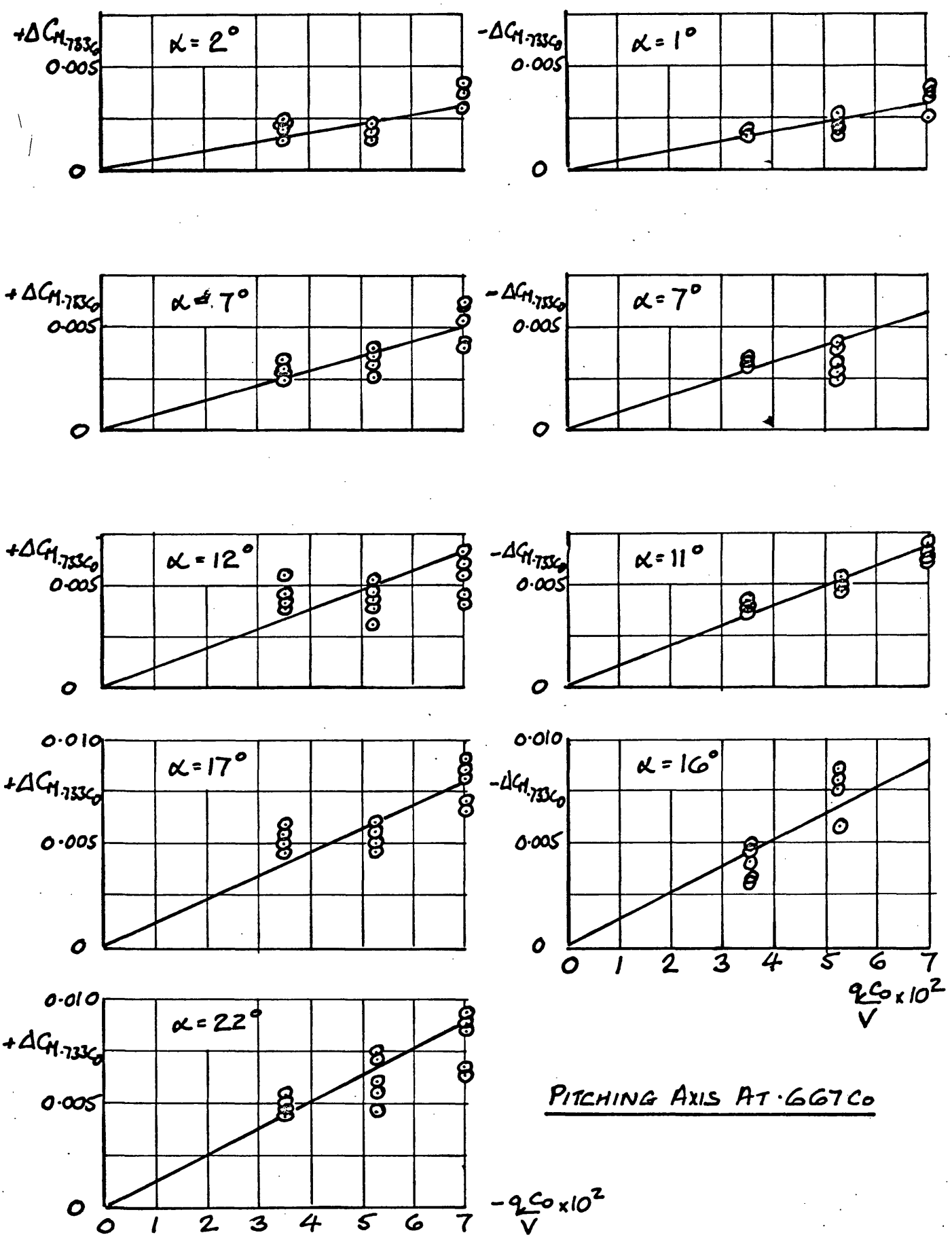

PITCHING AXIS AT ·667 Co

FIG 4.28 STEADY INCREMENT IN $C_{M\cdot733C_0}$ DURING CONSTANT $\dot{q}$ MANOEUVRE PLOTTED AGAINST q TO FIND DERIVATIVE

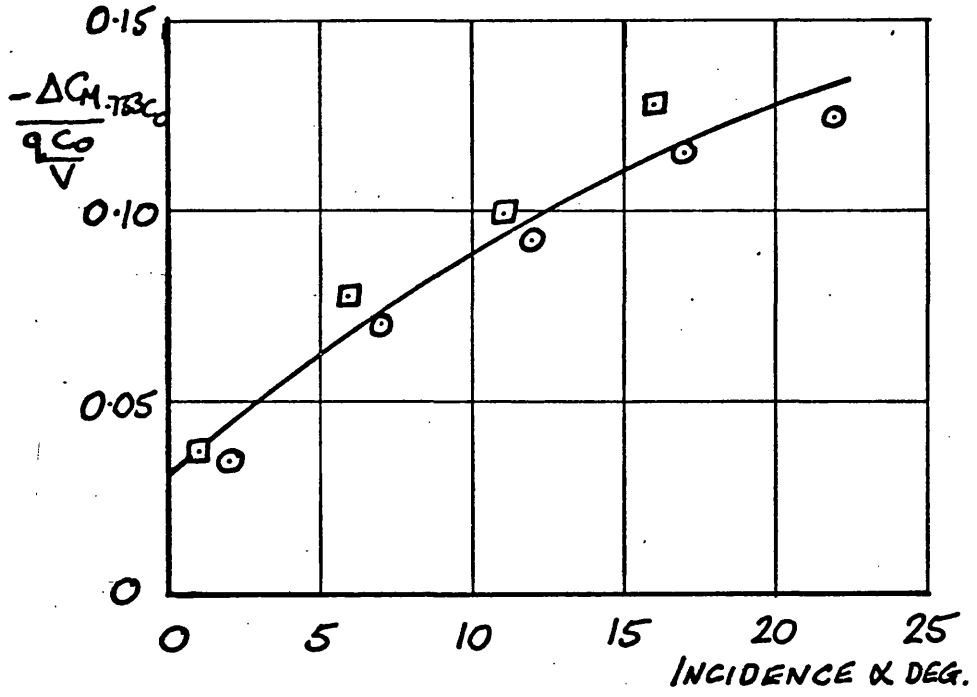

⊡ POSITIVE q_V
⊙ NEGATIVE q_V

PITCHING AXIS AT ·667 C_0

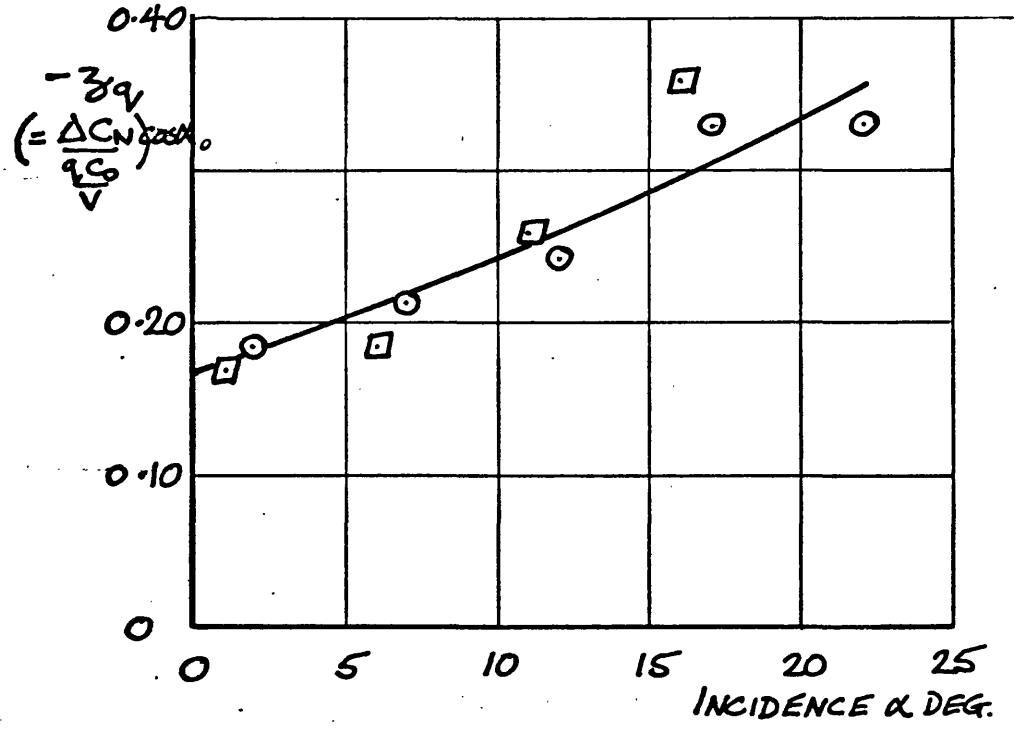

FIG. 4.29 VARIATION OF PITCHING MOMENT DERIVATIVE $\frac{\Delta C_{M\cdot 733 C_0}}{\frac{qC_0}{V}}$ AND NORMAL FORCE DERIVATIVE z_{q_V} WITH INCIDENCE

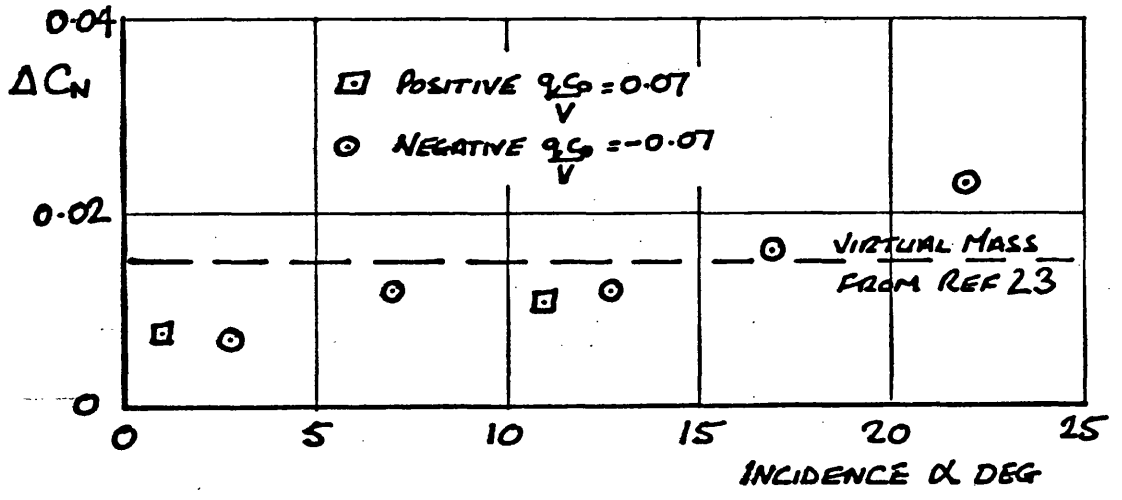

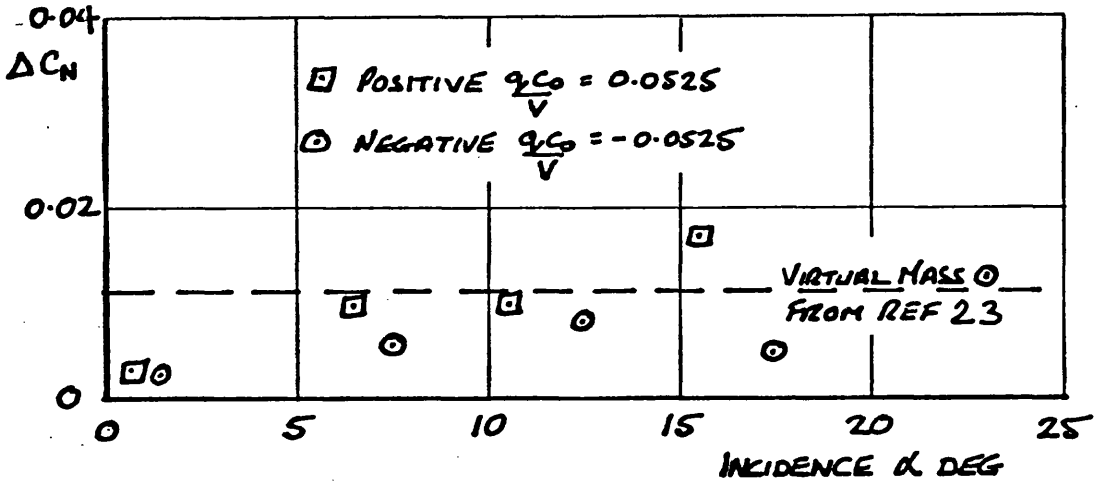

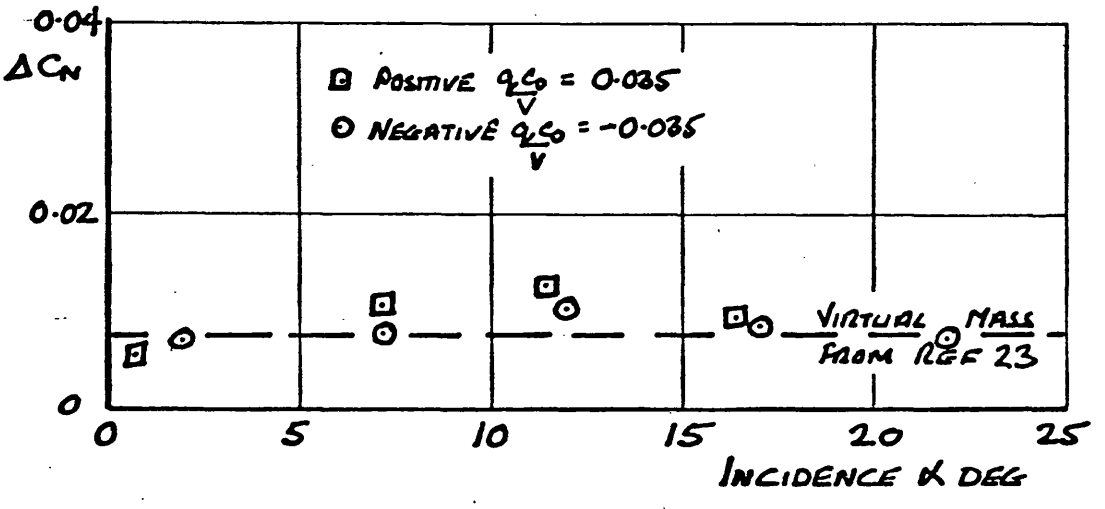

FIG 4.30 TRANSIENT IMPULSE IN NORMAL FORCE AT START OF CONSTANT q_∞ MANOEUVRE AND A COMPARISON WITH THE THEORETICAL VIRTUAL MASS

FIG 4.31 RUN AT CONSTANT $\dot{\theta}$ USING BOTH FILTERS

FIG 4.31

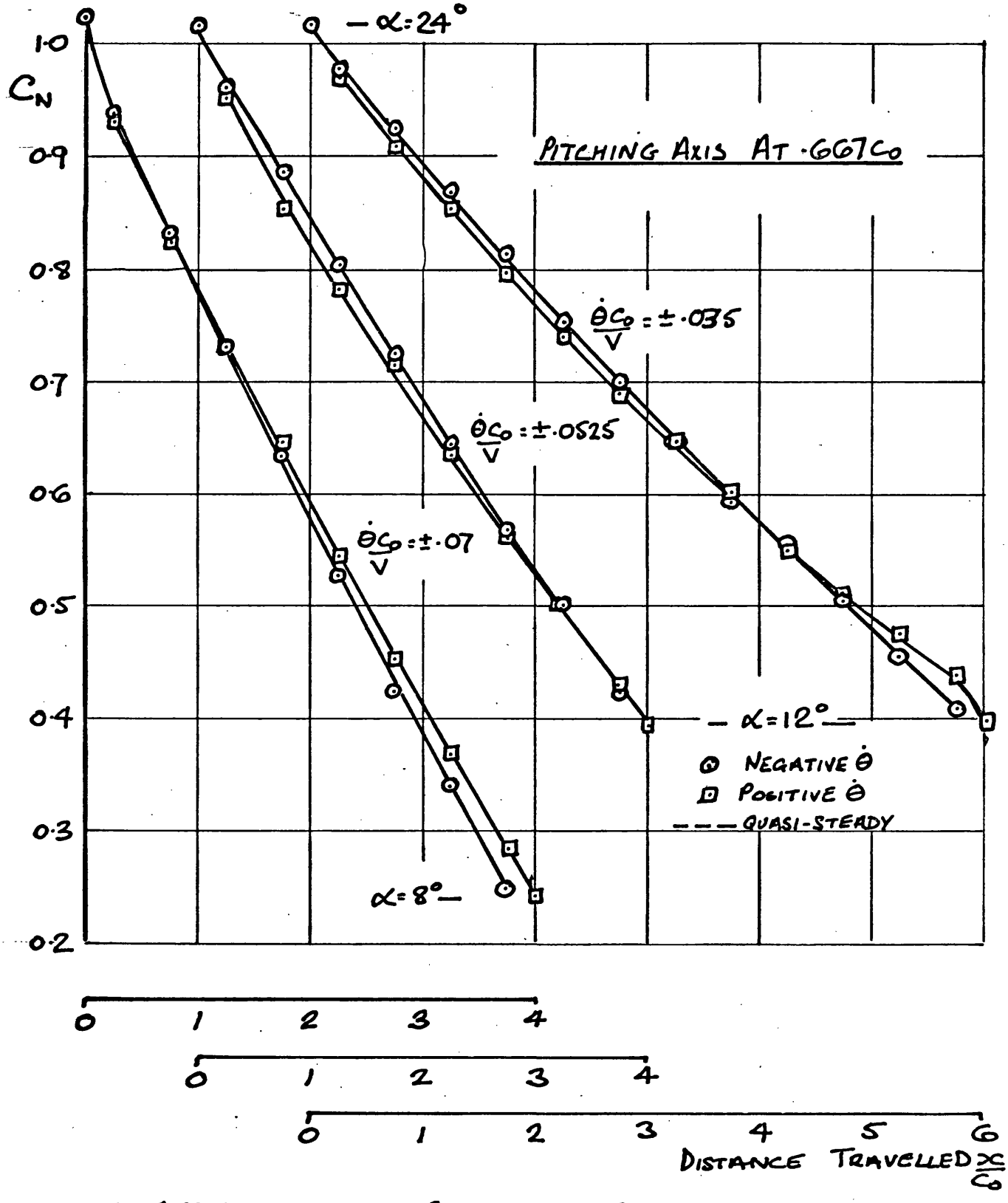

FIG 4.32 VARIATION OF C_N DURING PITCHING MANOEUVRE (CONSTANT $\dot{\theta}$) WITH INITIAL INCIDENCE 24° AND FOR 3 PITCHING RATES

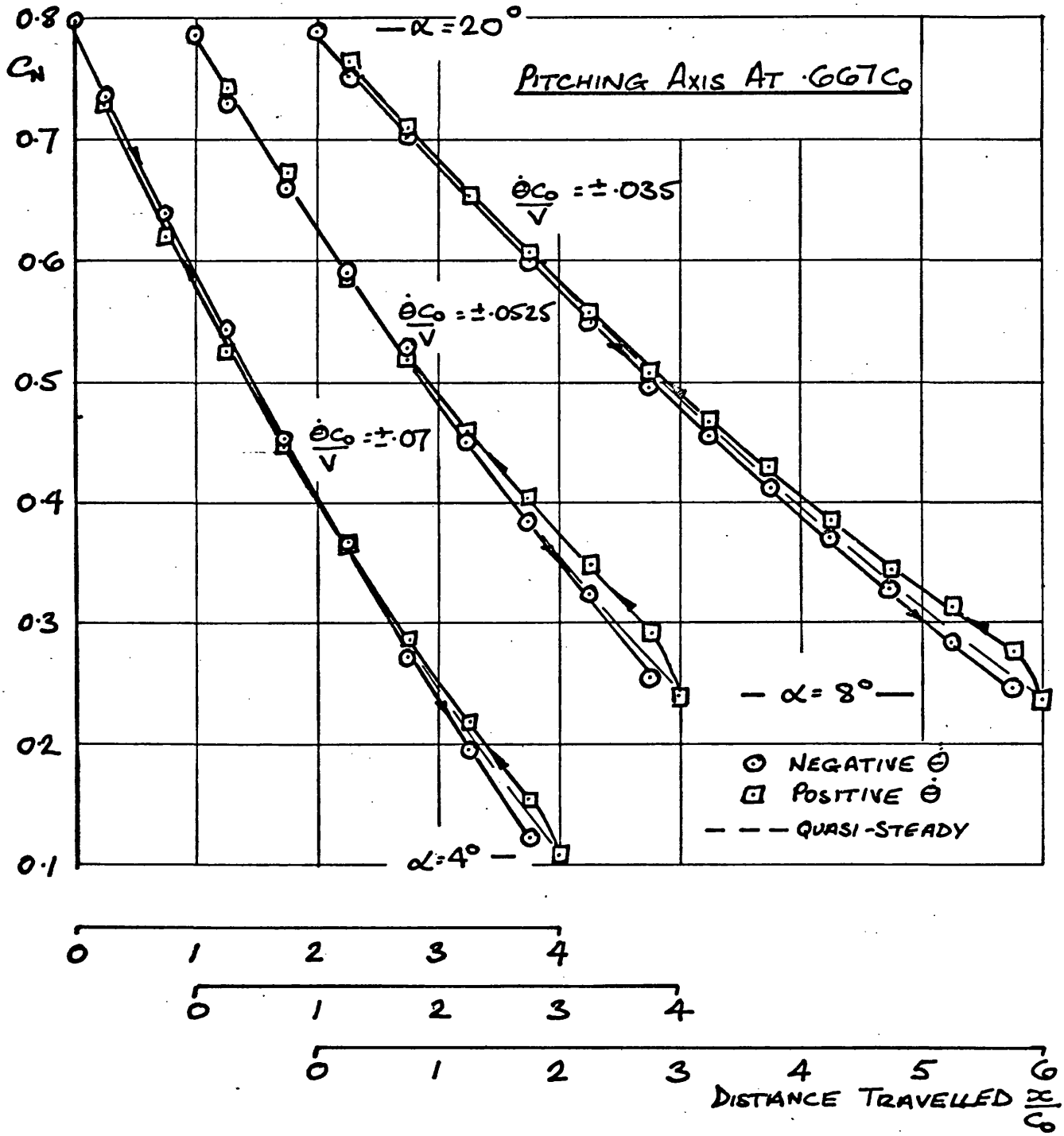

FIG 4.33 VARIATION OF C_N DURING PITCHING MANOEUVRE (CONSTANT $\dot{\theta}$) WITH INITIAL INCIDENCE 20° AND FOR 3 PITCHING RATES

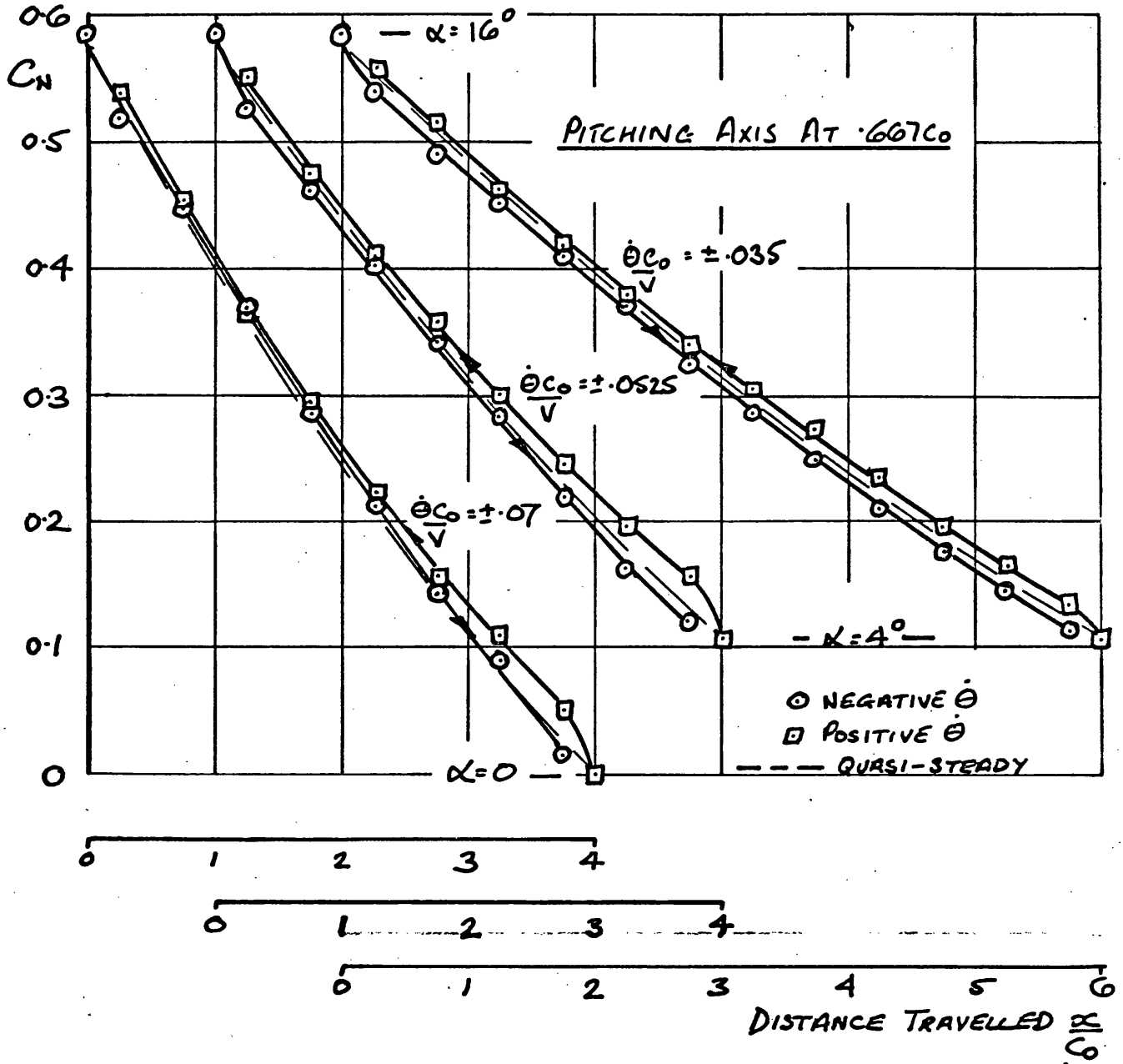

FIG 4.34 VARIATION OF C_N DURING PITCHING MANOEUVRE (CONSTANT $\dot{\theta}$) WITH INITIAL INCIDENCE 16° AND FOR 3 PITCHING RATES

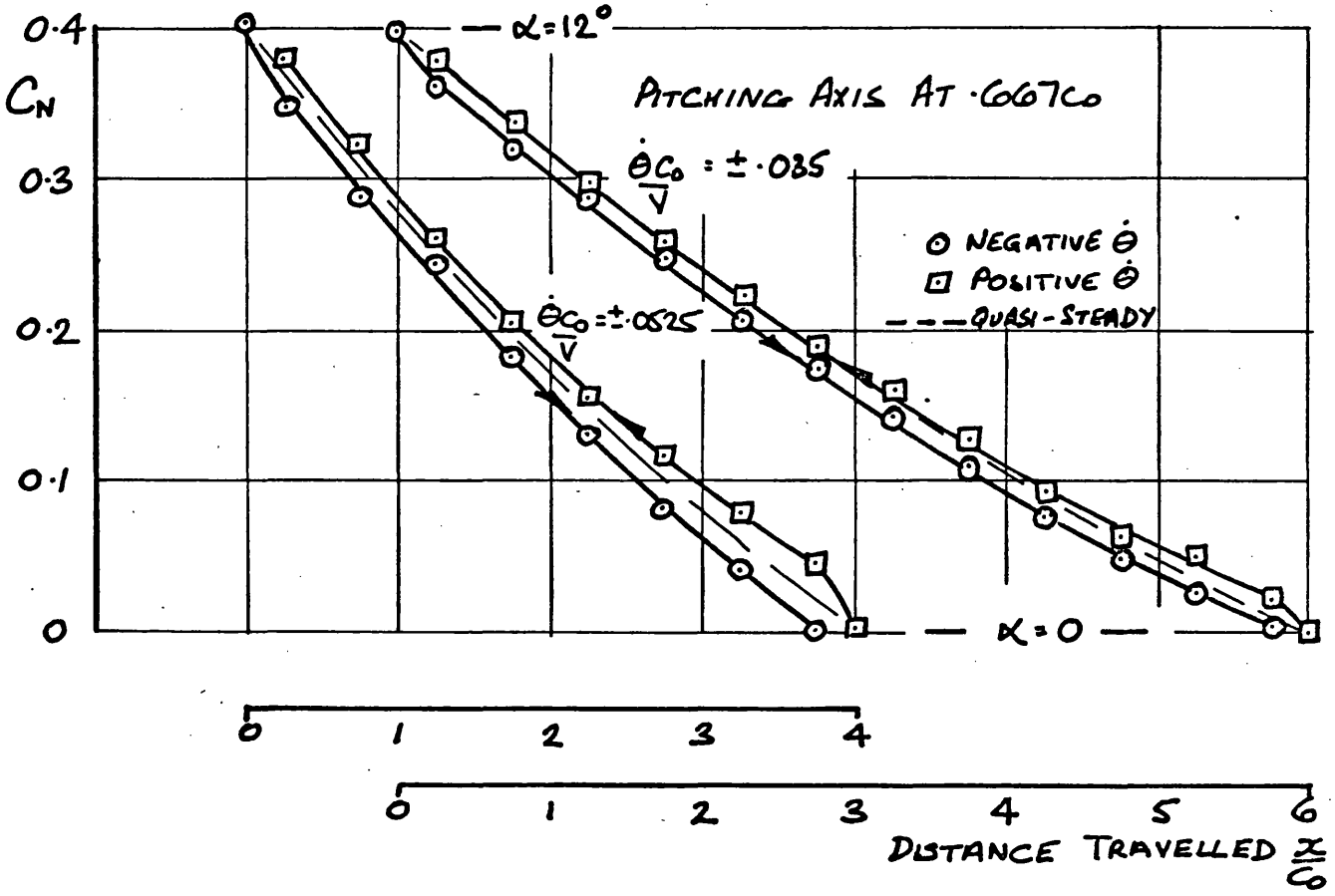

FIG 4.35 VARIATION OF C_N DURING PITCHING MANOEUVRE (CONSTANT $\dot{\theta}$) WITH INITIAL INCIDENCE 12° AND FOR 2 PITCHING RATES

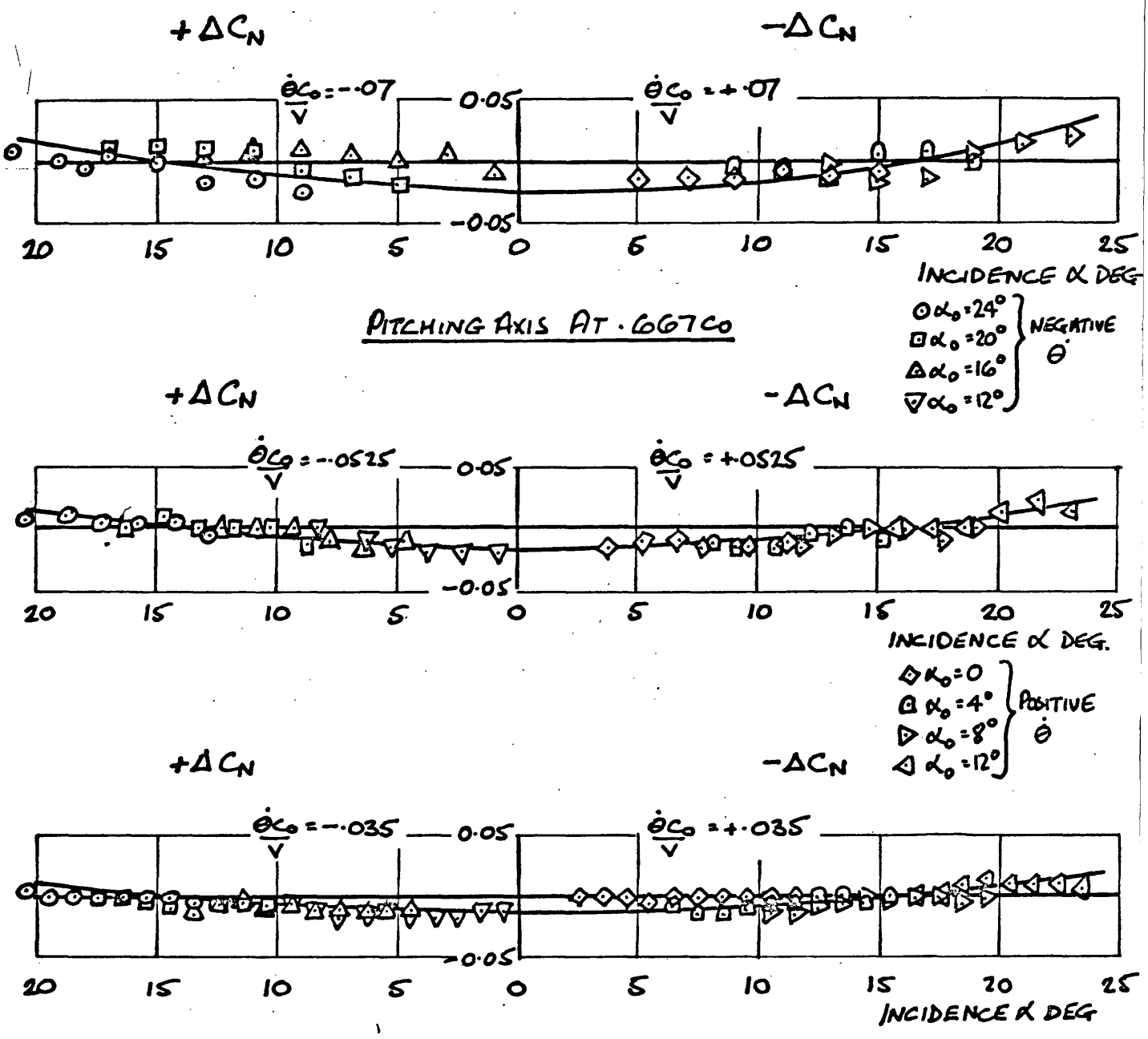

FIG 4.36 VARIATION OF ΔC_N WITH INCIDENCE DURING PITCHING MANOEUVRE (EXCLUDING TRANSIENT) FOR 3 PITCHING RATES

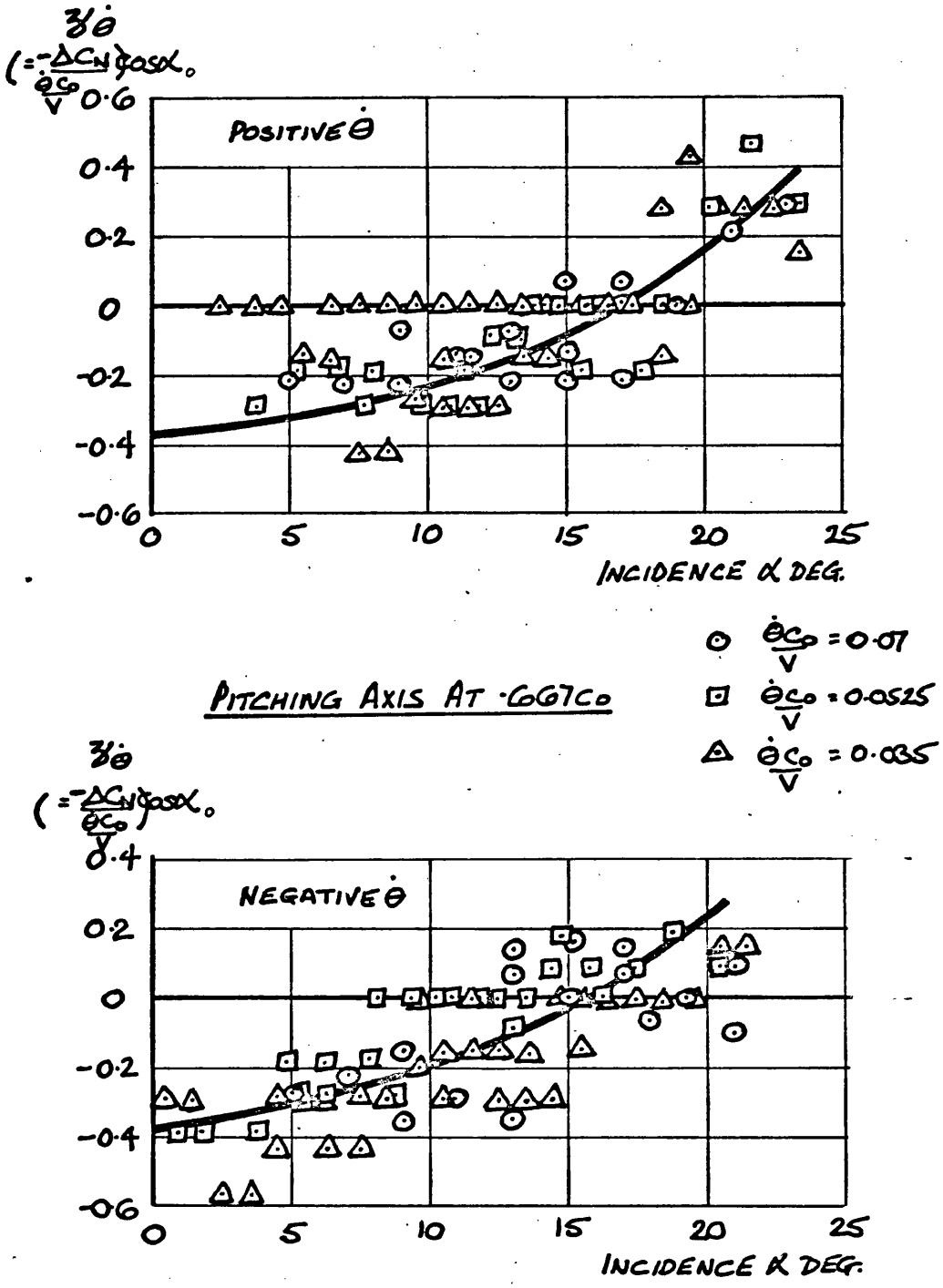

FIG 4.37 NORMAL FORCE DERIVATIVE $Z_{\dot\theta}$ FOR POSITIVE AND NEGATIVE PITCHING RATES

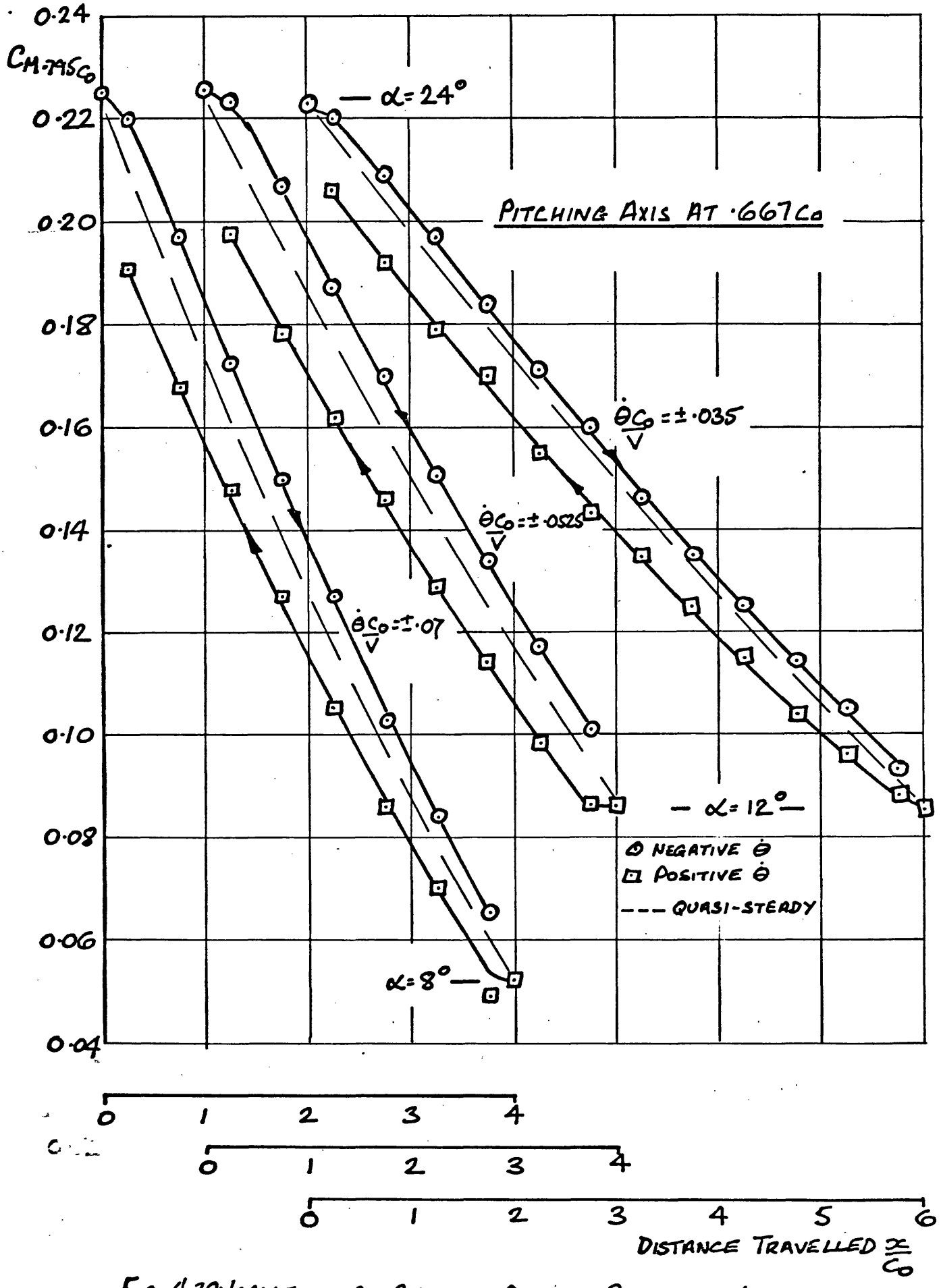

FIG 4.38 VARIATION OF $C_{M\cdot795C_0}$ DURING PITCHING MANOEUVRE (CONSTANT $\dot{\theta}$) WITH INITIAL INCIDENCE 24° AND FOR 3 PITCHING RATES

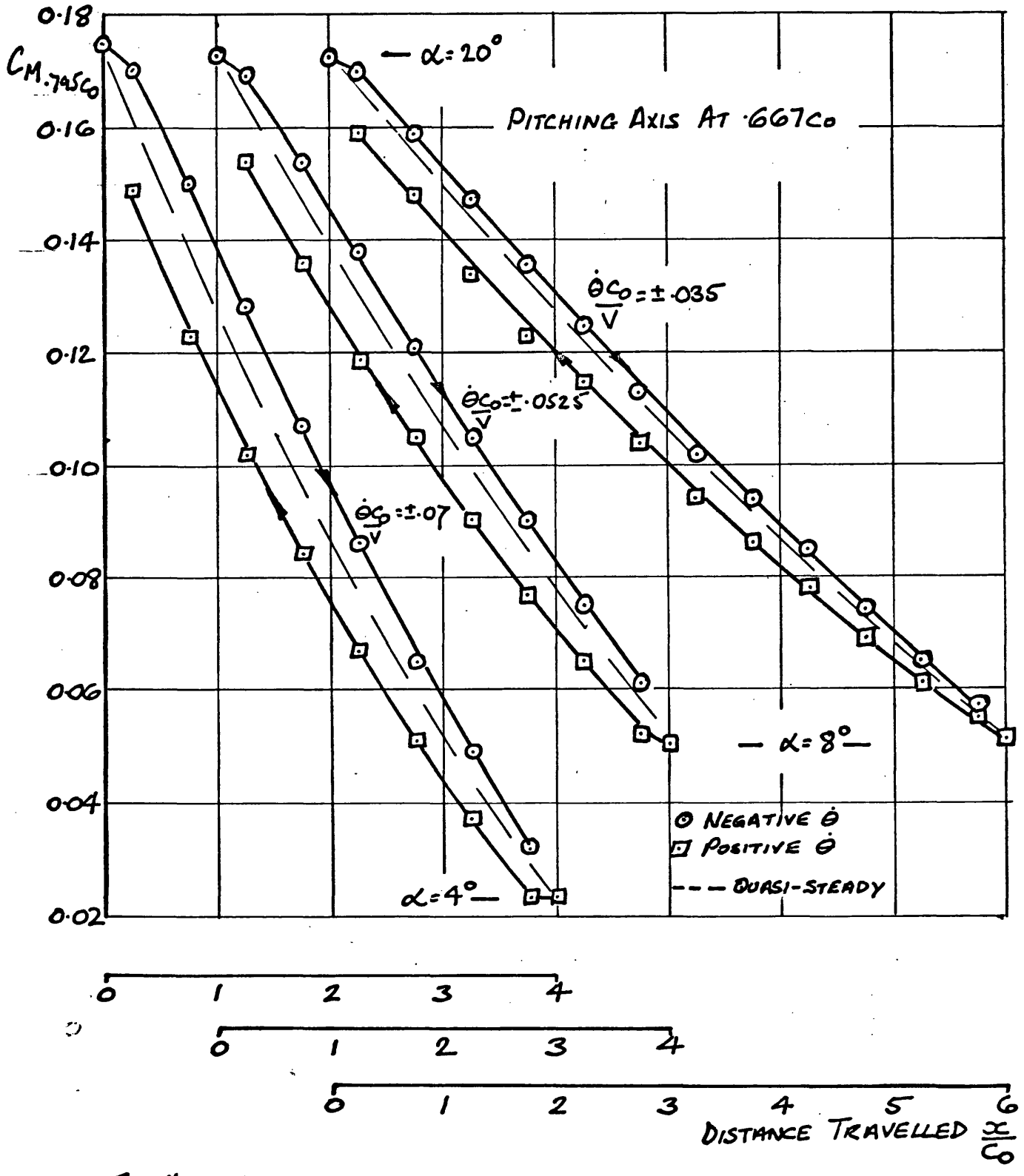

FIG 4.39 VARIATION OF $C_{M\cdot795C_0}$ DURING PITCHING MANOEUVRE (CONSTANT $\dot{\theta}$) WITH INITIAL INCIDENCE 20° AND FOR 3 PITCHING RATES

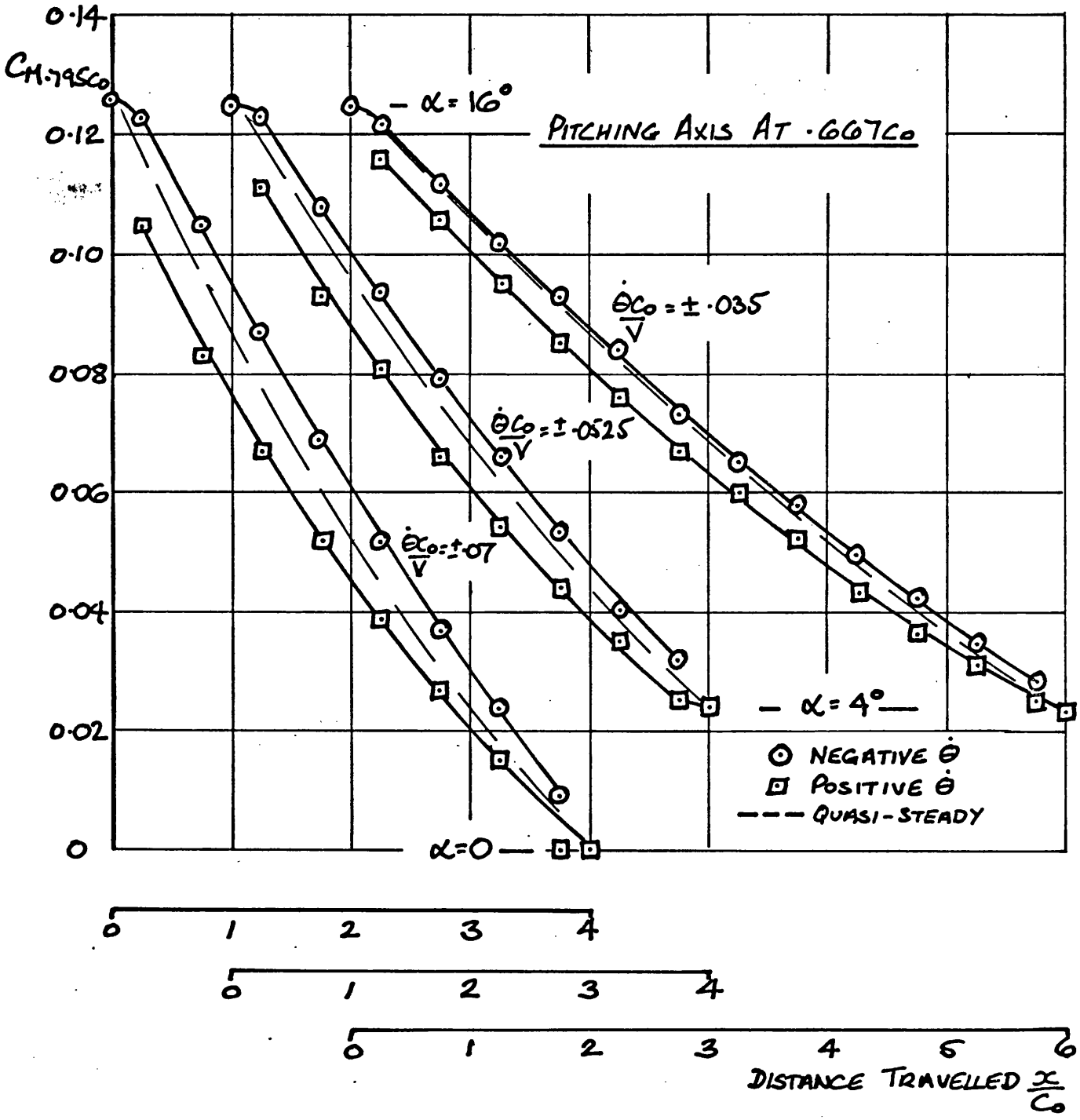

FIG 4.40 VARIATION IN $C_{M\cdot 795C_0}$ DURING PITCHING MANOEUVRE (CONSTANT $\dot{\theta}$) WITH INITIAL INCIDENCE 16° AND FOR 3 PITCHING RATES

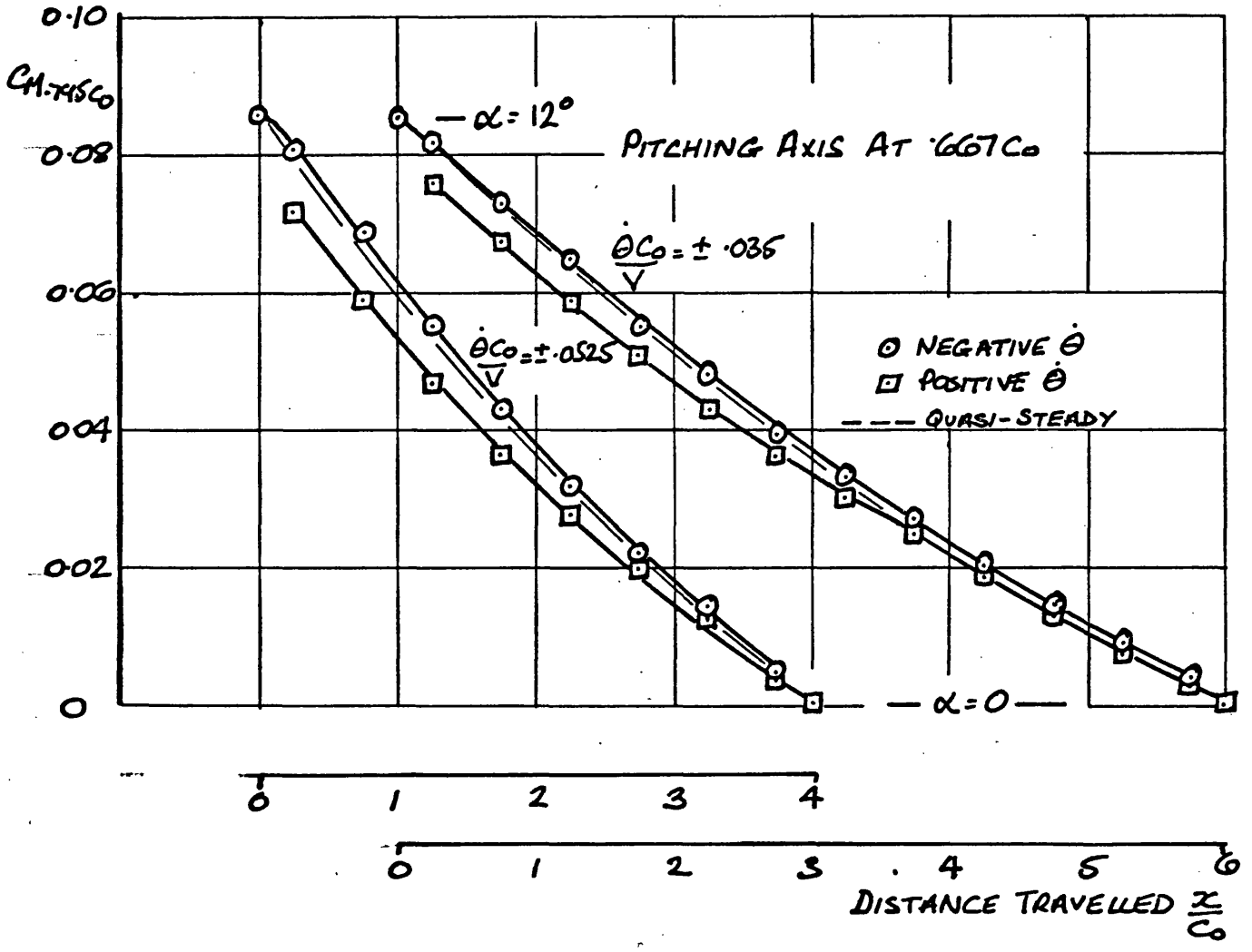

FIG 4.41 VARIATION OF $C_{M\cdot 75C_0}$ DURING PITCHING MANOEUVRE (CONSTANT $\dot{\theta}$) WITH INITIAL INCIDENCE 12° AND FOR 2 PITCHING RATES

FIG 4.42

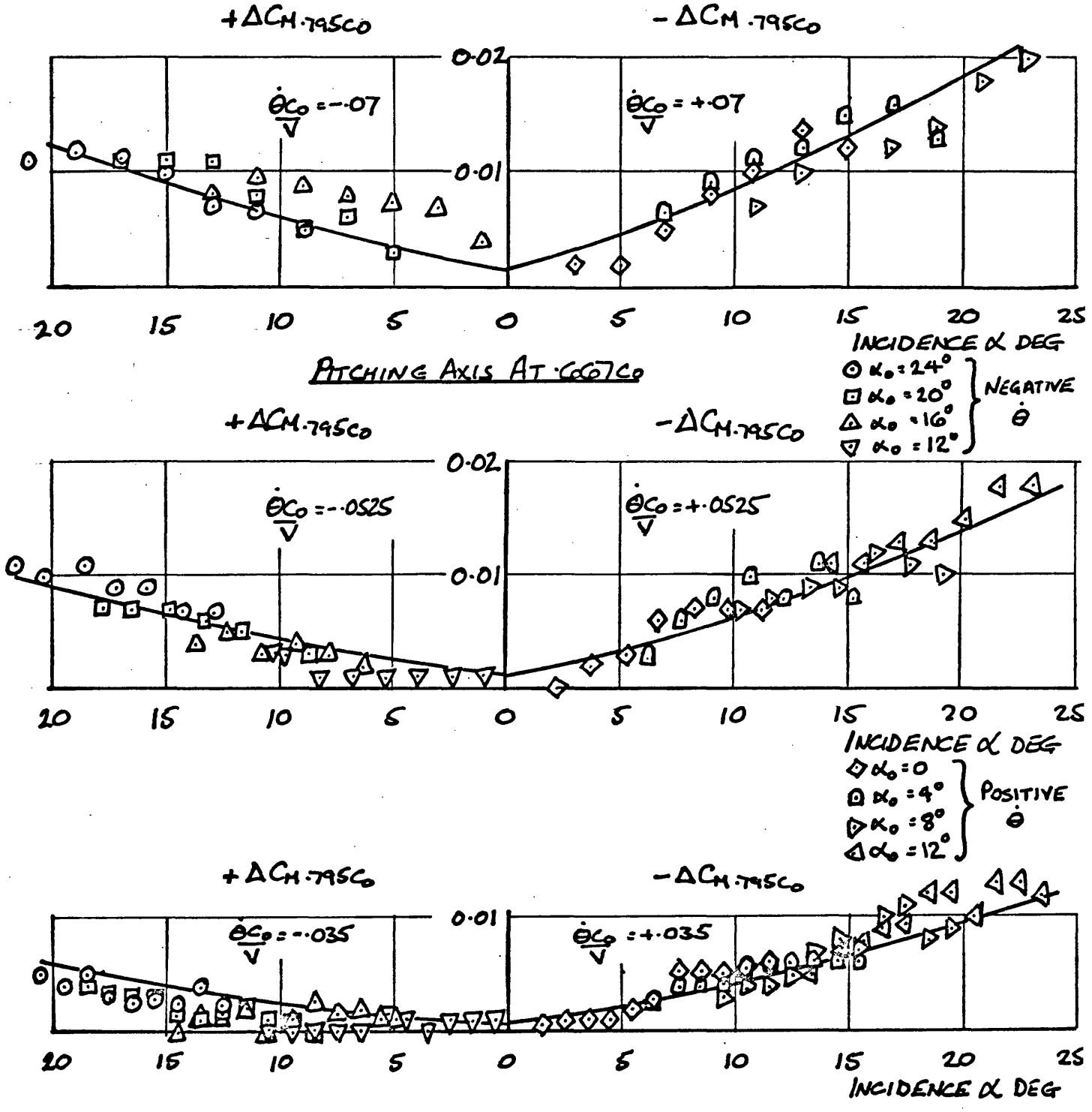

FIG 4.42 VARIATION OF ΔCM·795CO WITH INCIDENCE DURING PITCHING MANOEUVRE (EXCLUDING TRANSIENT) FOR 3 PITCHING RATES

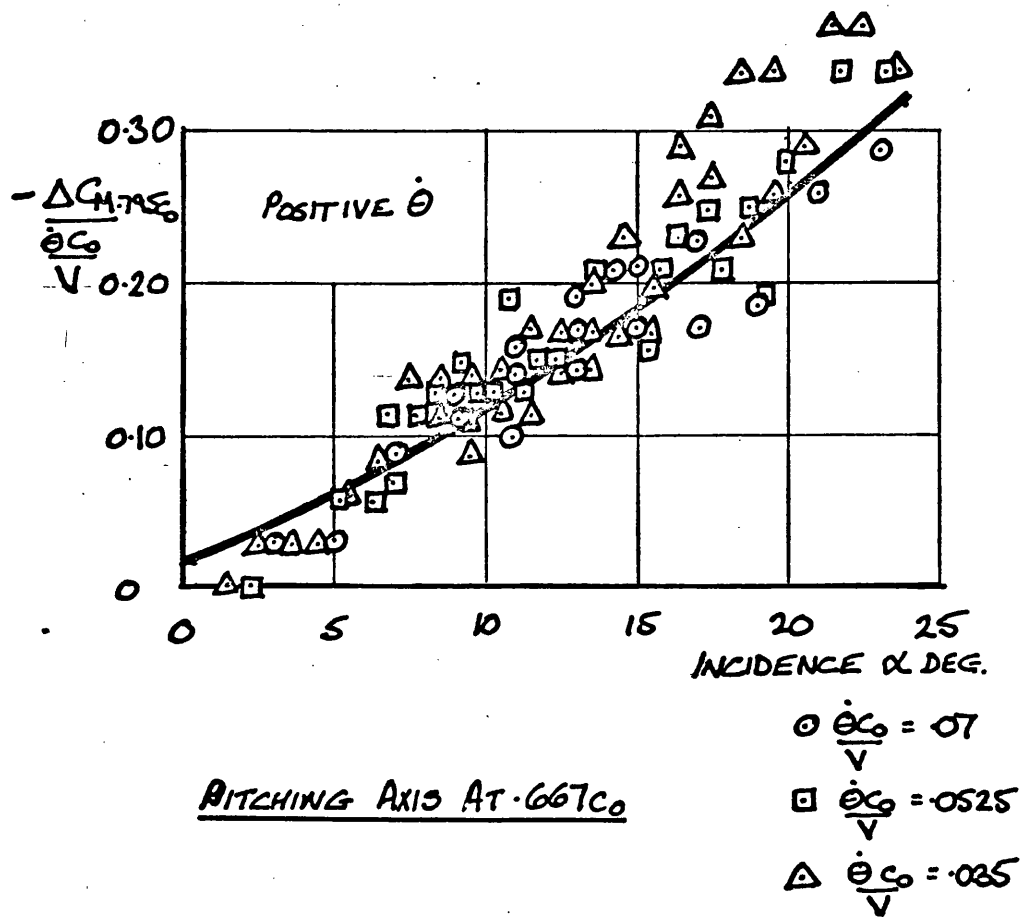

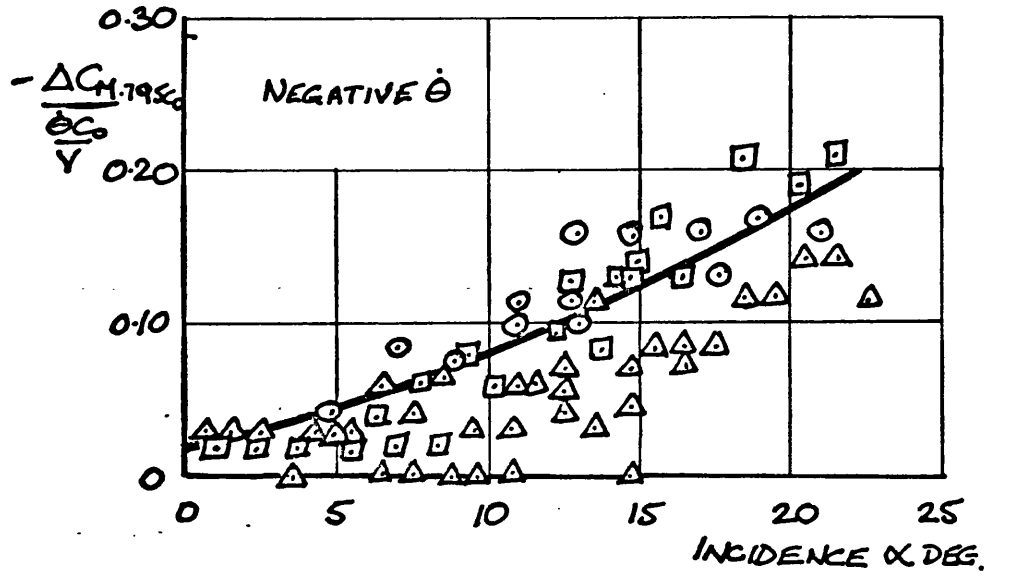

FIG 4.43 PITCHING MOMENT DERIVATIVE $\frac{\Delta C_{M\cdot 79 C_0}}{\frac{\dot\theta C_0}{V}}$ FOR POSITIVE AND NEGATIVE PITCHING RATES

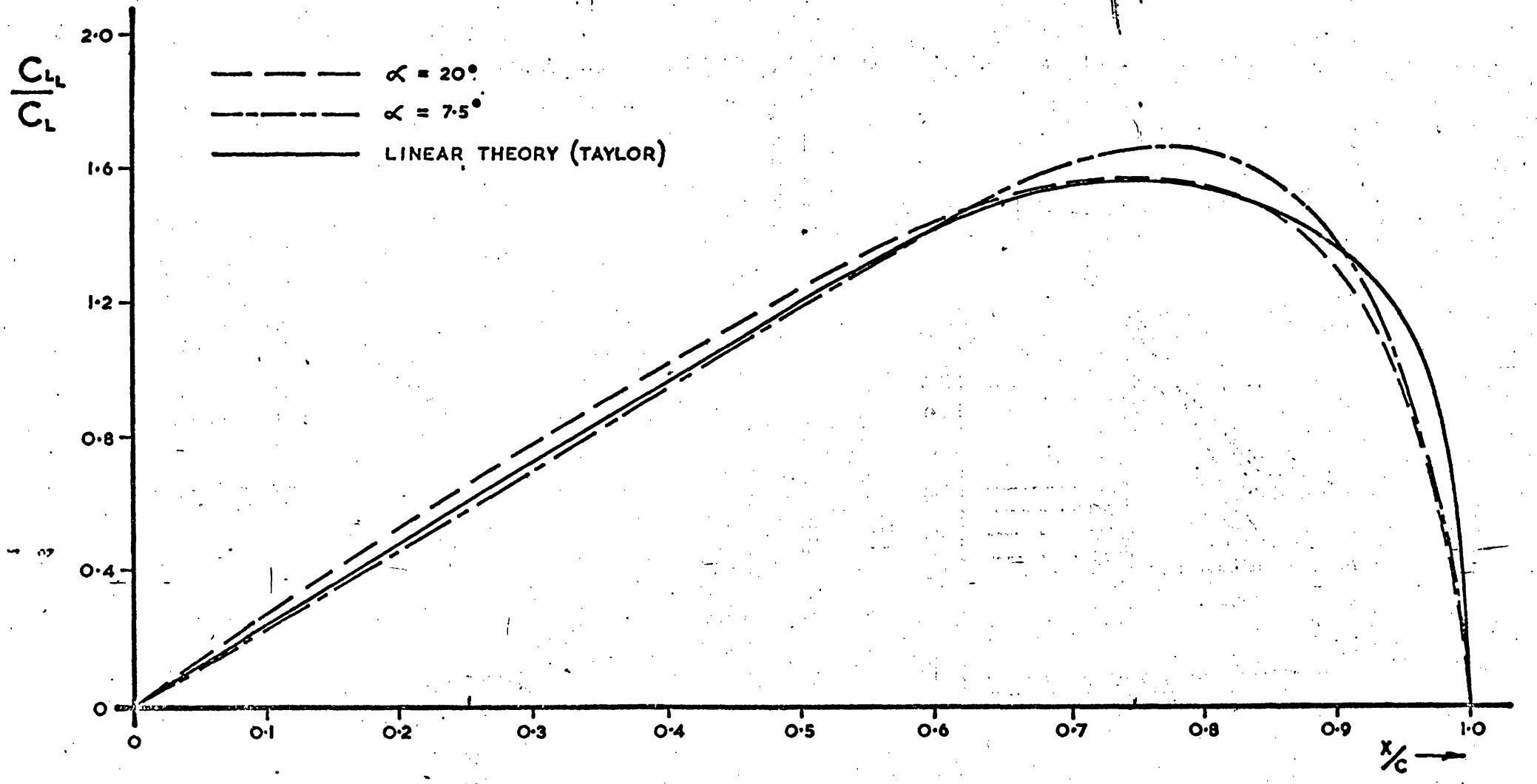

FIG 4.44 CHORDWISE LIFT DISTRIBUTION ON A SLENDER DELTA WING (FROM REF. 25)

FIG 4.44

PITCHING AXIS AT ·667 Co

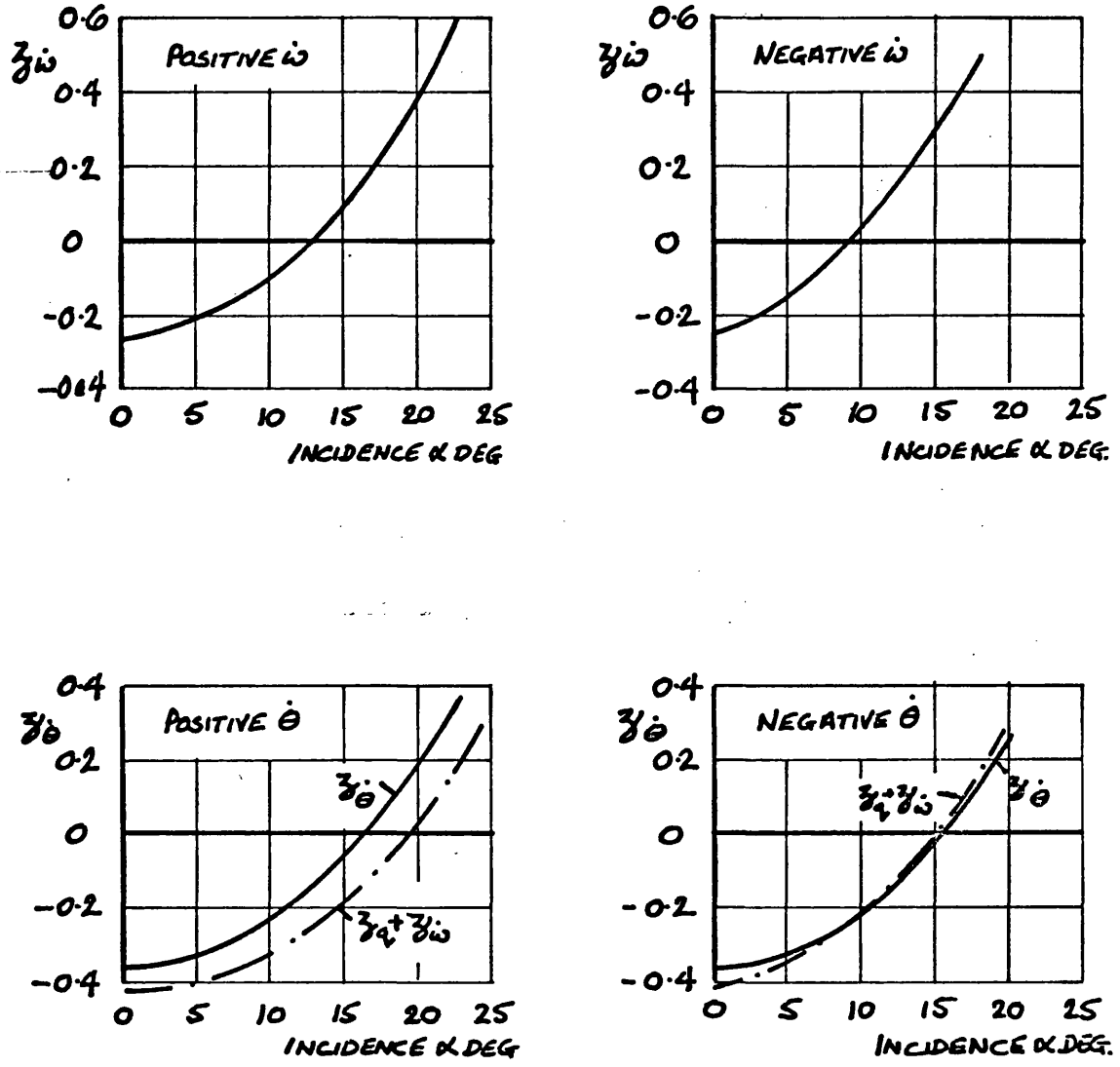

FIG 4.45 COMPARISON OF NORMAL FORCE DERIVATIVES $z_{\dot{w}}$, z_q, $z_{\dot{\theta}}$ AND THEIR VARIATION WITH INCIDENCE

ALL PITCHING MOMENTS CONVERTED TO THE PITCHING AXIS AT ·66 7C

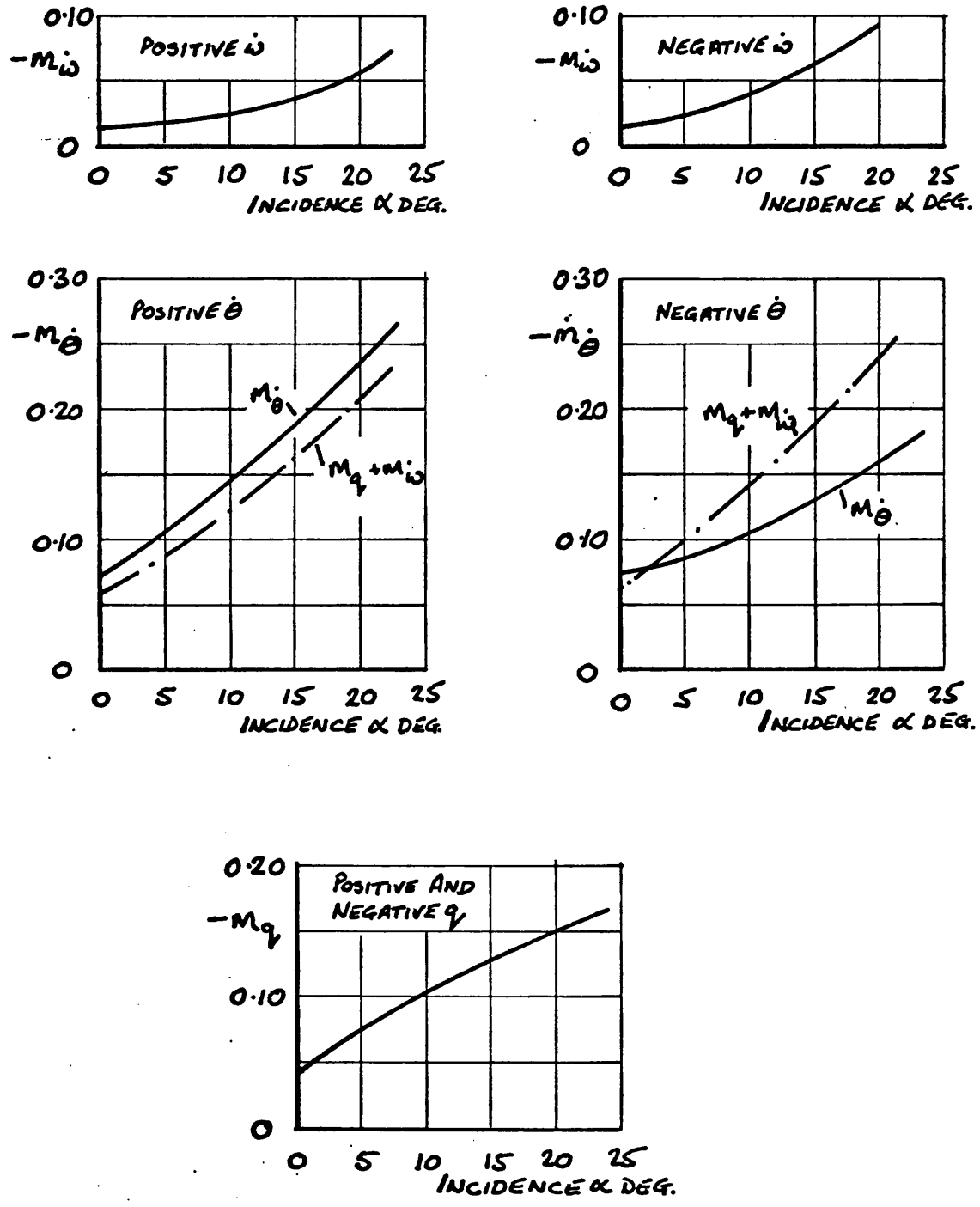

FIG 4.46 COMPARISON OF PITCHING MOMENT DERIVATIVES $M_{\dot{w}}, M_q, M_{\dot{\theta}}$ AND THEIR VARIATION WITH INCIDENCE

PITCHING AXIS AT ·667c₀

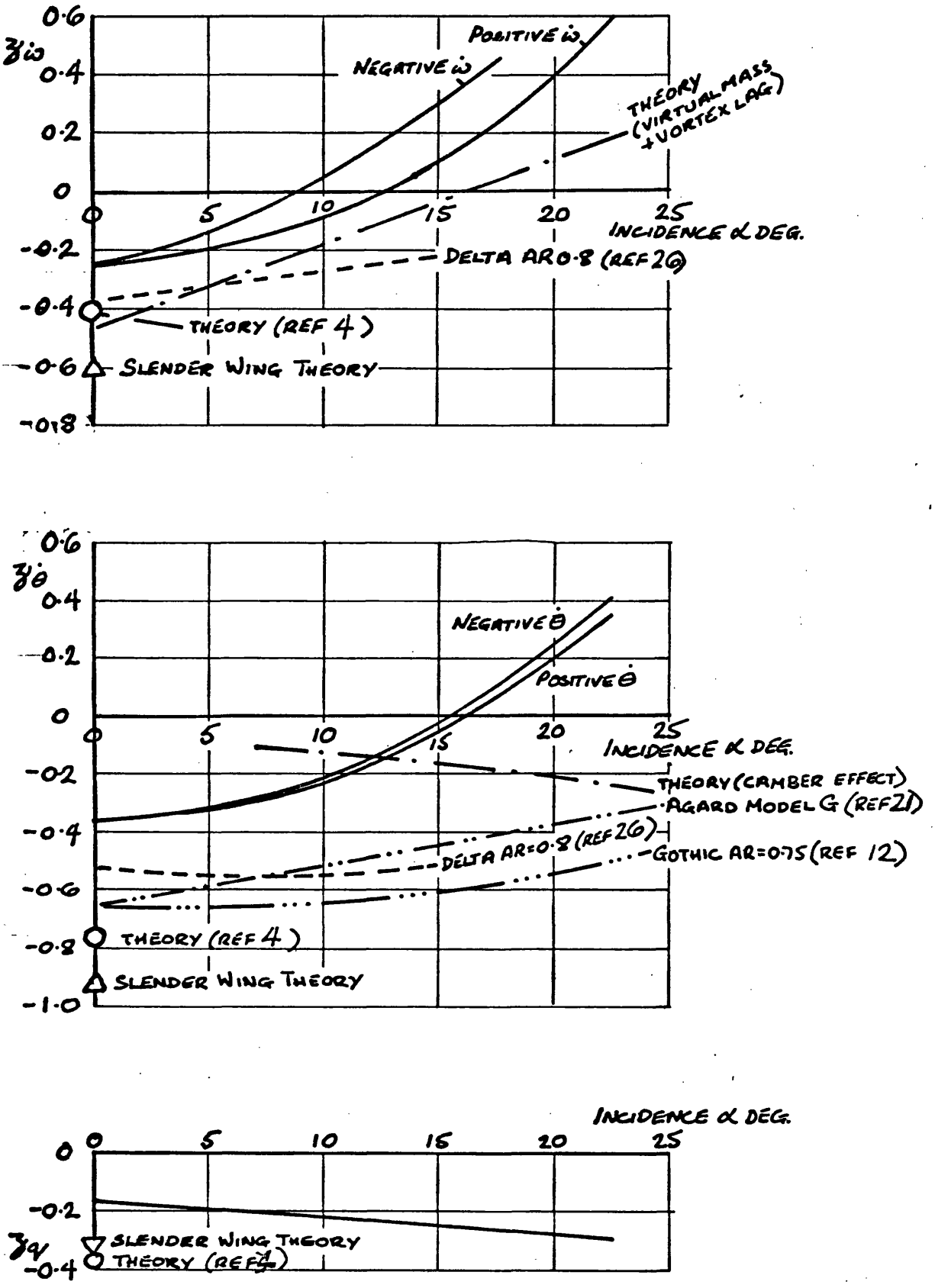

FIG 4.47 COMPARISON OF NORMAL FORCE DERIVATIVES $z_{\dot{w}}, z_q, z_{\dot{\theta}}$ WITH THEORY AND WITH OTHER EXPERIMENTAL RESULTS

ALL PITCHING MOMENTS CONVERTED TO THE PITCHING AXIS AT ·60 $\bar{c}_0$

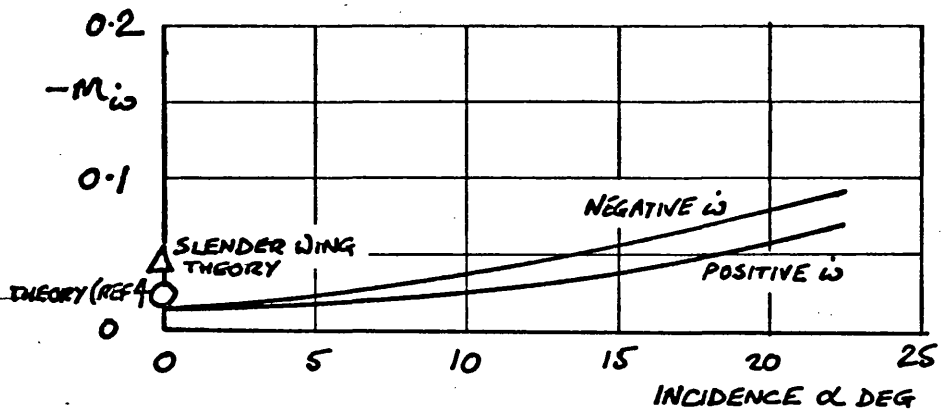

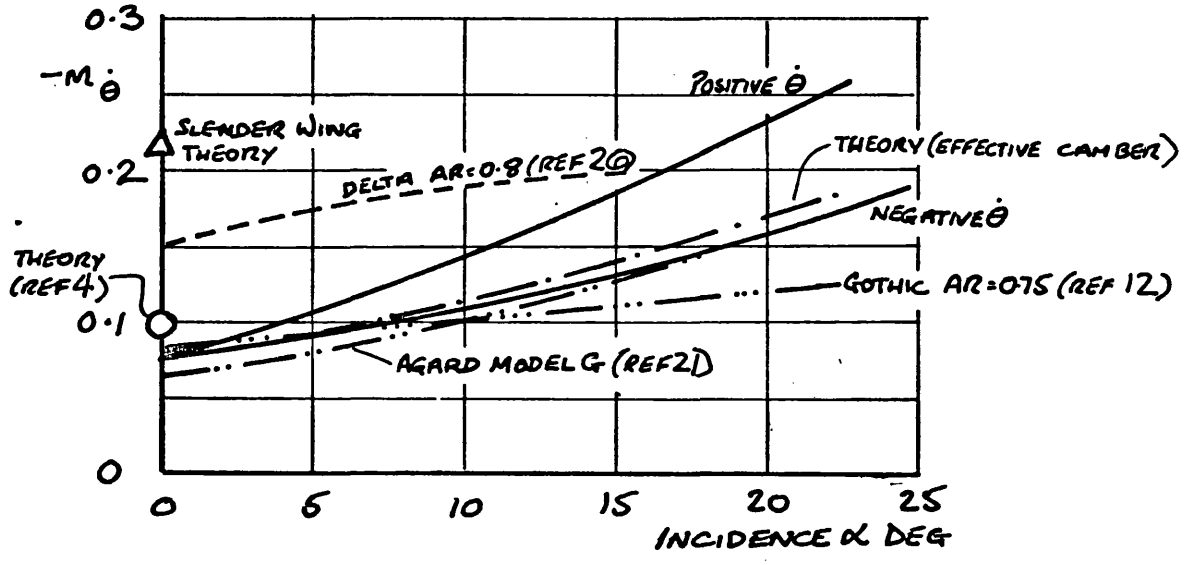

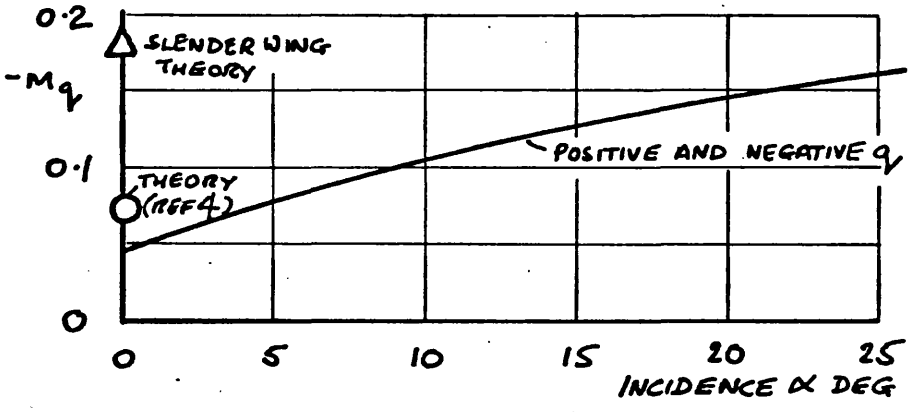

FIG 4.48 COMPARISON OF PITCHING MOMENT DERIVATIVES $M_{\dot{w}}, M_q, M_{\dot{\theta}}$ WITH THEORY AND OTHER EXPERIMENTAL RESULTS

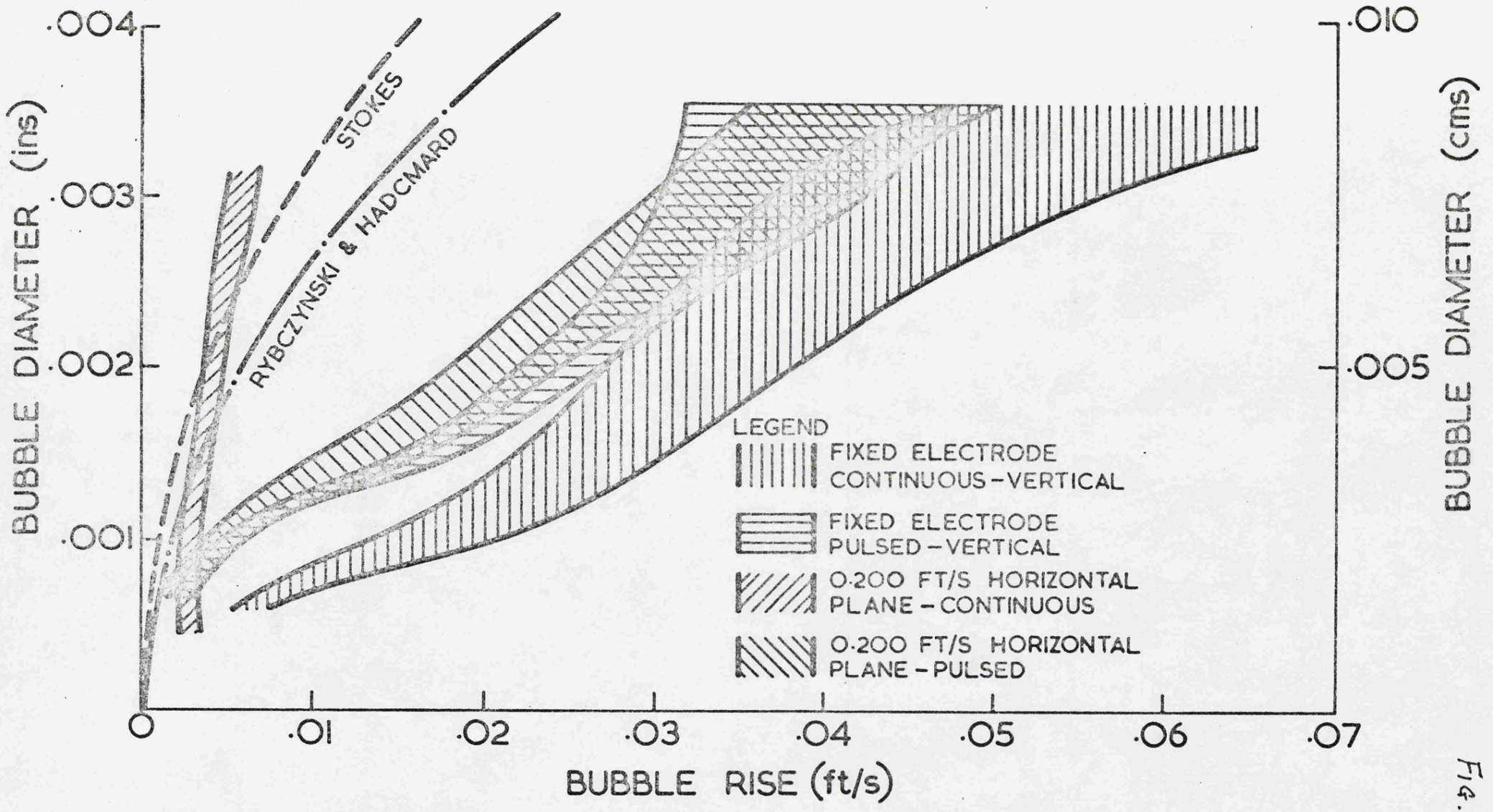

FIG 5.01 BUOYANCY OF HYDROGEN BUBBLES (FROM REF. 29)

Fig. 5.01

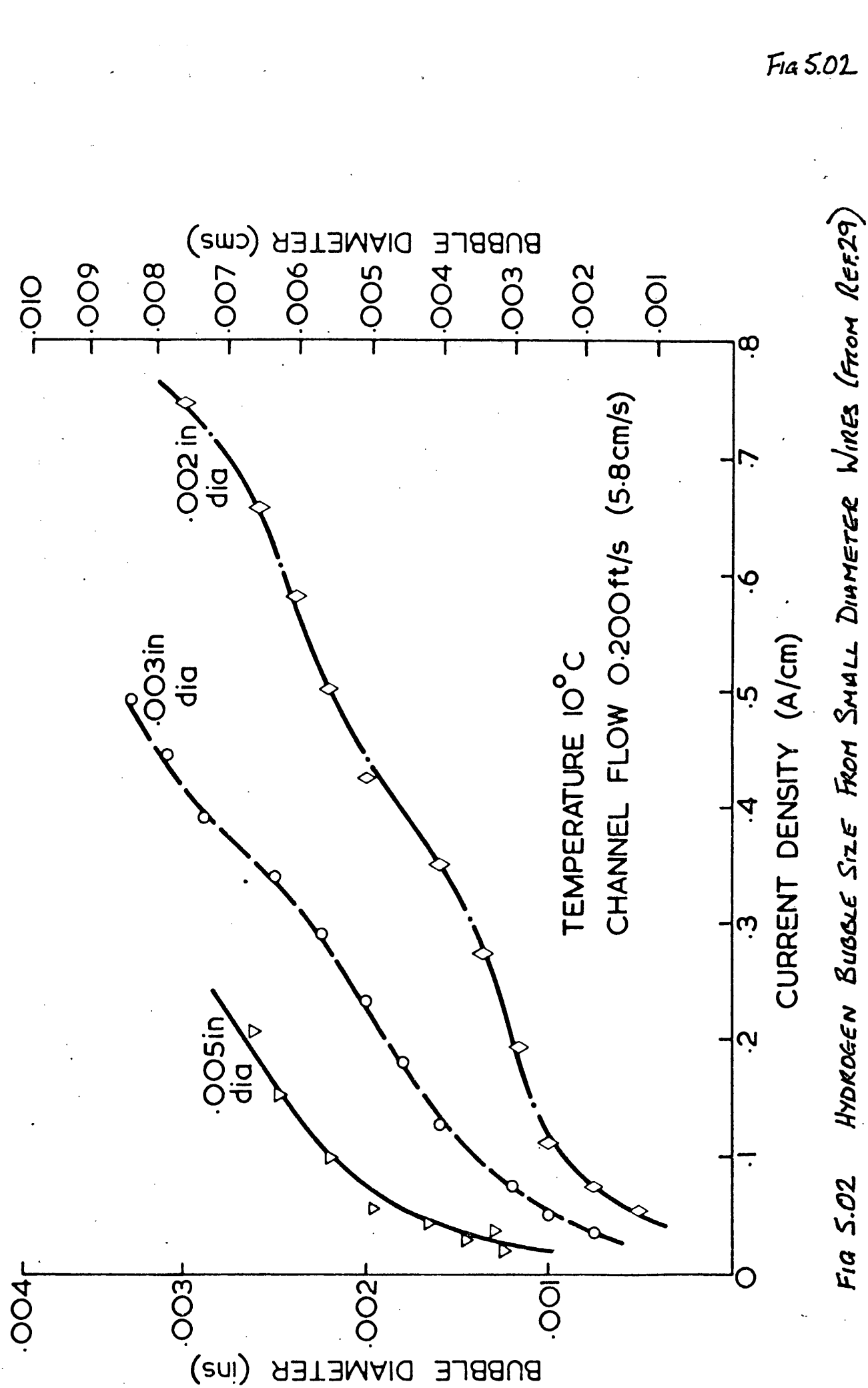

FIG 5.02 HYDROGEN BUBBLE SIZE FROM SMALL DIAMETER WIRES (FROM REF.29)

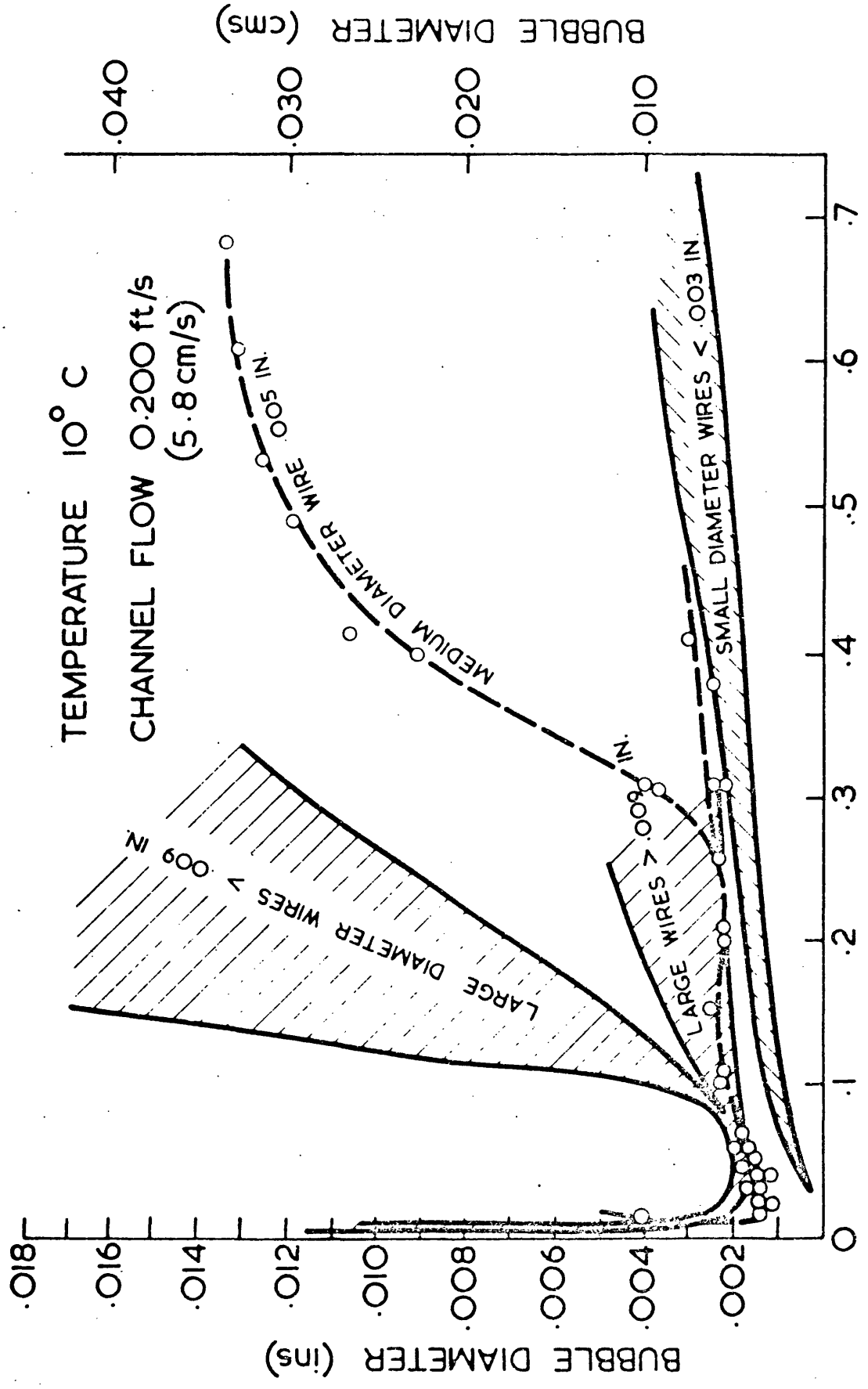

FIG 5.03 HYDROGEN BUBBLE SIZE FROM VARIOUS DIAMETER WIRES (FROM REF. 29)

FIGS 5.04
& 5.05

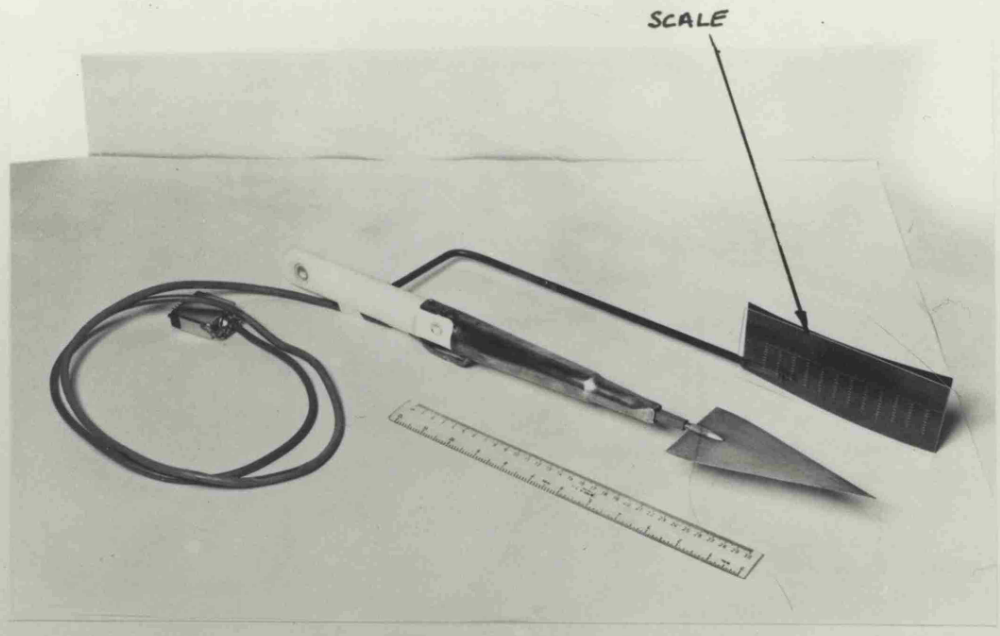

FIG 5.04 STING AND MODEL WING WITH SCALE FOR MEASURING POSITION OF LEADING EDGE VORTICES

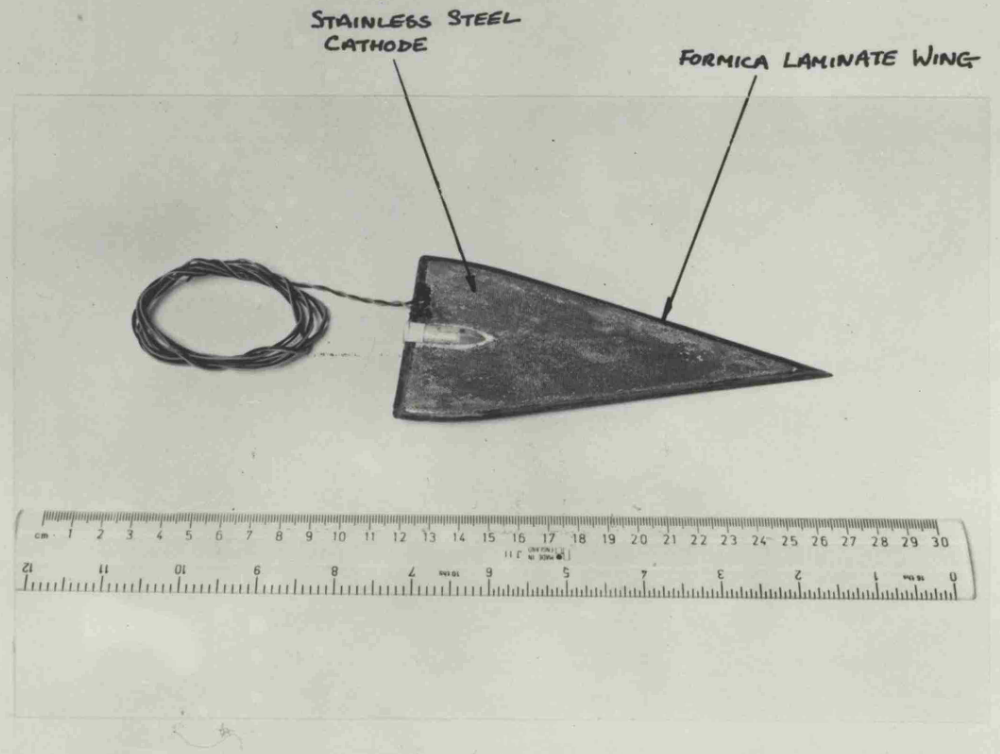

FIG 5.05 UNDERSIDE OF FORMICA LAMINATE WING USED FOR FLOW VISUALISATION SHOWING STAINLESS STEEL CATHODE

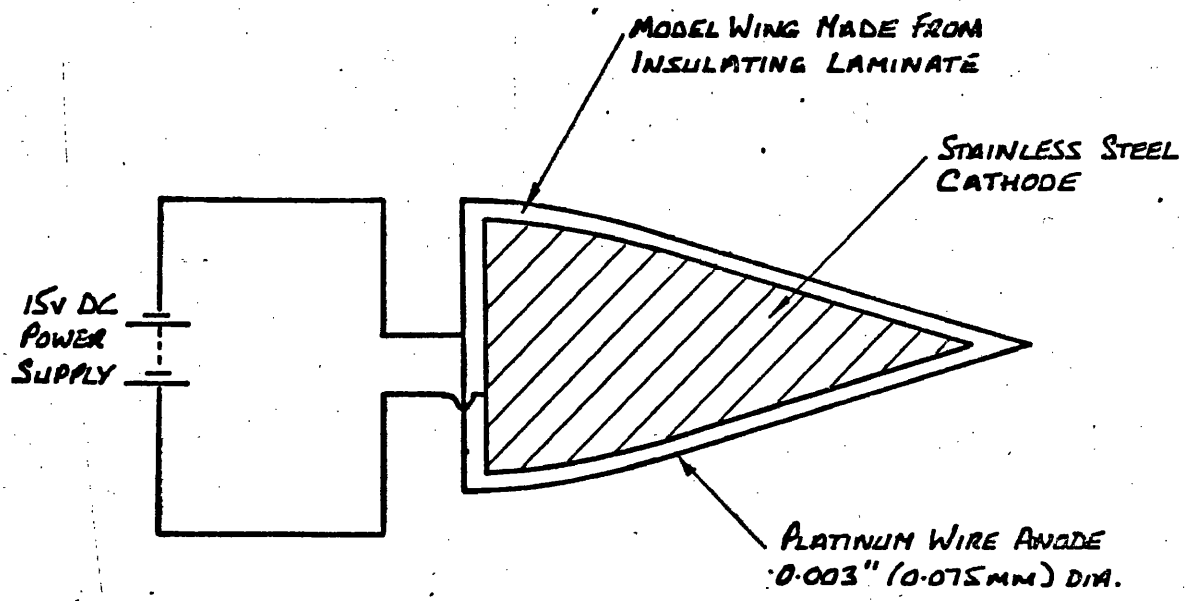

FIG 5.06 SCHEMATIC DIAGRAM OF ELECTROLYSIS CIRCUIT FOR HYDROGEN BUBBLE TECHNIQUE

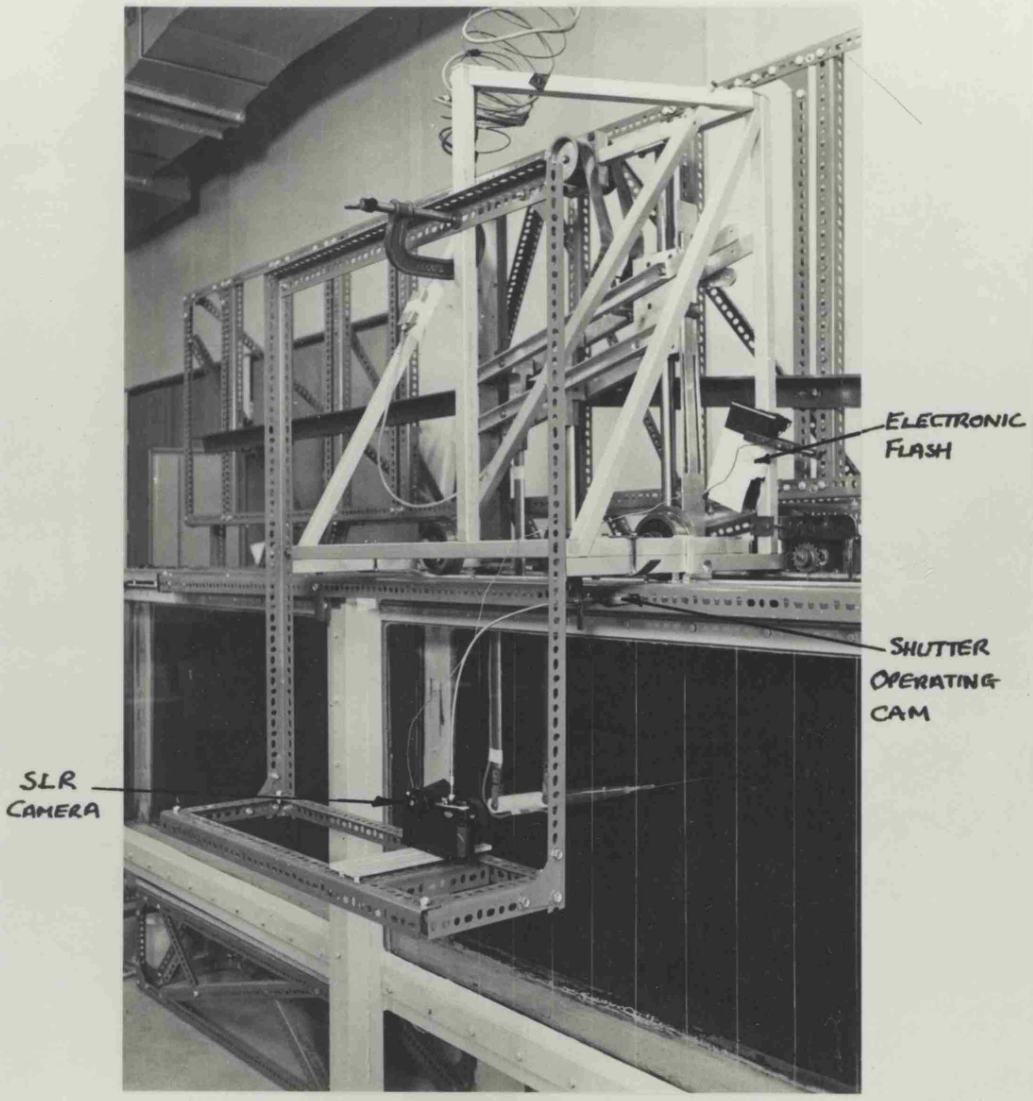

FIG 5.07 EXPERIMENTAL ARRANGEMENT FOR PHOTOGRAPHING LEADING-EDGE VORTICES WITH STILL CAMERA

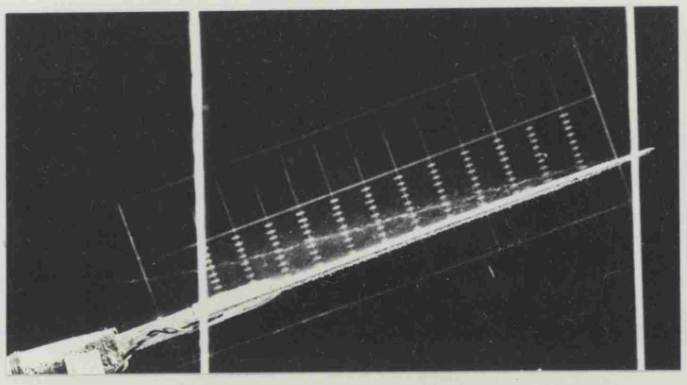

STEADY RUN AT CONSTANT INCIDENCE

$\alpha = 18°$

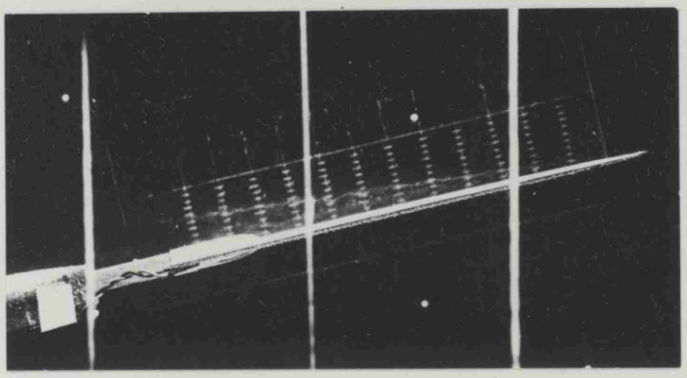

PLUNGING MANOEUVRE

$\frac{\dot{\omega} C_0}{V^2} = +0.0525$

$\alpha = 18°$

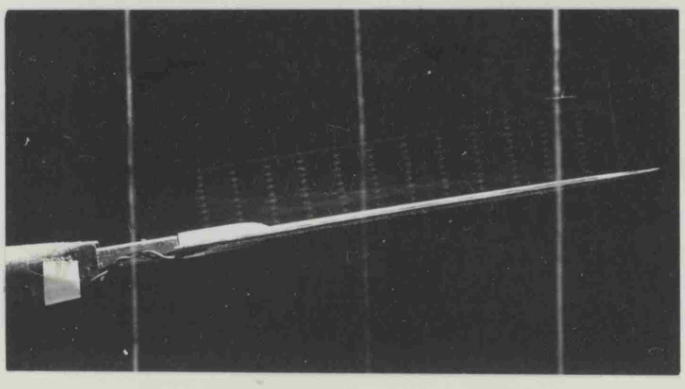

PLUNGING MANOEUVRE

$\frac{\dot{\omega} C_0}{V^2} = +0.0525$

$\alpha = 18°$

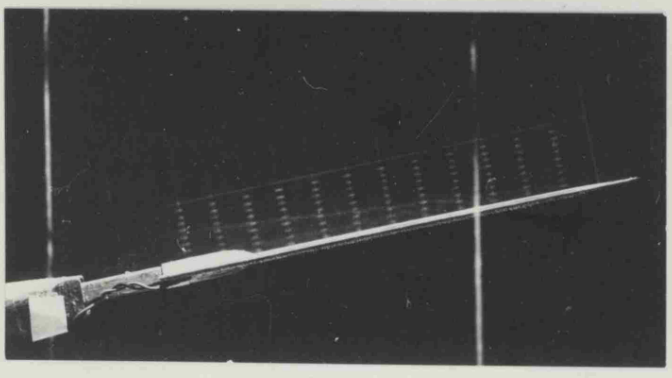

CONSTANT q_V MANOEUVRE

$\frac{q_V C_0}{V} = -0.0525$

$\alpha = 17° 20'$

FIG 5.08 POSITION IN ELEVATION OF LEADING EDGE VORTICES DURING STEADY AND UNSTEADY RUNS

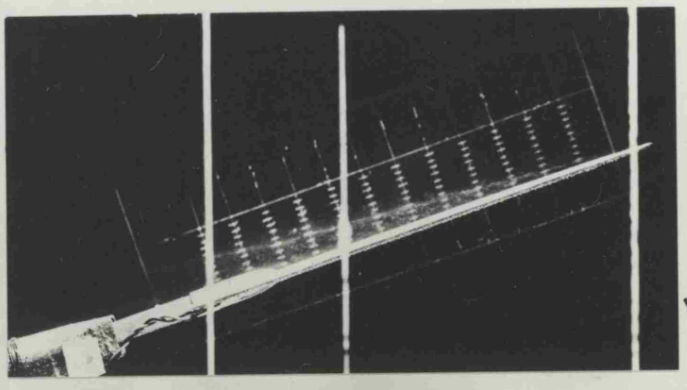

PITCHING MANOEUVRE

$\frac{\dot{\theta} c_0}{V} = +0.0525$

$\alpha = 18°$

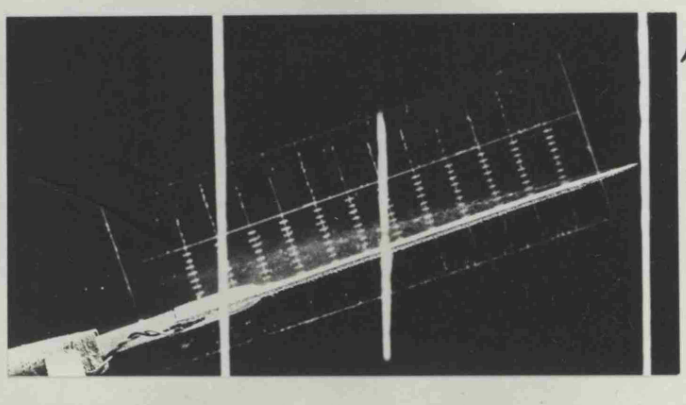

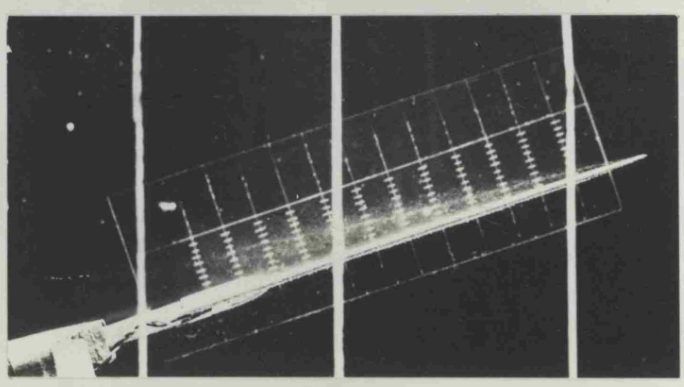

PITCHING MANOEUVRE

$\frac{\dot{\theta} c_0}{V} = -0.0525$

$\alpha = 18°$

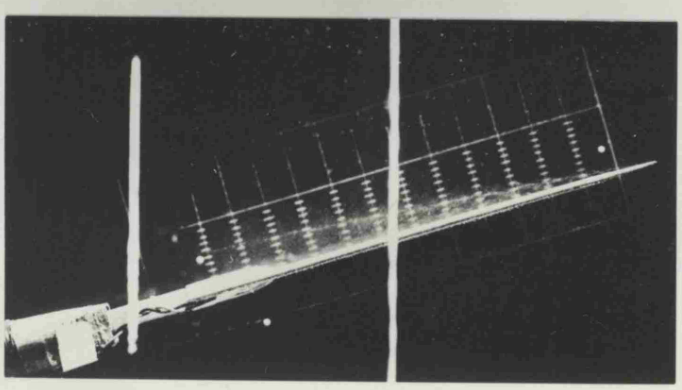

FIG 5.09 POSITION IN ELEVATION OF LEADING EDGE VORTICES DURING PITCHING MANOEUVRES

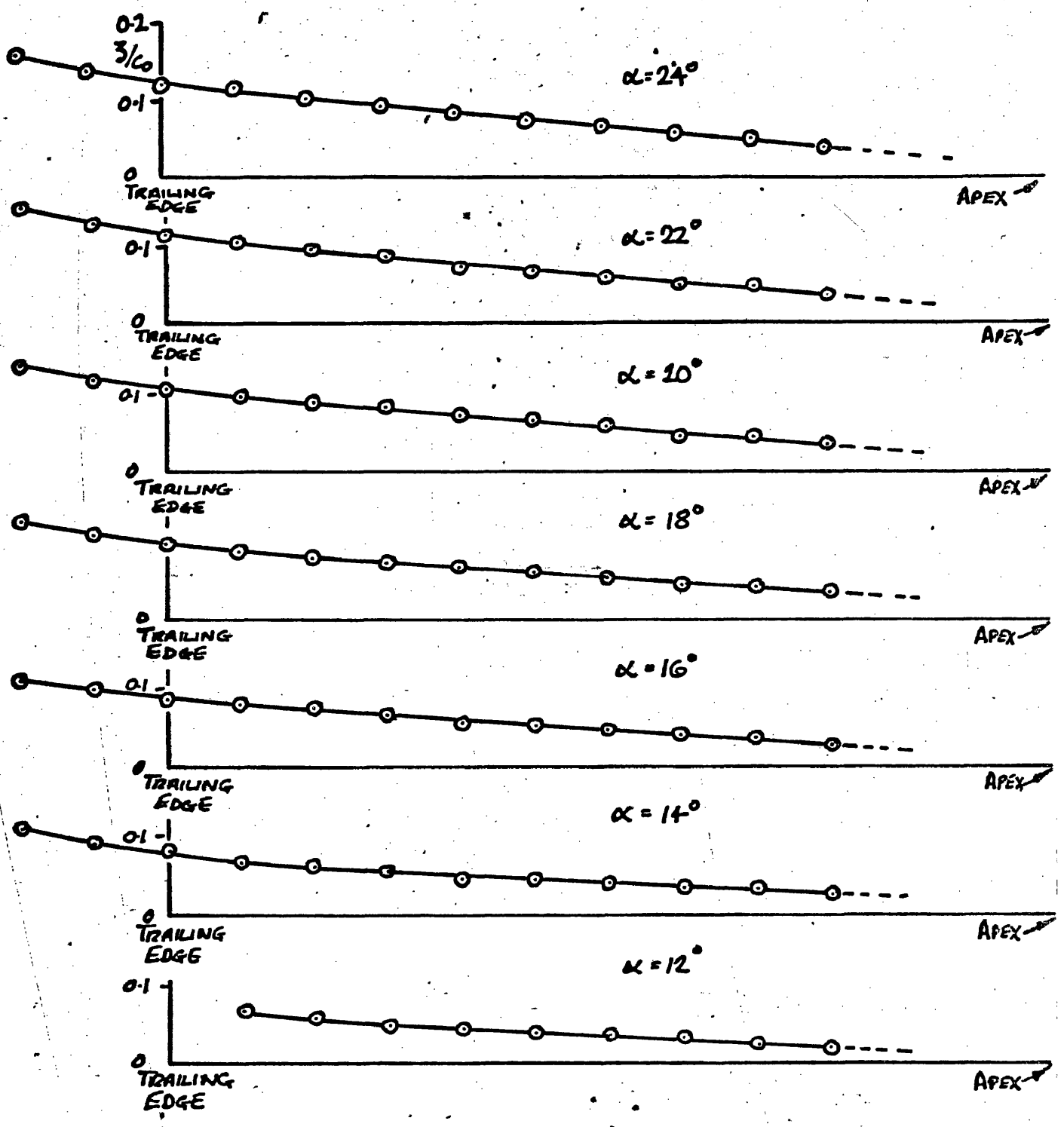

FIG 5.10 POSITION IN ELEVATION OF LEADING EDGE VORTEX CORE DURING STEADY RUN AT CONSTANT INCIDENCE

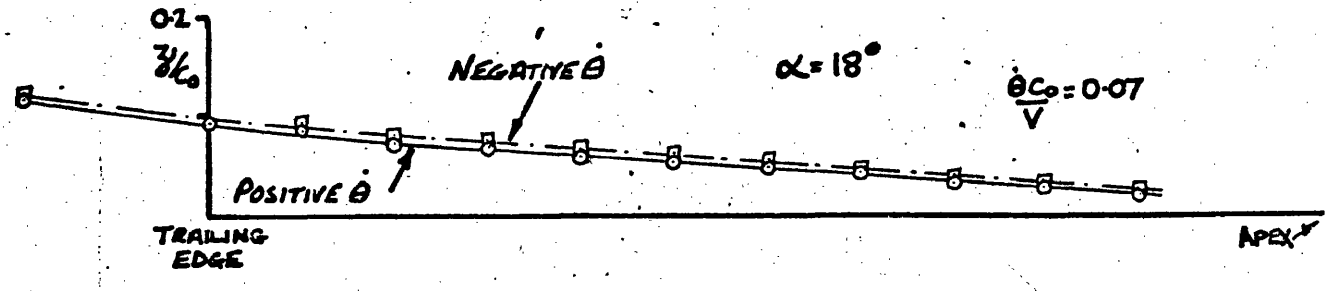

(a) PITCHING MANOEUVRE

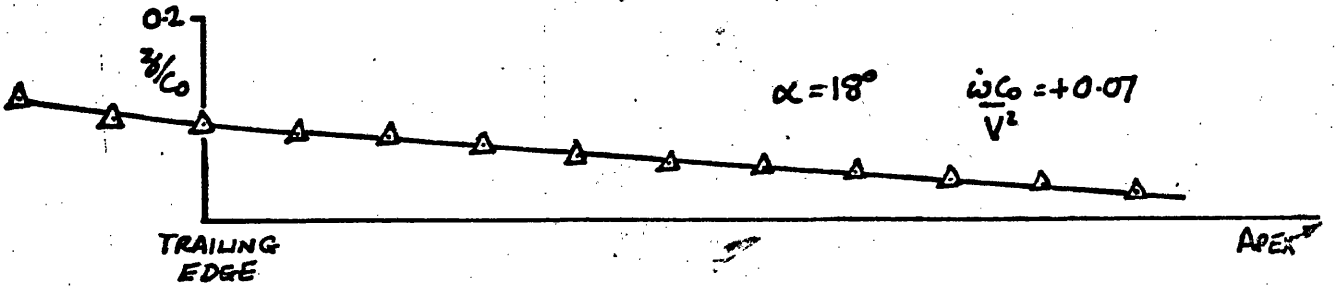

(b) PLUNGING MANOEUVRE

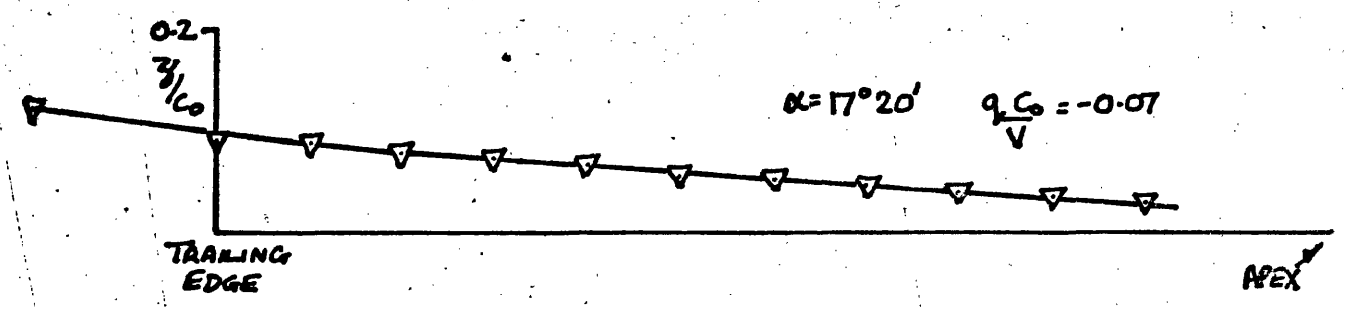

(C) CONSTANT q MANOEUVRE

FIG 5.11 POSITION IN ELEVATION OF LEADING EDGE VORTEX CORE DURING UNSTEADY MANOEUVRES

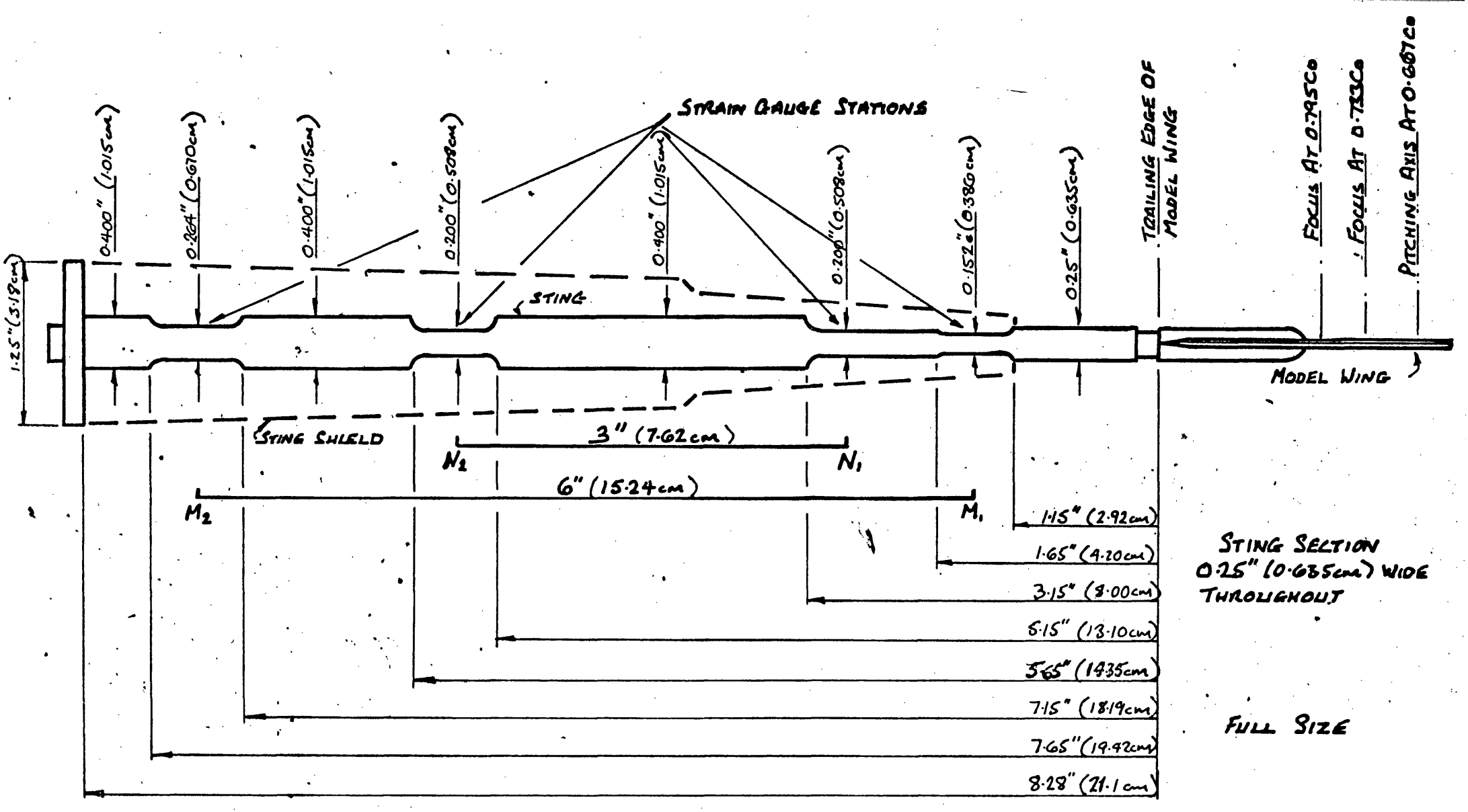

FIG A1.1 DETAIL OF STING SHOWING DIMENSIONS AND MEASUREMENT STATIONS AND STING SHIELD

FIG A1.1

FIG. A1.2

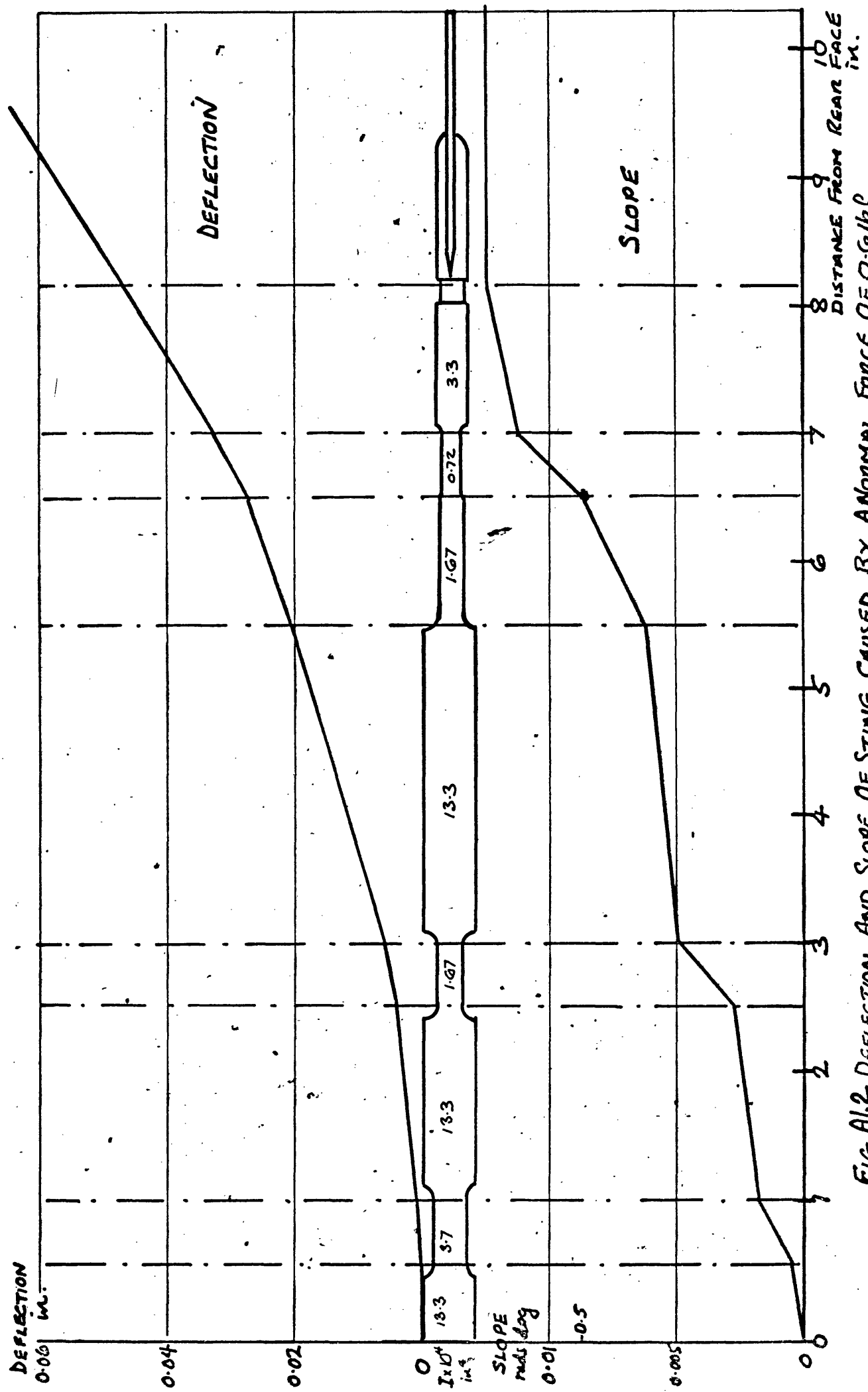

FIG A1.2 DEFLECTION AND SLOPE OF STING CAUSED BY A NORMAL FORCE OF 0·6 lbf

FIGS A2.1a & A2.1b

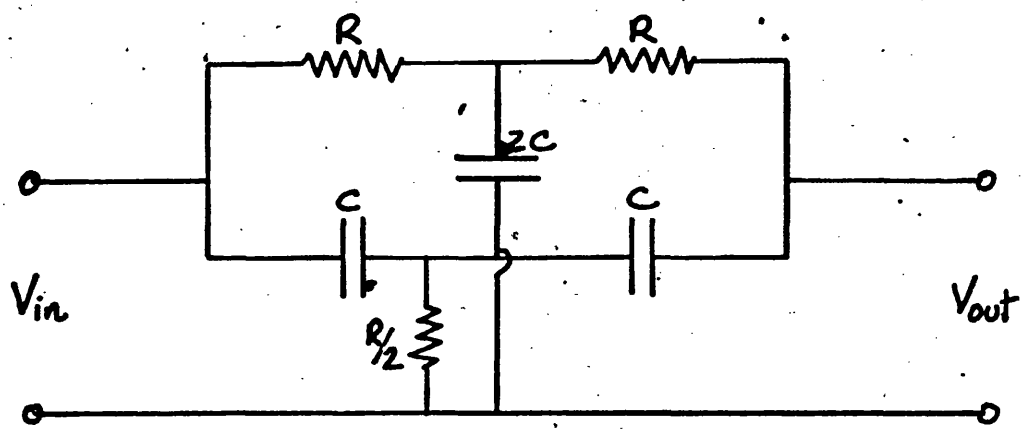

THE TRANSFER FUNCTION IS $\frac{V_{out}}{V_{in}} = \frac{1+(Ts)^2}{1+4Ts+(Ts)^2}$

AND THE PHASE ANGLE IS $\phi = \tan^{-1} \frac{2\zeta\omega/\omega_n}{[1-(\omega/\omega_n)^2]}$

WHERE $T = \frac{1}{\omega_n} = RC$ and $\zeta = 2$

FIG A2.1a CIRCUIT DIAGRAM OF NOTCH FILTER

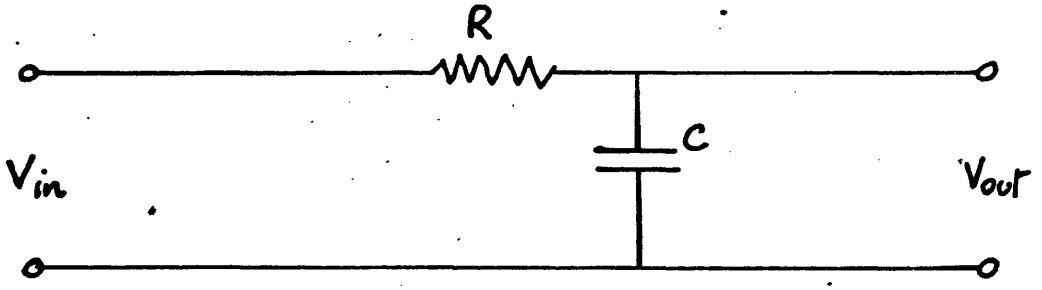

THE TRANSFER FUNCTION IS $\frac{V_{out}}{V_{in}} = \frac{1}{1+Ts}$

WHERE $T = RC$

FIG A2.1b CIRCUIT DIAGRAM OF LOW-PASS FILTER

FIGS A2.2a & A2.2b

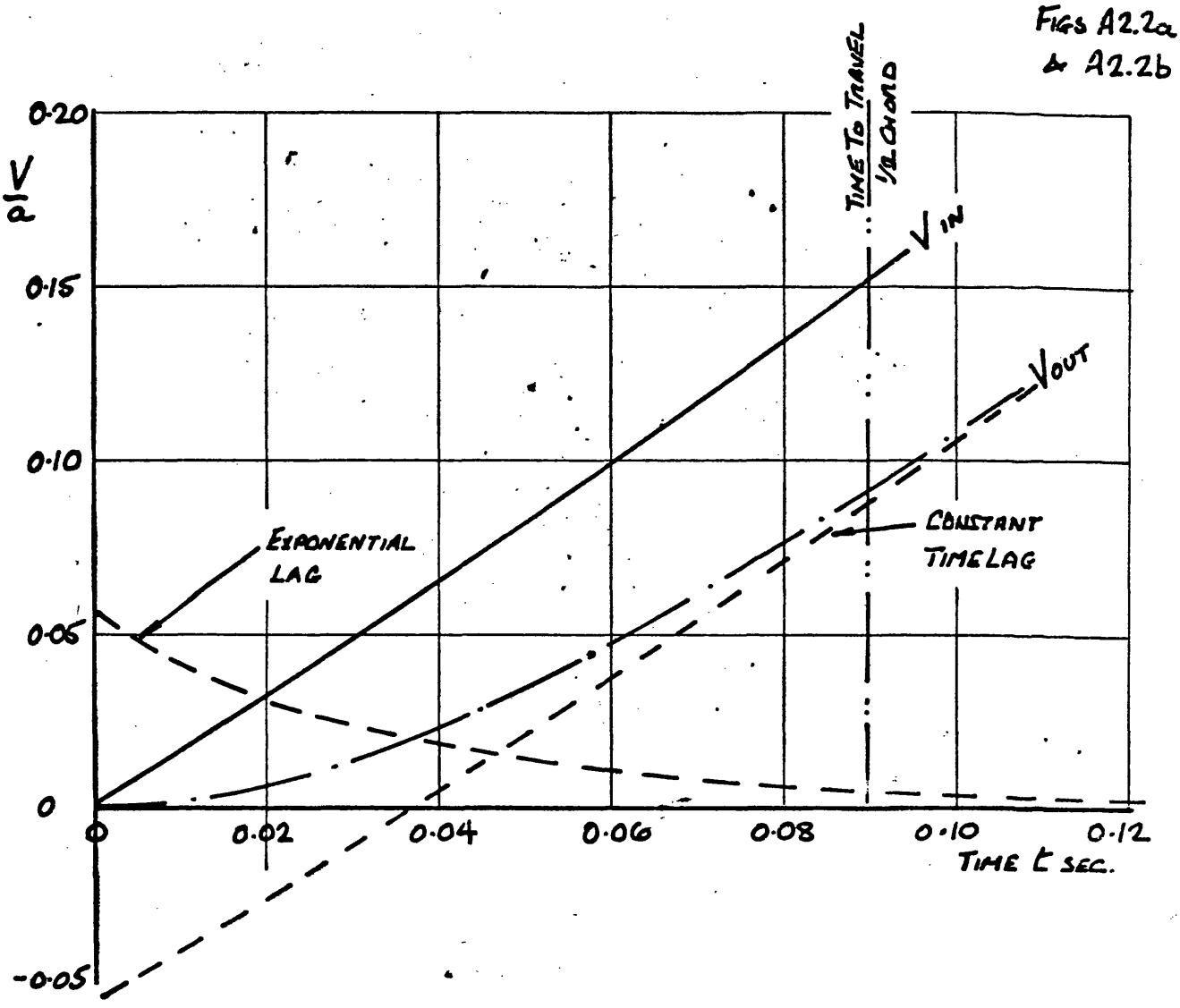

FIG A2.2a TIME LAG PRODUCED BY 17·5Hz NOTCH FILTER ON OUTPUT SIGNAL FOR $\frac{\dot{\theta}C_0}{V}$ OR $\frac{\dot{\omega}C_0}{V^2}$ = 0·07

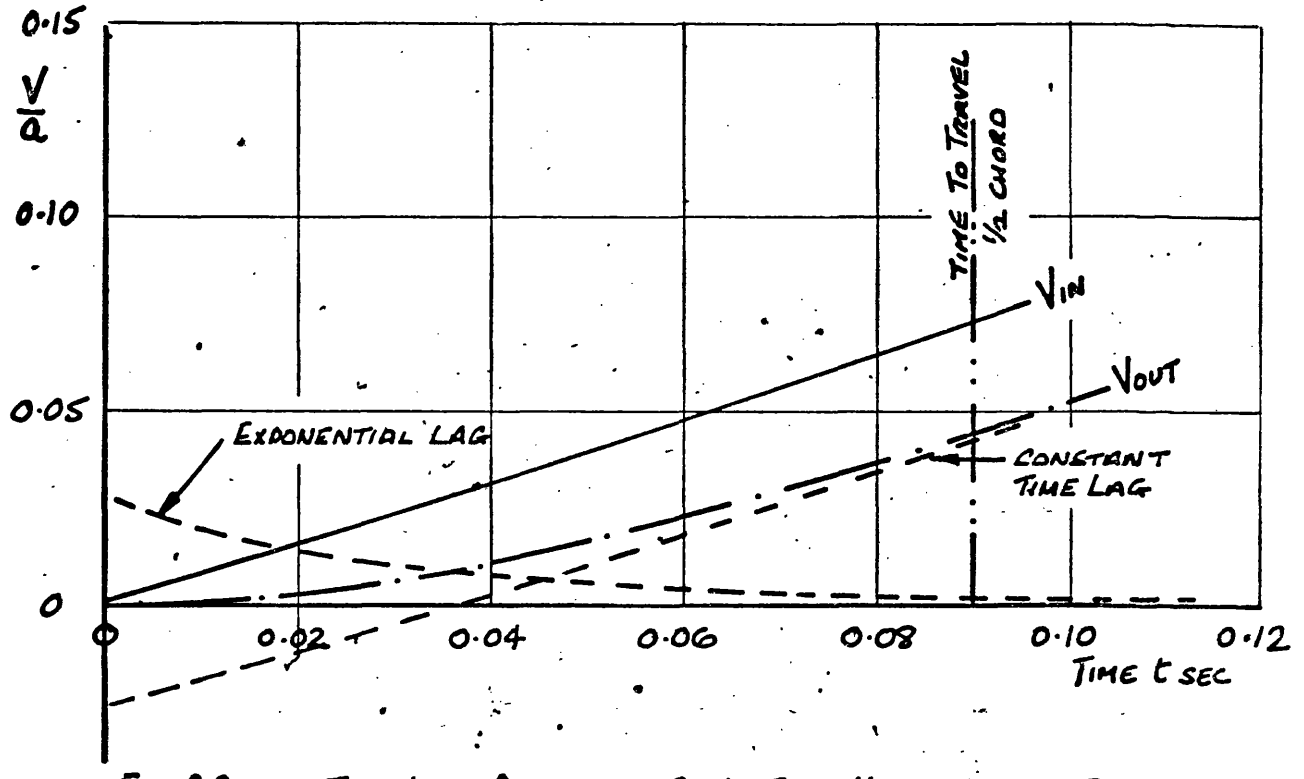

FIG A2.2b TIME LAG PRODUCED BY 17·5Hz NOTCH FILTER ON OUTPUT SIGNAL FOR $\frac{\dot{\theta}C_0}{V}$ OR $\frac{\dot{\omega}C_0}{V^2}$ = 0·035

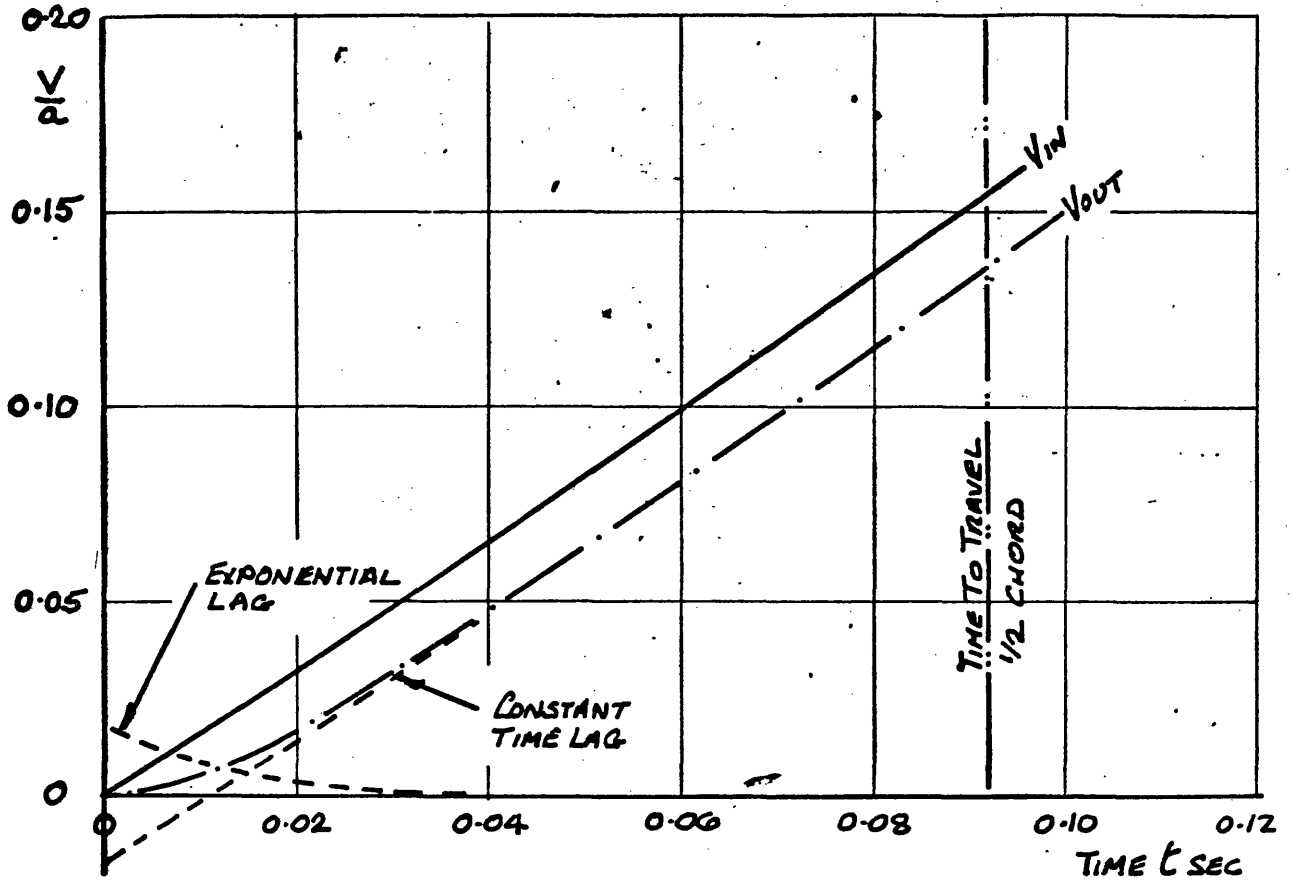

FIG A2.3 TIME LAG PRODUCED BY 14Hz LOW-PASS FILTER ON OUTPUT SIGNAL FOR $\frac{\dot{\theta}c_0}{V}$ OR $\frac{\dot{\omega}c_0}{V^2}$ = 0·07

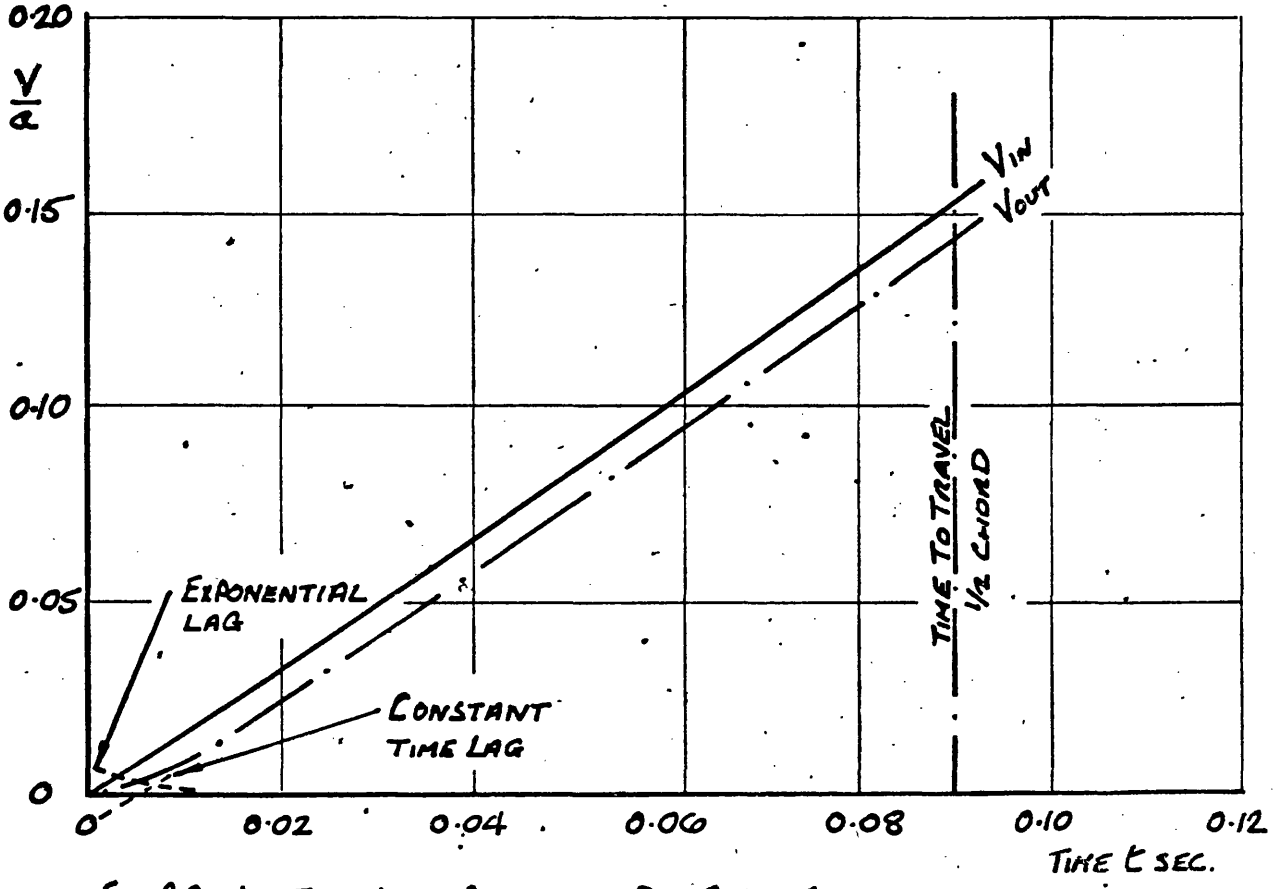

FIG A2.4 TIME LAG PRODUCED BY C.40 GALVANOMETER ON OUTPUT SIGNAL FOR $\frac{\dot{\theta}c_0}{V}$ OR $\frac{\dot{\omega}c_0}{V^2}$ = 0·07

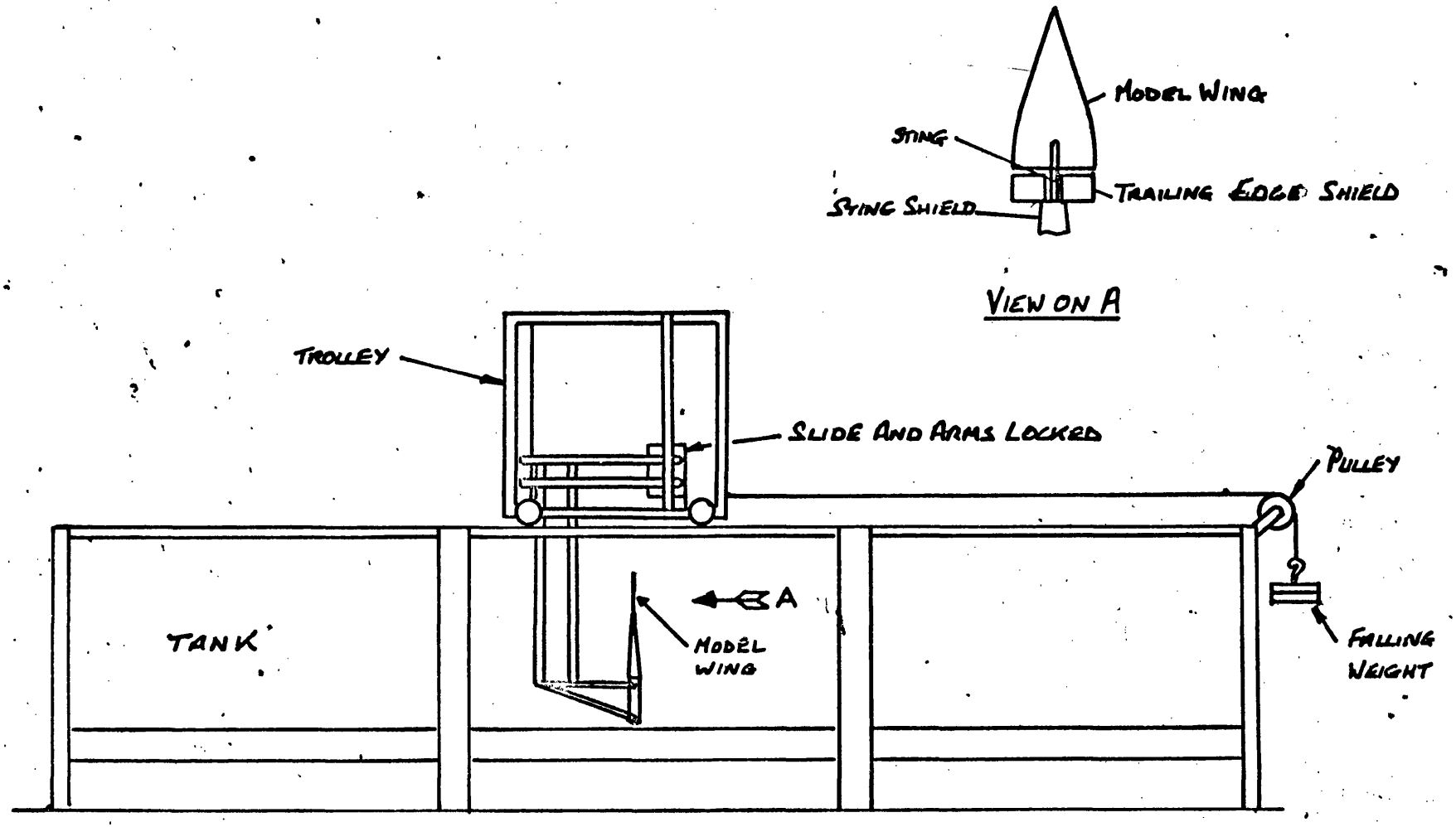

FIG A3.1 EXPERIMENTAL ARRANGEMENT FOR MEASURING VIRTUAL MASS

FIG A3.1

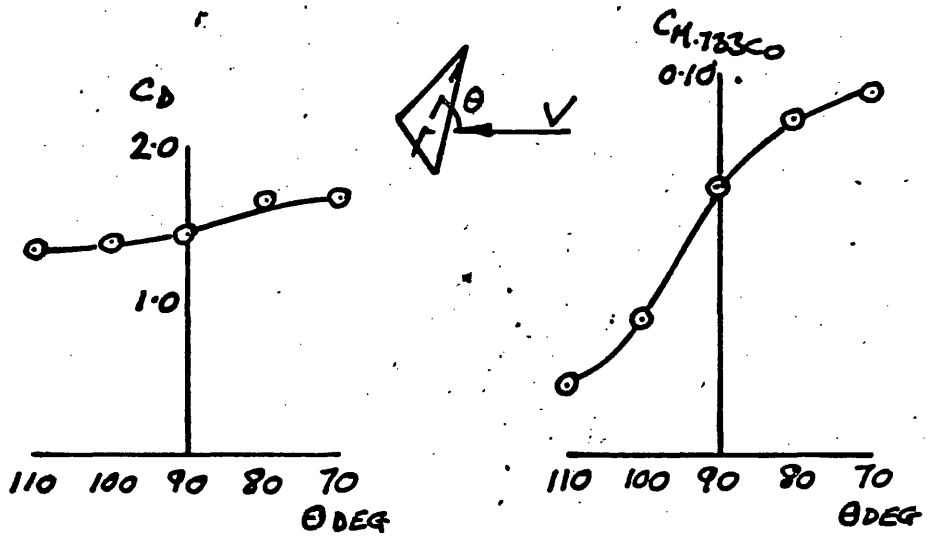

(a) CONSTANT SPEED DRAG AND PITCHING MOMENT

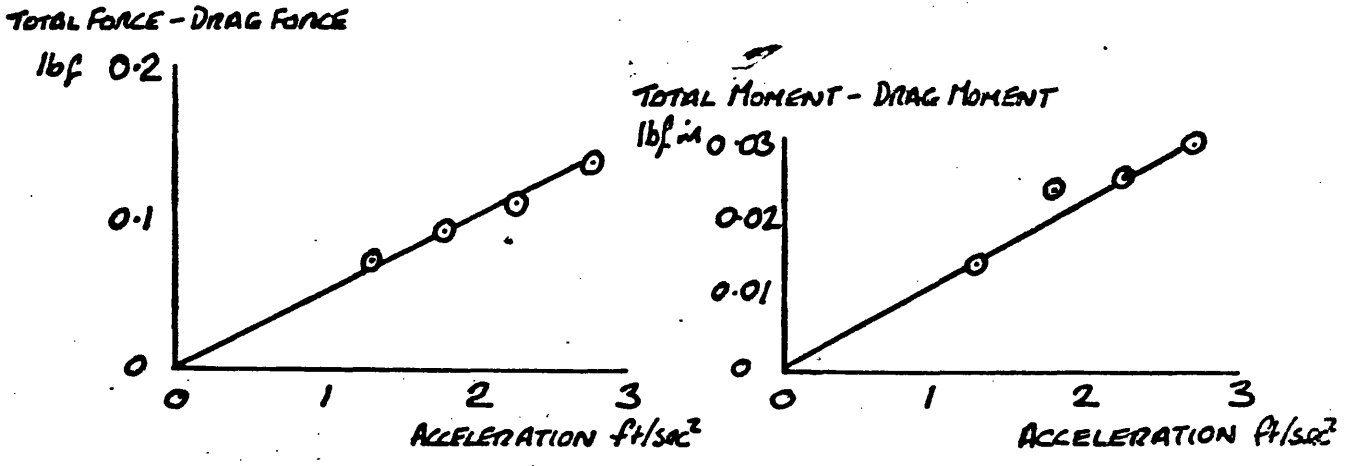

(b) ACCELERATION FORCE AND MOMENT

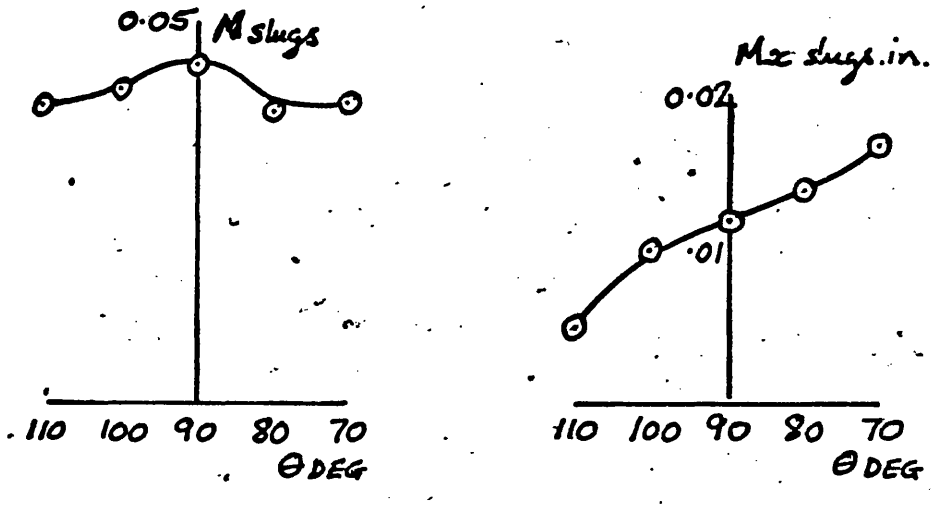

(c) VIRTUAL MASS

(d) MOMENT OF VIRTUAL MASS

FIG A3.2 RESULTS FROM EXPERIMENT TO MEASURE VIRTUAL MASS

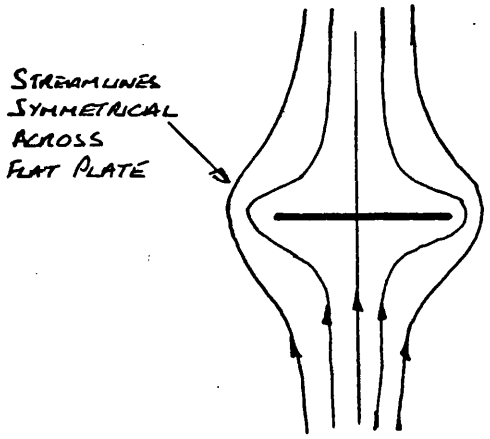

(a) POTENTIAL FLOW USED IN REF. 23

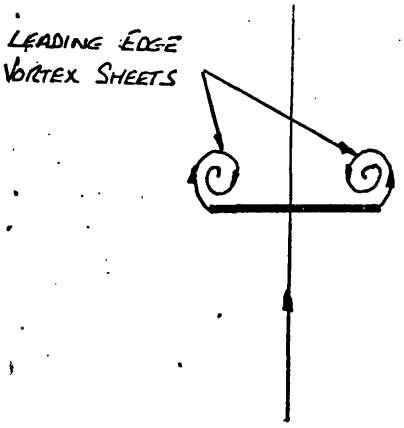

(b) ACTUAL FLOW OVER A SLENDER WING

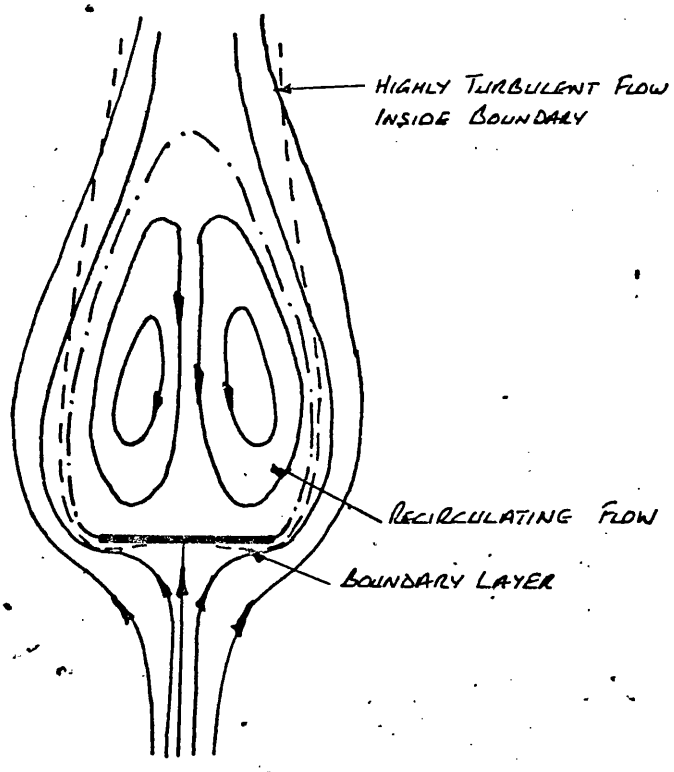

(c) SEPARATED FLOW PAST A FLAT PLATE NORMAL TO THE FREE STREAM

FIG A3.3 COMPARISON OF FLOW PATTERNS USED IN THE ESTIMATION OF VIRTUAL MASS

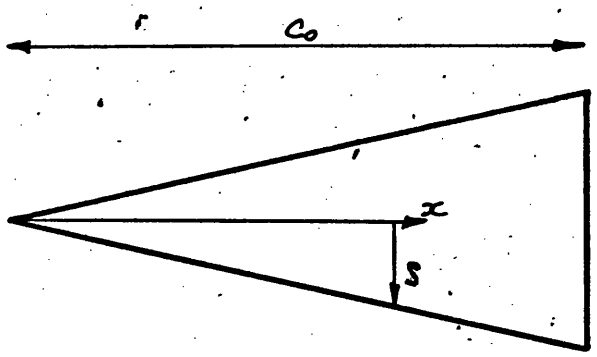

$$S = \frac{A}{4} x$$

(a) DELTA

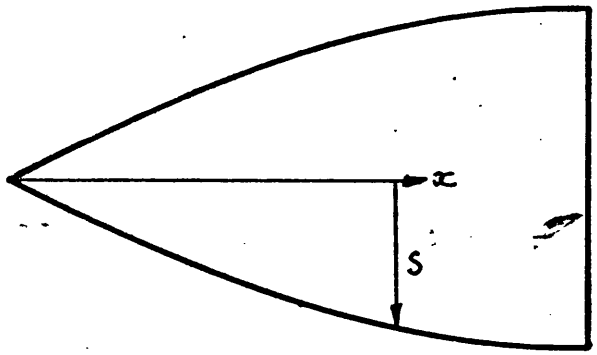

$$S = \frac{A}{3}\left(2x - \frac{x^2}{c_0}\right)$$

(b) GOTHIC

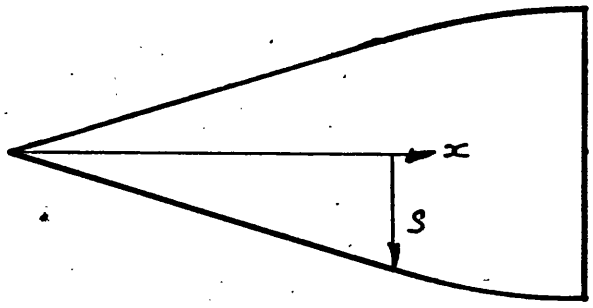

$S = 0.3x$ FOR $0 \leq \frac{x}{c_0} \leq \frac{2}{3}$

$$S = \left[x - \frac{3}{2} c_0 \left(\frac{x}{c_0} - \frac{2}{3}\right)^2\right]$$

FOR $\frac{2}{3} \leq \frac{x}{c_0} \leq 1$

(c) AGARD MODEL G

FIG A4.1 WING PLANFORMS WITH ASPECT RATIO 0·865 USED FOR CALCULATION OF DERIVATIVES BY SLENDER WING THEORY

FIGS A4.2a & A4.2b

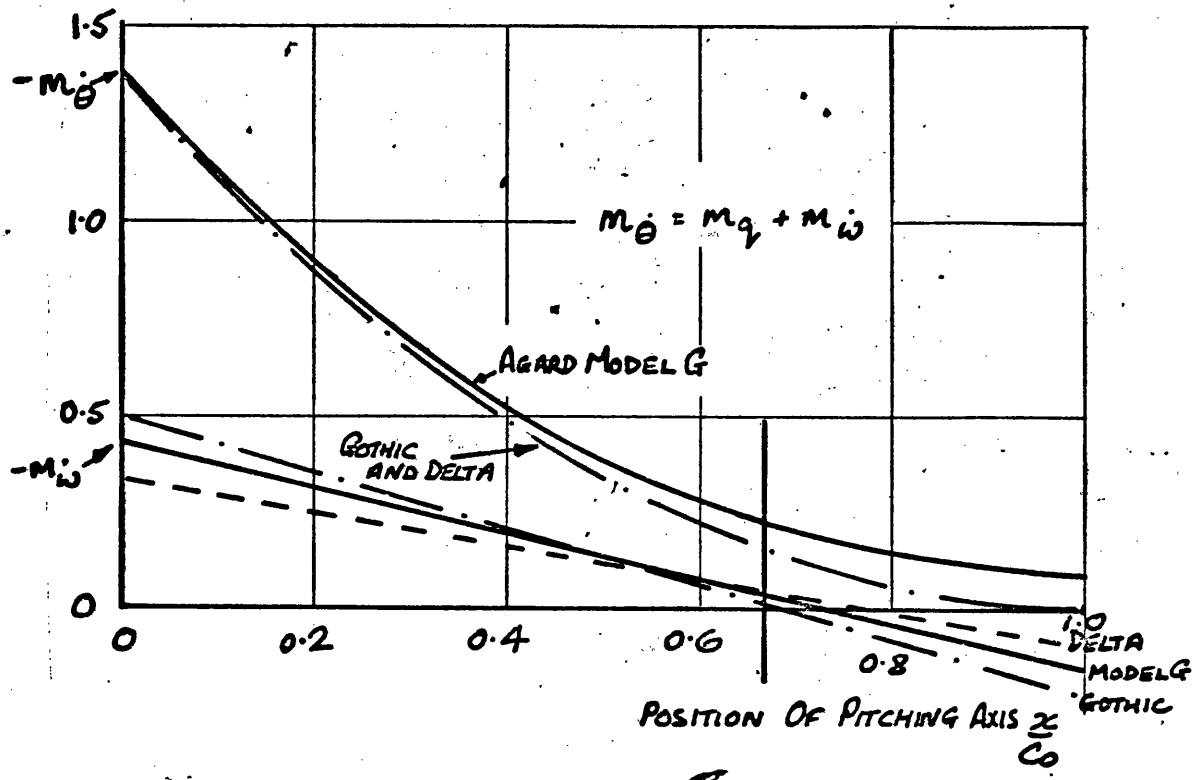

FIG A4.2a PITCHING MOMENT DERIVATIVES FOR WINGS WITH ASPECT RATIO 0·865 CALCULATED FROM SLENDER WING THEORY

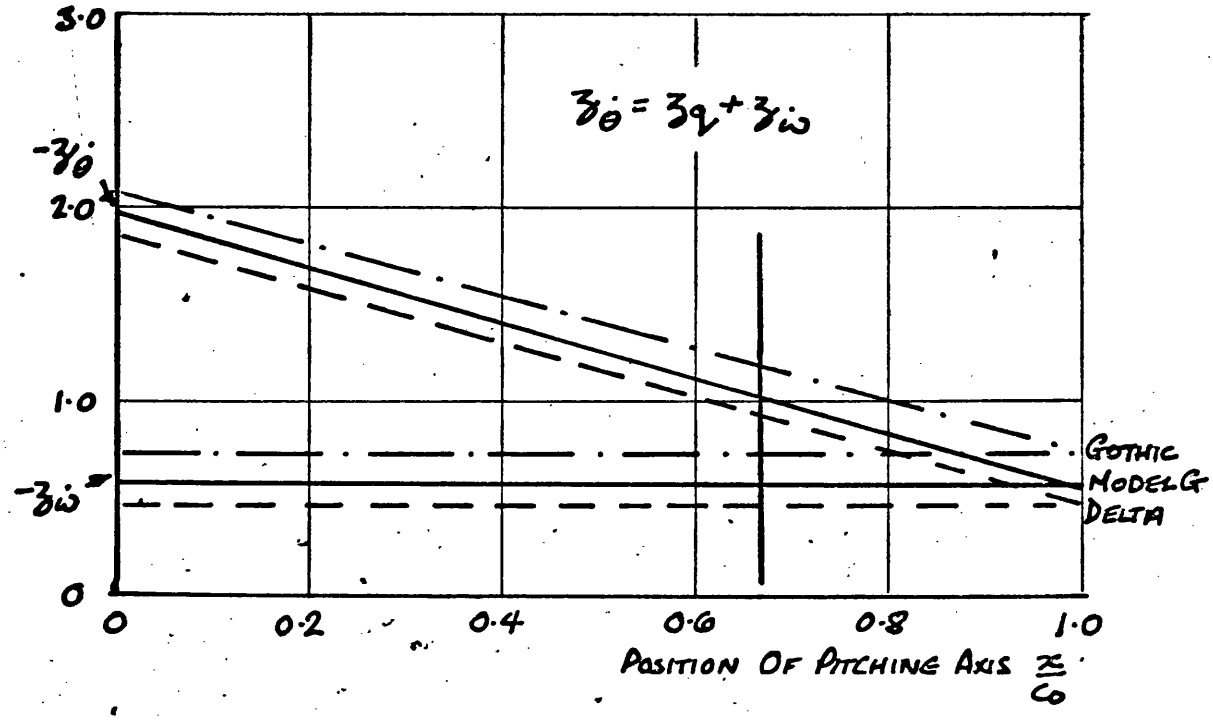

FIG A4.2b NORMAL FORCE DERIVATIVES FOR WINGS WITH ASPECT RATIO 0·865 CALCULATED FROM SLENDER WING THEORY